

RELAP5/MOD3 Code Manual

Validation of Numerical Techniques
in RELAP5/MOD3

Manuscript Completed: August 1994
Date Published: October 1994

Prepared by
A. S. Shieh, V. H. Ransom,¹ R. Krishnamurthy²

Idaho National Engineering Laboratory
Managed by the U.S. Department of Energy

EG&G Idaho, Inc.
Idaho Falls, ID 83415

Prepared for
Division of Systems Research
Office of Nuclear Regulatory Research
U.S. Nuclear Regulatory Commission
Washington, DC 20555-0001
NRC FIN L2245
Under DOE Contract No. DE-AC07-76ID01570

¹Now with Purdue University, Indiana
²Pacific-Nuclear Company, Westmont, IL

AVAILABILITY NOTICE

Availability of Reference Materials Cited in NRC Publications

Most documents cited in NRC publications will be available from one of the following sources:

1. The NRC Public Document Room, 2120 L Street, NW., Lower Level, Washington, DC 20555-0001
2. The Superintendent of Documents, U.S. Government Printing Office, P. O. Box 37082, Washington, DC 20402-9328
3. The National Technical Information Service, Springfield, VA 22161-0002

Although the listing that follows represents the majority of documents cited in NRC publications, it is not intended to be exhaustive.

Referenced documents available for inspection and copying for a fee from the NRC Public Document Room include NRC correspondence and internal NRC memoranda; NRC bulletins, circulars, information notices, inspection and investigation notices; licensee event reports; vendor reports and correspondence; Commission papers; and applicant and licensee documents and correspondence.

The following documents in the NUREG series are available for purchase from the Government Printing Office: formal NRC staff and contractor reports, NRC-sponsored conference proceedings, international agreement reports, grantee reports, and NRC booklets and brochures. Also available are regulatory guides, NRC regulations in the *Code of Federal Regulations*, and *Nuclear Regulatory Commission Issuances*.

Documents available from the National Technical Information Service include NUREG-series reports and technical reports prepared by other Federal agencies and reports prepared by the Atomic Energy Commission, forerunner agency to the Nuclear Regulatory Commission.

Documents available from public and special technical libraries include all open literature items, such as books, journal articles, and transactions. *Federal Register* notices, Federal and State legislation, and congressional reports can usually be obtained from these libraries.

Documents such as theses, dissertations, foreign reports and translations, and non-NRC conference proceedings are available for purchase from the organization sponsoring the publication cited.

Single copies of NRC draft reports are available free, to the extent of supply, upon written request to the Office of Administration, Distribution and Mail Services Section, U.S. Nuclear Regulatory Commission, Washington, DC 20555-0001.

Copies of industry codes and standards used in a substantive manner in the NRC regulatory process are maintained at the NRC Library, Two White Flint North, 11545 Rockville Pike, Rockville, MD 20852-2738, for use by the public. Codes and standards are usually copyrighted and may be purchased from the originating organization or, if they are American National Standards, from the American National Standards Institute, 1430 Broadway, New York, NY 10018-3308.

DISCLAIMER NOTICE

This report was prepared as an account of work sponsored by an agency of the United States Government. Neither the United States Government nor any agency thereof, nor any of their employees, makes any warranty, expressed or implied, or assumes any legal liability or responsibility for any third party's use, or the results of such use, of any information, apparatus, product, or process disclosed in this report, or represents that its use by such third party would not infringe privately owned rights.

ABSTRACT

The RELAP code has been developed for best-estimate transient simulation of light-water reactor coolant systems during large and small break loss-of-coolant accidents and as well as operational transients. The code models the coupled behavior of the reactor coolant system and the core during a severe accident transient and models large- and small-break loss-of-coolant accidents and operational transients, such as anticipated transient without scram, loss of offsite power, loss of feedwater, and loss of flow. A generic modeling approach is used that permits as much of a particular system to be modeled as necessary. Control system and secondary system components are included to permit modeling of plant controls, turbines, condensers, and secondary feedwater conditioning systems.

RELAP5/MOD3 code documentation is divided into five volumes: Volume I provides modeling theory and associated numerical schemes; Volume II contains detailed instructions for code application and input data preparation; Volume III provides the results of developmental assessment cases that demonstrate and verify the models used in the code; Volume IV presents a detailed discussion of RELAP5 models and correlations; Volume V contains guidelines that have evolved over the past several years through use of the RELAP5 code; and Volume VI contains descriptions of numerical modeling of two-phase flow used in RELAP5 and discussions on stability, accuracy, and convergence of the numerical techniques in RELAP5.

CONTENTS

ABSTRACT	iii
LIST OF FIGURES	viii
LIST OF TABLES	x
EXECUTIVE SUMMARY	xiii
ACKNOWLEDGEMENTS	xv
ACRONYMS	xvii
LIST OF SYMBOLS	xix
1. INTRODUCTION	1-1
2. MODELING OF TWO-PHASE FLOW PROBLEMS	2-1
2.1 Introduction to Two-Phase Flow	2-1
2.1.1 Flow Regimes	2-1
2.1.2 Thermodynamics of Two-Phase Systems	2-1
2.1.3 Two-Phase Flow Modeling	2-5
2.2 Fluid Dynamic Modeling	2-6
2.2.1 Microscopic Fluid Processes	2-6
2.2.2 Continuum Basis for Two-Phase Flow Models	2-6
2.2.3 Space-Time Averaged Two-Fluid Models	2-9
2.2.4 Closure Problem for the Two-Fluid Model	2-13
2.3 One-Dimensional Two-Fluid Model	2-14
2.3.1 Spatial Average in One Dimension	2-15
2.3.2 The One-Dimensional Averaged Two-Fluid Model	2-16
2.3.3 Constitutive Models	2-21
3. NUMERICAL METHODS FOR THE TWO-FLUID MODEL IN RELAP5/MOD3	3-1
3.1 Semi-Implicit Numerical Method	3-1
3.1.1 Phasic Balance Equations	3-2
3.1.2 Numerical Solution	3-4

3.1.3	Time Step Control	3-10
3.2	Nearly Implicit Scheme	3-11
3.2.1	Implications of Implicit Differencing	3-11
3.2.2	Time-Step Control	3-17
3.3	Truncation and Linearization Errors of the Numerical Methods in RELAP5	3-18
3.4	Special Numerical Techniques	3-19
3.4.1	Time Smoothing	3-20
3.4.2	Single to Two-Phase Transitions	3-23
3.5	Mass and Energy Errors	3-25
3.6	Comparisons of Numerical Methods	3-26
3.6.1	Single-Step Implicit Scheme	3-26
3.6.2	Comparison of the Three Complete Discretization Methods	3-27
3.6.3	Spatial Discretization Methods	3-28
4.	DOMAIN OF APPLICABILITY OF THE NUMERICAL TECHNIQUES	4-1
4.1	Well-Posedness of Equations with Complex Characteristics	4-2
4.1.1	Complex Characteristics of Two-Phase Flow Equations	4-2
4.1.2	Well-Posedness of Problems with Complex Characteristics	4-3
4.2	Region of Stability, Accuracy, and Convergence for the Semi-implicit Method	4-4
4.2.1	Stability, Consistency, and Convergence	4-4
4.2.2	Stability Analysis for the Semi-Implicit Case	4-8
4.2.3	Region of Stability, Accuracy, and Convergence	4-16
4.3	Region of Stability, Accuracy, and Convergence for the Nearly Implicit Scheme	4-18
4.3.1	Stability Analysis for the Nearly Implicit Method	4-18
4.3.2	Region of Stability, Accuracy, and Convergence	4-21
4.4	Conclusions	4-24

5.	COMPARISON WITH ANALYTICAL SOLUTION AND SEPARATE EFFECTS EXPERIMENTS	5-1
5.1	Convergence Test	5-1
5.2	Water Faucet Problem	5-2
5.3.1	Annulus Model	5-3
5.3	The Edward's Pipe Problem	5-12
5.4	Christensen Subcooled Boiling Test 15	5-15
5.5	Oak Ridge National Laboratory Void Profile Test	5-24
5.6	Time Smoothing Studies	5-29
5.6.1	One-Foot General Electric Level Swell Test 1000-3	5-34
5.7	Other Related Studies	5-34
5.8	Conclusions	5-37
6.	REFERENCES	6-1

LIST OF FIGURES

2-1.	Two-phase heat transfer and hydrodynamic regimes during reflooding	2-2
2-2.	Temperature—entropy diagram for two-phase system	2-4
2-3.	Length scale in fluid systems and models	2-7
2-4.	RELAP5/MOD2 horizontal flow regime map	2-23
2-5.	Transition void fraction between bubbly and slug flow regime	2-23
2-6.	Schematic of vertical flow regime map with hatchings indicating transitions	2-23
2-7.	Thermal energy flow diagram for the two-fluid model	2-30
3-1.	Difference equation discretization schematic	3-5
3-2.	Matrix representation of the semi-implicit difference scheme	3-8
3-3.	Matrix representation of the nearly-implicit difference scheme	3-15
3-4.	Illustration of conditions that result in water packing	3-25
5-1.	FAUCET, spatial convergence at 0.25 s, void versus length	5-4
5-2.	FAUCET, spatial convergence at 0.50 s, void versus length	5-4
5-3.	FAUCET, spatial convergence at 0.75 s, void versus length	5-5
5-4.	FAUCET, spatial convergence at steady state, void versus length	5-5
5-5.	FAUCET, spatial convergence at 0.50 s, mass versus length	5-6
5-6.	FAUCET, spatial convergence at steady state, mass versus length	5-6
5-7.	FAUCET, temporal convergence at 0.25 s, gas void versus length	5-7
5-8.	FAUCET, temporal convergence at 0.50 s, gas void versus length	5-7
5-9.	FAUCET, temporal convergence at 0.75 s, gas void versus length	5-8
5-10.	FAUCET, temporal convergence at steady state, gas void versus length	5-8
5-11.	FAUCET, temporal convergence at 0.50 s, mass in pipe versus length	5-9

5-12.	FAUCET, convergence at steady state, mass versus length	5-9
5-13.	FAUCET, ANNULUS MODEL, TIME = 0.25 s	5-10
5-14.	FAUCET, ANNULUS MODEL, TIME = 0.50 s	5-10
5-15.	FAUCET, ANNULUS MODEL, TIME = 0.75 s	5-11
5-16.	FAUCET, ANNULUS MODEL, TIME = 2 s	5-11
5-17.	EDWARDS, spatial convergence, pressure versus time	5-13
5-18.	EDWARDS, spatial convergence, liquid void versus time	5-13
5-19.	EDWARDS, spatial convergence, liquid void versus length	5-14
5-20.	EDWARDS, spatial convergence, mass versus length	5-14
5-21.	EDWARDS, temporal convergence, pressure versus time	5-16
5-22.	EDWARDS, temporal convergence, liquid void versus time	5-16
5-23.	EDWARDS, temporal convergence, liquid void versus length	5-17
5-24.	EDWARDS, temporal convergence, mass versus time step	5-17
5-25.	EDWARDS, spatial convergence (option 17), pressure versus time	5-18
5-26.	EDWARDS, spatial convergence (option 17), liquid void versus time	5-18
5-27.	EDWARDS, spatial convergence (option 17), liquid void versus length	5-19
5-28.	EDWARDS, temporal convergence (option 17, 20 nodes), pressure versus time	5-19
5-29.	EDWARDS, temporal convergence (option 17, 20 nodes), liquid void versus time	5-20
5-30.	EDWARDS, temporal convergence (option 17, 20 nodes), liquid void versus length	5-20
5-31.	EDWARDS, temporal convergence (option 17, 20 nodes), mass versus time step	5-21
5-32.	EDWARDS, temporal convergence (option 17, 80 nodes), pressure versus time	5-21

5-33.	EDWARDS, temporal convergence (option 17, 80 nodes), liquid void versus time	5-22
5-34.	EDWARDS, temporal convergence (option 17, 80 nodes), liquid void versus length	5-22
5-35.	EDWARDS, temporal convergence (option 17, 80 nodes), mass versus time step	5-23
5-36.	CHRISTENSEN, spatial convergence, void versus length	5-26
5-37.	CHRISTENSEN, temporal convergence (20 nodes)	5-26
5-38.	CHRISTENSEN, temporal convergence (80 nodes)	5-27
5-39.	ORNL, spatial convergence, rod temperature versus length	5-27
5-40.	ORNL, spatial convergence, steam temperature versus length	5-28
5-41.	ORNL, spatial convergence, void versus length	5-28
5-42.	ORNL, spatial convergence, sensitivity study	5-29
5-43.	ORNL, temporal convergence (24 vols.), steam temperature versus length	5-30
5-44.	ORNL, temporal convergence (24 vols.), void versus length	5-30
5-45.	ORNL, temporal convergence (96 vols.), rod temperature versus length	5-31
5-46.	ORNL, temporal convergence (96 vols.), steam temperature versus length	5-31
5-47.	ORNL, temporal convergence (96 vols.), void versus length	5-32
5-48.	ORNL, temporal convergence (24 vols.), rod temperature versus length	5-32
5-49.	ORNL, temporal convergence (24 vols.), sensitivity study	5-33
5-50.	ORNL, temporal convergence (96 vols.), sensitivity study	5-33
5-51.	EDWARDS, temporal convergence, Mod2.5 time smoothing	5-35
5-52.	GE, temporal convergence, Mod2.5 time smoothing	5-35

LIST OF TABLES

2-1.	Parameters of the general balance equation	2-8
------	--	-----

2-2.	Summary of the equations, dependent variables, and auxiliary parameters for the reduced one-dimensional space-time averaged two-fluid model	2-20
2-3.	RELAP5/MOD2 precritical heat flux bulk energy exchange models	2-32
2-4.	RELAP5/MOD2 postcritical heat flux bulk energy exchange models	2-33
2-5.	RELAP5/MOD2 wall vapor generation models	2-33
4-1.	Stewart's (1979) calculations	4-13
5-1.	RELAP5/MOD3 Nonequilibrium Model Development Assessment Matrix	5-24



EXECUTIVE SUMMARY

The RELAP5 code is used by government regulators and the power industry in the United States and many foreign countries to analyze the thermal-hydraulic transient behavior of reactors. The equations, the physical models used in the equations, the methods of solutions, and the recommended modeling and nodalization practices for users have been documented in specific RELAP5 user manuals. The mathematical basis for the numerical method of solution used, however, has not been fully documented in the RELAP5 manuals.

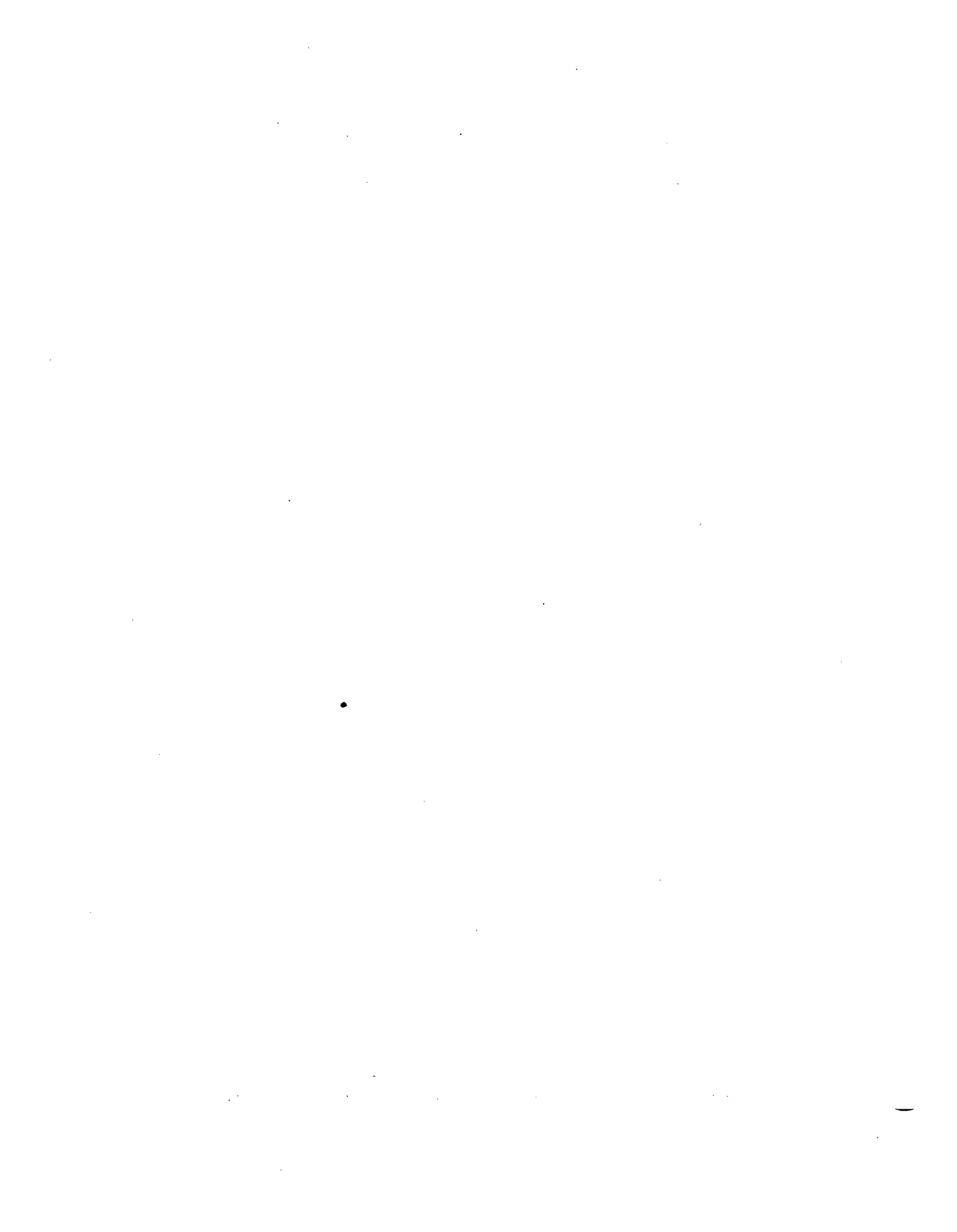
This research will describe the derivation process for the one-dimensional space-time averaged two-phase flow equations used in the code, the assumptions made in the derivations, the solution procedures, the constitutive models, and the accuracy, stability, and convergence of the calculations to a solution of the original equations. In addition, numerical comparisons to analytical solution and separate effects experiments are given for four simple problems, the water faucet problem, the Edwards pipe problem, the Christensen's subcooled boiling problem, and the Oak Ridge void profile problem.

The main results obtained in this work regarding the accuracy, stability, and convergence of the calculations are as follows:

- The computational mesh size used should be compatible with the modeling scale
- The restriction of the analytic problem to a compatible mesh constitutes a well-posed problem
- The numerical solutions are stable and convergent to a solution of the restriction of the analytic problem to a compatible computational mesh.

Numerical studies show that the solutions are stable and convergent to the experimental data for the Edwards pipe problem and the Christensen's subcooled boiling problem. In the absence of interphase drag, the numerical solution for the water faucet problem is oscillatory in the transient. The computed void fractions for the Oak Ridge void profile studies also show some oscillatory behavior when the number of volumes is increased to 192.

Time step sensitivity studies are done for both MOD3 and MOD2.5 time smoothings for the interphase heat transfer and drag coefficients for the Edwards pipe problem. It is shown that MOD3 time smoothing is time step insensitive and that the MOD2.5 time smoothing using Equation (3-57) instead of Equation (3-58) is also time step insensitive.



ACKNOWLEDGEMENTS

We thank Drs. P. T. Williams, M. W. Wendel, D. G. Morris, and W. G. Craddick and Professors J. Mahaffy and J. Doster for their painstaking effort to review the document and for their comments and suggestions. We are also indebted to Professor J. A. Trapp and Dr. R. A. Riemke for their review of the report. All together, their suggestions help to make this report a much better document than the first draft.

We are also indebted to Mr. J. Wright for his excellent work in technical editing and to Drs. L. Shotkin and C. Troutman of the NRC for their comments in the final review of this document and to the technical monitors responsible for directing the overall project: Dr. C. Troutman of the NRC and Mr. W. H. Rettig of the Department of Energy Idaho Operations Office.

ACRONYMS

CHF	critical heat flux
HEM	homogeneous equilibrium model
EM	evaluation model
LOCA	loss-of-coolant model
MCV	material Courant violating
HOT	high order terms
MOM _S	momentum sum
MOM _D	momentum difference
MASS _S	mass sum
MASS _D	mass difference
ENE _g	vapor energy
ENE _d	liquid energy
TE	truncation error
LE	linearization error
PDE	partial differential equation
ODE	ordinary differential equation
ASWR	asymmetric weighted residuals
ORNL	Oak Ridge National Laboratory
DFT	discrete Fourier transform

LIST OF SYMBOLS

h_g	=	gas enthalpy
h_f	=	liquid enthalpy
S_g	=	gas entropy
S_f	=	liquid entropy
P	=	pressure
T^s	=	saturation temperature
V_g	=	gas specific volume
V_f	=	liquid specific volume
P^s	=	saturation pressure
B_k	=	phasic isobaric expansivity
κ_k	=	phasic isothermal compressibility
C_{pk}	=	phasic specific heat at constant pressure
a	=	sound speed
V	=	specific volume of a two-phase mixture at equilibrium
x	=	mass fraction of vapor
J_k	=	phasic flux of a general property across a volume boundary
Ψ_k	=	phasic mass intensive property
Φ_k	=	phasic mass intensive source
ρ_k	=	phasic mass density
v_k	=	phasic velocity

g	=	gravitational force
Q_k	=	phasic internal energy source
τ_k	=	phasic stress tensor including pressure and viscous stresses
I	=	identity matrix
K_k	=	phasic thermal conductivity
U_k	=	phasic internal energy
P_k	=	phasic pressure
q_k	=	phasic heat flux vector
L	=	physical scale in length
$\bar{\beta}_k$	=	instantaneous volumetric fraction of phase k
$a_{wk}(x, t)$	=	phasic surrounding surface that consists of solid boundaries
$a_o(x, t)$	=	interface surface
n_{wk}	=	unit outward normal vector at the surface a_{wk}
ξ_k	=	unit outward normal vector at the surface a_o
\dot{m}_k	=	interfacial mass flux
Γ_k	=	source term for the phasic mass equations
V_k^T	=	interfacial velocity associated with mass transfer
M_{ok}^{iv}	=	phasic interphase drag parameters
M_{wk}^{iv}	=	fluid friction at the wall
M_{ok}^{nP}	=	virtual mass effect

$\alpha_k Q_k$	=	product of phasic volume fraction with volumetric heat generation
α_k	=	phasic volume fraction
$\mu\phi^2$	=	viscous dissipation term
$q_{ak} A_a$	=	averaged interfacial heat flux
$q_{wk} A_{wk}$	=	averaged heat flux at the wall
C_D	=	steady drag coefficient
ρ_c	=	continuous phase density
A_p	=	planform area per unit volume
d_{sm}	=	Sauter mean particle diameter
N_p	=	particle number density
FI	=	interphase steady drag coefficient
A_a	=	interfacial area per unit volume
α_d	=	dispersed phase volume fraction
We_c	=	critical Weber number
d_{ave}	=	average particle diameter
d'	=	most probable particle diameter
σ	=	surface tension
Re_p	=	particle Reynolds number
μ_m	=	mixture viscosity
α_b	=	volume fraction of Taylor bubbles in the mixture
α_{2s}	=	volume fraction of smaller bubbles in the film and trailing slug

ρ	=	mixture density
C_{vm}	=	virtual mass coefficient
Γ_{ok}	=	mass transfer at the bulk interface
Γ_{wk}	=	wall transfer at the bulk interface
Q_{wk}	=	wall heat transfer rate to the phase k
T_k	=	phasic temperature
h_k^*	=	bulk phase enthalpy if $T_{ok} < 0$ <i>phase saturation enthalpy if $T_{ok} > 0$</i>
H_{ok}	=	interfacial heat transfer coefficient for phase k
Q_{ok}^w	=	heat transfer from wall that produces mass transfer
A	=	area of cell
Γ_g	=	vapor generation rate
$(\tau_w)_g$	=	vapor phase wall friction
$(\tau_w)_f$	=	liquid phase wall friction
B_x	=	x component of the body force vector
τ_σ	=	interphase drag force
u_f	=	liquid internal energy
u_g	=	gas internal energy
q_{wg}	=	wall heat transfer rate to vapor
q_{wf}	=	wall heat transfer rate to liquid
q_{og}	=	interfacial heat transfer rate to vapor

q_{of}	=	interfacial heat transfer rate to liquid
$DISS_g$	=	gas phase dissipation term due to wall friction, dynamic loss, and pump inefficiency
$DISS_f$	=	liquid phase dissipation term due to wall friction, dynamic loss, and pump inefficiency
X_n	=	mass fraction of noncondensable component
V_j	=	volume of the j^{th} control volume
FWF	=	wall frictional force between wall and liquid
FWG	=	wall frictional force between wall and vapor
$VISF$	=	spatial artificial viscosity for the liquid momentum equation
$VISG$	=	spatial artificial viscosity for the vapor momentum equation
$\dot{\alpha}_k$	=	donored phasic void fraction
$\dot{\rho}_k$	=	donored phasic mass density
$\tilde{\Gamma}_g$	=	intermediate value of vapor generation rate
$\tilde{q}_{\alpha k}$	=	intermediate values of interfacial heat transfer rate to the phases
η	=	weighting factor for time smoothing
(\bar{f}_n)	=	time smoothed value at time level n
τ	=	time constant
D	=	hydraulic diameter
D^*	=	Bond number
α	=	void fraction (vapor phase volume fraction)
ρ_v	=	vapor mass density

- u_v = vapor velocity
- ρ_l = liquid mass density
- u_l = liquid velocity
- $||$ = Euclidean norm of a vector
- ϵ_i^n = local truncation error at time level n
- L_i^n = difference operator at time level n
- μ = characteristic of the differential equation
- K = interfacial drag coefficient
- A = Jacobian matrix for the system of partial differential equations
- Ω = diagonal matrix that contains the eigenvalues of the Jacobian matrix A
- λ_i = eigenvalues of the matrix A
- Z = transformed solution vector
- q^H = conjugate transpose of a vector q
- d_o = average diameter of bubbles

RELAP5/MOD3 Code Manual

Volume 6: Validation of Numerical Techniques in RELAP5/MOD3

1. INTRODUCTION

The RELAP5 code is used by government regulators and the power industry in the United States and many foreign countries to analyze the thermal-hydraulic transient behavior of reactors. The confidence a user can have in results from the code is determined by the clarity and depth of theory in the manuals describing the code and its limitations. At this time, manuals are available describing the physical models used in the equations, describing the equations and methods of solutions for programming purposes, and describing the recommended modelling and nodalization practices for users. However, the mathematical basis for the numerical method of solution used is found only in papers scattered through journals, in-house reports, and conference proceedings. Hence, there is no clear basis for the accuracy, stability, or convergence of the calculations to a solution of the original equations when applied to a specific problem.

This NUREG/CR provides RELAP5 documentation sufficiently detailed that the domain of applicability of the numerical techniques and necessary user procedures are both well defined and that the users have increased confidence in the ability to distinguish between model deficiencies and deficiencies in numerical techniques. This is achieved by providing a description of the origin of the space-time averaged two-fluid model and a concise overview of the constitutive models in Section 2, overview of the solution techniques in Section 3, a discussion of the regions of stability, accuracy, and convergence in Section 4, and a comparison between experimental data or theory and numerical simulations for several simple problems with various time steps and nodalizations in Section 5. The final conclusion on the domain of stability and convergence (and therefore also the domain of applicability of the numerical techniques from the users' point of view) is also given at the end of Section 5. In addition, the gap between the theory and the observed well-posedness for coarse meshes for the semi-implicit method in Stewart (1979) is bridged, in a certain sense, in this work.

Sections 2 and 3 borrow very heavily from Ransom (1989), who gives a very good account on numerical modeling of two-phase flow problems. Part of Section 5 was taken from the thesis of Krishnamurthy (1992).

2. MODELING OF TWO-PHASE FLOW PROBLEMS

2.1 Introduction to Two-Phase Flow

Two-phase processes are found in a variety of engineered and natural systems, including boiling systems used in nuclear power plants. The most distinguishing feature of two-phase processes is the presence of an interface across which the fluid properties are essentially discontinuous. Additional complications result from the fact that thermal nonequilibrium between the phases generally accompanies the phase separation, and the fluid can exist in both stable and metastable states (Lienhard 1984). During the past thirty years, the theoretical understanding and the empirical data base for two-phase flow has grown significantly, and attempts to analytically model such flows has progressed from early semi-empirical methods (Zuber and Staub 1967), to the more mechanistic two-fluid models of today (Ransom et al., Richards et al. 1980, 1982, 1985; Micaelli 1987; Allison et al. 1990).

2.1.1 Flow Regimes

Flow regimes are the result of a dynamic balance between the various forces at work in a two-phase flow. Gravitational force has a dominant effect largely because of the buoyancy effect that Other significant forces include surface tension and viscous stresses.

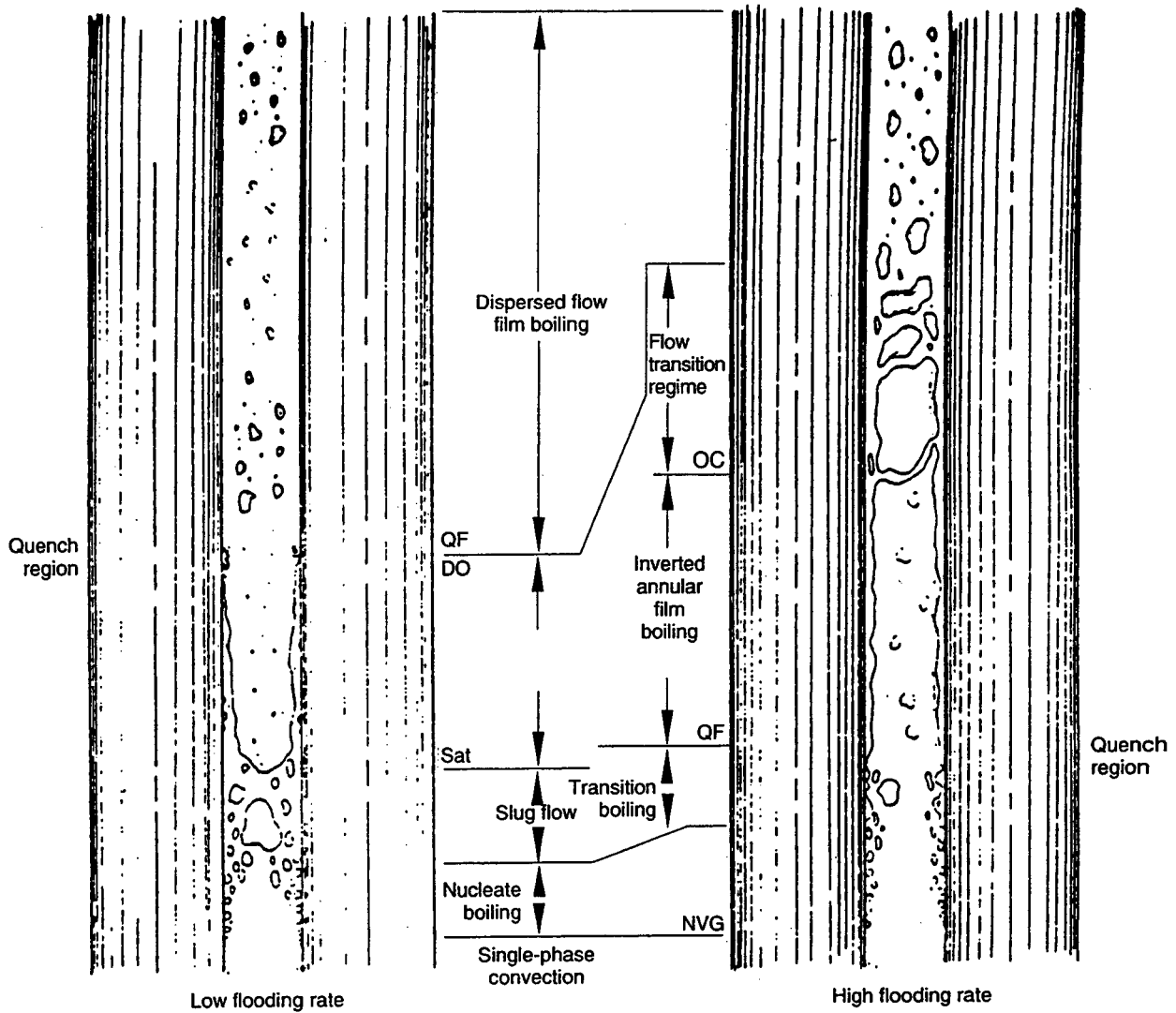
The classifications given here refer to pipe flow, mainly because such flows have few degrees of freedom and, therefore, are easier to classify. The major independent variables are orientation, horizontal or vertical, up flow versus down flow, and heated or unheated. Rouhani and Sohal (1983) identify six flow regimes for each pipe flow orientation, both horizontal and vertical: stratified smooth, stratified wavy, plug, slug, annular, and bubbly. The dominant effect of gravity is such that the film is significantly thicker at the bottom of the pipe than the top for horizontal annular flows.

When heat transfer is added, completely new flow regimes appear, such as inverted annular flow and dispersed droplet flow. These flow regimes are associated with postcritical heat flux (CHF) conditions. The post-CHF flow regimes that can exist with heat transfer under low and high flow have been identified by Yadigaroglu (1978) and are illustrated in Figure 2-1. Condensation-induced flow regime transitions are also observed and can result in severe water-hammer effects.

2.1.2 Thermodynamics of Two-Phase Systems

The thermodynamic behavior of a two-phase system is important for developing equations of the state of the phases, and for establishing the equilibrium conditions for use in heat and mass transfer modeling. Certain thermodynamics derivatives are also needed for linearizing the equations of the state and for calculating equilibrium state reference properties, such as the saturation temperature and the sound speed.

2.1.2.1 Conditions of Equilibrium. It is important that the phase of the two-phase equilibrium be in thermal and mechanical equilibrium and that each component have the same free



NVG - Net vapor generation point
 SAT - Slug-to-annular transition point
 QF - Quench front
 DO - Dryout point
 OC - Onset-of-carryover point

Figure 2-1. Two-phase heat transfer and hydrodynamic regimes during reflooding.

energy in each phase that it appears. In the case of a single-component system, this reduces to equal free energy for each phase. Hence,

$$h_g(P,T(P)) - Ts_g(P,T(P)) = h_f(P,T(P)) - Ts_f(P,T(P)) \quad (2-1)$$

where

$$h_k = \text{phasic enthalpy } (k = g, f)$$

$$s_k = \text{phasic entropy } (k = g, f)$$

$$P = \text{pressure}$$

$$T = \text{saturation temperature.}$$

Differentiation of Equation (2-1) yields the following Clausius-Claperon equation:

$$(dP^S/dT) = (s_g - s_f)/(V_g - V_f) \quad (2-2)$$

where V_k is the phasic specific volume, and P^S denotes the saturation pressure. This equation can also be derived from one of the Maxwell relations (Van Wylen and Sonntag 1965), using the mathematical condition for

$$dh = Tds + VdP$$

to be an exact differential. Equation (2-2) accurately represents the dependence of saturation pressure on temperature and can therefore be used to extrapolate the interfacial temperature dependence on pressure by a two-term Taylor series.

2.1.2.2 Equation of State. The thermal equations of state, $V_k = V_k(P_k, T_k)$, when combined with caloric data $h_k = h_k(P_k, T_k)$, can be used to construct a T-S diagram for the single phase, as well as the two-phase states of the system. Such diagrams are useful for identifying the subcooled liquid, two-phase, and superheated vapor states (see Figure 2-2). The metastable states corresponding to superheated liquid and subcooled vapor are illustrated in Figure 2-2 by extending the isobars for the liquid and the vapor into the two-phase region. The lines end on the spinodal curves (Lienhard 1984), which are the limit curves for the metastable states. States beyond these lines are impossible because they correspond to negative bulk modulus and are thus inherently unstable. In nonequilibrium systems, interphase energy and mass transfer occur from the metastable states such that the system tends toward the stable states. Hence, it is necessary for nonequilibrium modeling to represent the thermal and caloric behavior of the phases in the metastable states, as well as the stable and equilibrium states.

Modeling

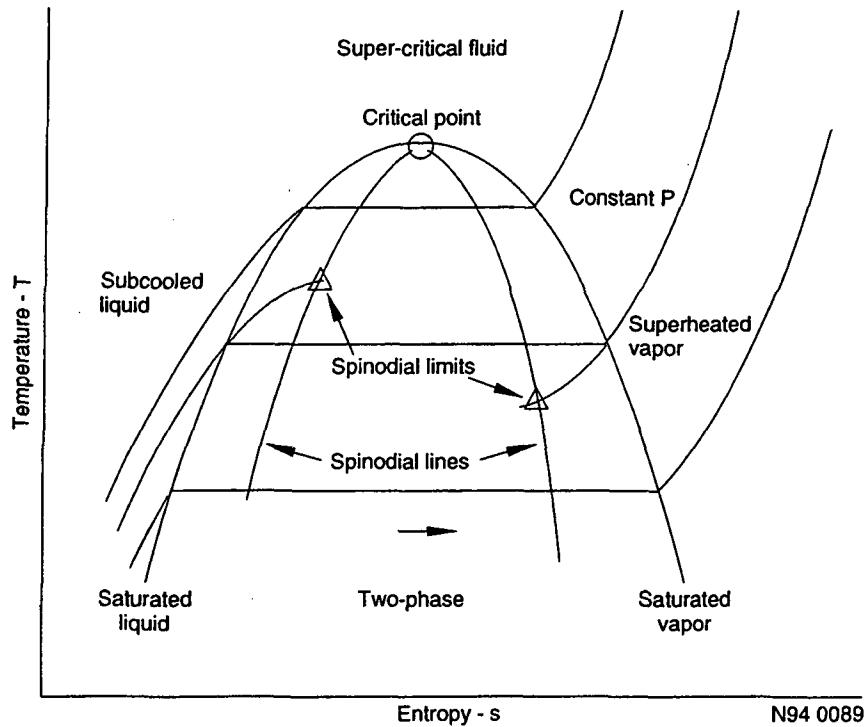


Figure 2-2. Temperature—entropy diagram for two-phase system.

Three thermodynamic derivatives are very useful in numeric modeling of two-phase flows. They are the coefficients of isobaric expansivity and isothermal compressibility as well as the specific heat at constant pressure:

$$\beta_k = (1/V_k) (\partial V_k / \partial T_k) P_k$$

$$\kappa_k = - (1/V_k) (\partial V_k / \partial P_k) T_k$$

$$C_{pk} = (\partial h_k / \partial T_k) P_k$$

The subscript k designates the liquid or vapor phase.

From these three derivatives, the following four partial derivatives, i.e., $(\partial \rho_k / \partial P_k)_{u_k}$, $(\partial P_k / \partial u_k)_{P_k}$, $(\partial T_k / \partial P_k)_{u_k}$, and $(\partial T_k / \partial u_k)_{P_k}$ can be evaluated by

$$(\partial \rho_k / \partial u_k)_{P_k} = \beta_k / [(C_{Pk} - V_k \beta_k P_k) V_k] \quad (2-3)$$

$$(\partial \rho_k / \partial P_k)_{u_k} = (C_{Pk} \kappa_k - T_k V_k \beta_k^2) / [(C_{Pk} - V_k \beta_k P_k) V_k] \quad (2-4)$$

$$(\partial T_k / \partial u_k)_{P_k} = 1 / (C_{Pk} - V_k \beta_k P_k) \quad (2-5)$$

$$(\partial T_k / \partial P_k)_{u_k} = -(P_k \kappa_k - T_k \beta_k) / (C_{Pk} - V_k \beta_k P_k) \quad (2-6)$$

Here, u_k is the phasic internal energy. Equations (2-3) and (2-4) are used in expanding the time derivatives of the phasic densities in terms of the dependent variables using two-term Taylor series expansions. Equations (2-5) and (2-6), when combined with dT^s/dP_k , are used in the implicit (linearized) evaluation of the interphase temperature potentials $T_f - T_\sigma$ and $T_g - T_\sigma$, where T_σ is the temperature that exists at the phase interphase and is usually assumed to be the saturation value defined in terms of the phase pressure P_k . The interphase temperature potentials are used in the interphase heat and mass transfer calculations. The isentropic sound speed, or bulk modulus, for an equilibrium process in a two-phase mixture at equilibrium can also be computed from the thermodynamic parameters previously defined. The sound speed is defined by

$$\alpha^2 = V^2 (dP^s/dT)^2 / D$$

where V is the specific volume of the mixture, α is the sound speed, and

$$D = X [C_{Pg}/T + V_g (dP^s/dT) (\kappa_g dP^s/dT - 2 \beta_g)] + (1 - X) [C_{Pf}/T + V_f (dP^s/dT) (\kappa_f dP^s/dT - 2 \beta_f)] \quad (2-7)$$

where x is the mass fraction of vapor, and dP^s/dT is given by Equation (2-2).

2.1.3 Two-Phase Flow Modeling

Prior to 1970, the predominant modeling approach was a pseudo-fluid model, the homogeneous equilibrium model (HEM), in which thermal and mechanical equilibrium was assumed to exist between the phases. This model was the basis for codes such as FLAASH, RELAPSE, RELAP2, RELAP3, and RELAP4. The limitations inherent in the HEM model made it necessary to adopt a conservative analytical approach called an evaluation model (EM). Uncertainties associated with this approach and the potential penalties of excessive conservatism allow the two-fluid model to evolve as the method of choice for modeling two-phase flows.

The advantage of the two-fluid model is that both mechanical nonequilibrium (slip between the phases) and thermal nonequilibrium (different temperatures of the phases) can be modeled. Mechanical nonequilibrium occurs in several physical processes present during a loss-of-coolant accident. Examples include emergency core cooling water (when it is injected into the system it does not immediately mix and flow at the same velocity as the steam) the core cooling water flowing down the downcomer counter current to escaping steam, counter-current flowing of steam and water occurring in the steam generator tubes during reflux cooling, and stratified flow occurring in horizontal piping components with little interaction between liquid and vapor.

Historically, the modeling of thermal and fluid processes has proceeded by averaging over the molecular details of the process to obtain a continuum description using the mathematics of continuous functions. Integral conservation principles are reduced to a system of partial differential equations by means of generalized transport theorems and cast as an initial/boundary value problem. Finally, the differential formulation is discretized for numerical solution. For problems involving stochastic processes such as turbulence and two-phase flow, a second integral averaging process is

Modeling

used to eliminate instantaneous details of the flow. In each averaging operation, information is lost and it is necessary to supplement the formulation with constitutive or closure models.

2.2 Fluid Dynamic Modeling

This section describes how the space-time partial differential equations used as the basis of RELAP5/MOD3 are derived.

2.2.1 Microscopic Fluid Processes

Averaged continuum models provide a means for describing macroscopic fluid processes. It is, however, important to keep in mind the underlying microscopic processes and the inherent limitations of the continuum description. Figure 2-3 illustrates the relevant length scales in two-phase physical processes and their contrast to the length scales associated with the modeling and computational processes.

The two-fluid model for two-phase flow is obtained from single-phase balance equations, augmented by the balance equations that apply at interfaces, by averaging over the mesoscales of the flow using either a sliding spatial volume and/or time segment, or an ensemble average at a point in space and time. As shown in Figure 2-3, the mesoscale can range from microbubbles or fog droplet, having scales that range from 10^{-5} m to as large as Taylor bubbles having dimensions up to 1 m.

Although the ensemble average is generally viewed as more fundamental (Drew and Wood 1985, Ransom and Ramshaw 1988, Arnold 1988), the space-time average is used here because of its ease in use in both experimentation and analysis.

2.2.2 Continuum Basis for Two-Phase Flow Models

2.2.2.1 Phasic Balance Equations. The balance between the time rate of change of the property in the material volume and the increase of the property due to flux of the property across the material boundaries and sources within the volume is

$$d/dt \int_R \rho \psi dV = - \int_S \underline{J} \cdot \underline{n} dA + \int_R \rho \phi dV \quad (2-8)$$

Here, the material volume, R , is at time t and is deforming in space with the fluid motion; \underline{J} is the flux (vector or tensor) of the general property across the volume boundary S ; ψ is a mass intensive property; ϕ is a mass intensive source (scalar or vector, but written herein as a vector) of the property; and ρ is the mass density. The operator d/dt is the ordinary derivative.

Mathematical manipulation of Equation (2-8) yields

$$\partial(\rho_k \underline{\Psi}_k) / \partial t + \text{div}(\rho_k \underline{\Psi}_k v_k) + \text{div}(\underline{J}_k) - \rho_k \underline{\Phi}_k = 0. \quad (2-9)$$

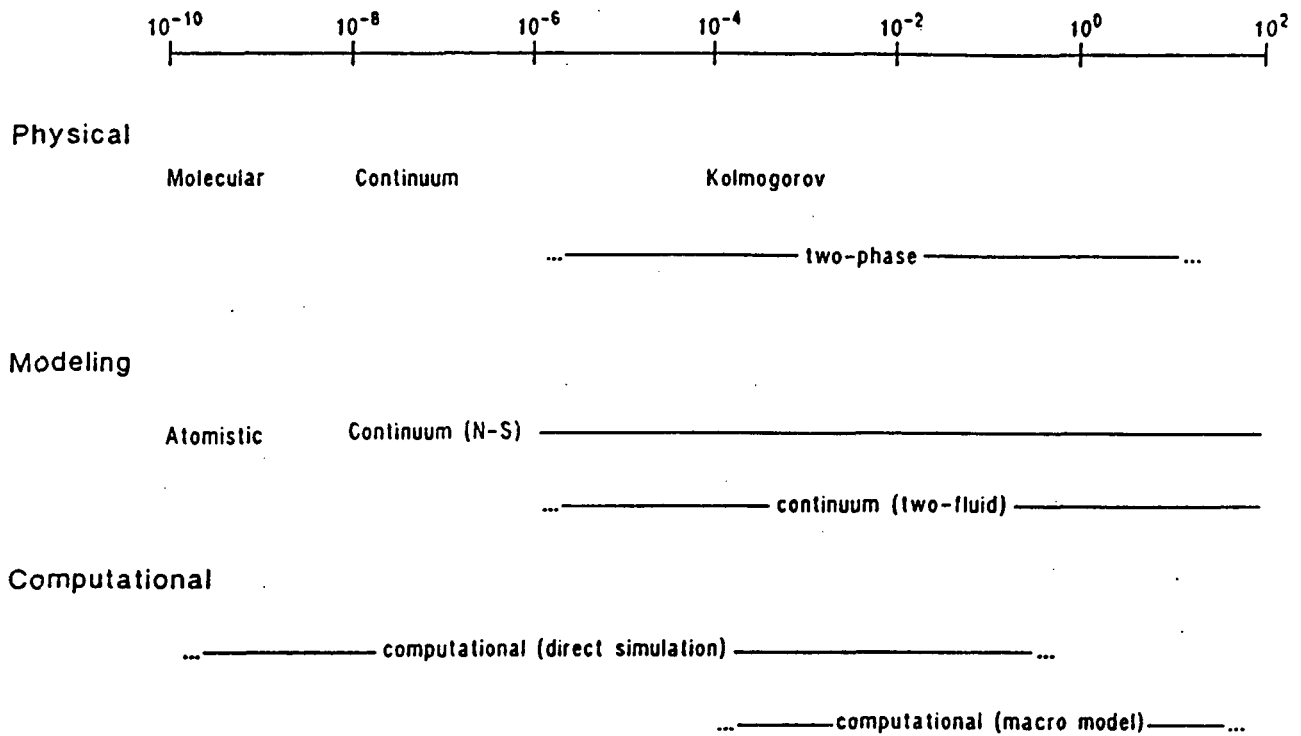


Figure 2-3. Length scale in fluid systems and models.

The equations for conservation of mass, momentum, and energy within each phase can be easily obtained from this relation. The respective conserved property, the corresponding surface flux, and volume source are given in the first three columns of Table 2-1.

The phasic mass and momentum conservation are

$$\frac{\partial \rho_k}{\partial t} + \nabla \cdot (\rho_k \underline{v}_k) = 0 \tag{2-10}$$

$$\frac{\partial (\rho_k \underline{v}_k)}{\partial t} + \nabla \cdot (\rho_k \underline{v}_k \underline{v}_k) = \nabla \cdot \underline{\tau}_k^* + \rho_k \underline{g} \tag{2-11}$$

where $\underline{\tau}_k^*$ is the stress tensor, including pressure and viscous stresses, and $\rho_k \underline{g}$ is the acceleration vector due to gravity or other body force.

The energy equation is obtained by taking Ψ to be the phasic total energy, i.e., internal energy plus kinetic energy; \underline{J} is the sum of the heat flux fluid velocity vector \underline{q}_k and the inner product of the stress tensor and the fluid velocity; and ϕ is the sum of internal energy sources Q_k and the inner product of the body force vector and the velocity ($\rho_k \underline{g} \cdot \underline{v}_k$), i.e., potential energy. (In this case, $\underline{\psi}$ becomes a scalar, \underline{J} a vector, and ϕ a scalar).

Modeling

Table 2-1. Parameters of the general balance equation.

Property/variables	ψ_k	\underline{J}_k	ϕ_k
Mass	1	0	0
Momentum	\underline{v}	$P_k \underline{I} - \underline{\tau}_k$	\underline{g}
Energy	$u_k + \underline{v}_k \cdot \underline{v}_k / 2$	$\underline{q}_k + (P_k \underline{I} - \underline{\tau}_k) \cdot \underline{v}_k$	$\underline{g} \cdot \underline{v}_k + Q_k / \rho_k$

By subtracting off the mechanical energy equation, which is obtained by forming the scalar product between the momentum equation and the velocity, term by term, and using the continuity equation, we obtain the following thermal energy equation

$$\partial(\rho_k u_k) / \partial t + \nabla \cdot (\rho_k u_k \underline{v}_k) = -\nabla \cdot \underline{q}_k + \underline{\tau}_k^* : \nabla \underline{v}_k + Q_k \quad (2-12)$$

where u_k is the phasic internal energy.

Equations (2-10), (2-11), and (2.12) are used to develop numerical models.

2.2.2.2 Interface Balance Equations. The main complications in two-phase flow modeling occur in modeling the interface between the two phases. Because the interface between two fluids is, in general, a non-Euclidean subspace, the methods of differential geometry need to be used to obtain a mathematical description for the dynamic behavior of the interface. See Section 3.2 of Ransom (1989) for a detailed discussion of the derivation of the interfacial differential conservation relation.

2.2.2.3 Constitutive Models. The constitutive models needed for the phasic balance equations are the equations of state for each fluid, transport property models, models for the stress tensors, the heat flux vector models, and models for the sources of momentum and energy. Each phase is considered to be homogeneous, and the thermal and caloric equations of state of each phase k are

$$\rho_k = \rho_k(u_k, P_k)$$

$$T_k = T_k(u_k, P_k), \quad k = f, g.$$

Each fluid is assumed to be Newtonian, so that the phasic stress tensor is the same as that for a single-phase fluid,

$$\underline{\tau}_k^* = -P_k \underline{I} + \mu_k \{ -2/3 (\nabla \cdot \underline{v}_k) \underline{I} + [\nabla \underline{v}_k + (\nabla \underline{v}_k)^T] \} \quad (2-13)$$

where the superscript T on the velocity gradient tensor designates the transpose; P_k is the thermodynamic pressure; and μ_k is the shear viscosity. The heat flux vector is simply defined using the Fourier law of heat conduction for an isotropic medium, so that the thermal conductivity is an invariant:

$$\underline{q}_k = -K_k \nabla T_k \quad (2-14)$$

where K_k is the thermal conductivity of phase k . Other constitutive models needed for the phasic balance equations include the source of momentum and energy models within each phase. Only the source of momentum due to body forces, the corresponding potential energy source, and internal energy generation are considered.

The interface balance equations also require constitutive models for the equation of state for the interfacial fluid, the interfacial stress tensor, and the heat flux vector. Vanderslice et al. (1966) discuss them in detail. Ransom (1989, Section 3.5) provides a good summary of the relevant results in this area. We note that the constitutive models for the two fluids and the interface, as well as additional boundary conditions associated with the interface, completely determine the solutions for the local instantaneous two-fluid model of the two-phase flow equations.

2.2.3 Space-Time Averaged Two-Fluid Models

The need for averaging arises for a variety of reasons. If a process has stochastic variations, then usually it is not possible to seek a definite numerical value that represents its instantaneous state. In such a case, it is necessary to describe the process in a statistical sense (i.e., by a mean and a deviation, with the understanding that we can only define a particular state in a probabilistic sense). The behavior of matter on the molecular level is an example in which we can define a definite average state; but the instantaneous state will fluctuate about this average in an apparently stochastic way. The continuum model for material was devised to eliminate this uncertainty about the microstate and replace it with a more deterministic macrostate model.

An additional reason for averaging is to seek a simpler description of a process. If the process possesses mesoscale phenomena or structure, it may not be feasible, practical, or desirable to describe the details of the mesoscale process. The classic example, other than two-phase flow, is flow in porous media. For some applications, we may want to seek a simpler description by reducing the dimensionality of the problem. Chordal or area averaging can be used to obtain a planar or one-dimensional description, such as is done for pipe flow.

There are many possible averaging techniques that can be devised. Ishii (1987) discusses many possibilities. The ensemble average is the most fundamental average and is the basis for statistical methods. Other types of average, such as spatial and time average, are useful concepts because we invariably experience the physical world in a spatial and time average sense. A local instantaneous value is a mathematical concept that can only be approximated.

The definition of a statistical or ensemble average is simply an arithmetic average over a number of realizations of the process or event. It is quite clear that when we are faced with stochastic behavior that the ensemble average is appropriate and has the desired effect of removing unwanted detail. In the case of multidimensional two-phase flow, this results in a local instant description in which the characteristics of each phase, as well as the interface, are blended together. However, such a description is still overly detailed, and it may be desirable to describe the system in terms of spatially averaged properties. The need for spatial averaging arises both because we can only determine the state of a system experimentally using finite volume instruments and also because we cannot, in general, obtain an exact mathematical solution and must resort to discrete numerical methods.

Modeling

It is apparent that there may be a need for more than one type of averaging in engineering problems. However, significant issues with regard to averaging are (a) what method is fundamental or should be employed, and (b) what are the relationships between the different methods of averaging? Drew and Wood (1985) and Ransom and Ramshaw (1988) argue the ensemble average is fundamental and all other averages should be considered approximations. This argument gains some support from statistical mechanics and kinetic theory, in which averages are generally over a phase, space that, in theory, contains an infinite number of realizations of the process. Temporal, spatial, and ensemble averages can be shown to be equivalent for stationary processes by means of the ergodic hypothesis (Lebowitz and Penrose 1973). It is not possible to relate the averages for the more general case of transient phenomena.

The averaging process most familiar in fluid mechanics is the *sliding* time average, which is used to obtain the Reynolds averaged Navier-Stokes equations. This averaging method consists of an integral of the quantity to be averaged over a time interval, T , that is taken sufficiently large such that the averaged quantity is smooth, yet sufficiently small such that the averaged variable retains the longer time variations

$$\bar{f}(x,t) = (1/T) \int_{t-T/2}^{t+T/2} f(x,t') dt' . \quad (2-15)$$

It is apparent that a physical scale, L , is implied by the time average since the time interval, T , corresponds to a physical length in the process, which is just the velocity times the time interval

$$L = |v|T . \quad (2-16)$$

Several contributions have been made to the averaging methods used in two-phase flow (Ishii 1987, Delhaye 1970, Drew 1971, Trapp 1986, Nigmatulin 1979, Gray and Lee 1977, Clemins 1988, Delhaye and Archard 1976). Ishii (1987) discusses the merits of several averaging methods but employs the single time average for his development of an averaged two-phase model. Delhaye and Archard (1976) detail the development of spatial averages, time average, double time average, and ensemble/or statistical averages. Their work is unique within the earlier work in that they considered the ensemble average operator. They found that problems arise due to discontinuities associated with the phasic density function, but they were able to overcome these difficulties by applying the ensemble operator after spatial averaging the instantaneous equations. However, they indicate that closure problems do exist due to nonlinearities of the equations. They also indicate that such problems have been studied for a single-phase flow, but that no work has been done for two-phase

There is no general agreement on the averaging method that should be used for two-phase flow, or which is more fundamental. The most common approach is to use spatial averaging and, frequently, to also time average. Ishii (1987), on the other hand, only used the time average. The development of the two-fluid model here will follow the development used by Lahey and Drew (1988) in which they first spatially averaged the local instant formulation and followed this by a single-time average. They have presented a very interesting development of the averaged model, which includes the steps necessary to obtain closure within the present state of knowledge. This is a very important part of any model development process and provides some insight to the immense complexity of two-phase flow.

2.2.3.1 Spatial Averaged Phasic Balance Equations. We first consider an *averaging* volume fixed in space and large enough to include a representative sample of the mesoscale structure associated with the two-phase mixture in order to define a smoothly varying average. In performing the phasic volume average, only that volume occupied by phase k will be included in order to obtain the averaged phasic balance equations. In general, the phase will be bounded by coordinate planes of the averaging volume, interfaces with the adjoining phase, $a_\sigma(\underline{x}, t)$, and solid boundaries, $a_{wk}(\underline{x}, t)$. Note that both the interface and the part of the solid boundary contacted by phase k change with time due to phasic motion, even though the wall boundary is fixed in space and time. The total averaging volume, V , is fixed in space, but the subvolume occupied by phase k , $V_k(\underline{x}, t)$, will vary arbitrarily and the average so obtained is a sliding volume average. The averaged formulation is obtained by first integrating the phasic balance equation, Equation (2-9), over the phasic subvolume contained within the averaging volume. The spatial integral of the phasic balance equation is then mathematically converted to the following equation (Ransom 1989):

$$\begin{aligned} \partial/\partial t [\bar{\beta}_k \langle \rho_k \psi_k \rangle] + (1/V) \nabla \cdot [V \bar{\beta}_k \langle \rho_k \psi_k \underline{v}_k + \underline{J}_k \rangle] - \bar{\beta}_k \langle \rho_k \psi_k \rangle \\ = - (1/V) \int_{a_\sigma} (\dot{m}_k \underline{\psi}_k + \underline{J}_k \cdot \underline{\xi}_k) dA - (1/V) \int_{a_{wk}} (\underline{J}_k \cdot \underline{n}_{wk}) dA \end{aligned} \quad (2-17)$$

where the phasic volume average for a phasic property is designated by an angle bracket and is defined by

$$\langle f_k \rangle \equiv (1/V_k) \int_{V_k(x,t)} f_k(x,t) dV \quad (2-18)$$

The instantaneous volumetric fraction of phase k is defined by

$$\bar{\beta}_k \equiv V_k(\underline{x}, t) / V(\underline{x}) \quad (2-19)$$

and the interfacial mass flux is defined as

$$\dot{m}_k \equiv \rho_k (\underline{v}_k - \underline{v}_\sigma) \cdot \underline{\xi}_k \quad (2-20)$$

where $\underline{\xi}_k$ is the unit outward normal vector at the surface a_σ .

2.2.3.2 Space-Time Averaged Phasic Balance Equations. The space-averaged formulation is still an instantaneous description of the flow process and will contain high-frequency and/or stochastic variations. Therefore, the sliding time-averaging process defined by Equation (2-15) is used here to attenuate the high-frequency behavior of the spatial-averaged phasic balance equations.

The development of the resulting equation and its reduction to a more useful formulation are given in detail in Sections 4.2 and 4.3 of Ransom (1989). The final form for the space-time averaged general balance equation is

Modeling

$$\begin{aligned}
 & \partial[(\alpha_k)(\bar{\rho}_k)_k (\bar{\Psi}_k)_k] / \partial t + (1/V) \nabla \cdot [V(\alpha_k)(\bar{\rho}_k)_k (\bar{\Psi}_k \nu_k)_k] \\
 & + (1/V)(\alpha_k) \nabla \cdot [V(\bar{J}_k)_k] \\
 & - (\alpha_k)(\rho_k)_k (\bar{\Phi}_k)_k^p = - (1/V) \int_{a_o} \overline{m_k \Psi_k} dA \\
 & - (1/V) \int_{a_o} \overline{\Delta J_k \cdot \xi_k} dA - (1/V) \int_{a_{wk}} \overline{\Delta J_k \cdot n_{wk}} dA
 \end{aligned} \tag{2-21}$$

where

$$\alpha_k \equiv \bar{x}_k$$

$$X_k(\underline{x}, t) = \begin{cases} 1, & \text{when phase } k \text{ is present at } \underline{x} \text{ and } t \\ 0, & \text{otherwise} \end{cases}$$

$$(g) \equiv (1/V) \int_V g dv, \text{ for any function } g$$

$$\bar{J}_k^x \equiv X_k \bar{J}_k^x / X_k, \text{ for any function } f$$

$$\overline{(f_k)}_k \equiv (\alpha_k \bar{f}_k^x) / (\alpha_k), \text{ for any function } f$$

$$(\bar{f}_k)_k^p \equiv (\alpha_k \overline{\rho_k f_k^x}) / [(\alpha_k)(\bar{\rho}_k)_k]$$

$$\underline{n}_k \equiv \text{unit outward normal vector at the surface } a_{wk}$$

We note that (α_k) is the familiar void fraction of phase k used in the two-phase flow equations of RELAP5/MOD2 and RELAP5/MOD3 (Ransom et al. 1985, Allison et al. 1990).

The space-time averaged mass, momentum, and total energy balance equations are obtained from Equation (2-21) by setting ϕ , J , and ψ to the values given by the first three columns in Table 2-1. The space-time averaged intrinsic thermal energy balance equations are developed by applying the space-time averaging technique directly to the thermal energy balance equation [Equation (2-12)]. The details are given in Sections 4.2–4.6 of Ransom (1989) where it is also pointed out that in order to put the space-time averaged equations in a tractable form auxiliary parameters have to be introduced.

Ransom also indicates that the space-time averaged mass, momentum, and energy equations require 4, 100, and 47 auxiliary parameters, respectively.

2.2.3.3 Space-Time Averaged Interface Balance Equations. The space-time averaged interface balance equations can also be derived from the respective continuum equation using the averaging techniques in this section. Ransom (1989) states that the space-time averaged interface mass, momentum, and energy equations require 0, 10, and 20 auxiliary parameters, respectively.

2.2.4 Closure Problem for the Two-Fluid Model

When averaging is employed in an attempt to simplify or reduce the level of description of a problem, information on the details of the process is lost and it is necessary to supplement the formulation with additional models and/or information. This is termed the *closure problem*, and it arises at each step of the averaging cascade. Closure models are required for the single-phase continuum model when it is derived by averaging from the more elementary kinetic theory model. Additional closure models are required for the Reynolds averaged model, and yet additional models are required when the two-fluid model is obtained by an average that includes the mesoscale phenomena. The closure problem for the single-phase continuum model consists of providing models for material properties such as viscosity, thermal conductivity, and species diffusivity. For the Reynolds averaged model, additional constitutive models are required for the Reynolds stresses and the Reynolds heat flux. Finally, the two-fluid model requires models for interphase interactions as well as the intraphase models.

Lahey and Drew (1988) give a good overview of the closure problem and the general principles that can be used to guide the formulation of closure or constitutive models. These guiding principles are extremely broad (e.g., the equipresence argument means that everything depends upon everything else). However, we generally assume, without guarantee, that closure can be obtained in terms of the local variables. This would appear to be a rather sweeping assumption; but it generally has been found adequate by most researchers. Thus, we proceed to seek closure in a manner similar to that used to obtain closure for the Reynolds averaged models.

Closure of the local instantaneous two-fluid model was achieved with little more difficulty than for the single-phase case. It was simply necessary to provide constitutive models for two materials rather than one, to provide an interfacial constitutive model, and additional boundary conditions associated with the interface. Unfortunately, the closure problem is much more difficult for the averaged two-fluid model for two-phase flow. Lahey and Drew (1988) found that 2,771 scalar functions would be needed for closure of their two-fluid model if the principle of equipresence were strictly adhered to. In addition, each of these 2,771 scalar functions could depend on the 679 scalar variables of the problem. Fortunately, such generality is not required for most engineering problems.

The purpose of this section is to discuss the major assumptions that reduce closure to a tractable problem. Typical constitutive and auxiliary models for key phenomena that are in use within the LWR industry are given in Section 2.3 in connection with the development of the one-dimensional two-fluid model.

The space-time averaged two-fluid model for two-phase flow consists of 15 field equations, 15 primary dependent variables, and 179 auxiliary parameters, most of which were introduced as a result of the averaging process. The closure problem at this level appears formidable. Fortunately, many of the parameters that were introduced in the process of developing the averaged model were included for the sake of generality. Simple approximations, or outright neglect of the effect for which they account for, result in a reasonably accurate engineering model, as is evidenced by the good agreement of numerical results with data shown in Section 5. However, some of the parameters represent significant effects, such as the parameters associated with turbulence, but they are poorly characterized at present and, thus, are omitted from most formulations. When turbulent effects are important in situations that involve high Reynolds numbers flows, the model may be less than

Modeling

reasonably accurate. Clearly, there are many areas for potential improvement of closure relationships in two-phase flow.

The averaging process introduces some conceptual, as well as real, difficulties. These result from averaging over spatial and temporal detail and from the associated loss of scalar and vectorial information. The averaged dependent and auxiliary variables all coexist at a point in the description, unless added information or models to determine the spatial orientation of the fluid within the averaging volume is used. Thus, in effect, both fluids exist in an average sense at each point in space. In such a model, it is conceptually difficult to visualize or to construct models for different phasic pressures or for the interfacial pressures. Geometric information about the orientation and geometry, or curvature, of the interface is lost, which is essential to relating the interphase stresses, including the pressures. Only in certain cases, such as horizontal stratified flow, can we assume the orientation of the interface. This assumption enables calculation of the macroscopic curvature of the interface and the hydrostatic contribution to the phasic pressures. As a result of this loss of spatial detail, it is generally assumed that all of the averaged pressures are equal even though this assumption conflicts with interface momentum considerations.

The equal-phase pressures approximation contradicts the interfacial momentum balance that shows when mass transfer occurs; the liquid-phase pressure is greater than the vapor-phase pressure at the interface for both condensation and evaporation. Thus, the equal-phase pressure assumption makes it impossible to satisfy the normal component of the interfacial momentum balance. Fortunately, in most cases of interest, these effects are small.

A second simplification that has been employed in most two-fluid models is to include all wall and interfacial viscous and turbulent stress effects as lumped Darcy-type friction models. Further simplifications and other considerations are discussed in the next section.

2.3 One-Dimensional Two-Fluid Model

In many situations, it will be desirable to seek further simplification of the multidimensional description, either for reasons of reducing the labor required to obtain solutions or because a multidimensional description is unwarranted when other uncertainties of the problem are considered. The most widely employed simplification is the reduction to a one-space dimensional description. The familiar pipe flow model used in fluid mechanics is the most common example of a one-dimensional description. Such a model is entirely adequate for many engineering purposes, including modeling of two-phase system transient behavior. An example in which this type of description is used is the simulation of the transient response of a nuclear power plant to postulated loss-of-coolant accidents. The motivations in this case have been twofold: first, a multidimensional description of an entire system would be prohibitive in terms of the computational resources that would be required to perform a simulation; second, the uncertainties associated with the constitutive models often exceed any uncertainty associated with reduction to a one-dimensional description. While this second statement is certainly true for piping and minor components, it may not always be true for vessels having large diameters compared to the system characteristic length. In such cases, a more complete spatial description may be appropriate.

The most common approach for obtaining a one-dimensional description is to employ an area average rather than the volume average as was used in the development of the multidimensional two-

fluid description developed in Section 2.2. However, this approach can lead to some misconceptions with respect to how we should interpret the dependent variables of the description. In particular, the formulation results in a system of partial differential equations in which the area-averaged dependent variables appear as continuous functions of the independent space dimension. This raises the question of how the short wavelength behavior of such variables should be interpreted. If the formulation is to be consistent with the multidimensional formulation, then the short wavelength character of the dependent variables is significantly attenuated by the averaging process. Therefore, the physical processes that are important, but originate at length scales less than the averaging scale, must be modeled. Since the description cannot include the responsible physical mechanisms, such effects cannot be resolved by computation on successively refined scales. As has been previously discussed, the sliding-volume average yields a formulation in terms of continuously-averaged variables, but the mathematical behavior of these variables at length scales less than the averaging scale does not have physical significance. Only if additional information of a physical nature is brought in to play can the accuracy of the description be improved. It is a common misconception that the accuracy of the solution can be improved by refining the discretization process ad infinitum. This view results from the consideration of the averaged equations as a system of partial differential equations, apart from their progenitors. The one-dimensional description seems to be frequently misinterpreted in this way for the single-phase description as well as for the two phase flows (Sirkoff 1964).

2.3.1 Spatial Average in One Dimension

Before proceeding to reduce the multi-dimensional two-fluid equations to one dimension, it is helpful to recall the basis for the spatial averaging operator that was used in the derivation of the multidimensional model and examine how it reduces in the one-dimensional case. The spatial average operator can be defined in terms of an area average:

$$\langle f_k \rangle = (1/V) \int_{x_1 - L_1/2}^{x_1 + L_1/2} \left[\int_{A_{23}} (X_k f_k) dA \right] dx_1 \quad (2-22)$$

where

X_k = phase indicator function

f_k = phasic parameter to be averaged

A_{23} = cross sectional area of the averaging volume orthogonal to the x_1 direction

L_1 = characteristic dimension of the averaging operator in the x_1 coordinate direction.

Equation (2-22) can be simplified to

$$\langle f_k \rangle = [1/(L_1 (A_{23})^{L_1})] \int_{L_1} (X_k f_k)^{A_{23}} A_{23}(x_1) dx$$

where

Modeling

$$(A_{23})^{L_1} = (1/L_1) \int_{L_1} A_{23}(x_1) dx$$

$$(f_k)^{A_{23}} = (1/A_{23}) \int_{A_{23}} (X_k f_k) dA$$

and the subscripts on the averaging operator, L and A, designate a segment and an area average, respectively (only the interval of the integrals are affixed as limits).

Section 8.1 of Ransom (1989) shows that the resulting form for the divergence operator in one dimension is

$$(1/V) \nabla \cdot \left[V \left(\alpha_k \bar{B}_k^x \right) \right] = (L_1/V) \frac{\alpha}{\alpha_1} \left[(A_{23})^{L_1} \left(\alpha_k \bar{B}_{1k}^x A_{23} \right)^{L_1} \right] \quad (2-23)$$

$$V \equiv \int_{L_1} A_{23} dx_1$$

for a typical vector or tensor quantity \underline{B}_k .

2.3.2 The One-Dimensional Averaged Two-Fluid Model

Using Equation (2-23), the reduction of the multidimensional space-time averaged two-fluid model for two-phase flow is straightforward. The main point is that the variables of the flow remain a volume average, and the temptation to interpret them as area average values that embody correct short-wavelength behavior in the remaining space dimension can be misleading.

2.3.2.1 One-Dimensional Phasic Mass Balance Equation. The phasic mass equation becomes

$$\partial(\alpha_k \rho_k) / \partial t + (L/V) \partial(A \alpha_k \rho_k v_k) / \partial x = \Gamma_k, \quad k = f, g, \quad (2-24)$$

where we have deleted the indicial notation and simply take the x coordinate to coincide with the single dimension to be represented. L is the corresponding averaging scale, and v_k is the scalar value of the velocity in the x direction. Thus, the formulation is applicable to flow in a channel in which the cross section varies in the streamwise direction. All other variables are space-time average quantities even though the average notation has been deleted for simplicity. In particular, the cross-sectional area is a segment average value.

2.3.2.2 One-Dimensional Phasic Momentum and Energy Balance Equation. The phasic momentum and energy equations are systems of three vector equations, and some further restrictions are needed to reduce them to one-dimensional formulations. We will neglect all terms in the description associated with variations in the x_2, x_3 coordinate directions. In addition, we will assume that the mean flow is aligned with the x_1 coordinate direction so that the average values for the x_2 and x_3 velocity components are zero.

These limitations alone will reduce the auxiliary parameters of the momentum and energy equations from 100 and 47 to 24 and 21, respectively (Sections 8.2-8.4 of Ransom (1989)). Further simplifications to the momentum and energy equations are made as follows.

First, the turbulence parameters, the Reynolds stresses, and the Reynolds heat flux, are neglected. This is a reasonable approximation since the one-dimensional model only retains the component associated with axial diffusion, and these effects are small compared to the axial mean flow convective flux of momentum and energy. This does not mean that turbulence effects are neglected; the more significant radial or transverse turbulent diffusion effects are included within the wall heat transfer and wall friction correlations, just as they are in the single-phase pipe flow model.

Another approximation is to assume the phasic pressures, P_k , are equal (termed the equal pressures assumption). The interfacial pressures are also assumed equal to the phasic pressures as well. The case of stratified flow is an exception to this rule, and so is the two-fluid model of the CATHARE code (Micaelli 1987), which is based on a formulation in which the difference of interfacial pressure and the phasic pressure is modeled as a function of the relative phase velocity.

Finally, covariance terms in Equation (2-21) are universally neglected, and, thus, unity is assumed for the covariance multipliers. All interfacial momentum and energy storage is neglected. Phasic viscous stresses and internal phasic heat transfer are neglected.

The interfacial velocity associated with mass transfer, v_k^I , is modeled by a donor formulation or as a weighted average of the bulk phasic velocities (Ransom 1985). The phasic pressure differences between the bulk and the interface and between the bulk and the wall are assumed to be zero except for stratified flows. This approximation is consistent with the usual *hydrostatic* approximation wherein both phasic pressures are set equal. In a few cases, models having unequal phase pressures have been considered (Ransom and Trapp 1984, Ransom and Schofield 1976). The CATHARE code, is formulated with an interfacial pressure that is assumed different than the phasic pressures, which are set equal (Micaelli 1987). The CATHARE formulation for the interface pressure is such that the system of equations always has real characteristics.

The remaining interphase force terms consist of viscous and form drag: Bassett forces due to viscous history, and virtual mass forces that arise from relative acceleration between the phases. The viscous and form drag are the major components of the interphase drag and are modeled using a Darcy-type friction factor formulation. The Bassett force is universally assumed small and neglected. The virtual mass force is a dynamic or differential force, and it can be significant for high-frequency effects. The model of Cheng et al. (1978) is used. The normal forces at the wall and the interphase are also neglected.

With these simplifications, the one-dimensional averaged momentum equation is

$$\begin{aligned} & \partial(\alpha_k \rho_k v_k) / \partial t + (L/V) \partial(A \alpha_k \rho_k V_k^2) / \partial x + \alpha_k (\partial P / \partial x) \\ & - (L/V) \partial(A \alpha_k \tau_{xxk}) / \partial x - \alpha_k \rho_k g_x \\ & = \Gamma_k V_k^I + \left(\frac{M^{fv}}{\alpha k} + \frac{M^{vw}}{\alpha k} \right) \cdot \underline{n}_x + \frac{M^{fp}}{\alpha k} \cdot \underline{n}_x \quad , k=f,g. \end{aligned} \quad (2-25)$$

Modeling

Here, \underline{n}_x represents the unit vector in the x direction, M_{ok}^{iv} and M_{wk}^{iv} are the phasic interphase drag parameters and fluid friction at the wall respectively, M_{ok}^{vp} is the virtual mass effect, and V_k^T is the interfacial velocity associated with mass transfer.

The one-dimensional averaged thermal energy equation is

$$\begin{aligned} \partial(\alpha_k \rho_k \mu_k) / \partial t + (L/V) \partial(A \alpha_k \rho_k \mu_k) / \partial x = & -P_k [\partial \alpha_k / \partial t \\ & + (L/V) \partial(A \alpha_k v_k) / \partial x] + \Gamma_k (u_k + P / \rho_k)_\sigma \\ & + q_{ok} A_\sigma + q_{wk} A_{wk} + \alpha_k Q_k + \alpha_k \mu_k \Phi_k^2 \end{aligned} \quad (2-26)$$

where $(\cdot)_\sigma$ designates an interfacial value, and the scalar products of the heat transfer vectors and associated area vectors are shown as ordinary products, for simplicity. Here, Q_k is the volumetric heat generation, $\mu \Phi^2$ is the viscous dissipation term, and $q_{ok} A_\sigma$ and $q_{wk} A_{wk}$ are the averaged interfacial heat flux and heat flux at the wall, respectively.

The viscous dissipation term in Equation (2-26) should be interpreted as all sources of dissipation resulting from viscous effects, including that from wall friction and interfacial friction, even though no viscous shear stresses appear directly. The lumped Darcy-type friction models replace the viscous effect, which is lost from the formulation as a result of the one-dimensional approximation. These friction forces are sources of kinetic energy dissipation, and even though they generally are not large effects for low Mach number flows, they should be included for completeness.

2.3.2.3 Interface Mass Balance. The mass balance simply relates the two phasic mass generation terms

$$\Gamma_1 = -\Gamma_2 .$$

2.3.2.4 Interface Momentum Balance. The one-dimensional interfacial momentum balances are not very useful, as was the case in the three-dimensional formulation. When the hydrostatic or equal-phase pressures assumption is used, it is impossible to satisfy the momentum balance normal to the interface. We assume the tangential balance is satisfied by reason of the no-slip condition; however, the averaged formulation lacks sufficient detail to be able to define the bulk phasic fluid velocity gradients and the interfacial velocity. In practice, the interfacial momentum balances are replaced with a macroscopic momentum balance, in which we require that all of the interfacial forces sum to zero so that the interphase processes do not affect the mixture momentum. Thus, the forces due to mass exchange, viscous and form drag, and virtual mass effects sum to zero. It is common to require that detailed balance be satisfied as well. By this principle, it is required that the individual momentum processes balance by themselves (i.e., the viscous drag forces balance, momentum transfers due to mass exchange balance, and dynamic forces balance). Since the Cheng et al. (1978) virtual mass formulation is used, it is equal and opposite in sign for each phase, and, thus, these terms exactly balance. We further require, as in the RELAP5 formulation, that the interphase steady drag forces balance so that

$$M_{\sigma 1}^{iv} = -M_{\sigma 2}^{iv} \quad (2-27)$$

and that the momentum transfer due to mass exchange balances

$$\Gamma_1 v_1^\Gamma = -\Gamma_2 v_2^\Gamma. \quad (2-28)$$

When this result is combined with mass continuity, we obtain the result

$$v_1^\Gamma = v_2^\Gamma. \quad (2-29)$$

We note that Equation (2-29) does not necessarily imply that the phasic velocities for momentum transfer due to mass transfer for condensation and evaporation are equal. It is only required that the momentum that leaves one phase be equal to the momentum entering the other phase.

2.3.2.5 Interface Energy Balance. The interface energy balance is used to determine the interphase mass transfer rate from the interphase energy exchange process. We neglect energy storage at the interface due to surface tension.

The interface energy balance with these approximations reduces to

$$\sum_{k=1}^2 [q_{\sigma k} A_{\sigma} + q_{wk} A_{wk} + \Gamma_k (u_k + P_k/\rho_k)_{\sigma}] = 0. \quad (2-30)$$

2.3.2.6 Interfacial Balance Summary. The interfacial balance equations, while entirely correct and proper statements of physical principles, are not very useful because they are local relations at the interface. They must, in effect, be supplemented by models that relate the phasic variables to the corresponding bulk values. The resultant relationships are macroscopic balances between bulk phase conditions rather than interfacial balances. These bulk balances are formulated so that the principles of bulk mixture mass, momentum, and energy conservation are satisfied. The detailed balance principle is subsequently employed to yield a tractable system. These interphase bulk balances are the forms of interfacial balances actually employed as the basis for numerical modeling of multiphase flows.

Table 2-2 lists the variables and parameters retained in the reduced one-dimensional models. The interfacial equations reduce to algebraic relations (in fact they are replaced by equivalent balances between the bulk phase states) that the interfacial mass and energy balance equations determine, Γ_k . The interphase momentum balance can be used to eliminate one of the phasic interphase drag parameters, $\underline{M}_{\sigma k}^{IV}$.

With these simplifications and modeling approach, the system reduces to six differential equations, four algebraic equations (the volumetric continuity and the three interphase balance equations), and seven dependent variables. Twenty-six auxiliary parameters remain. The required number of additional independent relationships or models needed to obtain a *just-set* system (i.e., the same number of independent equations as number of variables) is 23.

Modeling

Table 2-2. Summary of the equations, dependent variables, and auxiliary parameters for the reduced one-dimensional space-time averaged two-fluid model.

Equations (number)	Dependent variables (number)	Auxiliary parameters (number)
Volumetric continuity (1)	α_k (2)	
Mass conti- nuity (2)	v_k (2)	Γ_k (2) ρ_k (2)
Momentum (2)	P (1)	v_k^Γ (2)
		$M_{\sigma k}^{nP}$ (2) $M_{\sigma k}^{IV}$ (2) M_{wk}^{IV} (2)
Energy (2)	u_k (2)	$u_{\sigma k}$ (2) $q_{\sigma k}$ (2) q_{wk} (2) A_σ (1) A_{wk} (2) Q_k (2) Φ_k^2 (2)
Interface mass (1)		
Interface momentum (1)		
Interface energy (1)		$v_{\sigma k}$ (1)
Totals (10)	(7)	(26)

2.3.3 Constitutive Models

The constitutive models are probably the most important element of the two-fluid model for two-phase flow, in terms of realized capability, to simulate physical system behavior. The balance equations and associated numerical scheme provide a framework for simulation, but the constitutive models constitute the statement of observed behavior. Consequently, this is a very important component of the model. The development of comprehensive constitutive models is a subject well beyond the scope of what can be presented herein. Here we simply outline the major interphase physical processes that the constitutive models should encompass and give some specifics of a particular modeling approach used in the RELAP5 codes (Ransom 1985 Allison 1990).

The specific constitutive models required for a complete one-dimensional description include (1) material behavior, (2) flow regime modeling, (3) interphase momentum and interaction (4) interphase energy and mass exchange, (5) wall momentum exchange, and (6) wall heat transfer. The first three models are unique to two-fluid models for two-phase flow and, thus, will be discussed, in greater detail. The wall momentum and heat transfer interaction models bear considerable similarity to single-phase models and are not discussed in the interest of brevity. See Dimenna et al. (1988) for an extensive discussion of the RELAP5 wall interaction models. Similar treatments can be found in other published literature (Micaelli 1987, Forge et al. 1988, Liles et al. 1988).

2.3.3.1 Material Behavior. Here, we include the equation of state for the phases, and the models for the phasic transport properties as well. These models are identical to those needed to support the multidimensional description, and, thus, we will not repeat the discussion found in Section 5 on this same subject. It is sufficient that we can establish the phasic densities and temperatures in terms of the pressure and internal energy, or equivalent thermodynamic independent variables. These same relationships must provide the thermodynamic derivatives needed for linearization and calculation of sound speed. The transport properties are mostly formulated as functions of temperature. (Near the critical point it may be necessary to consider property variation with pressure as well as temperature.)

Highly developed methods exist for their material behavior models, so we will not discuss this area. We only interject a note of caution that consistency in property representation is important, because differences of thermodynamic variables are used as driving potentials in modeling energy exchange rates, sometimes with large coefficients. Thus, if the saturation state is represented both in terms of pressure and in terms of temperature as independent variables (for convenience), then consistency between these two representatives may be important.

2.3.3.2 Flow Regime Models. The one-dimensional two-fluid model must be supported by empirical, or semi-empirical models for the geometry of the flow. The geometry has a first-order influence on the physical processes of mass, momentum, and energy transfer, both between the phase and between the flow and the walls. There is no complete agreement on either the flow regimes that can exist in pipeflow or the parameters used to characterize the flow regime. Rouhani and Sohal (1983) provide a good summary of flow regime research and describe the various approaches that have been taken in flow regime modeling. Dimenna et al. (1988) provide general information on flow regimes as they relate to the constitutive models used in RELAP5 and have conducted a quality assurance review for the implementation of these models.

Modeling

The primary independent variables affecting the flow regime are the geometry of the flow system and its orientation [i.e., pipes (round or rectangular and vertical or horizontal)]. Thus, it is common to find specific maps or correlations for each such geometry that is considered. The flow map for horizontal pipes used in RELAP5 is shown in Figure 2-4. The map includes five distinct flow regimes with transition regions separating most of the regimes. Generally, the transition regimes are a linear weighted average of the flow regime models that adjoin the transition region. The vapor volume fraction, α_2 , and the critical velocity are the primary independent variables. The critical velocity is a parameter suggested by Taitel and Duckler (1976) to govern transition to stratified conditions. They recommend that the critical velocity be identified with the vapor velocity, but more recent evidence, Kukita et al. (1986) indicate that the use of the relative phase velocity is a preferred choice. The critical velocity is defined by

$$v_{crit} = \left(\frac{1}{2}\right) \left[\frac{(\rho_1 - \rho_2) g \alpha_2 A}{\rho_2 D \sin \phi} \right]^{1/2} (1 - \cos \phi) \quad (2-31)$$

where

A = cross sectional area of the pipe

D = hydraulic diameter

ϕ = angle between the vertical and a radius to the intercept of the stratified liquid level with the wall.

The flow is considered to be stratified if $v_g < v_{crit}$.

The void fraction transition parameters can also vary with mass velocity. For example, the bubbly-to-slug flow transition void fraction, α_{AB} , is shown in Figure 2-5.

The presence of wall heat transfer under two-phase conditions also strongly influences the flow regime. The vertical flow map used in RELAP5 is shown in Figure 2-6 (Dimenna et al. 1988). The basic heat transfer parameter that influences the flow map is the critical heat flux (CHF) because the liquid cannot contact the wall under post-CHF conditions. Here again, the transition parameters such as α_{AB} , are variable. The details of these maps are given in Dimenna et al (1988).

In summary, the flow map is used to identify the flow regime as a function of pipe geometry and orientation and of flow variables such as void fraction and the velocities. Once the flow regime is identified, then appropriate models must be applied that establish parameters such as bubble/droplet radius, interfacial area, and phasic wall areas. These parameters can, thus, be used to establish interphase momentum and energy interactions.

2.3.3.3 Interphase Momentum Transfer. The interphase momentum exchange can be categorized and modeled as consisting of three basic mechanisms: (1) steady drag, (2) dynamic drag,

Modeling

and (3) momentum transfer due to mass transfer. The steady drag is modeled using a Darcy-type friction factor in which the dynamic pressure is formulated in terms of the continuous phase density and the relative velocity,

$$M_{\sigma 1}^{fv} = (1/2)C_D \rho_c |v_2 - v_1| A_p (v_2 - v_1) \quad (2-32)$$

where

C_D = steady drag coefficient

ρ_c = continuous phase density

A_p = planform area per unit volume.

The planform area per unit volume is related to the interfacial area, since if d_{sm} is the Sauter mean particle diameter, then the particle number density is

$$N_p = A_\sigma / (\pi d_{sm}^2) \quad (2-33)$$

Thus, the planform area per unit volume is

$$A_p = N_p \left(\frac{\pi d_{sm}^2}{4} \right) = A_\sigma / 4 \quad (2-34)$$

With this result, Equation (2-32) becomes

$$M_{\sigma 1}^{fv} = (1/8)C_D \rho_c A_\sigma |v_2 - v_1| (v_2 - v_1) \quad (2-35)$$

For convenience, we will define the interphase steady drag coefficient to be

$$FI = (1/8)C_D \rho_c A_\sigma |v_2 - v_1| \quad (2-35)$$

so that the steady viscous drag becomes

$$M_{\sigma 1}^{fv} = FI (v_2 - v_1) \quad (2-36)$$

It is usual to also assume, by reason of the detailed balance argument, that the phasic steady drag components balance,

$$M_{\sigma 2}^{fv} = - M_{\sigma 1}^{fv} \quad (2-37)$$

so that $FI_1 = FI_2 = FI$.

We will discuss the application of this steady interphase drag model to four representative flow regimes: the bubbly, slug, annular mist, and droplet. For the bubbly and droplet flow regimes, the

interfacial area per unit volume can be expressed in terms of the vapor volume fraction and the Sauter mean diameter by

$$A_{\sigma} = N_p \pi d_{sm}^2 = 6\alpha_d/d_{sm} \quad (2-38)$$

where α_d is the dispersed phase volume fraction (i.e., $\alpha_d = \alpha_2$ for bubbly flow and $\alpha_d = \alpha_1$ for droplet flow).

The Sauter mean diameter must be expressed in terms of dynamic variables of the flow. For equilibrium bubble and droplet distributions, the maximum bubble or droplet diameter has been correlated in terms of the relative velocity and surface tension, by using a constant critical Weber number,

$$We_c = d_{\max} \rho_c (v_2 - v_1)^2 / \sigma = \begin{cases} 10 & \text{for bubbles} \\ 3 & \text{for droplets} \end{cases} \quad (2-39)$$

where the constant values for the Weber number have been empirically established. The average particle diameter is assumed to be

$$d_{ave} = (1/2)d_{\max} \quad (2-40)$$

The Nukiyama-Tanasawa distribution can be used to relate the average particle diameter, d_{ave} , to the most probable particle diameter, d ,

$$d_{ave} = 3/2d' \quad (2-41)$$

$$d_{sm} = 5/2d' \quad (2-42)$$

and also to relate the Sauter mean diameter, d_{sm} , to d ,

The relation between the Sauter mean diameter and the average particle diameter is therefore

$$d_{sm} = (5/3)d_{ave} \quad (2-43)$$

The Sauter mean diameter can now be expressed in terms of the maximum particle diameter, obtained from the critical Weber number criterion by Equation (2-40).

The interfacial area is now established in terms of the volume fraction, the relative velocity, the surface tension, and the continuous-phase density by using Equations (2-38, 2-39, 2-40, 2-43). The resultant relation is

$$A_{\sigma} = (36/5)\alpha_d \rho_c (v_2 - v_1)^2 / (We_c \sigma) \quad (2-44)$$

Modeling

where α_d is the dispersed phase volume fraction, ρ_c is the continuous phase density, σ is the surface tension, and the critical Weber number is defined by Equation (2-39).

The Darcy drag coefficient is a function of the particle Reynolds number, which is based on the average particle diameter,

$$Re_p = d_{ave} |v_2 - v_1| \rho_c / \mu_m \quad (2-45)$$

where μ_m is the mixture viscosity, defined as

$$\mu_m = \mu_1 / \alpha_1 \text{ for bubbles} \quad (2-46)$$

and

$$\mu_m = \mu_2 / (\alpha_2)^{2.5} \text{ for droplets} \quad (2-47)$$

The slug flow regime can be modeled by considering the flow as a mixture of Taylor bubbles and small bubbles in the film and the trailing slug. A relationship between the volume fraction of the Taylor bubbles in the mixture, α_b , the overall volume fraction, α_2 , and the volume fraction of the smaller bubbles in the film and trailing slug, α_{2s} , can be obtained from purely geometric considerations as

$$\alpha_b = (\alpha_2 - \alpha_{2s}) / (1 - \alpha_{2s}) \quad (2-48)$$

The volume fraction of bubbles in the slug and film, α_{2s} , can vary from equal to α_2 , pure bubbly flow, or to zero, which corresponds to pure annular flow. Thus, the parameter α_{2s} provides a smooth transition between the bubbly and annular regimes. The interfacial area in the slug regime is modeled using the work of Ishii and Mishima (1984) where they found the volume to surface area ratio for a Taylor bubble to be 4.5D. This relationship, when used to model the Taylor bubble, results in the following equation for the interfacial area in terms of the α_{2s} parameter:

$$A_\sigma = (4.5/D)\alpha_b + (3.6\alpha_{2s}/d_{ave})(1 - \alpha_b) \quad (2-49)$$

with α_b defined in terms of α_{2s} by Equation (2-48). The critical Weber number criterion for bubbles is used to establish d_{ave} . The transition boundaries between the bubbly flow ($\alpha_{2s} = \alpha_2$) and the annular regime ($\alpha_{2s} = 0$) are defined by the flow regime map.

For the case of annular flow, a skin friction drag formulation is used in which the planform area is taken to be the lateral area. In this case, Equation (2-34) becomes

$$A_p = A_\sigma \quad (2-50)$$

When an annular mist flow is modeled, the steady drag components for both the dispersed phase and the film must be summed and the interfacial area apportioned between the annular and the dispersed components of the flow. In the RELAP5 code, a simple entrainment correlation is used

to apportion the liquid between the film and dispersed droplets. In order to determine the appropriate drag coefficient for the dispersed phase, the characteristic droplet or bubble diameter must be determined. Again, a critical Weber number formulation for drops is used [Equation (2-39)]. The particle Reynolds number can then be computed and the drag coefficient obtained from an appropriate correlation, such as that as Ishii and Chawla (1979), in which

$$C_d/8 = (5.0 + 0.37 Re_p^{0.75})/Re_p \quad (2-51)$$

This discussion has presented a brief overview of a method illustrative of those used to model steady interphase momentum transfer, or interphase drag in two-fluid models for two-phase flow. To obtain a general prescription, it is necessary to consider many other flow regimes, including any special flow passage geometries such as nuclear reactor core flows and steam generator tube bank external flow. A complete description of all the flow regimes modeled in RELAP5 is given by Dimenna et al (1988). A similar discussion of the modeling method used in the TRAC code is included in Liles et al (1988).

In addition to the steady interphase drag forces, the transient forces that result from relative acceleration of the phases, usually called virtual mass effects, may also be modeled. The most common model for these effects is that of Cheng, (1978), which is an objective or frame invariant formulation. These dynamic drag effects are manifested as variations in the interfacial pressure and can be considered a model for the term M_{ok}^{np} in the momentum equation. The objective dynamic drag model has the form

$$M_{ok}^{np} = \alpha_1 \alpha_2 \rho C_{vm} [D_1 v_1 / Dt] - (D_2 v_2 / Dt) \quad (2-52)$$

where

$$(D_1 v_1 / Dt) = \partial v_1 / \partial t + v_1 (\partial v_1 / \partial x) \quad (2-53)$$

$$(D_2 v_2 / Dt) = \partial v_2 + v_2 (\partial v_2 / \partial x) \quad (2-54)$$

$$\rho = \alpha_1 \rho_1 + \alpha_2 \rho_2 \quad (2-55)$$

The virtual mass coefficient, C_{vm} , is theoretically equal to one half for dispersed spherical particles; this is the value normally used. However, in some models, such as that used in the CATHENA code (Richards et al. 1985), the virtual mass coefficient is made sufficiently large to ensure that real characteristics are obtained under all flow regimes.

The momentum transfer associated with mass transfer requires a model for v_k^F . A donored velocity formulation can be shown to be always dissipative (Ransom et al. 1980), and provides a physically reasonable model. This formulation yields

Modeling

$$v_1^\Gamma = v_2^\Gamma = \begin{cases} v_1 & \text{if } \Gamma_1 \leq 0 \\ v_2 & \text{if } \Gamma_1 > 0 \end{cases} \quad (2-56)$$

In conclusion, this brief sketch has overviewed an interphase momentum exchange modeling approach for a few typical regimes. Similar models have been constructed for other regimes using formulations and correlations specific to the particular circumstances. Recently, there has been some move toward more empirical formulations where the interphase steady-drag component is modeled from a unified drift-flux correlation, valid for all flow regimes in vertical flow. This approach is strictly empirical and is limited to those flows from which the drift-flux correlation was developed. For example, the model of Chexal and Lellouche (1985) is not valid for vertical downflow, especially with boiling. It seems that the use of strictly empirical correlations for the interphase momentum interaction defeats the original purpose for using the general two-fluid framework. In any event, it is still necessary to provide additional models for the thermal interactions that closely parallel the momentum formulation. The strictly empirical approach seems a step backward in terms of developing an understanding of two-phase system behavior.

2.3.3.4 Interphase Energy and Mass Transfer. The interphase energy and mass transfer are closely linked, and the mass transfer rate is primarily established from an interphase energy balance. It has previously been mentioned that the spatial and time average operations render the interface momentum balance of little value, and we replace the interfacial balance by a bulk interphase balance. The same is true of the interfacial energy balance. The average phasic balance equation formulation is in terms of bulk phase properties and includes terms to relate the interfacial conditions to bulk conditions. Additional models are necessary for these interfacial variations. An alternate approach consists of using a bulk *interphase* balance rather than an *interfacial* balance. The interphase energy balance is consistent with the use of a Newton-cooling-law formulation to express the thermal energy exchange in terms of a bulk potential and a heat transfer coefficient. This is the approach used in most two-fluid formations. Thus, even though it is often stated in the literature that the *interfacial jump* consideration is used as the basis for interphase energy exchange (Lahey, and Drew 1988), in fact what is used is a bulk balance where the details of the intraphase energy exchange between the bulk fluid and the fluid at the interface are not needed. We further apply the principle of detailed balance, in which the wall interphase energy exchange and associated mass transfer are assumed to balance separately from the bulk energy and mass exchange process.

In modeling interphase energy and mass exchange, we will generally be interested in boiling and condensation processes where the wall heat transfer process plays a significant, if not dominant, role. Thus, we must consider the wall heat transfer process as well as the interphase energy exchange process in order to obtain models of general usefulness. Further description of the energy exchange modeling requires that we become more specific with regard to the approach. There are undoubtedly a variety of possible ways to proceed in modeling the constitutive relationship for the interphase mass and energy exchange process; however, the approach that will be discussed herein is confined to the specific experience accumulated in the process of developing the RELAP5 code. This description should be viewed as an example of one approach, which has been reduced to practice for modeling these phenomena.

The approach used for the RELAP5 model consists of dividing the mass generation and associated interphase energy exchange process into two parts: a wall heat transfer-dominated part and a bulk process part. Thus, the interphase mass transfer is a sum of two parts:

$$\Gamma_k = \Gamma_{\alpha k} + \Gamma_{wk} \quad (2-57)$$

where

$\Gamma_{\alpha k}$ = mass transfer at the bulk interface

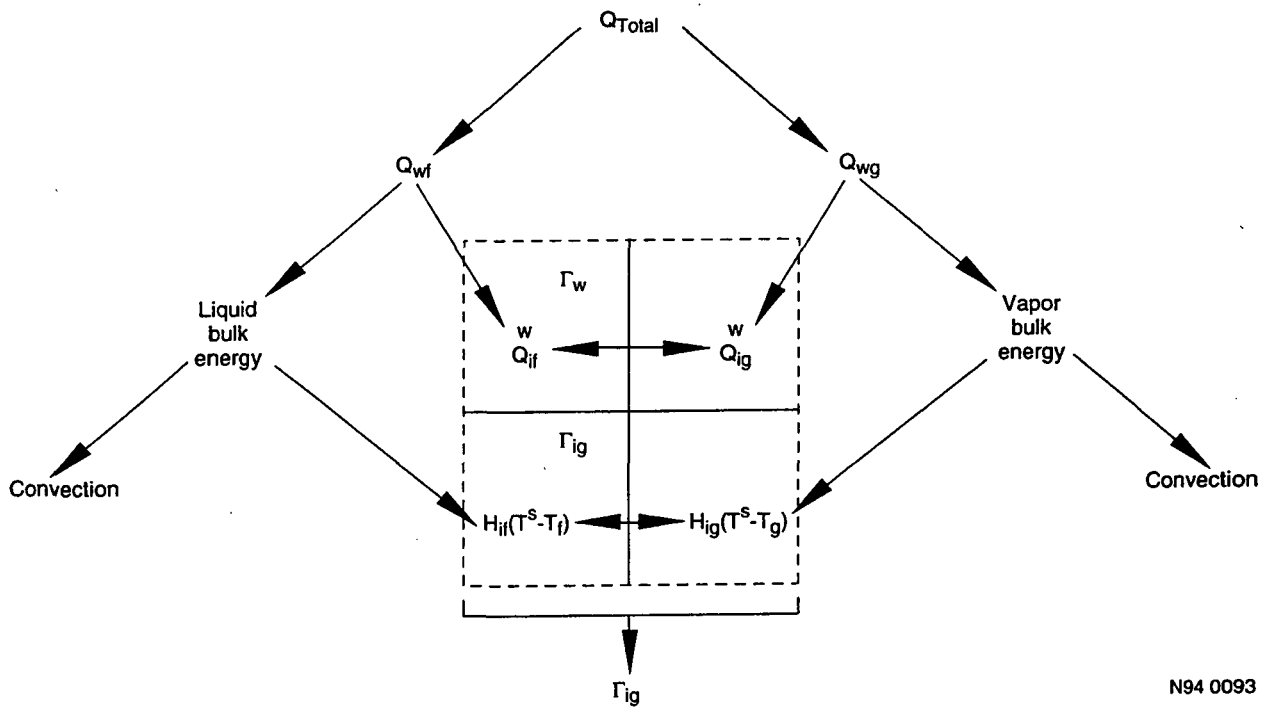
Γ_{wk} = wall transfer at the bulk interface.

The energy processes associated with the wall and bulk exchange are also considered separate, consistent with the principle of detailed balance; however, the wall process is also linked to the interphase process through the field equations, and it is necessary to partition the wall heat transfer into components that result in mass transfer and bulk phase heating, respectively. Figure 2-7 presents a flow diagram of the energy process with all the intra- and interphase energy exchange processes clearly identified. These include mass generation at the wall, bulk phase heating, bulk mass exchange, and convection of energy by the mean flow. The actual situation is not quite as complex as implied by Figure 2-7, since the wall process is assumed to either consist of boiling or condensation, and, consequently, only Q_{wf} or Q_{wg} is nonzero for a given set of conditions. In addition, we will require that the wall processes and the bulk processes balance independently. These conditions result in some simplification of the modeling.

In order to proceed further in constructing the balances and developing the needed correlations, we make further assumptions about the wall and bulk processes. In particular, the wall mass generation process is considered to produce vapor (boiling) or liquid (condensation) at the saturation state, and the bulk liquid or vapor film from which boiling or condensation is taking place is also assumed at saturation. Thus, the energy exchange process associated with mass transfer at the wall only involves the latent heat of vaporization (i.e., $h_2^s - h_1^s$). The bulk process, on the other hand, involves change in sensible heat from the bulk state of the phase, from which mass transfer is occurring to the saturation state of that phase, in addition to the latent heat of vaporization for phase change. Any sensible energy change between the saturation state and the bulk state of the phase the mass is entering is assumed to be provided by an intraphase process of conduction or convective mixing. This process is analogous to the common *donor* formulation used for numerical modeling of convection. With these process assumptions, we can now write out the phasic energy terms and derive the bulk balance that must be satisfied. The wall and interphase energy exchange terms from the energy equation, Equation (2-26), are

$$q_{\alpha k} A_{\sigma} = q_{wk} A_{wk} + \Gamma_k (u_k + P_k / \rho_k)_{\sigma} = q_{\alpha k} A_{\sigma} + Q_{wk} + \Gamma_{\alpha k} h_k^* + \Gamma_{wk} h_k^s \quad (2-58)$$

Modeling



N94 0093

Figure 2-7. Thermal energy flow diagram for the two-fluid model.

where

Γ_{ak} = mass transfer at the bulk interface

Γ_{wk} = mass transfer at the wall

Q_{wk} = wall heat transfer rate to the phase k

h_k^* = bulk phase enthalpy if $\Gamma_{ak} < 0$ or phase saturation enthalpy if $\Gamma_{ak} > 0$.

In Equation (2-58), not all of the wall heat transfer, Q_{wk} , results in mass transfer; some will result in bulk phase energy increase. The proportion, or split, of Q_{wk} between these two processes must be specified as a result of the wall heat transfer/mass transfer model, such as a subcooled boiling model. Also, in Equation (2-58), the interphase energy transfer term $q_{ak} A_o$ must also include any energy transfer that results in mass transfer, including that associated with the wall generation rate, Γ_{wk} . Thus, we will partition the interphase energy exchange for phase k into two parts:

$$q_{ak} A_o = H_{ak}(T_k^s - T_k) + Q_{ak}^w \quad (2-59)$$

where

$H_{\sigma k}$ = interfacial heat transfer coefficient for phase k , including the interfacial area

$Q_{\sigma k}^w$ = heat transfer from the wall that produces mass transfer

T_k^s = saturation temperature at P_k .

Replacing the terms in Equation (2-58) associated with interphase energy exchange (all the terms that would sum to zero for a mixture energy equation) using Equation (2-59), and introducing the interphase mass balance, we obtain

$$H_{\sigma 1}(T_1^s - T_1) + Q_{\sigma 1}^w - T_{\sigma 2}h_1^* - \Gamma_{w2}h_1^s + H_{\sigma 2}(T_2^s - T_2) + Q_{\sigma 2}^w + \Gamma_{\sigma 2}h_2^* + \Gamma_{w2}h_2^s = 0 \quad .$$

The principle of detailed balance can be employed to further require that all terms associated specifically with the wall process, sum to zero, so that

$$Q_{\sigma 1}^w - \Gamma_{w2}h_1^s + Q_{\sigma 2}^w + \Gamma_{w2}h_2^s = 0$$

and thus

$$\Gamma_{w2} = -(Q_{\sigma 1}^w + Q_{\sigma 2}^w)/(h_2^s - h_1^s) \quad . \quad (2-60)$$

With this result, we can now obtain for the bulk mass exchange process

$$\Gamma_{\sigma 2} = -[H_{\sigma 1}(T_1^s - T_1) + H_{\sigma 2}(T_2^s - T_2)]/(h_2^* - h_1^*) \quad . \quad (2-61)$$

Here we have identified two saturation temperatures, T_1^s and T_2^s consistent with the general two-phase pressure formulation. When the hydrostatic or single pressure model is employed, these become simply T^s .

All that remains for a complete constitutive model for the interphase energy exchange process is to specify the heat transfer coefficient and interfacial area for each flow/heat transfer condition of interest. This is no small task, and we do not mean to minimize its importance. However, a full development is well beyond the scope of this outline. Therefore, we will simply indicate the modeling approaches that are used in the RELAP5 code, in table form. For detailed information, see Ransom et al. (1982), and Dimenna et al. (1988).

The interface area formulations and the associated heat transfer film coefficients are tabulated in Table 2-3 in the form of formulas, specific numerical values, or a reference to the author of the correlation employed. The relationship between the heat transfer coefficients that we have used and the film coefficients in Table 2-3 is

$$H_{\sigma k} = h_{\sigma k} A_{\sigma} \quad (2-62)$$

Modeling

Table 2-3. RELAP5/MOD2 precritical heat flux bulk energy exchange models.

	Bubbly	Slug		Annular mist		Horizontal	Vertical
		Bubbles	Taylor bubble	Drops	Liquid film	Stratified	Stratified
α_{gf}	$\frac{3.6 \alpha_{pub}}{d_b}$	$\frac{3.6 \alpha_{gs} (1-\alpha_{TB})}{d_b}$	$\frac{4.5}{D} \alpha_{TB} (2.c)$	$\frac{3.6 \alpha_{fd}}{d_d} (1-\alpha_{ff})$	$\frac{4}{D} (1-\alpha_{ff})^{1/2} (2.5)$	$\frac{4 \sin \theta}{\pi D}$	$\frac{A_c}{V}$
$h_{if,SCL}$	Unal ^M	Unal ^M	Seider-Tate ^M	Brown ^M	Theofanous ^M	Dittus-Boelter	14.7k _f
$h_{if,SHL}$	Plesset-Zwick Lee-Ryley ^M	Plesset-Zwick Lee-Ryley ^M	3x10 ⁶	$\frac{k_f}{d_d} f(\Delta T_{sf})$	3x10 ⁶	Dittus-Boelter $\pi f(\Delta T_{sf})$	14.7k _f
$h_{ig,SHG}$	10 ⁴	10 ⁴	Lee-Ryley ^M	Lee-Ryley ^M	Dittus-Boelter	Dittus-Boelter 10 ⁴ f(ΔT_{sg})	81.4 k _g
$h_{ig,SCG}$	10 ⁴ f(ΔT_{sg})	10 ⁴ f(ΔT_{sg})	10 ⁴ f(ΔT_{sg})	10 ⁴ f(ΔT_{sg})	10 ⁴ f(ΔT_{sg})	10 ⁴ f(ΔT_{sg})	81.4 k _g

SCL = subcooled liquid

SHL = superheated liquid

SHG = superheated gas

SCG = subcooled gas

M = modified

f(ΔT_{sg}) = quadratic function of $\Delta T_{sg} = T^s - T_g$

f(ΔT_{sf}) = quadratic function of $\Delta T_{sf} = T^s - T_f$

where h_o should not be confused with the enthalpy. Also, tabulated in Table 2-3 are entries for two thermodynamic states of the two phases [i.e., subcooled liquid (SCL), superheated liquid (SHL), superheated vapor (SHG), and subcooled vapor (SCG)]. Note that two of the states, SCL and SHG, are stable states, whereas the states SHL and SCG are metastable states. The boxed-in areas of Tables 2-3 and 2-4 show the states and flow regimes in which the rates are not mechanistically modeled. These are generally the metastable states where spontaneous mass transfer is possible, and, with exceptions to be mentioned, little is known about modeling such rates in terms of heat transfer effects. The exceptions to this statement are bubble growth in superheated liquid, in which the Plesset-Zwick model is used, and the stratified flow regimes, where a simple thermal diffusion model is assumed. The same statement applies to the subcooled vapor state in which only the stratified flow case is modeled mechanistically.

The correlations used for the post-CHF regimes are shown in Table 2-4. The superheated liquid states are again only modeled in the bubbly regime using the Plesset-Zwick correlation. On the other hand, only the bubbly regime is made large for the subcooled vapor. However, because of the nature of the postcritical heat flux processes (i.e., substantial boiling and wall temperatures exceeding saturation temperature), it is unlikely that the subcooled vapor state would ever exist, at least in transient situations of interest in light water reactor safety.

Table 2-5 lists the formulation that is used in RELAP5/MOD3 for the wall mass transfer rate. As mentioned, only boiling or condensation processes are assumed (not simultaneously).

Table 2-4. RELAP5/MOD2 postcritical heat flux bulk energy exchange models.

	Inverted annular		Inverted slug		Mist
	Bubbles	Vapor film	Drops	Taylor drop	
α_{gf}	$\frac{3.6 \alpha_{bub}}{d_b} (1-\alpha_g)$	$\frac{4}{D} (1-\alpha_B)^{1/2} (2.5)$	$\frac{3.6 \alpha_{drb}}{d_d} (1-\alpha_B)$	$\frac{4.5}{D} \alpha_B (2.5)$	$\frac{3.6 \alpha_{drb}}{d_d}$
$h_{if,SCL}$	Unal ^M	Dittus-Boelter	Brown ^M	Brown ^M	Brown ^M
$h_{if,SHL}$	Plesset-Zwick Lee-Ryley ^M	3×10^6	$\frac{k_f}{d_d} f(\Delta T_{sf})$	$\frac{k_f}{d_d} f(\Delta T_{sf})$	$\frac{k_f}{d_d} f(\Delta T_{sf})$
$h_{ig,SHG}$	10^4	$\frac{k_g}{D}$	Lee-Ryley ^M	$\frac{k_g}{D}$	Lee-Ryley ^M
$h_{ig,SCG}$	$10^4 f(\Delta T_{sg})$	$\frac{k_g}{D}$	Lee-Ryley ^M	$\frac{k_g}{D}$	$10^4 f(\Delta T_{sg})$

SCL = subcooled liquid
 SHL = superheated liquid
 SHG = superheated gas
 SCG = subcooled gas
 M = modified
 $f(\Delta T_{sg})$ = quadratic function of $\Delta T_{sg} = T^s - T_g$
 $f(\Delta T_{sf})$ = quadratic function of $\Delta T_{sf} = T^s - T_f$

Table 2-5. RELAP5/MOD2 wall vapor generation models.

	Single-phase	Condensation	Nucleate boiling	Transition film	Single-phase
	Liquid convection			and film boiling	Vapor convection
Γ_w	0	$\frac{Q_{wg}}{h_{fg} + 0.375 C_{pg}(T_g - T^s)}$	$\frac{h_{mic}(T_w - T^s) A_w V}{h_{fg} [1 + C_{pf}(T^s - T_f) \rho_f / (\rho_g h_{fg})]^2}$	$\frac{Q_{wf}}{h_{fg} + (1/2) C_{pg}(T_g - T^s)}$	0
		Nusselt (vertical) ^M Chato (horizontal) ^M Carpenter/Colburn ^M	Chen ^M	Chen ^M Bromley ^M	

In summary, it is possible to mechanistically model most of the interphase energy exchange processes (in terms of empirical heat transfer coefficients). However, with a few exceptions, little is known about the behavior of the metastable fluid states in this regard, and large heat transfer coefficients are used, which have the effect of causing equilibration of the metastable states. This appears to be an acceptable approximation for most engineering calculations and most processes of interest in LWR reactor safety.

In particular, depressurization and vaporization of superheated liquid is a state that can be modeled using the Plesset-Zwick model.

3. NUMERICAL METHODS FOR THE TWO-FLUID MODEL IN RELAP5/MOD3

RELAP5 solves a system of quasi-linear two-phase flow equations that embodies phenomena that have large variations in the associated time constant. The smallest time constant is associated with the interphase energy and mass transfer. These processes are closely coupled to the pressure and energy fields and, to a large extent, behave as source terms in the equations. The next fastest time constant is associated with relaxation of stress waves propagated relative to the fluid at the sound speed. The largest time constant is associated with mass and energy convection propagated with the material velocity.

These time constants affect the development of a numerical process in slightly different ways. The mass transfer effect results in a *stiff* system and will require, for accuracy, that the source terms associated with mass transfer be evaluated implicitly (in terms of the dependent variables at the new time level). The propagated effects result in Courant-type time-step limits for explicit differencing of the governing terms of the equations. Generally, the detailed resolution of the stress waves will not be of interest, and, thus, implicit treatment of these terms, will be desirable in order to eliminate the sound speed Courant limit. The semi-implicit differencing scheme has this property, and the permissible time step is limited by the material Courant limit. If desired, this process can be carried one step further. The material Courant limit can be eliminated by use of more implicit schemes. In this last case, two methods exist that are not material Courant time-step limited. These are the nearly implicit schemes (Mahaffy 1982, Trapp and Riemke 1986, and the fully implicit schemes (Micaelli 1987, Richards et al. 1985, Rosten and Spalding 1987). Thus, the numerical schemes of most interest, and the ones which we shall discuss further, are the semi-implicit and those with sufficient implicitness to eliminate the material Courant limit. The RELAP5 codes use only the semi-implicit and the nearly implicit methods (Ransom et al. 1985, Allison et al 1990).

One further aspect of numerical methods for two-phase flow, which was also considered in the development of methods for the linear system, is the use of staggered grids. This approach evolves naturally when the conservation equations are considered in an integral sense. The mass and energy variables or scalars, are considered to exist at cell centers. The velocities appear in the flux terms at the cell edges. The two-fluid models that have been developed for LWR safety use are based on this method of constructing difference equations.

3.1 Semi-Implicit Numerical Method

The semi-implicit numerical method will be described as it is implemented in the RELAP5 code (Ransom 1985, Allison et al. 1990). These implementations differ from the semi-implicit implementations in COBRA, and earlier versions of TRAC, (Liles and Reed 1978), mainly in the way that the momentum flux terms of the momentum equations are evaluated. In RELAP5, the momentum flux terms use a centered difference on the velocity squared with an artificial viscosity added explicitly. The artificial viscosity is formulated in such a way that it has no effect on the steady state flow in a variable area duct. The formulation is similar to a donored or upwind difference formulation for incompressible flow in a constant area duct. The COBRA and TRAC formulations simply used a donored momentum flux and no added viscosity term. The formulation used in

Numerical Methods

RELAP5 has the advantage that pressure recovery in a diffusing flow is correctly calculated, while the direct donor formulation incorrectly predicts a loss in total pressure for a diffusing flow.

The general guidelines used in developing the semi-implicit numerical scheme are to evaluate the source terms that appear in the equations, implicitly if possible, but maintain linearity in the dependent variables. The spatial derivatives of the mass and energy fluxes are evaluated by using donored old-time quantities for the scalars and evaluating the velocity with which the quantities are fluxed implicitly. In addition, the only spatial derivative in the momentum equations that is evaluated implicitly is the pressure gradient. This permits the momentum equations to be solved for the velocities in terms of the adjoining cell pressures at each velocity node. The terms *old-time* and *new time* are used to designate the current time level and the time level at which the solution is being obtained, respectively. We will also use the terms of *cell* to refer to the center of the control volume for mass and energy, and *junction* to refer to the center of the momentum control volume at which the velocity is evaluated (the edge of the mass and energy cell). Throughout this section, subscripts *f* and *g* will designate liquid and vapor respectively.

3.1.1 Phasic Balance Equations

The phasic continuity, momentum, and energy equations are the basic field equations for the two-fluid model. They will be listed here as they are used in the RELAP5 code (Ransom et al. 1985, Allison et al. 1990), except that consideration of virtual mass effects is omitted for simplicity. The mass and momentum equations are used as sum and difference equations in the numerical scheme and are recorded here in that form. The reason for using this form is ease of degeneration of the model to the single-phase case.

The mass conservation relations are a mixture mass equation,

$$\partial(\alpha_g \rho_g + \alpha_f \rho_f) / \partial t + (1/A) [\partial(\alpha_g \rho_g v_g A + \alpha_f \rho_f v_f A) / \partial x] = 0 \quad (3-1)$$

and a difference of the phasic mass equations

$$\begin{aligned} \partial(\alpha_g \rho_g - \alpha_f \rho_f) / \partial t + (1/A) [\partial(\alpha_g \rho_g v_g A) / \partial x] \\ - (1/A) [\alpha_f \rho_f v_f A] / \partial x = 2\Gamma_g \end{aligned} \quad (3-2)$$

For simplicity, the equations are written in the area average notation wherein the term L_x/V has been reduced to $1/A$. Strictly speaking, all variables must be considered as space-time averaged quantities.

The momentum equations are used in the expanded form. Two convenient independent momentum equations are obtained by a sum and a difference of the phasic momentum equations (the difference is taken after dividing through by the product of the respective volume fraction and phasic density). The sum equation is

$$\begin{aligned} \alpha_g \rho_g (\partial v_g / \partial t) + \alpha_f \rho_f (\partial v_f / \partial t) + 1/2 \alpha_g \rho_g (\partial v_g^2 / \partial x) + 1/2 \alpha_f \rho_f (\partial v_f^2 / \partial x) \\ = -\partial P / \partial x + \rho B_x - (\tau_w)_g - (\tau_w)_f - \Gamma_g (v_g - v_f) \end{aligned} \quad (3-3)$$

where B_x is the x component of the body force vector ($B_x = g \cos \theta$) and the difference equation

$$\begin{aligned} & \partial v_g / \partial t - \partial v_f / \partial t + 1/2 (\partial v_g^2 / \partial x) - 1/2 (\partial v_f^2 / \partial x) \\ & = -(1/\rho_g - 1/\rho_f) (\partial P / \partial x) - (\tau_w)_g / \alpha_g \rho_g + (\tau_w)_f / \alpha_f \rho_f + \Gamma_g [\rho v_o \\ & - (\alpha_f \rho_f v_g + \alpha_g \rho_g v_f)] / (\alpha_g \rho_g \alpha_f \rho_f) - \rho \tau_o / (\alpha_g \rho_g \alpha_f \rho_f) \end{aligned} \quad (3-4)$$

where the sum equation contains one interphase interaction term, the momentum transfer associated with mass transfer, which results from the expanded momentum equation form. The difference equation contains interphase momentum exchange terms due to mass exchange, and interphase friction. The particular forms for Equations (3-3) and (3-4) were chosen to provide smooth degeneration to the single-phase case. Under single-phase conditions, both equations remain determinant, and the constitutive model for interphase drag is formulated such that interphase friction remains finite. Thus, in the single-phase limit, Equation (3-2) reduces to a statement that the phasic velocities are equal.

The two phasic thermal energy equations are

$$\begin{aligned} & \partial(\alpha_g \rho_g \mu_g) / \partial t + (1/A) \partial(\alpha_g \rho_g \mu_g v_g A) / \partial x = -P \partial \alpha_g / \partial t \\ & - (P/A) \partial(\alpha_g v_g A) / \partial x + q_{wg} + q_{og} + \Gamma_g h_g^* + DISS_g \end{aligned} \quad (3-5)$$

$$\begin{aligned} & \partial(\alpha_f \rho_f \mu_f) / \partial t + (1/A) \partial(\alpha_f \rho_f \mu_f v_f A) / \partial x = -P \partial \alpha_f / \partial t \\ & - (P/A) \partial(\alpha_f v_f A) / \partial x + q_{wf} + q_{of} - \Gamma_g h_f^* + DISS_f \end{aligned} \quad (3-6)$$

The q_{wg} and q_{wf} are the wall heat transfer rates to the vapor and liquid phases, respectively. The q_{og} and q_{of} are the interfacial heat transfer rates from the interface to the vapor and liquid phases, respectively. The values for the enthalpy associated with mass transfer, h_g^* and h_f^* are the values defined in Section 2 to account for all the energy associated with interphase mass transfer. The volumetric heating rates have been omitted for simplicity. The terms $DISS_g$ and $DISS_f$ are the dissipation terms due to irreversible degradation of kinetic energy to internal energy. Only the dissipation effects due to wall friction, dynamic losses, and pump inefficiencies are included, while minor effects due to interphase drag and mass transfer are neglected. The vapor generation rate, Γ_g , is defined in terms of the interphase energy transfer rates using the interphase balance

$$\Gamma_g = -(q_{og} + q_{of}) / (h_g^* - h_f^*) \quad (3-7)$$

The interphase energy transfer rates, q_{og} and q_{of} , and the associated interphase energy, $h_g^* - h_f^*$, are formulated to account for flow regime and wall heat transfer effects on the interphase mass transfer rate. In all cases, the sum of Equations (3-5) and (3-6), with the definition of Γ_g from Equation (3-7), yields the correct mixture thermal energy equation. The interphase mass transfer rate consists of a wall and a bulk contribution. The interphase energy transfer is, therefore, also partitioned accordingly.

The system of field equations is closed, insofar as relating differential quantities is concerned, by inclusion of the equations of state for the fluids. Additional constitutive models are needed for

Numerical Methods

evaluation of the nondifferential terms. The fluid state properties are defined using tables with interpolation to the equation-of-state data. The liquid phase density is a function of the pressure and the liquid phase energy:

$$\rho_f = \hat{\rho}_f(P, u_f) \quad (3-8)$$

The vapor phase density is a function of the system pressure, vapor phase energy, and the mass fraction of noncondensable component:

$$\rho_g = \hat{\rho}_g(P, u_g, X_n) \quad (3-9)$$

We require a two-term Taylor series approximation of these functions and, thus, also require that the partial derivatives of $\hat{\rho}_k$ with respect to P and u_k be obtainable.

3.1.2 Numerical Solution

The numerical solution method for the hydrodynamic model uses a finite difference scheme having fixed, but staggered, spatial noding. Partial implicitness is used for stability and avoidance of the acoustic Courant limit on the time step.

The spatial discretization is illustrated on Figure 3-1 for flow in a variable cross-sectional area duct. Computational spatial increments, or control volumes, are denoted by an integer index, j . The scalar variables P , ρ_g , ρ_f , α_g , u_g , and u_f are evaluated at the centers of these control volumes. The volume of the j^{th} control volume is denoted by V_j . The edges, or junctions, between adjoining control volumes are denoted by an index which is an integer multiple of 1/2 (i.e., the nodalization is staggered by a half volume). The vector quantities v_g and v_f are evaluated at these points.

In order to maintain linearity in the dependent variables, and, thus, enable a direct solution, it is necessary to linearize the state relationship as well as any product terms appearing in the time derivatives. (The space derivatives are made linear by the choice of difference operator.) Mass and energy truncation errors are inherent in the linearization, and these errors must be controlled to avoid excessive accumulation. Such truncation error can for example, be controlled by appropriate time-step selection. The time-smoothing schemes discussed in Section 3.4 may also help to reduce linearization errors in some situations.

The difference equations corresponding to the balance equations, before linearization, are the mixture mass equation at cell j

$$\begin{aligned} & (\alpha_g \rho_g + \alpha_f \rho_f)^{n+1}_j - (\alpha_g \rho_g + \alpha_f \rho_f)^n_j + \left\{ \left[\dot{\alpha}_g^n \dot{\rho}_g^n (v_g)_{j+1/2}^{n+1} + \dot{\alpha}_f^n \dot{\rho}_f^n (v_f)_{j+1/2}^{n+1} \right] A_{j+1/2} \right. \\ & \left. - \left[\dot{\alpha}_g^n \dot{\rho}_g^n (v_g)_{j-1/2}^{n+1} + \dot{\alpha}_f^n \dot{\rho}_f^n (v_f)_{j-1/2}^{n+1} \right] A_{j-1/2} \right\} (\Delta t / V_j) = 0 \end{aligned} \quad (3-10)$$

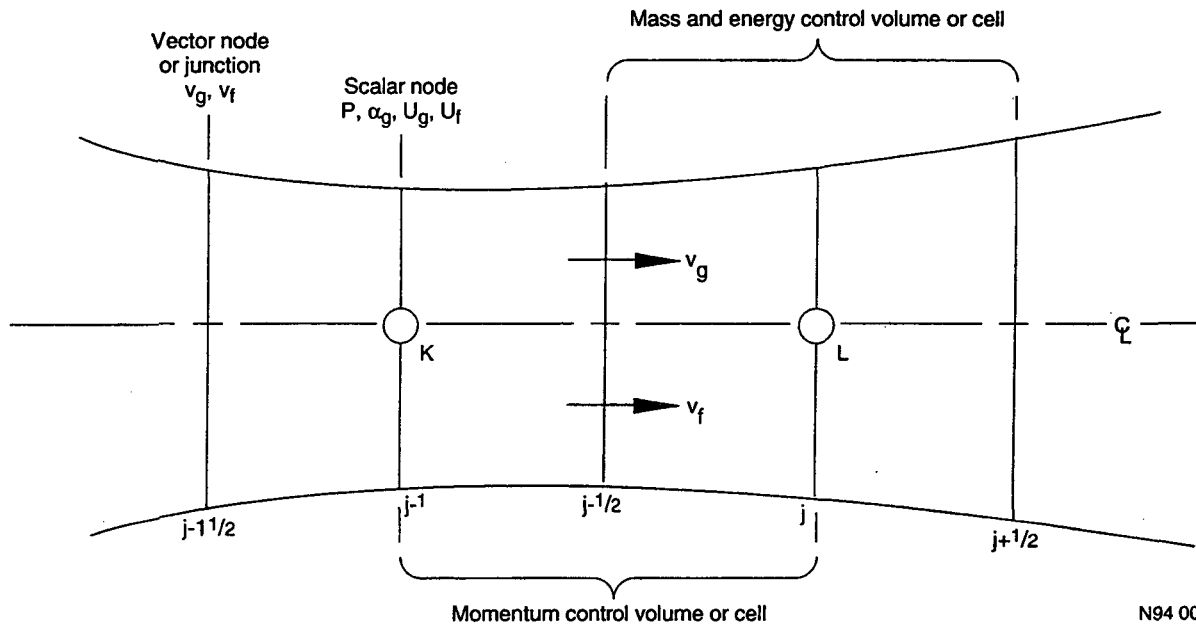


Figure 3-1. Difference equation discretization schematic.

the difference of phasic mass equations,

$$\begin{aligned}
 & (\alpha_g \rho_g - \alpha_f \rho_f)_{j+1/2}^{n+1} - (\alpha_g \rho_g - \alpha_f \rho_f)_j^n + \left\{ \left[\dot{\alpha}_g^n \dot{\rho}_g^n (v_g)_{j+1/2}^{n+1} - \dot{\alpha}_f^n \dot{\rho}_f^n (v_f)_{j+1/2}^{n+1} \right] A_{j+1/2} \right. \\
 & \left. - \left[\dot{\alpha}_g^n \dot{\rho}_g^n (v_g)_{j-1/2}^{n+1} - \dot{\alpha}_f^n \dot{\rho}_f^n (v_f)_{j-1/2}^{n+1} \right] A_{j-1/2} \right\} (\Delta t / V_j) = 2(\Gamma_g)_{j+1/2}^{n+1} \Delta t
 \end{aligned} \tag{3-11}$$

the mixture momentum equation at junction $j+1/2$,

$$\begin{aligned}
 & \left[(\alpha_g \rho_g)_{j+1/2}^n (v_g^{n+1} - v_g^n)_{j+1/2} + (\alpha_f \rho_f)_{j+1/2}^n (v_f^{n+1} - v_f^n)_{j+1/2} \right] \Delta x_{j+1/2} \\
 & + \frac{1}{2} (\alpha_g \rho_g)_{j+1/2}^n \left[(v_g^2)_{j+1}^n - (v_g^2)_j^n \right] \Delta t \\
 & + \frac{1}{2} (\alpha_f \rho_f)_{j+1/2}^n \left[(v_f^2)_{j+1}^n - (v_f^2)_j^n \right] \Delta t - \frac{1}{2} \left[(\alpha_g \rho_g)_{j+1/2}^n VISG_{j+1/2}^n \right. \\
 & + \left. (\alpha_f \rho_f)_{j+1/2}^n VISF_{j+1/2}^n \right] \Delta t = - (P_{j+1} - P_j)^{n+1} \Delta t + \left[\rho_{j+1/2}^n B_x \right. \\
 & - \left. (\alpha_g \rho_g)_{j+1/2}^n (v_g)_{j+1/2}^{n+1} FWG_{j+1/2}^n - (\alpha_f \rho_f)_{j+1/2}^n (v_f)_{j+1/2}^{n+1} FWF_{j+1/2}^n \right. \\
 & \left. - (\Gamma_g)_{j+1/2}^n (v_g - v_f)_{j+1/2}^n \right] \Delta x_{j+1/2} \Delta t
 \end{aligned} \tag{3-12}$$

the difference of phasic momentum equations,

Numerical Methods

$$\begin{aligned}
 & \left[\left(v_g^{n+1} - v_g^n \right) - \left(v_f^{n+1} - v_f^n \right) \right]_{j+1/2} \Delta x_{j+1/2} + \left\{ \frac{1}{2} \left[\left(v_g^2 \right)_{j+1}^n - \left(v_g^2 \right)_j^n \right] \right. \\
 & \quad \left. - \frac{1}{2} \left[\left(v_f^2 \right)_{j+1}^n - \left(v_f^2 \right)_j^n \right] - \frac{1}{2} [VISG - VISF]_{j+1/2}^n \right\} \Delta t \\
 & = \left[(\rho_f - \rho_g) / (\rho_g \rho_f) \right]_{j+1/2}^n (P_{j+1} - P_j)^{n+1} \Delta t - \left\{ FWG_{j+1/2}^n (v_g)_{j+1/2}^{n+1} \right. \\
 & \quad + FWF_{j+1/2}^n (v_f)_{j+1/2}^{n+1} + \left[\Gamma_g (\rho v_o - \alpha_f \rho_f \nu_g - \alpha_g \rho_g \nu_f) / (\alpha_g \rho_g \alpha_f \rho_f) \right]_{j+1/2}^n \\
 & \quad \left. - (\rho FI)_{j+1/2}^n (v_g - v_f)_{j+1/2}^{n+1} \right\} \Delta x_{j+1/2} \Delta t
 \end{aligned} \tag{3-13}$$

the vapor energy equation,

$$\begin{aligned}
 & (\alpha_g \rho_g \mu_g)_j^{n+1} - (\alpha_g \rho_g \mu_g)_j^n + P_j^n \left(\alpha_g^{n+1} - \alpha_g^n \right) \\
 & \quad + \left[(\dot{\alpha}_g \dot{\rho}_g \dot{\mu}_g)_{j+1/2}^n + \left(\dot{\alpha}_g^n \right)_{j+1/2} P_j^n \right] (v_g)_{j+1/2}^{n+1} A_{j+1/2} (\Delta t / V_j) \\
 & \quad - \left[(\dot{\alpha}_g \dot{\rho}_g \dot{\mu}_g)_{j-1/2}^n + \left(\dot{\alpha}_g^n \right)_{j-1/2} P_j^n \right] (v_g)_{j-1/2}^{n+1} A_{j-1/2} (\Delta t / V_j) \\
 & = \left\{ [-h_f^* / (h_g^* - h_f^*)]^n q_{og}^{n+1} - [h_g^* / (h_g^* - h_f^*)]^n q_{of}^{n+1} \right. \\
 & \quad \left. + q_{wg}^n + DISS_g^n \right\}_j \Delta t
 \end{aligned} \tag{3-14}$$

and the liquid energy equation,

$$\begin{aligned}
 & (\alpha_f \rho_f \mu_f)_j^{n+1} - (\alpha_f \rho_f \mu_f)_j^n + P_j^n \left(\alpha_f^{n+1} - \alpha_f^n \right) \\
 & \quad + \left[(\dot{\alpha}_f \dot{\rho}_f \dot{\mu}_f)_{j+1/2}^n + \left(\dot{\alpha}_f^n \right)_{j+1/2} P_j^n \right] (v_f)_{j+1/2}^{n+1} A_{j+1/2} (\Delta t / V_j) \\
 & \quad - \left[(\dot{\alpha}_f \dot{\rho}_f \dot{\mu}_f)_{j-1/2}^n + \left(\dot{\alpha}_f^n \right)_{j-1/2} P_j^n \right] (v_f)_{j-1/2}^{n+1} A_{j-1/2} (\Delta t / V_j) \\
 & = \left\{ [+h_f^* / (h_g^* - h_f^*)]^n q_{og}^{n+1} + [h_g^* / (h_g^* - h_f^*)]^n q_{of}^{n+1} \right. \\
 & \quad \left. + q_{wf}^n + DISS_f^n \right\}_j \Delta t
 \end{aligned} \tag{3-15}$$

The terms FWG, FWF, and FI designate the wall frictional forces between the wall and the two phases, and the interphase drag coefficients, respectively. The superposed dot denotes a donored scalar quantity based on the vapor or liquid water velocity. Thus quantities appear in the mass and energy flux terms and are simply an *upwind* evaluation of the fluxed quantities based on the velocity at the *n*th time level.

The terms VISF and VISG appearing in the momentum equations are *viscous-like* numerical terms necessary to obtain a well-posed numerical problem. These terms are formulated so that they contribute no unphysical force for steady flow in a variable area duct, and are defined by

$$\begin{aligned}
 VISG_{j+1/2}^n = & \left\{ |v_{g,j+1}^n| \left[(v_g)_{j+3/2}^n (A_{j+3/2}/A_{j+1/2}) - (v_g)_{j+1/2}^n \right] \right. \\
 & \left. - |v_{g,j}^n| \left[(v_g)_{j+1/2}^n - (v_g)_{j-1/2}^n (A_{j-1/2}/A_{j+1/2}) \right] \right\}
 \end{aligned} \quad (3-16)$$

$$\begin{aligned}
 VISF_{j+1/2}^n = & \left\{ |v_{f,j+1}^n| \left[(v_f)_{j+3/2}^n (A_{j+3/2}/A_{j+1/2}) - (v_f)_{j+1/2}^n \right] \right. \\
 & \left. - |v_{f,j}^n| \left[(v_f)_{j+1/2}^n - (v_f)_{j-1/2}^n (A_{j-1/2}/A_{j+1/2}) \right] \right\}
 \end{aligned} \quad (3-17)$$

where the fluid velocities at the integer indicies are *volume average* velocities. In the simplest case of a straight passage, these values are arithmetic averages of the adjoining junction values.

The viscous damping terms, in combination with the centered difference approximation to the spatial derivative of the square of the phasic velocity in Equations (3-12) and (3-13), correspond to the use of an upwind approximation to the momentum flux terms in the form of derivatives of the velocities squared as in Equations (3-3) and (3-4).

The difference of product terms are linearized by ignoring second-order terms. Examples can be seen for the $(\alpha_g \rho_g)$ product:

$$(\alpha_g \rho_g)^{n+1} - (\alpha_g \rho_g)^n = \alpha_g^n \left(\rho_g^{n+1} - \rho_g^n \right) + \rho_g^n \left(\alpha_g^{n+1} - \alpha_g^n \right) \quad (3-18)$$

and the $(\alpha_g \rho_g \mu_g)$ product

$$\begin{aligned}
 (\alpha_g \rho_g \mu_g)^{n+1} - (\alpha_g \rho_g \mu_g)^n = & (\alpha_g \rho_g)^n \left(\mu_g^{n+1} - \mu_g^n \right) + (\alpha_g \mu_g)^n \left(\rho_g^{n+1} - \rho_g^n \right) \\
 & + (\rho_g \mu_g)^n \left(\alpha_g^{n+1} - \alpha_g^n \right) .
 \end{aligned} \quad (3-19)$$

The phasic densities are expressed in terms of the state variables by a two-term Taylor series approximation for the equation of state. For example for the vapor phase

$$\rho_g^{n+1} = \rho_g^n + (\partial \rho_g / \partial P)_{u_g}^n (P^{n+1} - P^n) + (\partial \rho_g / \partial u_g)_{P_g}^n \left(u_g^{n+1} - u_g^n \right) \quad (3-20)$$

$$\rho_f^{n+1} = \rho_f^n + (\partial \rho_f / \partial P)_{u_f}^n (P^{n+1} - P^n) + (\partial \rho_f / \partial u_f)_{P_f}^n \left(u_f^{n+1} - u_f^n \right) . \quad (3-21)$$

The system of difference equations, consisting of Equations (3-10) through (3-15), along with the linear equations of state, Equations (3-20) and (3-21), are solved simultaneously by a forward elimination scheme and subsequent direct solution for the pressure field. This process is illustrated in matrix form in Figure 3-2. The system of difference equations is illustrated in Figure 3-2 by designating nonzero coefficients of the dependent variables by x's in each equation, as identified in

	j-1		j-1/2		j		j+1/2		j+1		
j Vapor EOS		$[P]_{j-1}^{n+1}$		$\begin{bmatrix} v_g \\ v_f \end{bmatrix}^{n+1}$	$\begin{bmatrix} x & x & x \\ x & x & x \end{bmatrix}$		$\begin{bmatrix} p \\ \rho_g \\ \rho_f \\ \alpha_g \\ u_g \\ u_f \end{bmatrix}^{n+1}$	$\begin{bmatrix} v_g \\ v_f \end{bmatrix}^{n+1}$	$[P]_{j+1}^{n+1}$	$\begin{bmatrix} x \\ x \end{bmatrix}^n$	
j Liquid EOS											
j Mixture Mass											
j Phasic Mass Diff											
j Vapor Energy											
j Liquid Energy											
j-1/2 MOM SUM	x										
j-1/2 MOM DIFF	x										
j+1/2 MOM SUM											
j+1/2 MOM DIFF											
FIRST REDUCTION	$\begin{bmatrix} y \\ y \end{bmatrix}$	+	$\begin{bmatrix} y & y \\ 1 & 1 \end{bmatrix}$	+	$\begin{bmatrix} y \\ y \\ y \\ y \\ y \end{bmatrix}$	+	$\begin{bmatrix} y & y \\ 1 & 1 \end{bmatrix}$	+	$\begin{bmatrix} y \\ y \end{bmatrix}$	=	$\begin{bmatrix} y \\ y \\ y \\ y \\ y \end{bmatrix}$
SECOND REDUCTION	$[z]$	+	$[]$	+	$[z]$	+	$[]$	+	$[z]$	=	$[z]$

Figure 3-2. Matrix representation of the semi-implicit difference scheme.

the left-most column. The $n+1$ or new-time value for the volume variables at node j comprises the vector, $(P, \rho_g, \rho_f, \alpha, u_g, u_f)$, and the junction variables for junctions $j+1/2$ and $j-1/2$ comprise the vector (v_g, v_f) . Pressures are shown only for nodes $j-1$, j , and $j+1$, as they are the only volume variables that appear in the system of equations for node and junctions $j-1/2$ and $j+1/2$. All other terms of the equation are shown as source terms in the right-most column in Figure 3-2. In particular, this column contains all terms evaluated at the n^{th} or current time level.

The momentum equations couple the velocities to the pressure field and are applied at junctions $j+1/2$ and $j-1/2$ for the control volume j , illustrated above the matrix in Figure 3-2. The mass and energy conservation equations apply to volume j and express the volume pressure in terms of the volume mass and energy variables. The linear structure of the system of equations and the fact that the junction velocities are only functions of the pressures at the $n+1$ time step level, permit the volume equation to be reduced to a single equation in terms of the volume pressure and junction velocities at the $n+1$ time level. This is illustrated as the first reduction step in Figure 3-2. The momentum equations can also be solved for the liquid and vapor velocities in terms of the adjoining volume pressures as a part of this first step or reduction. In the second reduction step, the junction velocities are eliminated from the j volume pressure equation to yield a single equation for each control volume in terms of pressures in the j^{th} volume and the adjoining $(j+1)^{\text{th}}$ and $(j-1)^{\text{th}}$ volumes. For a sequentially coupled system, this results in a tridiagonal matrix of equations for the system pressures. For branched systems, the matrix is no longer tridiagonal but remains sparse, and a sparse matrix solution algorithm is used to obtain a direct solution for all new-time system pressures.

A back-substitution procedure is used to evaluate all system masses, energies, and velocities. Evaluation of the state parameters from the full nonlinear equation of state completes the basic time advancement algorithm.

The semi-implicit algorithm for two-phase to two-phase transition can, therefore, be summarized in the following seven steps:

- Step 1: Update variable P^{n+1} by constructing linear system $Ax = b$ and solving with sparse matrix solver for P^{n+1} using the state-variable data at t^n .
- Step 2: Update the phasic velocities at time level $n+1$ by solving for the phasic velocities using explicit advancement of momentum equations with pressure data P^{n+1} from Step 1.
- Step 3: Update the intermediate values for the noncondensable qualities, the phasic voids, and specific internal energies by solving for the intermediate values using pressure from Step 1 and phasic velocities from Step 2.
- Step 4: Calculate mass errors from Equations (3-22) and (3-23) and compare them to prescribed tolerances. If the test fails, reduce Δt and restart advancement at Step 1. If the tests succeed, proceed to Step 5.
- Step 5: Update Γ_g^{n+1} by computing the interphase mass transfer from Equation (3-7).
- Step 6: Update the noncondensable qualities and the phasic voids and internal energies using the pressure from Step 1, the phasic velocities from Step 2, and Γ_g^{n+1} from step 5.

Numerical Methods

Step 7. Advance to the next time station and return to Step 1.

3.1.3 Time Step Control

A variety of checks on solution acceptability are used to control the time step. These include material Courant limit checks, mass error checks, material properties out of defined ranges, water property errors, or excessive extrapolation of state properties in the metastable regimes.

The material Courant limit check is made before a hydrodynamic advancement takes place. The material Courant limit is evaluated for each hydrodynamic volume using the volume mass average velocity:

$$(\Delta t_c)_i = [\Delta x \max(\alpha_f^n, \alpha_g^n) / \max(|\alpha_f^n V_f^n|, |\alpha_g^n V_g^n|)]_i \\ i = 1, 2, \dots, N,$$

where N is the total number of volumes in the entire system.

The minimum Courant limit for all of the N volumes is the Courant limit for the entire system.

The mass error check is made after the time step solution is nearly complete. Two types of mass error measures are computed. The first one checks the validity of density linearization and is defined as

$$E_m = \max(|\rho_{mi} - \rho_i|/\rho_i, i = 1, 2, \dots, N) \quad (3-22)$$

where ρ_{mi} is the total density of the i^{th} volume computed from the state relationship. The second one is a measure of overall system mass error and is given by

$$E_{rms} = 2 \sum_{i=1}^N [V_i(\rho_i - \rho_{mi})]^2 / \sum_{i=1}^N (V_i \rho_i)^2 \quad (3-23)$$

where V_i is the volume of the i^{th} volume.

If either E_m or E_{rms} is $> 8 \times 10^{-3}$, the time step is rejected and repeated with one half of the time step size. Otherwise, the time step is accepted, and the next time step size is doubled if both E_m and E_{rms} are $< 8 \times 10^{-4}$.

If at any point in the solution flow a material property is found to lie outside the defined range, the time step is halved and repeated. This process will proceed until the user-specified minimum time step is reached. If the minimum time step is reached without obtaining a valid solution, the code calculation is terminated and the last time step is repeated with a diagnostic dump printed. A program stop is encountered at completion of the step. This same procedure is applied for all property or extrapolation features.

3.2 Nearly Implicit Scheme

As discussed earlier, it is possible to employ increased implicitness to achieve stability for time steps that exceed the time interval corresponding to propagation through the spatial discretization interval. The semi-implicit scheme, previously discussed, has sufficient implicitness to eliminate stability limits associated with propagation of pressure waves. We now turn to consideration of schemes having sufficient implicitness to eliminate Courant-type stability limits associated with material transport. Before discussing the details of the nearly implicit scheme, we will again review the accuracy limitations inherent in the use of such schemes.

The motive for the use of increased implicitness is to achieve faster running algorithms. However, the inherent compromise in accuracy that can result has not always been properly considered. Therefore, we resort to consideration of a simple, single advection equation to examine the conditions under which Material Courant Violating (MCV) schemes should be used. We note that when an MCV scheme is run at time steps that correspond to the Courant limit, then the scheme is as accurate as an explicit or semi-implicit scheme and the only disadvantage is the increased computational effort required to maintain the increased implicitness. Thus, a clear advantage of implicit schemes is the time-step flexibility that results from being able to follow transient evolution by running at a reduced time step and also being able to run at a large time step when it is not important to follow the detailed evolution or where the time evolution is very slow.

3.2.1 Implications of Implicit Differencing

The properties of an implicit difference scheme can be illustrated by using the following advection equation:

$$\partial\phi/\partial t + B \partial\phi/\partial x = - C(\phi - \phi_0) \quad (3-24)$$

which represents the propagation and decay of dependent variable, ϕ , used here as a scalar to its steady state value ϕ_0 . The velocity of propagation is B , the time constant of the decay is $(1/C)$, and the steady state value that the system approaches is ϕ_0 . If we examine the predicted behavior of a typical Fourier component of the solution for a simple implicit central difference operator at a spatial point x_j , we obtain the following result:

$$\phi_j^{n+1} = \left[\phi_j^n + C \phi_0 \Delta t \right] / [1 + C \Delta t + i(B \Delta t / \Delta x) \sin(k \Delta x)] \quad (3-25)$$

where k is the wavenumber ($= 2\pi/\lambda$) for a particular Fourier mode of wavelength λ . If we take the limit to Equation (3-25) for large $C \Delta t$, then only the steady state component of the solution remains (i.e., $\phi_j^{n+1} \rightarrow \phi_0$). The transient response is completely eliminated for sufficiently large $C \Delta t$.

Now, consider Equation (3-24) with the right hand side set to zero for a large Δt such that the Courant number $B(\Delta t/\Delta x)$ is large. The exact solution in this case is a periodic wave propagating with speed B and without decay. The Fourier components of the numerical solution with wavenumbers k such that $B(\Delta t/\Delta x)\sin(k \Delta x)$ are large will nonetheless decay to zero as $t \rightarrow \infty$. In this case, the undamped dynamic wave propagation phenomena present in the differential system has been filtered out completely by the numerical solution. Reference 3-2 qualified the above statement by noting that

Numerical Methods

if the wavelength is extremely long (small k) such that $B(\Delta t/\Delta x)\sin(k \Delta x)$ is still much less than one, then these long waves may be accurately represented, whereas the short waves are effectively filtered out of the calculation. The above qualification, however, is flawed because at the shortest wavelength, $2\Delta x$, $\sin(k \Delta x) = \sin(\pi) = 0$. Hence, the short waves with large wave numbers are not filtered out of the calculation if implicit central differencing is used. If, instead, upwind differencing is used to difference the spatial derivative term in Equation (3-24), then the $i \sin(k \Delta x)$ term in Equation (3-25) is replaced by $(1 - e^{-ik\Delta x})$ and the qualification made in reference 3-2 holds. Because short waves are usually not present at the steady state, the use of implicit upwind differencing is recommended if the objective is to reach steady state quickly by taking large time steps.

If Δt is restricted to the Courant limit corresponding to the propagation speed B , then whether or not the transient is accurately resolved will depend on the time-step size relative to the time constant ($1/C$). For example, for accurate resolution we must require

$$(B \Delta t/\Delta x) \text{ and } (C \Delta t) \leq 1$$

where $(B\Delta t/\Delta x)$ is the convective Courant number.

Thus, we see that if the time-step size is large compared to the Courant number associated with the advection or the time constant of the decay ($1/C$), the transient response is effectively filtered out of the solution. Whether or not this is acceptable in a given situation requires knowledge of the process and will depend on the reason that a solution is desired. Clearly, if only the steady state behavior of the system is desired, then the implicit scheme does what we want. On the other hand, if the transient response is desired, then the implicit scheme may require more computation effort compared to more explicit methods, since the time step must be restricted in order to accurately resolve convective phenomena.

To avoid the problem of solving fully implicit difference schemes, fractional step (sometimes called *multiple-step* since all of the steps are for the same time step) methods have been developed (Mahaffy 1982, Trapp and Riemke 1986). The equations can be split into fractional steps based on physical phenomena. This is the basic idea that motivated the development of the nearly implicit scheme. The fraction step method developed by Trapp and Riemke (1986) differs from that of the earlier developments in the reduced number of steps required to evaluate the momentum equations. This method is called the nearly implicit method of RELAP5 and is presented below.

The nearly implicit scheme consists of a first step that solves all six conservation equations, treating all interphase exchange processes, the pressure propagation process, and the momentum convection process, implicitly. This step uses the finite difference equations in the same form as for the semi-implicit scheme, except that the momentum flux terms of the sum and difference equations are evaluated in a linearly implicit fashion, and the added numerical viscosities are deleted. Thus, only the modified form for the momentum equations will need to be described here. The mass and energy equations are identical to Equations (3-10), (3-11), (3-14), and (3-15).

The sum and difference momentum equations for the nearly-implicit scheme are

$$\begin{aligned}
 & [(\alpha_g \rho_g)_{j+1/2}^n (v_g^{n+1} - v_g^n)_{j+1/2} + (\alpha_f \rho_f)_{j+1/2}^n (v_f^{n+1} - v_f^n)_{j+1/2}] \Delta x_{j+1/2} \\
 & + 1/2 (\dot{\alpha}_g \dot{\rho}_g)_{j+1/2}^n \left\{ (v_g^2)_{j+1}^n + 2(v_g)_{j+1}^n [(v_g)_{j+1}^{n+1} - (v_g)_{j+1}^n] \right. \\
 & - (v_g^2)_j^n - 2(v_g)_j^n [(v_g)_j^{n+1} - (v_g)_j^n] \left. \right\} \Delta t \\
 & + 1/2 (\dot{\alpha}_f \dot{\rho}_f)_{j+1/2}^n \left\{ (v_f^2)_{j+1}^n + 2(v_f)_{j+1}^n [(v_f)_{j+1}^{n+1} - (v_f)_{j+1}^n] \right. \\
 & - (v_f^2)_j^n - 2(v_f)_j^n [(v_f)_j^{n+1} - (v_f)_j^n] \left. \right\} \Delta t \\
 & = - (P_{j+1} - P_j)^{n+1} \Delta t + \left[\rho_{j+1/2}^n B_x \right. \\
 & - (\alpha_g \rho_g)_{j+1/2}^n (v_g)_{j+1/2}^{n+1} FWG_{j+1/2}^n - (\alpha_f \rho_f)_{j+1/2}^n (v_f)_{j+1/2}^{n+1} FWF_{j+1/2}^n \\
 & \left. - (\Gamma_g)_{j+1/2}^n (v_g - v_f)_{j+1/2}^n \right] \Delta x_{j+1/2} \Delta t \tag{3-26}
 \end{aligned}$$

$$\begin{aligned}
 & [(v_g^{n+1} - v_g^n) - (v_f^{n+1} - v_f^n)]_{j+1/2} \Delta x_{j+1/2} + \left\{ 1/2 [(\dot{\alpha}_g \dot{\rho}_g) / (\alpha_g \rho_g)]_{j+1/2}^n (v_g^2)_{j+1}^n \right. \\
 & + 2(v_g)_{j+1}^n [(v_g)_{j+1}^{n+1} - (v_g)_{j+1}^n] - (v_g^2)_j^n - 2(v_g)_j^n [(v_g)_j^{n+1} \\
 & - (v_g)_j^n] \left. \right\} \Delta t - 1/2 [(\dot{\alpha}_f \dot{\rho}_f) / (\alpha_f \rho_f)]_{j+1/2}^n \left\{ (v_f^2)_{j+1}^n + 2(v_f)_{j+1}^n [(v_f)_{j+1}^{n+1} \right. \\
 & - (v_f)_{j+1}^n] - 2(v_f^2)_j^n - 2(v_f)_j^n [(v_f)_j^{n+1} - (v_f)_j^n] \left. \right\} \Delta t \\
 & = [(\rho_f - \rho_g) / (\rho_g \rho_f)]_{j+1/2}^n (P_{j+1} - P_j)^{n+1} \Delta t - \left\{ FWG_{j+1/2}^n (v_g)_{j+1/2}^{n+1} \right. \\
 & + FWF_{j+1/2}^n (v_f)_{j+1/2}^{n+1} + [\Gamma_g (\rho_f v_g - \alpha_f \rho_f v_g - \alpha_g \rho_g v_f) / (\alpha_g \rho_g \alpha_f \rho_f)]_{j+1/2}^n \\
 & \left. - (\rho_f \Gamma)_{j+1/2}^{n+1} (v_g - v_f)_{j+1/2}^{n+1} \right\} \Delta x_{j+1/2} \Delta t \tag{3-27}
 \end{aligned}$$

Although the additional implicitness in Equations (3-26) and (3-27) involves only the momentum convective terms, it has a large impact on the algebraic solution algorithm in the first step. In the semi-implicit and in the nearly implicit scheme, the mass and energy equations, Equations (3-10), (3-11), (3-14), and (3-15), can be solved locally to give a single equation of the form

$$P_j^{n+1} = A v_{g,j+1/2}^{n+1} + B v_{g,j-1/2}^{n+1} + C v_{f,j+1/2}^{n+1} + D v_{f,j-1/2}^{n+1} + E \tag{3-28}$$

for pressure at node j , where A , B , C , D , and E contain only (n) -level variables (see Figure 3-1 for cell indexes). This is the first step of the semi-implicit reduction shown in Figure 3-2.

In the semi-implicit scheme, the momentum equations could be solved locally to obtain velocities in terms of the pressures. This requires a two-by-two matrix solution at each junction to obtain

$$v_{g,j-1/2}^{n+1} = A^1 (P_j^{n+1} - P_{j-1}^{n+1}) + C^1 \tag{3-29}$$

$$v_{f,j-1/2}^{n+1} = B^1 (P_j^{n+1} - P_{j-1}^{n+1}) + D^1 \tag{3-30}$$

Numerical Methods

where A^1 , B^1 , C^1 , and D^1 , again, contain only (n) -level variables. These two reductions are also included in the first step of the semi-implicit scheme illustrated on Figure 3-2.

In the nearly implicit scheme, because the momentum flux terms are implicit, the momentum Equations (3-26) and (3-27) cannot be locally solved to obtain a form like Equations (3-29) and (3-30), since the convective terms involve the $(n+1)$ -level upstream and downstream velocities. The phasic mass and energy equations, on the other hand, can still be used to obtain Equation (3-28). Thus, in the nearly-implicit scheme, the process is inverted, and Equation (3-28) is used to eliminate the $(n+1)$ -level pressure terms from the momentum equations. A coupled pair of momentum equations for each junction involving only $(n+1)$ -level velocities is, thus, obtained. However, because of the $(n+1)$ -level momentum flux terms, this results in a globally coupled system when the pressures are eliminated. For a straight pipe of 100 junctions, a block tridiagonal matrix system 200 by 200 with 2 by 2 blocks is obtained. This system can be solved using a sparse matrix solution algorithm. Once the v_f^{n+1} and v_g^{n+1} solution is obtained, P^{n+1} can be obtained by back substitution. Back substitution into the mass and energy equations produces intermediate/provisional $n+1$ values for α_g , u_g , and u_f , denoted by $\tilde{\alpha}_g^{n+1}$, \tilde{u}_g^{n+1} , and \tilde{u}_f^{n+1} . This completes the first step of the nearly implicit scheme and is illustrated in Figure 3-3, using a similar matrix format as shown in Figure 3-2 for the semi-implicit scheme. If we stopped at this point, we would find that the level of implicitness is insufficient to eliminate the material Courant time-step limit. Thus, a second step in which the convected variables are evaluated implicitly is required. (By way of contrast, this single step replaces three steps used in the SETS scheme, Mahaffy (1982), in which the steps are the prediction step for velocities, the velocity convection stabilization step, and the semi-implicit step involving implicit pressures.)

The second step in the nearly implicit scheme is used to implicitly evaluate the convective terms in the mass and energy balance equations. This step uses the final $(n+1)$ level velocities from the first step along with the interphase exchange terms resulting from the first step. For example, the interphase heat and mass exchange terms for Step 2 are calculated using P^{n+1} , \tilde{u}_g^{n+1} , and \tilde{u}_f^{n+1} from Step 1. The phasic continuity and energy equations in this second step have the fluxed variables evaluated at the $n+1$ time level [implicitly as compared to their explicit evaluation in the first step (and as in the semi-implicit method)].

The mixture mass equation is

$$\begin{aligned}
 & (\alpha_g \rho_g + \alpha_f \rho_f)_j^{n+1} - (\alpha_g \rho_g + \alpha_f \rho_f)_j^n + \left\{ (\dot{\alpha}_g \dot{\rho}_g)_{j+1/2}^{n+1} (v_g)_{j+1/2}^{n+1} \right. \\
 & + (\dot{\alpha}_f \dot{\rho}_f)_{j+1/2}^{n+1} (v_f)_{j+1/2}^{n+1} A_{j+1/2} - (\dot{\alpha}_g \dot{\rho}_g)_{j-1/2}^{n+1} (v_g)_{j-1/2}^{n+1} \\
 & \left. + (\dot{\alpha}_f \dot{\rho}_f)_{j-1/2}^{n+1} (v_f)_{j-1/2}^{n+1} A_{j-1/2} \right\} (\Delta t/V_j) = 0 \quad . \quad (3-31)
 \end{aligned}$$

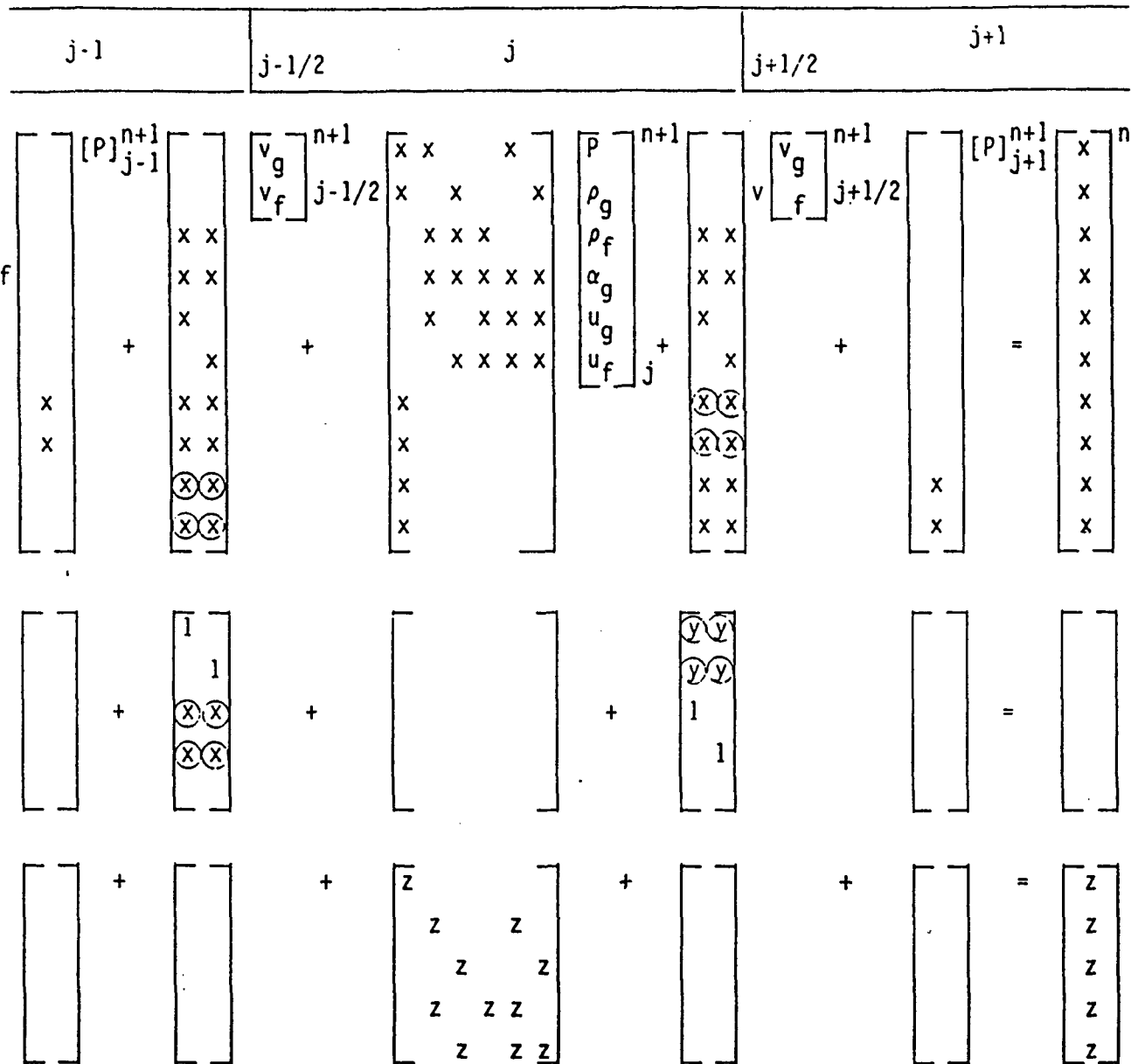


Figure 3-3. Matrix representation of the nearly-implicit difference scheme.

Numerical Methods

The difference of phasic mass equation is

$$\begin{aligned}
 & (\alpha_g \rho_g - \alpha_f \rho_f)_j^{n+1} - (\alpha_g \rho_g - \alpha_f \rho_f)_j^n + \left\{ \left(\dot{\alpha}_g \dot{\rho}_g^{n+1} \right)_{j+1/2} (v_g)_{j+1/2}^{n+1} \right. \\
 & \quad - \left(\dot{\alpha}_f \dot{\rho}_f \right)_{j+1/2}^{n+1} (v_f)_{j+1/2}^{n+1} A_{j+1/2} - \left(\dot{\alpha}_g \dot{\rho}_g \right)_{j-1/2}^{n+1} (v_g)_{j-1/2}^{n+1} \\
 & \quad \left. - \left(\dot{\alpha}_f \dot{\rho}_f \right)_{j-1/2}^{n+1} (v_f)_{j-1/2}^{n+1} A_{j-1/2} \right\} (\Delta t / V_j) = 2(\bar{\Gamma}_g)_j^{n+1} \Delta t \quad (3-32)
 \end{aligned}$$

In these continuity equations, the mass exchange $\bar{\Gamma}_g^{n+1}$ is evaluated using the provisional values from the first step.

The vapor energy equation is given by

$$\begin{aligned}
 & (\alpha_g \rho_g \mu_g)_j^{n+1} - (\alpha_g \rho_g \mu_g)_j^n + P_j^n (\alpha_g^{n+1} - \alpha_g^n)_j \\
 & \quad + \left[\left(\dot{\alpha}_g \dot{\rho}_g \dot{\mu}_g \right)_{j+1/2}^{n+1} + \left(\dot{\alpha}_g \right)_{j+1/2}^{n+1} P_j^{n+1} \right] (v_g)_{j+1/2}^{n+1} A_{j+1/2} (\Delta t / V_j) \\
 & \quad - \left[\left(\dot{\alpha}_g \dot{\rho}_g \dot{\mu}_g \right)_{j-1/2}^{n+1} + \left(\dot{\alpha}_g \right)_{j-1/2}^{n+1} P_j^{n+1} \right] (v_g)_{j-1/2}^{n+1} A_{j-1/2} (\Delta t / V_j) \\
 & = \left\{ -[h_f^* / (h_g^* - h_f^*)]^n \bar{q}_{og}^{n+1} A_\sigma - [h_g^* / (h_g^* - h_f^*)]^n \bar{q}_{of}^{n+1} A_\sigma \right. \\
 & \quad \left. + q_{wg}^n A_{wg} + DISS_g^n \right\}_j \Delta t \quad (3-33)
 \end{aligned}$$

The liquid energy equation is given by

$$\begin{aligned}
 & (\alpha_f \rho_f \mu_f)_j^{n+1} - (\alpha_f \rho_f \mu_f)_j^n + P_j^n (\alpha_f^{n+1} - \alpha_f^n)_j \\
 & \quad + \left[\left(\dot{\alpha}_f \dot{\rho}_f \dot{\mu}_f \right)_{j+1/2}^{n+1} + \left(\dot{\alpha}_f \right)_{j+1/2}^{n+1} P_j^{n+1} \right] (V_f)_{j+1/2}^{n+1} A_{j+1/2} (\Delta t / V_j) \\
 & \quad - \left[\left(\dot{\alpha}_f \dot{\rho}_f \dot{\mu}_f \right)_{j-1/2}^{n+1} + \left(\dot{\alpha}_f \right)_{j-1/2}^{n+1} P_j^{n+1} \right] (V_f)_{j-1/2}^{n+1} A_{j-1/2} (\Delta t / V_j) \\
 & = + \left\{ [h_f^* / (h_g^* - h_f^*)]^n \bar{q}_{og}^{n+1} A_\sigma + [h_g^* / (h_g^* - h_f^*)]^n \bar{q}_{of}^{n+1} A_\sigma \right. \\
 & \quad \left. + q_{wf}^n A_{wf} + DISS_f^n \right\}_j \Delta t \quad (3-34)
 \end{aligned}$$

This second step uses the mass and energy balance equations only. If the structure of Equations (3-31) through (3-34) is examined, it is seen that each equation only involves one unknown variable: Equation (3-31) contains $(\alpha\rho)_g^{n+1}$, Equation (3-30) contains $(\alpha\rho)_f^{n+1}$, Equation (3-33) contains $(\alpha\rho u)_g^{n+1}$, and Equation (3-34) contains $(\alpha\rho u)_f^{n+1}$. This is because the new-time velocities, v_g^{n+1} and v_f^{n+1} , are known from Step 1. Provisional $(n+1)$ values from Step 1 are used in the exchange terms. This second step is also shown schematically in Figure 3-3. Hence, each equation is uncoupled from the other and can be solved independently. In addition, the two equations involving the gas phase, Equations (3-31) and (3-33), have the same structural form for the convective terms (i.e., convection in each equation is with velocity v_g^{n+1}).

The matrix multiplying the unknown new-time variable in Equation (3-31) is decomposed only once, and then this decomposition is used with different right-hand sides to solve both Equations (3-31) and (3-33). Hence, for a straight pipe problem of 100 cells, only one 100 by 100 tridiagonal system must be decomposed to obtain $(\alpha\rho)_g^{n+1}$ and $(\alpha\rho u)_g^{n+1}$. In like manner, the liquid phase Equations (3-32) and (3-34) have the same structure and require only one decomposition to be carried out to solve both equation sets, giving $(\alpha\rho u)_f^{n+1}$ and $(\alpha\rho)_f^{n+1}$.

With the above four new variables known, we obtain u_g^{n+1} , u_f^{n+1} , and α_f^{n+1} as

$$u_g^{n+1} = (\alpha\rho u)_g^{n+1} / (\alpha\rho)_g^{n+1} \quad (3-35)$$

$$u_f^{n+1} = (\alpha\rho u)_f^{n+1} / (\alpha\rho)_f^{n+1} \quad (3-36)$$

$$\alpha_f^{n+1} = (\alpha\rho)_f^{n+1} / \rho_f^{n+1} \quad (3-37)$$

where ρ_f^{n+1} is the liquid density calculated from the linearized state relationship using u_f^{n+1} and P^{n+1} .

This second step permits implicit evaluations of the convective terms in the mass and energy equations, and it does so with very little computational effort because of the fractional step nature of the scheme.

3.2.2 Time-Step Control

The time-step control checks used for the nearly-implicit method are the same as that for the semi-implicit method except that the maximum Courant numbers in the most limiting volume are 10.0 in the transient mode and 20.0 in the steady-state mode.

3.3 Truncation and Linearization Errors of the Numerical Methods in RELAP5

The truncation errors of the semi-implicit method and nearly implicit method are found by considering the difference between Lu and $L_{m,n}(\Delta x, \Delta t)u$, where L and $L_{m,n}$ are the differential and difference operators in question, respectively, and u is the analytical solution of the differential equation.

The truncation error (TE) for the sum and difference momentum and mass equations, and the phasic energy equation for the semi-implicit method are

$$TE(MOM_s) = 1/2 \left(\alpha_g \rho_g \cdot \Delta t \cdot \frac{\partial^2 v_g}{\partial t^2} + \alpha_f \rho_f \cdot \Delta t \cdot \frac{\partial^2 v_f}{\partial t^2} \right) + 1/2 \left(\alpha_g \rho_g \frac{VISG}{(\Delta x)^2} + \alpha_f \rho_f \frac{VISF}{(\Delta x)^2} \right) \Delta x + HOT. \quad (3-38)$$

$$T.E.(MOM_D) = 1/2 \left(\Delta t \left(\frac{\partial^2 v_g}{\partial t^2} - \frac{\partial^2 v_f}{\partial t^2} \right) + \left(\frac{VISG}{(\Delta x)^2} - \frac{VISF}{(\Delta x)^2} \right) \Delta x \right) + H.O.T. \quad (3-39)$$

$$T.E. (MASS_s) = 1/2 \Delta t \frac{\partial^2 (\alpha_g \rho_g + \alpha_f \rho_f)}{\partial t^2} + HOT. \quad (3-40)$$

$$T.E. (MASS_D) = 1/2 \Delta t \frac{\partial^2 (\alpha_g \rho_g + \alpha_f \rho_f)}{\partial t^2} + H.O.T. \quad (3-41)$$

$$T.E.(ENE_g) = 1/2 \Delta t \left(\frac{\partial^2 (\alpha_g \rho_g \mu_g)}{\partial t^2} + P_j^n \cdot \frac{\partial^2 \alpha_g}{\partial t^2} \right) + H.O.T. \quad (3-42)$$

$$T.E.(ENE_f) = 1/2 \Delta t \left(\frac{\partial^2 (\alpha_f \rho_f \mu_f)}{\partial t^2} + P_j^n \cdot \frac{\partial^2 dg}{\partial t^2} \right) + H.O.T. \quad (3-43)$$

Here HOT stands for high order terms; MOM_s , MOM_D , $MASS_s$, and $MASS_D$ stand for momentum sum and difference and mass sum and difference equations, respectively; ENE_g and ENE_f stand for vapor and liquid energy difference equations, respectively. The terms $\frac{VISG}{(\Delta x)^2}$ and $\frac{VISF}{(\Delta x)^2}$ are difference approximations to $\frac{\partial}{\partial x} \left(|V| \frac{\partial v}{\partial x} \right)$. Hence, these two terms can be combined with the first

$$1/2 \left((\Delta x - V_g \cdot \Delta t) \frac{VISG}{(\Delta x)^2} - (\Delta x - V_f \cdot \Delta t) \frac{VISF}{(\Delta x)^2} \right) + H.O.T.$$

terms of Equation (3-39) to form the expression for the truncation error for the momentum difference equation with a similar expression for that of the momentum sum equation. The truncation error is, therefore, at a minimum when the Courant number is equal to one. In general, the method is of first order accuracy in Δt and Δx .

The truncation errors for the nearly implicit method are almost identical in form. The only difference is that the terms involving VISF and VISG are no longer present in the T.E.

When the nonlinear equations (including equations of state) are linearized, the phasic densities and temperatures at the new time levels are linearized against their old time values. The linearization errors (L.E.) incurred are as follows:

$$\begin{aligned} L.E. (\rho_k) = & 1/2 \left[\frac{\partial^2 \rho_k}{\partial p^2} (P^{n+1} - P^n)^2 + 2 \frac{\partial^2 \rho_k}{\partial p \partial v_k} (P^{n+1} - P^n) (u_k^{n+1} - u_k^n) \right. \\ & \left. + \frac{\partial^2 \rho_k}{\partial u_k^2} (u_k^{n+1} - u_k^n)^2 \right] \\ & + H.O.T., \quad k = f, g \end{aligned} \quad (3-44)$$

$$\begin{aligned} L.E. (T_k) = & \frac{1}{2} \left[\frac{\partial^2 T_k}{\partial p^2} (P^{n+1} - P^n)^2 + 2 \frac{\partial^2 T_k}{\partial p \partial U_k} (P^{n+1} - P^n) (u_k^{n+1} - u_k^n) \right. \\ & \left. + \frac{\partial^2 T_k}{\partial U_k^2} (u_k^{n+1} - u_k^n)^2 \right] \\ & + H.O.T., \quad k = f, g. \end{aligned} \quad (3-45)$$

Here, we have ignored the effects of the noncondensibles. In the presence of the noncondensibles, the quadratic forms in Equations (3-44) and (3-45) have six terms instead of three for the gas phase ($k = g$); and terms such as $1/2 \partial^2 \rho_k / \partial x_n^2$ and $1/2 \partial^2 T_k / \partial x_n^2$ should be added to the respective quadratic forms in Equations (3-44) and (3-45).

3.4 Special Numerical Techniques

In the implementation of numerical integration methods that have been discussed, many special situations arise that require some modification of the basic procedure in order to achieve acceptable results. These problems arise from two basic sources. First, the equations embody transitions from two-phase to single-phase conditions and vice-versa. We will call this phase transition. This transition invariably involves discontinuous change in the partial derivatives of the dependent variables, most notably the void fraction. Significant truncation errors occur at such points of discontinuous change, and the only effective method to date for controlling the growth of such errors is the use of a small

Numerical Methods

time-step at, or across, the point of discontinuous change. Even this procedure is not always effective, as we shall see.

In general, the Courant limit violating schemes have been only partially effective because of the problems associated with phase transition. The need to use small time-steps at such transitions reduces the overall efficiency. In almost all schemes, a single time-step is used for all spatial nodes. Thus, the solution at all nodes suffers a loss in efficiency for each need to reduce the time-step because of a transition in a single node. Invariably, the more nodes included in the solution, the greater the likelihood of phase transitions.

The second characteristic of two-phase models is the use of constitutive models based on flow regime maps that involve essentially nonsmooth transitions between flow regimes. Thus, the constitutive parameters associated with interphase friction, wall friction, interphase heat transfer, and wall heat transfer can all suffer rapid change in magnitude from one time-step to the next. Such transitions are for the most part nonphysical, but real flows even exhibit hysteresis for some transitions, which, if implemented in a numerical scheme, introduce significant complications and possible stability problems associated with numerical noise.

A variety of procedures have been developed to ameliorate the effects of anomalous numerical behavior. Some of these methods will be discussed in this section .

3.4.1 Time Smoothing

The constitutive models used in most two-phase models are formulated as algebraic functions of the dependent variables, and the models to be used are selected based on flow regime considerations. As has been mentioned, this can result in nonsmooth functions and/or a very rapid change in the constitutive parameters. Naturally, such formulations impact accuracy of the numerical scheme. An approach in wide usage to ameliorate the effect of such formulations is time smoothing (sometimes also called under-relaxation). This process has been effective in permitting a larger time-step and thus increasing computational speed. However, this process can have significant effects on the computed results (Ransom and Weaver 1987). Thus, we will discuss this method and show how time smoothing can be implemented in a time-step insensitive manner.

The usual way that time smoothing for certain constitutive parameters is implemented is to weight the current time value of a parameter with the running-weighted value. A linear weighting process is defined by the recursion relation

$$\bar{f}_{n+1} = \eta \bar{f}_n + (1 - \eta) f_{n+1} \quad (3-46)$$

where

n = time level index

f = function to be smoothed

\bar{f} = smoothed value

η = weighting factor.

If we now consider that the function f changes discontinuously at $t = t_1$ so that

$$f = (f)_1 \text{ for } t < t_1 \quad (3-47)$$

$$f = (f)_2 \text{ for } t \geq t_1 \quad (3-48)$$

where

$$t = t_1 + n\Delta t \quad (3-49)$$

For initial conditions, we assume

$$\bar{f}_0 = (f)_1 \quad (3-50)$$

Under these conditions, the recursion process defined by Equation (3-46) reduces to

$$\bar{f}_n = (f)_1 + (1 - \eta^n)[(f)_2 - (f)_1] \quad (3-51)$$

or in terms of the time variable defined by Equation (3-49),

$$\bar{f}_n = (f)_1 + [1 - \eta^{(t-t_1)/\Delta t}][(f)_2 - (f)_1] \quad (3-52)$$

It is clear from this result that \bar{f}_n will vary differently with time, t , if different values for the time step, Δt , are used. Clearly, this is an undesirable result.

A time-step insensitive procedure is obtained if we use for η

$$\eta = e^{-\Delta t/\tau} \quad (3-53)$$

where τ is a time constant, possibly associated with the physical transition process. Now, we obtain from Equation (3-46)

$$\bar{f}_n = (f)_1 + (1 - e^{-(t-t_1)/\tau})[(f)_2 - (f)_1] \quad (3-54)$$

which traces out the same function regardless of the time-step size.

It is also possible to use a logarithmic form of Equation (3-46) in which

$$\ln(\bar{f})_n = \eta \ln(\bar{f})_{n-1} + (1 - \eta)\ln(f)_n \quad (3-55)$$

and here, again, if η is defined as in Equation (3-53), a time-step insensitive function is again obtained, for example,

$$\ln(\bar{f})_n = \eta \ln(\bar{f})_1 + (1 - e^{-(t-t_1)/\tau})[\ln(f)_2 - \ln(f)_1] \quad (4-56)$$

Numerical Methods

It is clearly desirable to use a time-step insensitive formulation for time smoothing.

The choice of time constant for the time smoothing of interphase heat transfer and drag coefficient in RELAP5/MOD3, however, has stirred considerable debate. Ransom (1985) suggests that the value of the time constant should be related to the physics of the process if possible. Empirical observation has shown that the time constant associated with flow regime transition is approximately 0.01 s. The use of this value as time constant, however, has caused considerable problems for early developmental versions of RELAP5/MOD3. Riemke^c indicates that widely oscillating voids have been observed in the GE level swell 1-ft diameter problem if 0.01 s is used for the time constant for the time smoothing of interphase heat transfer and drag coefficients. The value currently used in the code is 0.1 s.

The code also allows the user the option to use MOD2.5 time smoothing. This is a scheme developed by Bryce (Feinauer et al. 1984). It assumes the following form:

$$\eta = \exp [- \min \{0.693, \max [\Delta t/\tau_c, \min (\Delta t/\tau_F, \gamma_s)]\}] \quad (3-57)$$

where

$$\tau_c = \Delta x / [0.7 \alpha_f \min (|v_g|, |v_f|)]$$

$$\tau_F = 1.0 / \text{SQRT} [\min (g, 0.516 \cdot D^*) / D]$$

$$D^* = D \cdot \text{SQRT} [g \cdot (\rho_f - \rho_g) / \sigma] \quad D = \text{hydraulic diameter}$$

$$\gamma_s = \max [0.010536, (\min (|V_g|, |V_f|) + 10^{-7}) / \max (10^{-7}, |V_g|, |V_f|)]$$

for the time smoothing of interphase heat transfer coefficients. A slightly different form described later in this section is used for the time smoothing of interphase drag coefficients.

In Equation (3-57), τ_c is a Courant type of time constant, γ_s is a term that is large when there is a large slip velocity between the liquid and gas at low velocities. It is used (Feinauer et al. 1984, p. 75) because of the dependence of the calculated interfacial heat transfer H_{if} on the slip velocity for some flow regimes.

The τ_F term is a gravity-related time constant to cover the cases when velocities are small. For $D^* > 19$, $\tau_F = (D/g)^{1/2}$ and is proportional to the time required for a Taylor bubble to rise above a cell (Allison et al., 1950, Vol. 1, p.3.3-4). This is consistent with the suggestion of Taitel and Dukler (1976) that bubbly flow may not exist in tubes of small diameter where the rise velocity of small bubbles exceeds that of Taylor bubbles and that the limiting tube diameter allowing the presence of bubbly flow is $D^* \geq 19$.

c. Private communication.

For $D^* < 19$, $\tau_F = [(D/g) \cdot (19/D^*)]^{1/2}$.

Bryce^d indicates that this form is chosen because the critical Kutateladze number, K , is an increasing function of D^* for $D^* < 19$ Wallis and Makkenchery. The critical Kutateladze number is the dimensionless gas flux below which a hanging liquid film in vertical annular two-phase flow will flow downward. The dimensionless tube diameter D^* is sometimes called the Bond number and is the ratio of tube diameter to the Laplace capillary constant.

For small Δt , $\min(\Delta t/\tau_F, \gamma_s) = \Delta t/\tau_F$.

Hence, the η in Equation (3-57) is in the form $\eta = e^{-\Delta t/\tau}$, and the computed solutions should be time-step insensitive. Krishnamurthy (1992) reports (see also Section 5) that the computed solutions are actually time-step sensitive for the Edwards pipe blow down problem.

This is because the time smoothing constant η for the interphase drag coefficients is of the form

$$\eta^* = \min(0.90, \eta) \quad (3-58)$$

where η is given by Equation (3-57). If the 0.90 is removed so that $\eta^* = \eta$, then the computed solutions are no longer time step sensitive (Section 5.7).

One of the main advantages of using MOD2.5 time smoothing is that it allows the code to use smaller time constants when Δt is small. This limits the time smoothing to some extent for small Δt but allows the code to use larger time smoothing when the code is running close to Courant Δt with large slip velocities. Experience shows that MOD2.5 time smoothing, in general, allows the code to run to completion for large plant simulation without excessive restarts to change requested maximum time steps.

3.4.2 Single to Two-Phase Transitions

The two-fluid model has two mechanisms that can contribute to phase transition. The first is simply the convective process in which the phases flow at different velocities. The second is the interphase mass transfer process, which can contribute to phase appearance or disappearance. Experience has shown that the most troublesome transition is between single-phase liquid and two-phase conditions. This transition can result in the calculation of extremely large amplitude pressure pulses, called water packing, and in large mass and energy truncation errors. Often, the water-packing pressure pulses are so large that the predicted pressures exceed the range of validity of the equations of state, and code failures result. This water-packing characteristic is completely nonphysical, though somewhat analogous to water-hammer phenomena in real fluid flows.

Water packing occurs or is affected by several factors. Chief among these is the great change in the bulk modulus between the liquid state and the two-phase state. The sound speed is related to this property and can be used as an indication of the wide range of variation. The speed of sound

d. Private communication.

Numerical Methods

in liquid water is 1,822 m/s at 6.0 bars pressure. The homogeneous-equilibrium sound speed for a steam-water mixture at void fractions approaching zero is 5.37 m/s at the same pressure. Thus, it is clear that the compressibility of the mixture suffers a significant discontinuity at the phase boundary. This extreme variation in bulk modulus is partially responsible for the water packing numerical anomaly.

Another factor that contributes to water packing is the method of discretizing the momentum equations, especially under special situations of interfacial mass transfer. This anomalous feature is best illustrated. In Figure 3-4 illustrates a physical process in which steam is condensing on a liquid interface. The velocities of vapor and liquid at junction $j-1/2$ are from bottom to top, and the velocity of liquid and vapor at junction $j+3/2$ is from top to bottom. Cell j is about to fill with water, both from convection of water into the cell from junction $j-1/2$ and from condensation in cell j . The momentum equations written between cell j and $j+1$ (the momentum control volume is indicated by the dashed lines) will contain a significant mass of water and, therefore, have a large inertia. At the instant or time step that cell j fills with water, the liquid velocity at junction $j+1/2$ must reverse in order to satisfy continuity, and a large pressure increase results. So far, this course of events is physical and the result expected. What is nonphysical is that an extremely large pressure increase is required to reverse the liquid velocity at junction $j+1/2$ because of the artificially large inertia that results from including the water within the dotted control volume and assuming that it is moving with the velocity at junction $j+1/2$. The severity of the water-packing pressure spike will depend on the velocity of flow, the condensation rate, and the node size. Clearly reducing the node size proportionately reduces the inertia and, thus, the magnitude of the nonphysical overpressure, but this approach is usually impractical since fine nodalization is required everywhere because it cannot be predicted a priori where such a situation will arise.

Many modifications have been tried for ameliorating these water-packing effects. Perhaps the procedure that has worked best is the one in which inertia is made artificially small for one or several time steps so that the velocity reversal can occur with only a small pressure increase (Mahaffy and Liles 1983). A variant of this approach is now used in RELAP5/MOD3 (see Vol. 3 of Allison et al. (1990) for details). The real trick is to detect where such a \bar{f}_x needs to be applied and for how many time-steps. These procedures are difficult to generalize and are more or less *art forms* that have evolved in each numerical procedure development. Shiela^e has also found that the time smoothing of interphase heat transfer coefficients can have a significant effect on how well the water-packing ameliorating effort in the code works. Too large an η in the time smoothing Equation (3-46) can interfere with the proper condensation of steam in cell j , thus causing pressure spikes or incorrect computation of pressure in the MIT pressurizer problem described in Volume III of Allison et al (1990).

Mass and energy errors also occur at phase transitions when more net mass of either phase is predicted to flow from a volume on one time-step than is contained within the volume. Such errors are controllable to acceptable tolerance by time-step reduction. A small time-step is needed only at the point of transition, but, unfortunately, it is difficult to predict when such a transition will occur. Thus, many small time-steps may be required to effect the transition. This method was developed

e. The INEL author.

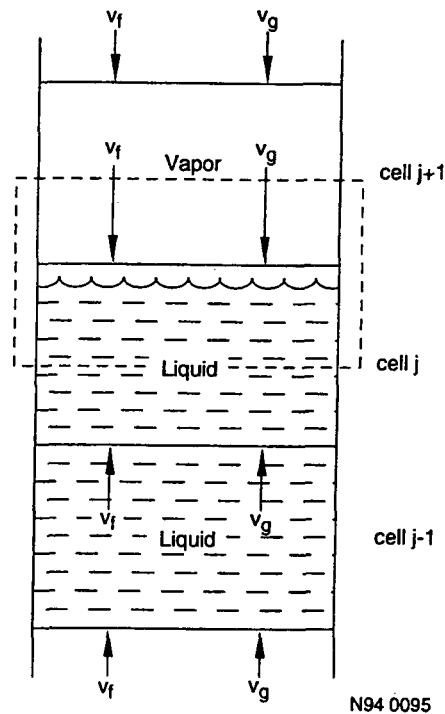


Figure 3-4. Illustration of conditions that result in water packing.

and implemented in the RELAP5 Code, (ransom et al. 1985) and has been quite successful in mitigating mass errors caused by phase transition. Generally, it is assumed that control of mass errors due to phase transition also controls associated energy errors, but usually no global energy balance is made to evaluate such effects. Experience indicates that these effects are at least small enough to not be noticeable.

3.5 Mass and Energy Errors

Mass and energy errors not only occur when phase transitions occur, as discussed, but also when the donored properties are incorrect due to flow reversal within a time step. When donor formulations are used, they are usually based on an explicit prediction of the new-time velocity and then kept fixed during the semi-implicit or implicit solution step. If the implicit velocity changes sign, the donored mass and energy properties are from the incorrect volume. This can be corrected by repeating the time advancement process for the time-step. However, while this solves the problem, it is inefficient and can also lead to nonconvergence due to oscillations. A scheme for assessing the consequence of incorrect donoring is used in the RELAP5 Code (Ransom et al. 1985, Allison et al. 1990). In this scheme, the mass error is estimated, and the time step is only repeated if significant error would result. In addition, the RELAP5 scheme is designed to detect the error before completion of the time step and can efficiently reverse the donor decision and subsequently complete the time step, thus minimizing wasted computation.

Another source of energy error that does not result in net loss or gain of energy but results in nonphysical phasic energy distribution is use of incorrect energies associated with interphase mass transfer. These errors show up as nonphysical phase heating or cooling, which can be in violation of second-law considerations. In most physical situations, the phase interface will exist at very near

Numerical Methods

the local saturation temperature, defined by the local pressure. In view of this fact, it is usually assumed that interface mass transfer will occur from saturation state to saturation state. Locally, this is a close approximation to the physical situation, but when the averaged formulation is used it is necessary to account for the energy difference between the bulk state and the interface for the mass which is transferred. In the general formulation, this energy exchange would be accounted for by the intraphase heat flux caused by conduction and/or turbulent diffusion. These terms are invariably omitted owing to inability to characterize them, and, so, the energy difference between bulk and the interface must be included in the overall energy exchange associated with mass exchange. Chow et al.^f show that a reasonable formulation results when the phasic bulk enthalpy for the exchanged mass is used in the interfacial energy balance rather than the corresponding saturation enthalpy. This accounts for the phase internal process responsible for the intraphase energy gradient.

3.6 Comparisons of Numerical Methods

There are essentially only two kinds of numerical methods for solving coupled systems of PDEs: complete discretization methods and spatial discretization (or semidiscrete) methods. The complete discretization methods can be further classified into three methods: explicit or semi-implicit, fractional-step nearly implicit, and single-step fully implicit. In this section, we first examine some better known single-step fully implicit methods and then give a comparison of the semi-implicit method, the fractional step nearly implicit method, and the single-step fully implicit method. Finally, briefly mention some of the better-known (to the author's) spatial discretization methods.

3.6.1 Single-Step Implicit Scheme

We will use the term *fully implicit scheme* to refer to those schemes not Courant limited and that accomplish the time advancement in a single step. The single-step solution may be accomplished by linearization of the equations and solution of a system of linear difference equations for the entire system, or the nonlinear equations can be solved using interactive methods. Examples for both of these approaches exist. The CATHENA code is based on the use of linearized equations, which are solved by direct inversion using a sparse matrix routine (the authors of this method retain the term semi-implicit to describe their scheme, since not all terms are evaluated at the new time level; however, the implicitness is sufficient that no time-step stability limits remain) (Richards et al., 1985). The second example is the CATHARE code, in which a fully implicit formulation is used and is solved by a Newton-Raphson iterative method (Micaelli 1987). Both of these codes use donor formulations for the mass and energy flux terms to enhance stability and are based on a staggered difference mesh in which the scalar variables are evaluated at cell centers, and the velocities are evaluated on the cell faces. Both examples are one-dimensional formulations.

The CATHENA method will be described as an example of the single-step implicit method. It was chosen mainly because the difference equations have been published in some detail (Richards et al., 1985). The linearization of the difference equations, when products of the dependent variable appear, is accomplished by expanding about the current time level and neglecting second order terms. The linearization of the mass flux term used in CATHENA is

$$(\alpha\rho v)^{n+1} = \rho^n v^n (\alpha^{n+1} - \alpha^n) + \alpha^n \rho^n (v^{n+1} - v^n) + (\alpha\rho v)^n \quad (3-59)$$

f. H. Chow et al, 1989 " Anomalous Numerical Behavior in Two-Phase Flow Simulations," submitted to *Journal of Computational Physics*, unpublished.

where the variation of the density is neglected. The linearization is extended to donor quantities and, while not stated in Richards et al., (1985) it is assumed that the donor formulation is based on the current time velocities; otherwise, a direct solution would not be possible.

An interesting feature of the CATHENA formulation is that the energy equations are used in an expanded or so-called nonconservative form such that the energy flux terms appear as velocity derivatives. The energy density then appears as the coefficient of the velocity derivative, and these quantities are donor. This is an unusual approach and is unique among the methods that have been reviewed in this work. The remaining features of the difference equation formulation are fairly standard, so the detailed difference equations will not be recorded here. See Richards et al., (1985).

3.6.2 Comparison of the Three Complete Discretization Methods

The semi-implicit, nearly implicit, and fully implicit methods discussed have all been implemented and used to simulate two-phase problems. Thus, we can make some comparisons based on this experience. It is clear from the development that all of the schemes are of the same order of accuracy (i.e., first-order accurate in space and time), so the local error is second-order. When such schemes are used for integration over fixed intervals in space and/or time, the accumulated error is first-order in the discretization interval. Thus, in terms of accuracy at a comparable time-step, all schemes are essentially the same. One can also conclude that when the Courant limit violating schemes are run with a large time step, the accumulated error can be expected to increase in proportion to the time-step size.

The relative execution times for the three schemes are reported by trapp and Riemke (1986). The time required to solve for one time step per node relative to the semi-implicit scheme is 1.6 for the nearly implicit scheme and 2.5 for the single step or fully implicit scheme. The differences in the execution times are due primarily to the larger matrix that must be inverted in each case. For a 100-node problem with connecting junctions, the semi-implicit scheme requires the inversion of a 100 by 100 matrix; the nearly implicit scheme requires inversion of a 200 by 200 matrix for the velocities followed by inversion of four 100 by 100 sparse matrices in the back substitution step; and the fully implicit scheme requires the inversion of one 600 by 600 block sparse matrix. Which scheme is best in a given situation requires further consideration and will depend on the type of transient problem to be solved. One distinct advantage that the CLV schemes have is that they are flexible and can use large time-steps when a null transient is encountered. The maximum time-step for the semi-implicit scheme will be limited by the Courant condition, even in stationary situations.

The experience to date has shown that the nearly implicit and fully implicit schemes have not been able to achieve as fast a running capability as might be expected, considering that they are unconditionally stable. A possible explanation for this result lies in the nature of the two-phase problem, particularly the discontinuities that occur in the derivatives of the dependent variables, such as the derivative of the void fraction at the pure-phase limits. The flow regime transitions also result in near-discontinuous behavior of the constitutive models, which is also a factor. Another factor, which will be discussed in the next section, is anomalous numerical behavior that affects the implicit schemes in the same way as the semi-implicit schemes. These anomalies effectively limit the achievable time step. Thus, when the increased computational effort is balanced with the achievable increase in time step, the more implicit schemes are only marginally successful though they enjoy a clear advantage in quasi-steady problems.

Numerical Methods

3.6.3 Spatial Discretization Methods

If only the spatial differential operators are discretized, then the system of PDEs can be converted to a system of ODEs

$$\frac{dU}{dt} = \underline{F}(x,t,U) \quad (3-60)$$

and various well-known ODE integrators. For example, Gear (1971) can be used to integrate Equation (3-60). The two-phase flow codes that use this approach include (but are not limited to) HIPA-BWR4, RAMONA 3, and ALMOD4 (Wulff et al., 1984a, 1984b). Below is a brief description of the codes taken from Wulff (1987).

Mixture mass balance, momentous balance, and energy balance equations are used in the HIPA-BWR 4 code. The numerical integration with respect to time of the system of ODEs is achieved by combining explicit first-order Euler-Cauchy and third-order Adams-Bashford algorithms. Spatial discretization is fixed. It is chosen to yield insignificant space discretization errors for the fastest transients of interest. Time-step size is fixed during transients and limited for all transients by accuracy requirements.

Mixture mass balance, momentum balance, and energy balance equations are also used in the RAMONA 3 code. Calculations are carried out by a combination of analytical integrations and first-order Euler-Cauchy integrations.

ALMOD4/ASWR is based on the finite element method using asymmetric weighted residuals (ASWR). This allows the code to attain good accuracy through high order spatial discretation with only a few nodes.

Among the three complete discretization methods compared in Section 3.6.2, only the single step fully implicit method is directly amenable to this approach. It is known, however, that if the Jacobian matrix of $\underline{F}(x,t,U)$ has complex eigenvalues, then Equation (3-60) may have oscillatory solutions and there are considerable difficulties in solving Equation (3-60) numerically (Gear 1971).

This difficulty is not present in the HIPA-BWR4 code nor the RAMONA-3B code because the underlying system of PDEs does not have complex characteristics. As we shall see in the next section, the presence of complex characteristics in the underlying system of PDEs does not necessarily cause any problem if the mesh size is not too small. Hence, the approach used by the ALMOD4/ASWR code may be of some interest if high order accuracy solution is desired on a coarse mesh.

4. DOMAIN OF APPLICABILITY OF THE NUMERICAL TECHNIQUES

The system of partial differential equations the code solves has complex characteristics (Stewart 1979, Ransom and Hicks 1984, Stewart and Wendroff 1984). Conceptually, this poses problems in the areas of stability, well-posedness, and convergence. It is plausible that the numerical solutions may show oscillatory behavior and yield undesirable results.

Stewart and Wendroff (1984) and Stewart (1979), on the other hand, show that the numerical solutions are well behaved if the number of mesh points is sufficiently small. Stewart gives a numerical example where the solutions are converging even for rather small mesh sizes.

In this section, we examine the theoretical aspects of an important mechanism that plays a critical role in stabilizing the calculations. The mechanism is the effects of the interfacial drag coefficients on the long wavelengths of the analytical solution. The interfacial drag is known to play a critical role in stabilizing the long wavelengths of the numerical solutions (Stewart 1979, Stewart and Wendroff 1984). We show analytically that it is also a key factor in stabilizing the calculations for all wavelengths if the mesh size is not too small. This is because short wavelengths of the analytical solution cannot be represented on a coarse mesh, so that the long wavelength stabilizing effect of the interphase drag becomes a dominant factor for coarse grids. The theoretical details of this aspect are given in Sections 4.2.4 and 4.3.2.

The original Lax-Richtmyer theory of stability, consistency, and convergence provides conditions related to the concept of convergence as the mesh-sizes tend to zero (Lax and Richtmyer 1956, Richtmyer and Morton 1967). A similar theory is developed in Section 4.2.1 for a finite sequence of meshes for both linear and nonlinear finite difference operators. Estimates for the regions of stability and convergence are given in Sections 4.2 and 4.3 for the semi-implicit and the nearly implicit schemes, respectively.

The important issue of well-posedness of the equations we are solving is discussed in Section 4.1. It is shown that within the region of stability and convergence, the problem is actually well-posed. The growth factor for some of the wavelengths, however, may be bigger than one for a brief period of time. This permits the code to model certain physical phenomena such as Helmholtz instability so that results predicted by the code are potentially more accurate than those computed by codes without complex characteristics.

We note also that the theoretical results on stability presented here are based on the analysis of linearized constant coefficient difference equations only. Nonlinear effects such as the cascading down of the wavelengths (the combination of long wavelengths to give rise to short wavelengths) described in Krishnamurthy (1992) and in Section 5.8 have not been taken into account. The method of analysis, the energy norm method, however, can be directly applied to nonlinear difference equations with a slight modification. Hence, the conclusion of the theorems on stability are expected to be valid at a given time-step for nonlinear difference equations. Because the upwind differencing schemes used in the code have significant damping effects at the shortest wavelengths of the calculations, the cascading down of the wavelengths has a beneficial effect. It is shown in Section 5.6 that even though instabilities did occur for the ORNL void profile problem when the mesh size is very small, the oscillations did not get any worse when the number of time-steps was increased.

Domain of Applicability

Finally, we mention that the effects of virtual mass coefficients on the behavior of the solutions have not been taken into account in this work. These effects will, in general, reduce the magnitude of the imaginary part of the complex roots in the characteristics of the equations we are solving. Hence, ignoring these effects makes the results presented in this section more conservative.

4.1 Well-Posedness of Equations with Complex Characteristics

We shall show in this section that the complex characteristics of the two-phase flow equation does not always cause ill-posedness for the numerical solutions. First, we examine the characteristics of the two-phase flow equations.

4.1.1 Complex Characteristics of Two-Phase Flow Equations

Ransom and Hicks (1984), Stewart and Wendroff (1984), and Stewart (1979) have examined the characteristics of two phase flow equations. The following system of PDEs was studied.

$$\frac{\partial \alpha \rho_v}{\partial t} + \nabla \cdot \alpha \rho_v \mathbf{u}_v = 0 \quad (4-1)$$

$$\frac{\partial (1-\alpha) \rho_l}{\partial t} + \nabla \cdot (1-\alpha) \rho_l \mathbf{u}_l = 0 \quad (4-2)$$

$$\alpha \rho_v \left[\frac{\partial \mathbf{u}_v}{\partial t} + \mathbf{u}_v \cdot \nabla \mathbf{u}_v \right] + \alpha \nabla P = K(u_l - u_v) \quad (4-3)$$

$$(1-\alpha) \rho_l \left[\frac{\partial \mathbf{u}_l}{\partial t} + \mathbf{u}_l \cdot \nabla \mathbf{u}_l \right] + (1-\alpha) \nabla P = K(u_v - u_l). \quad (4-4)$$

Here, the subscript l and v denote the liquid and vapor phases, respectively. Stewart (1979) shows that, under the assumption that the liquid is incompressible compared to the vapor (reasonable unless α is very small), the characteristic roots μ of these four equations satisfy

$$\alpha \rho_l (\mu - u_l)^2 + (1-\alpha) \rho_v (\mu - u_v)^2 - \alpha \rho_l c_v^{-2} (\mu - u_v)^2 (\mu - u_l)^2 = 0$$

where $c_v^{-2} = \partial \rho_v / \partial P$. It follows that there are two real roots, one slightly less than $u_v - c_v$ and one slightly greater than $u_v + c_v$. The other two roots are complex roots if $|u_v - u_l| > 0$. If $u_v, u_l \ll c_v$, these complex roots are approximately

$$\mu = \frac{u_l + \epsilon u_v}{1 + \epsilon} \pm i \frac{\epsilon}{1 + \epsilon} (u_v - u_l) \quad (4-5)$$

where

$$\epsilon^2 = (1-\alpha) \rho_v / \alpha \rho_f$$

4.1.2 Well-Posedness of Problems with Complex Characteristics

Definition. The initial and boundary value problem of two-phase flow is *well-posed* (Richtmyer and Morton 1967, p. 39-41) if the solution depends continuously on the initial and boundary data. Or, in other words, if $u(t)$ and $v(t)$ are genuine solutions corresponding to initial elements u_0 and v_0 , then

$$|u(t) - v(t)| < G |u_0 - v_0| \tag{4-6}$$

so that if the initial states are very nearly equal, the latter states are very nearly equal also, at corresponding times (Richtmyer and Morton 1967, p. 41). For this to be true, the growth factor G should not be much greater than one. In fact, for hyperbolic problems with no source terms, the growth factor is, in general, not greater than one.

It is generally thought that the presence of complex roots in the characteristics of an initial value problem lead to ill-posed and intractable problems. We shall show that this is not always the case. Assume that the method of characteristics is used to cast the system of PDE in the characteristics form,

$$\frac{\partial u}{\partial t} + \Omega \frac{\partial u}{\partial x} = 0 \tag{4-7}$$

where $\Omega = [\mu_1, \mu_2, \mu_3, \mu_4]$, and $\underline{u} = [u_1, u_2, u_3, u_4]$ and $\mu_i, i = 1, 4$ are the characteristic roots of the equations. Let $\mu \equiv \mu_j$, where μ_j is complex valued, and let $u \equiv u_j$.

We are interested in investigating the effect of the complex roots on the analytical solution of the following differential equation:

$$\frac{\partial u}{\partial t} + \mu \frac{\partial u}{\partial x} + K u = 0$$

where $\mu = \mu_r + i\mu_i$; μ_r and μ_i are constants independent of x and t . Let $u = u_0 \exp [i(kx - wt)]$. It follows that

$$w = \frac{K - k\mu_i}{i} + k\mu_r$$

so that

$$u = u_0 \exp [ikx + ik\mu_r t - (K - k\mu_i)t].$$

Domain of Applicability

Hence, the differential equation will have a bounded solution as $t \rightarrow \infty$ if at $t=t_0$, u is a finite linear combination of Fourier components $\exp [i(kx-wt_0)]$ with $k < K/\mu_i$. In other words, if the initial solution of a linear problem is sufficiently smooth, then the presence of the complex roots will not cause any problem if the exact solution is generated at each time step. Hence, for the one equation case, the well-posedness of the problem depends only on the smoothness of the initial solution and the magnitude of the interfacial drag coefficients. Since high-frequency components of the analytical solution cannot be represented on a coarse mesh, this implies that if spatial discretization methods are used to reduce the equations to a set of ODEs, the reduced problem is well-posed on coarse meshes if the drag coefficient is sufficiently large.

In two-phase flow problems, the magnitude of the imaginary part of the complex root is proportional to both the magnitude of the slip velocity and the interphase drag. Hence, one might expect that the reduced analytical problem is well-posed on coarse meshes. It is shown, however, in Section 4.2 that in the four equations case, the transformed solution vector \underline{Z} needs to have a positive component in the eigenvector corresponding to the largest eigenvalue of the drag matrix in order for all the wavelengths to be decaying. This is consistent with the observation that Helmholtz instability does occur in nature and that under certain circumstances the growth factor G in inequality (4-6) should be greater than one for a brief period of time. Stewart (1979) shows (see also Section 5.8) where RELAP5/MOD3 is used to investigate the Helmholtz instability that soon after the growth factor G exceeds one all wavelengths of the solution decay. Hence, when measured over an extended period of time, the underlying reduced analytical problem on coarse mesh can still be viewed as well-posed.

We note also that in the above one-equation model, the viscous stress is not included in the discussion because physical viscosity is usually very small, whereas numerical viscosity depends on the Courant number, the mesh size, and the numerical method used. It is, therefore, important that neither the mesh size nor the interphase drag is so small that the underlying reduced analytical problem is not ill-posed even in the absence of viscous stresses. This allows the code to run at the Courant limit and, in general, gives the most accurate results for a given problem, since the numerical viscosity is at its minimum at Courant number equal to one.

4.2 Region of Stability, Accuracy, and Convergence for the Semi-implicit Method

4.2.1 Stability, Consistency, and Convergence

The original Lax-Richtmyer's (1956) theory of stability, consistency, and convergence applies only to the solution of initial-boundary value problems for hyperbolic-parabolic partial differential equations when the mesh size tends to zero. Because the primary concern is the behavior of the wavelengths of the solution in length scales where the constitutive relationships are valid, a new theory of stability, consistency, and convergence relative to a finite sequence of mesh sizes is developed here. Here, the word stability must be understood to refer to the behavior of the numerical solution for fixed values of the mesh-sizes, as the number of computed time-level grows (as distinct from the notions of Lax-Richtmyer stability, which provide conditions related to the concept of convergence as the mesh-sizes tend to zero.)

Unless otherwise noted, the mathematical symbol $\| \cdot \|$, when applied to a vector, will in this work denote the Eudidean norm of a vector

$$\|x\|^2 = \sum_{i=1}^N |x_i|^2$$

where N is the dimension of the vector.

Stability. When the simple model equation (4-12) is differenced by the upwind differencing method, the stability criterion used here is

$$\|U^{n+1}\| \leq \|U^n\| \tag{4-8}$$

where U^n is the numerical solution at time level n. In general, as in Richtmyer and Morton, we require that if $U^{n+1} = C(\Delta t)U^n$, then $C(\Delta t)^n$ should be bounded in norm for all n as Δt tends to zero if $t < T$. In the absence of complex characteristics, it is known that the inequality [Equation (4-8)] holds if the simplistic model given by Equation (4-12) with $K = 0$ is solved using the first-order upwind differencing method. In this work, we establish conditions such that the same holds in the presence of complex characteristics.

For a fixed mesh size, any spatial discretization reduces the original set of equations to a system of ODEs. Temporal convergence for this fixed mesh is then a simple consequence of stability and consistency in the sense used by Lax and Richtmyer (1956). We are also interested in spatial convergence at time $t = T$ when the nodalization is refined. New definitions on consistency and convergence are introduced because only a finite sequence of grid levels is involved.

Consistency. In this work we assume that a coarser grid is always a subset of a finer grid so that a coarse grid difference operator operating on a fine grid function will always operate on the restriction of the fine grid function to the coarse grid. Because we are studying the behavior of the solution on a finite number of grid levels, the following definition is pertinent if there are only M grid levels, and M is the finest grid level.

Definition. Let U_i^n and L_i^n denote the numerical solution and finite difference operator on grid level i and time level n so that the finite difference equations at the current time level n+1 are given by

$$U_i^{n+1} = L_i^n(U_i^n), \quad i = 1, 2, \dots, M.$$

Let U^n and L^n denote the numerical solution and difference operator on level M and time level n. Then, the numerical method is said to be consistent with respect to the sequence of grid levels $i = 1, 2, \dots, M$ if at any time level n,

$$(L_i^n - L^n) U^n = \epsilon_i^n, \quad i = 1, 2, \dots, M \tag{4-9}$$

with

$$|\epsilon_j^n| > |\epsilon_i^n|$$

Domain of Applicability

if $j < i \leq M$.

Convergence. The following definition of convergence is used here for a finite sequence of grid levels.

Definition. Let U_i^n , $i = 1, 2, \dots, M$ be a finite sequence of numerical solutions at time level n on increasing finer grid levels 1 to M with M being the finest grid level. The sequence of solutions is said to be converging if

$$\|U_i^n - U^n\| < \|U_j^n - U^n\|$$

if $j < i \leq M$.

Definition. A difference operator L is said to be monotone if $L(f - g) > 0$ whenever $f > g$. Then, the following holds.

Definition. The maximum norm of a vector $\underline{x} = (x_1, x_2, \dots, x_M)^T$ is defined by

$$\|\underline{x}\|_\infty = \max |x_i|, i=1, 2, \dots, M.$$

Theorem 4.1. Let the sequence of difference operators, L_i , be linear, monotone. Assume that any pair of operators L_i^n and L_j^n with $j < i \leq M$ satisfies the following stability conditions in the maximum norm:

$$\|L_i^n(U_i^n - U^n)\|_\infty \leq \|U_i^n - U^n\|_\infty. \quad (4-10a)$$

and

$$\|U_j^n - U^n\|_\infty \leq \|L_j^n(U_j^n - U^n)\|_\infty + \gamma \min_k |\epsilon_j^n(x_k)| - \|\epsilon_i^n\|_\infty. \quad (4-10b)$$

with $\gamma = 1$. In addition, assume that the method is consistent and that both the ϵ_i^n in Equation (4-9) and $U_i^n - U^n$ have the same sign at any time level n for all i 's. Then, if the solutions are converging in the maximum norm at time level n , they are also converging in the maximum norm at time level $n+1$.

Proof. At each mesh point x_k , we have

$$|(U_i^{n+1} - U^{n+1})(x_k)| = |(L_i^n - L^n)U^n(x_k)| + |L_i^n(U_i^n - U^n)(x_k)| \quad (4-11a)$$

since the terms on the right hand side of the above equation have the same sign because of both the assumptions on the sign of ϵ_i^n and $U_i^n - U^n$ and the monotonicity of the operators L_i^n . It then follows from the Equation (4-11a) that the following holds:

$$\|U_i^{n+1} - U^{n+1}\|_\infty \geq \min_k |\epsilon_i^n(x_k)| + \|L_i^n(U_i^n - U^n)\|_\infty. \quad (4-11b)$$

By applying first the stability condition (4-10a), the consistency condition (4-9), and the assumptions on the solutions at time level n, and then the stability condition (4-10b), and the inequality (4-11b) for grid level j, we have

$$\begin{aligned}
 \|U_i^{n+1} - U^{n+1}\|_\infty &\leq \|\epsilon_i^n\|_\infty + \|L_i^n(U_i^n - U^n)\|_\infty \\
 &\leq \|\epsilon_i^n\|_\infty + \|U_i^n - U^n\|_\infty \\
 &\leq \|\epsilon_i^n\|_\infty + \|U_j^n - U^n\|_\infty \\
 &\leq \|L_j^n(U_j^n - U^n)\|_\infty + \min_k |\epsilon_j^n(x_k)| \\
 &\leq \|U_j^{n+1} - U^{n+1}\|_\infty
 \end{aligned}$$

the theorem easily follows. Hence, in a certain sense consistency plus stability implies convergence.

We note that if ϵ_j^n 's are constant functions Equation (4-10b), then the $\min_k |\epsilon_j^n(x_k)|$ term in condition (4-10b) is identically equal to $\|\epsilon_j^n\|_\infty$. In this case condition (4-10b) with $\gamma = 1$ merely states that the truncation error at grid level j is sufficiently greater than that at level i so that inequality (4-10b) holds. In cases when Equation (4-10b) holds for $\gamma < 1$, theorem (4-1) can be extended to the nonlinear case.

Corollary 4.1. Assume that any pair of L_i^n and L_j^n nonlinear operators (not necessarily monotone) with $j < i \leq M$ satisfies

$$\|L_i^n(U_i^n) - L_i^n(U^n)\|_\infty \leq \|L_i^n(U_i^n - U^n)\|_\infty + \beta(1-\gamma) \min_k |\epsilon_j^n(x_k)|$$

$$\|L_j^n(U_j^n - U^n)\|_\infty \leq \|L_j^n(U_j^n) - L_j^n(U^n)\|_\infty + (1-\beta)(1-\gamma) \min_k |\epsilon_j^n(x_k)|$$

with both nonnegative constants β and γ (the same γ as in Equation (4-10b)) less than one and that the stability conditions (4-10a) and (4-10b) hold with $\gamma < 1$. If the method is consistent and that both the ϵ_i^n in Equation (4-9) and $L_i^n(U_i^n) - L_i^n(U^n)$ have the same sign at any time level n for all i's, then if the solutions are converging in the maximum norm at time level n, they are also converging in the maximum norm at time level n+1.

Proof: At each mesh point x_k , we have

$$|(U_i^{n+1} - U^{n+1})(x_k)| = |(L_i^n - L^n)U^n(x_k)| + |L_i^n(U_i^n) - L_i^n(U^n)(x_k)|$$

because of the assumptions on the signs of each term on the right hand side of the above equation. Hence, we have

Domain of Applicability

$$\begin{aligned}
 \|U_i^{n+1} - U^{n+1}\|_\infty &\leq \|\epsilon_i^n\|_\infty + \|L_i^n(U_i^n) - L_i^n(U^n)\|_\infty \\
 &\leq \|\epsilon_i^n\|_\infty + \|L_i^n(U_i^n - U^n)\|_\infty + \beta(1-\gamma) \min_k |\epsilon_j^n(x_k)| \\
 &\leq \|\epsilon_i^n\|_\infty + \|U_i^n - U^n\|_\infty + \beta(1-\gamma) \min_k |\epsilon_j^n(x_k)| \\
 &\leq \|\epsilon_i^n\|_\infty + \|U_j^n - U^n\|_\infty + \beta(1-\gamma) \min_k |\epsilon_j^n(x_k)| \\
 &\leq \|L_j^n(U_j^n - U^n)\|_\infty + (\beta(1-\gamma) + \gamma) \min_k |\epsilon_j^n(x_k)| \\
 &\leq \|L_j^n(U_j^n) - L_j^n(U^n)\|_\infty + \min_k |\epsilon_j^n(x_k)| \\
 &\leq \|U_j^{n+1} - U^{n+1}\|_\infty
 \end{aligned}$$

the theorem easily follows.

In the above discussion, we've assumed that Δt has the same value for all the grid levels in the finite sequence of grids. We now address the issue of temporal convergence of the numerical methods at a given fixed grid within the finite sequence of grid levels. Assume that the coupled system of PDE's is first discretized by an upwind differencing or central differencing scheme. If the reduced analytical problem is then solved by the forward or backward Euler method, then the problem is reduced to a set of ODE's. The classical theory of stability, consistency, and convergence of numerical initial value problems of nonlinear ODE's is then fully applicable. In this work, for simplicity, only fully explicit and fully implicit schemes are considered in the theoretical stability analysis of a simple model problem discretized spatially by either the upwind differencing scheme (the fully explicit case) or the central differencing scheme (the fully implicit case). For a fixed grid, the classical theory for the numerical solution of nonlinear ODE's as $\Delta t \rightarrow 0$ is also applicable here. Hence, it is only necessary to investigate the stability of the numerical methods considered at a fixed grid so that we can determine the maximum regions of stability that the methods can be used without the occurrence of unphysical instability.

4.2.2 Stability Analysis for the Semi-Implicit Case

Stability analysis for the semi-implicit method for the two-phase flow equations was investigated (e.g., by Stewart (1979)). It was found that the interfacial drag coefficients play a critical role in stabilizing the long wave length calculations for coarse nodalizations. Here, we extend the result to show that criterion (4-8) is valid for all wavelengths of the numerical solution U for mesh sizes that are sufficiently coarse. We first examine the stability of numerical solution in a one-equation case.

4.2.2.1 Stability Analysis for the One-Equation Case. In the following, u and U denote the analytical and numerical solutions, respectively. Assume that the method of characteristics has been used to decompose the four two-phase flow Equations (4-1) through (4-4) into four decoupled PDEs. Suppose we are solving the initial value problem of

$$u_t + (\mu_r + i\mu_i) u_x + Ku = 0 \quad (4-12)$$

where

$$\mu_r = \frac{u_t + \epsilon u_v}{1 + \epsilon}, \quad \mu_i = \frac{\epsilon}{1 + \epsilon} (u_v - u_t),$$

$$\epsilon^2 = (1 - \alpha) \rho_v / \alpha \rho_t$$

with periodic boundary conditions by the explicit upwind differencing method. Upwind differencing of Equation (4-12) yields for $\mu_r > 0$,

$$\frac{U_j^{n+1} - U_j^n}{\Delta t} + (\mu_r + i\mu_i) \frac{(U_j^n - U_{j-1}^n)}{\Delta x} + KU_j^{n+1} = 0 \quad (4-13)$$

or

$$(1 + K\Delta t) U_j^{n+1} = (1 - a) U_j^n + a U_{j-1}^n - i b (U_j^n - U_{j-1}^n)$$

where $a = \mu_r \frac{\Delta t}{\Delta x}$, $b = \mu_i \frac{\Delta t}{\Delta x}$, $a > 0$.

Assume that the complex valued numerical solution U at time level n is relative Lipschitz continuous with relative Lipschitz constant L

$$|U_j^n - U_{j-1}^n| \leq L |x_j - x_{j-1}| (|U_j^n| + |U_{j-1}^n|) / 2. \quad (4-14)$$

It follows that

$$\begin{aligned} (1 + K\Delta t)^2 |U_j^{n+1}|^2 &\leq |(1 - a)U_j^n + a U_{j-1}^n|^2 \\ &\quad + L^2 |\mu_i|^2 \Delta t^2 (|U_j^n| + |U_{j-1}^n|)^2 / 4 \\ &\quad + L |\mu_i| \Delta t (|U_j^n| + |U_{j-1}^n|) |(1 - a) U_j^n + a U_{j-1}^n|. \end{aligned}$$

Here we have used the identity

$$|z|^2 = z\bar{z} = c^2 + d^2 \quad \text{if } z = c + id.$$

Using the Cauchy-Schwarz inequality,

$$\sum_j (\overline{U_j^n} U_{j-1}^n + \overline{U_{j-1}^n} U_j^n) \leq \sum_j |U_j^n|^2 + \sum_j |U_{j-1}^n|^2$$

and the periodic boundary conditions, it follows that if $0 \leq a \leq 1$, then

$$\sum_j |(1 - a)U_j^n + a U_{j-1}^n|^2 \leq \sum_j |U_j^n|^2.$$

Domain of Applicability

Similarly, we have

$$\sum_j |U_j^n| |(1-a)U_j^n + aU_{j-1}^n| \leq \sum_j |U_j^n|^2.$$

It then follows that

$$\sum_j |U_j^{n+1}|^2 \leq \sum_j |U_j^n|^2$$

if $0 \leq a \leq 1$ and $L |\mu_i| \leq K$.

Hence, we have the following result.

Theorem 4.2.

$$\|U^{n+1}\|_{L_2} \leq \|U^n\|_{L_2}$$

if U^n, U^{n+1} satisfy Equation (4-13)

$$0 \leq \mu, \frac{\Delta x}{\Delta t} \leq 1$$

U^n is relative Lipschitz continuous with relative Lipschitz constant L and $L |\mu_i| \leq K$. We note that all mesh functions on a mesh with mesh size $\Delta x \geq 2/L$ satisfy condition (4-14) because the condition in this case is a mere consequence of the triangle inequality although smooth functions on fine mesh may also satisfy condition (4-14). Hence, the theorem holds if $\Delta x \geq 2|\mu_i|/K$ and the other conditions are satisfied.

4.2.2.2 Stewart's Stability Results for the Four Equations Case. Assume that the semi-implicit method is used to discretize Equations (4-1) through (4-4). Then, we have the following equations, with $u_v, u_v > 0$ for donor-cell differencing of the adjective terms:

$$\begin{aligned} & \left(\alpha_j^{n+1} \rho_{vj}^{n+1} - \alpha_j^n \rho_{vj}^n \right) / \Delta t \\ & - \left(\alpha_{j-1}^n \rho_{vj-1}^n u_{vj-1/2}^{n+1} - \alpha_j^n \rho_{vj}^n u_{vj+1/2}^{n+1} \right) / \Delta x = 0 \end{aligned} \tag{4-15}$$

$$\begin{aligned} & \left((1-\alpha_j^{n+1}) \rho_{lj}^{n+1} - (1-\alpha_j^n) \rho_{lj}^n \right) / \Delta t \\ & - \left((1-\alpha_{j-1}^n) \rho_{lj-1}^n u_{lj-1/2}^{n+1} - (1-\alpha_j^n) \rho_{lj}^n u_{lj+1/2}^{n+1} \right) / \Delta x = 0 \end{aligned} \tag{4-16}$$

$$\alpha_j^n \rho_v^n \left[(u_{v,j+1/2}^{n+1} - u_{v,j+1/2}^n) / \Delta t + u_{v,j+1/2}^n (u_{v,j+1/2}^n - u_{v,j-1/2}^n) / \Delta x \right] \quad (4-17)$$

$$+ \alpha_j^n (P_{j+1}^{n+1} - P_j^{n+1}) / \Delta x = K_{j+1/2} (u_{l,j+1/2}^{n+1} - u_{v,j+1/2}^{n+1}),$$

$$(1 - \alpha_j^n) \rho_l^n \left[(u_{l,j+1/2}^{n+1} - u_{l,j+1/2}^n) / \Delta t + u_{l,j+1/2}^n (u_{l,j+1/2}^n - u_{l,j-1/2}^n) / \Delta x \right] \quad (4-18)$$

$$+ (1 - \alpha_j^n) (P_{j+1}^{n+1} - P_j^{n+1}) / \Delta x = K_{j+1/2} (u_{v,j+1/2}^{n+1} - u_{l,j+1/2}^{n+1}).$$

Stewart (1979) analyzed the stability of the numerical solutions for the above equations using von-Neumann linearized stability analysis method. He showed that when $K = 0$, the eigenvalues of the amplification matrix satisfy

$$\lambda^2 C_n^2 [(\lambda - 1 + \bar{U}_l)^2 + (1 - \alpha) \rho_l / (\alpha \rho_v) (\lambda - 1 + \bar{U}_v)^2] + (\lambda - 1 + \bar{U}_v)^2 (\lambda - 1 + \bar{U}_l)^2 = 0$$

where

$$C_n = (c_v \Delta t / \Delta x) (2 \sin(\pi / 2n)), \quad \bar{U}_v = (u_v \Delta t / \Delta x) [1 - \exp(-ik \Delta x)]$$

$$\bar{U}_l = (u_l / u_v) \bar{U}_v$$

$$k = \pi / (n \Delta x), \quad n = 1, 2, \dots, N, \quad \text{where } N \text{ is the total number of mesh intervals.}$$

From this, he concluded that the stability conditions for the short wavelengths are

$$u_l \frac{\Delta t}{\Delta x} < 1, \quad u_v \frac{\Delta t}{\Delta x} < 1 \quad (4-19)$$

and that for $K = 0$, wavelengths with large n are unstable. Stewart (1979) then showed that the stability condition for large n when $K > 0$ is as follows:

$$K (n \Delta x) / \rho_v \gg |u_v - u_l| (\rho_l / \rho_v). \quad (4-20)$$

Stewart showed that in the case of certain bubbly or droplet flows, this reduces to the following stability condition:

$$n \Delta x \gg (\rho_l / \rho_v C_D) r \quad (4-21)$$

Domain of Applicability

where r is the bubble or droplet radius, and C_D is the drag coefficient. In other words, the wavelength $n\Delta x$ will not have a growing mode if it is larger than a certain multiple of the radius of an individual bubble or droplet.

4.2.2.3 Stewart's Numerical Example. Stewart also found that results of many calculations with schemes similar to Equations (4-15) through (4-18) have shown that they appear to be well behaved at all wavelengths (that is, no geometrically growing modes) in a large number of practical cases unless Δx is very small.

Stewart (1979) carried out some trial calculations to illustrate this, choosing as an example the flow of a steam-water mixture in a horizontal 20-mm-diameter tube, including wall friction and a momentum exchange law proposed for annular flow (Rubin and Lin 1980). Although equations of state for liquid water and steam were used, it was assumed that no phase change occurred. The boundary conditions were $\alpha = 0.5$, $P = 150.1$ bars, and saturation temperatures at the inlet, and $P = 150$ bars at the outlet. The transient calculation began from initial conditions of constant α , T_e , T_v equal to those values at the inlet valves, and $u_v = u_l$ and $G = \alpha\rho_v u_v + (1 - \alpha)\rho_l u_l = 10^3$ kg/m²/sec. Calculations were performed for a tube 15-mm long with 5, 10, 15, 25, 50, and 75 equal steps between boundary pressure points. The time step was 0.12 msec with five space steps, and proportional to Δx for the other cases. Table 4-1 shows the values of G at the inlet after 6 msec. The right column gives the slope between successive data points in a plot of G ($t = 6$ msec) versus Δx .

Stewart (1979) observed that for a first-order accurate approximation to a well-posed problem, one would expect the figures in the slope column to tend toward a constant value as the number of nodes increases. In fact the slopes decrease slightly in the first-four instances, implying slightly less than first order convergence. With 75 nodes, this trend is broken, showing the first signs of a geometrically growing oscillation.

By substituting the value used for K into Equation (4-20) above and taking $\Delta x = 15\text{mm}/75 = 0.2$ mm, one would find equality in Equation (4-20) with $\bar{n} = 150$. In other words, using Equation (4-21) with $n = 1$ as a criterion for Δx would in this case be conservative by a factor of 150. We also note in this case that the smallest well-behaved mesh spacing is more than 50 times smaller than the tube diameter.

4.2.2.4 Stability Analysis for the Four Equation Case. The von-Neumann stability analysis given by Stewart (1979) yields the material Courant stability criterion (4-19). In order to give a good estimate for the maximum theoretical region of stability for the semi-implicit method, we again use the energy norm method of Section 4.2.2.1. For simplicity, we assume that the explicit upwind differencing scheme is used in Equations (4-15) through (4-18). The method of characteristics is used together with a matrix transformation technique to obtain two sets of stability conditions. The conditions related to the speed of sound are discarded in favor of the material Courant stability Conditions (4-19), whereas the conditions pertaining to the two complex roots are used as an estimate for the theoretical maximum region of stability.

Table 4-1. Stewart's (1979) calculations.

Number of nodes	Mass flow rate G after 6 msec	Slope of G versus Δx (relative units)
5	3338.59817	>1,000
10	3338.89185	>0.984
15	3338.98815	>0.978
25	3339.06476	>0.975
50	3339.12202	>1.088
75	3339.14332	

Let $U = (\alpha, \rho_v, u_v, u_\theta)^T$. Then, equations (4-15) through (4-18) can be written in the matrix form,

$$\frac{U_j^{n+1} - U_j^n}{\Delta t} + \frac{A_j(U^n) U_j^n - A_{j-1}(U^n) U_{j-1}^n}{\Delta x} + K^* U_j^{n+1} = 0 \quad (4-22)$$

where

$$K^* = \begin{bmatrix} 0 & & & \\ & 0 & & \\ & & K & -K \\ & & -K & K \end{bmatrix}$$

and K is the interfacial drag coefficient.

Assume that the coefficients of the equations are treated as constants locally (hence, local linear). Then, the matrix equation becomes

$$\frac{U_j^{n+1} - U_j^n}{\Delta t} + \frac{A(U_j^n) (U_j^n - U_{j-1}^n)}{\Delta x} + K^* U_j^{n+1} = 0 \quad (4-23)$$

Let Ω and P be the matrices of eigenvalues and eigenvectors of the matrix $A(U_j^n)$, respectively:

$$AP = P\Omega, \text{ or } P^{-1}AP = \Omega$$

Domain of Applicability

where

$$\Omega = \begin{bmatrix} \lambda_1 & & & \\ & \lambda_2 & & \\ & & \lambda_3 & \\ & & & \lambda_4 \end{bmatrix}$$

and λ_i , $i = 1$ to 4 are the distinct eigenvalues of the matrix A. Let P be chosen such that the L_2 norm of P is one. Let the vector $\underline{Z} = [Z_1, Z_2, Z_3, Z_4]^T$ be defined by

$$\underline{Z} \equiv P^{-1}\underline{U}.$$

Then, \underline{Z} satisfies

$$\frac{\underline{Z}_j^{n+1} - \underline{Z}_j^n}{\Delta t} + \Omega \frac{(\underline{Z}_j^n - \underline{Z}_{j-1}^n)}{\Delta x} + Q \underline{Z}_j^{n+1} = 0 \quad (4-24)$$

where

$$Q \equiv P^{-1} K^* P.$$

It then follows that the matrix Equation (4-24) can be written as follows:

$$(I + Q\Delta t) \underline{Z}_j^{n+1} = f(\underline{Z}_j, \underline{Z}_{j-1})^n \quad (4-25)$$

where

$$f(\underline{Z}_j, \underline{Z}_{j-1}) \equiv \begin{bmatrix} f_1(Z_{1j}, Z_{1j-1}) \\ f_2(Z_{2j}, Z_{2j-1}) \\ f_3(Z_{3j}, Z_{3j-1}) \\ f_4(Z_{4j}, Z_{4j-1}) \end{bmatrix}$$

$$f_k(Z_{kj}, Z_{kj-1}) \equiv (1-a_k) Z_{kj} + a_k Z_{kj-1} - i b_k (Z_{kj} - Z_{kj-1}) \quad k = 1, \dots, 4$$

$$\text{where } i = \sqrt{-1}, a_k = \text{Re}(\lambda_k) \frac{\Delta t}{\Delta x}, b_k = \text{Im}(\lambda_k) \frac{\Delta t}{\Delta x},$$

$$\text{and } \lambda_k \equiv \text{Re}(\lambda_k) + i \text{Im}(\lambda_k) \quad k = 1, \dots, 4$$

Let $f(\underline{Z}_j, \underline{Z}_{j-1})^n = C_1 \underline{q}_1 + C_2 \underline{q}_2 + C_3 \underline{q}_3 + C_4 \underline{q}_4$, where \underline{q}_i , $i = 1$ to 4 are the eigenvectors of the matrix $(I+Q\Delta t)^{-1}$ and μ_i are the corresponding eigenvalues. The matrix Q has a complete set of eigenvectors and the matrices K^* and Q have the same eigenvalues, since Q is obtained from the symmetric matrix K^* by a similarity transformation. It follows that $\mu_1 = \mu_2 = \mu_3 = 1$ and $\mu_4 = (1+2K\Delta t)^{-1}$. Hence, we have

$$\underline{Z}_j^{n+1} = C_1 \underline{q}_1 + C_2 \underline{q}_2 + C_3 \underline{q}_3 + \frac{C_4}{1+2K\Delta t} \underline{q}_4 \quad (4-26)$$

In the special case when $C_1 = C_2 = C_3 = 0$, $C_4 = 1$, and $\underline{q}_4 = f(\underline{Z}_j, \underline{Z}_{j-1})^n$, we have, as in Section 4.2.2.1, that if $0 \leq a_i \leq 1$,

$$\sum_{i=1}^4 \sum_{j=1}^N |Z_{ij}^{n+1}|^2 \leq \frac{(1 + \max |Im(\lambda_i)| L \Delta t)^2}{(1 + 2K\Delta t)^2} \sum_{i=1}^4 \sum_{j=1}^N |Z_{ij}^n|^2 \quad (4-27)$$

where L is the relative Lipschiltz constant of the function \underline{Z} , and Z_{ij} is the value of the i^{th} component of \underline{Z} at the j^{th} mesh point. Since $\underline{U} = P\underline{Z}$ and P is a unitary transformation, we have the following theorem.

Theorem 4.3.

$$\|\underline{U}^{n+1}\| \leq \|\underline{U}^n\|$$

if $C_1 = C_2 = C_3 = 0$ in Equation (4-26), $|Im(\lambda_i)| L \leq 2K$, and $Re(\lambda_i) \Delta t/\Delta x \leq 1$, $i = 1, \dots, 4$.

Let \underline{p} and \underline{q} denote $C_1 \underline{q}_1 + C_2 \underline{q}_2 + C_3 \underline{q}_3$ and $c_4 \underline{q}_4$ respectively. A straightforward computation shows that the following result holds:

Lemma. The necessary and sufficient condition for

$$\|\underline{p} + \underline{q}\|^2 < \|\underline{p} + \mu_4 \underline{q}\|^2 \quad (4-28)$$

to hold is

$$-(\underline{q}^H \underline{p} + \underline{p}^H \underline{q}) < (1 + \mu_4) \underline{q}^H \underline{q}. \quad (4-29)$$

Here, H denotes the conjugate transpose of a vector. The left side of Equation (4-29) is the negative of the symmetric inner product between the two vectors \underline{p} and \underline{q} . If this inner product is negative, increasing the drag coefficient K and, hence, decreasing μ_4 will actually increase the magnitude of the \underline{Z}^{n+1} vector relative to its value at the last time step. Since, in general for two-phase flow problems, we expect [with the exception of the onset of the Helmholtz instability which lasts only a brief moment in time (see also Section 5.8)] the scheme to be more stable with increasing values of K , the inner product in question can be assumed to be nonnegative for physical problems. In this case, we have the following result:

Domain of Applicability

$$|Z_j^{n+1}|^2 \leq \frac{1}{(1+2K'\Delta t)} |f(Z_j, Z_{j-1})^n|^2 .$$

Here $K' < K$ is a positive number dependent on K , on the angle between the vectors \underline{p} and \underline{q} , and on the magnitude of \underline{q} relative to \underline{p} . Hence, we have the following theorem.

Theorem 4.4.

$$|U^{n+1}| \leq |U^n| \tag{4-30}$$

$$\text{if } |Im(\lambda_i)|L \leq 2K'$$

where K' is the same as above, and $Re(\lambda_i) \Delta t/\Delta x \leq 1$.

Hence, the numerical method is always stable on a sufficiently coarse mesh since the relative Lipschitz constant for an arbitrary mesh function on a coarse mesh, is quite small, or, in other words, the short wavelengths of an analytic function cannot be represented on a coarse mesh.

4.2.3 Region of Stability, Accuracy, and Convergence

In RELAP5/MOD3, the liquid and vapor energy equations are added to the four Equations (4-1) through (4-4) so that in the absence of noncondensibles six equations are solved simultaneously. It is known (see Ransom and Hicks 1984) that the addition of the energy equations does not cause significant differences related to the complex roots in the characteristic polynomial. Hence, we expect that the stability results in the last section hold.

We next discuss the important question of the choice of time-step and mesh size for large-scale computations with RELAP5. Although in principle the accuracy of the computation increases as the mesh size decreases, care should be taken so that the mesh size does not fall below a critical length associated with the interfacial drag. In view of Theorem 4.3, the theoretical maximum region of stability is

$$Re(\lambda_i) \frac{\Delta t}{\Delta x} \leq 1$$

and

$$|Im(\lambda_i)| \cdot L \leq 2K$$

where

$$\lambda_{1,2} \sim c_v \pm u_v, \lambda_{3,4} \sim \frac{u_l + \epsilon u_v}{1+\epsilon} \pm i \frac{\epsilon}{1+\epsilon} (u_v - u_l).$$

Here, ϵ and c_v are the same as in Equation (4-5) and we assume that the eigenvalues of the A matrix in Equation (4-23) are good approximations to that of the analytical problems (4-1) through (4-4). The conditions

$$\lambda_{1,2} \frac{\Delta t}{\Delta x} \leq 1 \quad (4-31)$$

arise due to the fully explicitness of the theoretical scheme studied. If conditions (4-31) are ignored, the stability criteria

$$\left(\frac{u_t + \epsilon u_v}{1 + \epsilon} \right) \frac{\Delta t}{\Delta x} \leq 1 \quad (4-32)$$

and

$$\frac{\epsilon}{1 + \epsilon} |u_v - u_t| \cdot L \leq 2K \quad (4-33)$$

yield the theoretical maximum stability and accuracy region. Condition (4-32) is similar to the condition

$$\max (|u_t|, |u_v|) \frac{\Delta t}{\Delta x} \leq 1 \quad (4-34)$$

obtained in section 4.2.2.2. Condition (4-33) can be restated in terms of mesh size Δx . For a Fourier component with wavelength r , the relative Lipschitz constant L is $1/(r\Delta x)$. Since short wavelengths are damped by numerical viscosity, it is only necessary to stabilize calculations with respect to wavelengths not shorter than $4\Delta x$. The condition (4-33), therefore, reduces to

$$\Delta x \geq \frac{\epsilon}{(1 + \epsilon)} \frac{|u_v - u_t|}{8K} \quad (4-35)$$

Example: For nonvertical bubbly flow,

$$K = \frac{1}{8} \frac{3.6}{\alpha_t \rho_v} \frac{C_D}{d_o} |u_v - u_t|$$

where C_D is the drag coefficient and d_o is the average diameter of the bubbles (Allison, et al., 1990) from Condition (4-35),

$$\Delta x_{\min} \geq \frac{1}{3.6} \frac{\alpha_t \rho_v d_o}{C_D} \cdot \frac{\epsilon}{1 + \epsilon} \quad (4-36)$$

Domain of Applicability

The theoretical maximum region of stability is, therefore, the set of Δt , Δx that satisfies Conditions (4-34) and (4-35). This is also the theoretical maximum region of accuracy and convergence. Outside this region, the solution may show oscillatory behavior. The Δx given by (4-35) is expected to be smaller than the averaging scale. This, again, indicates that the computational mesh size should not be smaller than the averaging scale.

We note that condition (4-35) is obtained by assuming that a fully explicit upwind differencing scheme is used. Since the region of stability is usually larger when more implicitness is added to the numerical scheme (see also Section 4.3), condition (4-35) can be viewed as a conservative estimate for the theoretical maximum stability region for the semi-implicit scheme. Because the momentum flux is treated explicitly in the semi-implicit method, it is expected that the actual stability condition for the semi-implicit method will not differ from (4-35) greatly. Whether this is actually the case needs further research.

It is also important that Δt be chosen such that the linearization and truncation errors given in Section 3.3 do not exceed a certain predetermined tolerance. Because of the importance of the interfacial drag coefficient K in stabilizing the calculations, it is also desirable that K does not vary greatly from one time level to another or from one spatial volume to another. The use of time smoothing to reduce the variance of K is expected to enhance the stability of the calculations. The time smoothing of the interphase heat transfer coefficients, on the other hand, may help to reduce the linearization errors, since the interphase heat transfer terms are important contributors to the energy equation. The suitable use of time smoothing of interphase heat transfer and drag coefficients may, therefore, help stabilize the calculations during flow regime transitions. On the other hand, smooth transition from pre-CHF to post-dry-out flow regimes will also help stabilize the calculations for certain problems, as we see in Section 5.

4.3 Region of Stability, Accuracy, and Convergence for the Nearly Implicit Scheme

The presence of the complex roots in the characteristic polynomial does not pose any serious problem for the nearly implicit scheme if Δt is sufficiently large. As before, we first analyze the stability of the numerical method in the one-equation case using the energy norm method, and then extend the analysis to the four equations case.

4.3.1 Stability Analysis for the Nearly Implicit Method

Assume that the PDE (4-12) is discretized by the implicit central differencing method. Then, we have

$$\frac{U_j^{n+1} - U_j^n}{\Delta t} + (\mu_r + i\mu_i) \frac{(U_{j+1}^{n+1} - U_{j-1}^{n+1})}{2\Delta x} + KU_j^{n+1} = 0 \quad (4-37)$$

or

$$(1 + K\Delta t) U_j^{n+1} + a (U_{j+1}^{n+1} - U_{j-1}^{n+1}) + ib (U_{j+1}^{n+1} - U_{j-1}^{n+1}) = U_j^n$$

where

$$a \equiv \mu_r \frac{\Delta x}{2\Delta x}, \quad b \equiv \mu_i \frac{\Delta x}{2\Delta x}$$

Assume that

$$U_{j+1}^{n+1} - U_{j-1}^{n+1} = 2i L_j U_j^{n+1} \Delta x$$

where L_j is real value, and $i = \sqrt{-1}$. In the case when $U_j^{n+1} = e^{ijrk}$, $k = \Delta x$, we have $L_j = \sin rk$. Then we have

$$\begin{aligned} & (1 + K\Delta x) \operatorname{Re} \left(U_j^{n+1} \right) - \mu_r \Delta x L_j \operatorname{Im} \left(U_j^{n+1} \right) - \mu_i \Delta x L_j \operatorname{Re} \left(U_j^{n+1} \right) \\ & + i \left[(1 + K\Delta x) \operatorname{Im} \left(U_j^{n+1} \right) + \mu_r \Delta x L_j \operatorname{Re} \left(U_j^{n+1} \right) - \mu_i \Delta x L_j \operatorname{Im} \left(U_j^{n+1} \right) \right] = U_j^n \end{aligned}$$

Equating the squares of the magnitudes of the complex numbers on both sides of the above equation gives

$$(1 + K\Delta x)^2 \left(|U_j^{n+1}|^2 \right) + \left[(\mu_r \Delta x)^2 + (\mu_i \Delta x)^2 \right] L_j^2 |U_j^{n+1}|^2 - 2(1 + K\Delta x) \mu_i \Delta x L_j |U_j^{n+1}|^2 = |U_j^n|^2$$

For $K = 0$, the stability condition for

$$|U_j^n|^2 \geq |U_j^{n+1}|^2$$

to hold is

$$L_j^2 \left[(\mu_r \Delta x)^2 + (\mu_i \Delta x)^2 \right] > |2\mu_i \Delta x L_j| \tag{4-38}$$

Condition (4-38) can be simplified to

$$|L_j| \Delta x (\mu_r^2 + \mu_i^2) > 2|\mu_i|$$

This analysis can be extended to the four equations case in the same manner as before. We again cast the equations in the following form:

$$\frac{Z_j^{n+1} - Z_j^n}{\Delta x} + \Omega \frac{(Z_{j+1}^{n+1} - Z_{j-1}^{n+1})}{2\Delta x} + Q Z_j^{n+1} = 0 \tag{4-39}$$

Domain of Applicability

where

$$Q \equiv P^{-1} K^* P$$

and \underline{Z} , K^* , P , and Ω have the same form as in Equation (4-24).

Then, we have

$$(I + Q\Delta t) \underline{Z}_j^{n+1} + \Omega \frac{\Delta t}{2\Delta x} (\underline{Z}_{j+1}^{n+1} - \underline{Z}_{j-1}^{n+1}) = \underline{Z}_j^n \quad (4-40)$$

As before, assume that

$$\underline{Z}_{j+1}^{n+1} - \underline{Z}_{j-1}^{n+1} = 2i \Delta x \cdot D_j \underline{Z}_j^{n+1} \quad (4-41)$$

where

$$D_j \equiv \begin{bmatrix} L_{1j} & & & \\ & L_{2j} & & \\ & & L_{3j} & \\ & & & L_{4j} \end{bmatrix}$$

so that Equation (4-40) becomes

$$(I + Q\Delta t + i\Omega \Delta t D_j) \underline{Z}_j^{n+1} = \underline{Z}_j^n \quad (4-42)$$

We then apply the method of fractional steps or operator splitting to Equation (4-42) and solve in succession

$$(I + i\Omega \Delta t D_j) \underline{Z}_j^{n+1/2} = \underline{Z}_j^n$$

$$(I + Q \Delta t) \underline{Z}_j^{n+1} = \underline{Z}_j^{n+1/2}$$

We note that this amounts to adding a term, $\Omega D_j Q \Delta t^2$, to Equation (4-42). It then follows from the methods used in the last section that the following theorem holds.

Theorem 4.5.

$$|U^{n+1}| \leq |U^n| \quad (4-43)$$

if

$$|L_{kj}|(\mu_{kr}^2 + \mu_{ki}^2) \Delta t > 2|\mu_{ki}|, \quad k = 1, \dots, 4 \quad (4-44)$$

or if

$$|L_{kj}|(\mu_{kr}^2 + \mu_{ki}^2) \Delta t \cdot (1 + 2K' \Delta t) > 2|\mu_{ki}|, \quad k = 1, \dots, 4 \quad (4-45)$$

where K' is the same as above (see the discussion before Theorem 4.4), and L_{kj} are the same as in Equation (4-41).

For Fourier components of wavelength $4m\Delta x$ ($m = 1, 2, \dots, N/2$, $N = 1/\Delta x$), $L_j = 1/m\Delta x$; Theorem 4.5, therefore, can be restated (taking $m = N/2$) as follows.

Theorem 4.6.

$$|U^{n+1}| \leq |U^n|$$

if

$$\Delta t \left[\left(\frac{\epsilon}{1+\epsilon} |u_v - u_\ell| \right)^2 + \left(\frac{u_\ell + \epsilon u_v}{1+\epsilon} \right)^2 \right] \cdot (1 + 2K' \Delta t) > \frac{\epsilon}{1+\epsilon} |u_v - u_\ell|. \quad (4-46)$$

Here K' is the same as above, and we assume that μ_k , $k = 1, \dots, 4$ are the same as the characteristics for the continuous problem (4-1) through (4-4).

4.3.2 Region of Stability, Accuracy, and Convergence

In view of Theorem 4.6, the nearly implicit scheme is stable and convergent regardless of mesh size as long as Condition (4-46) is satisfied. Condition (4-46) is a minimum time step condition that typically arises when implicit central differencing is used to discretize problems with complex characteristics (see Ruben and Lin (1980) for a discussion of similar problems that arise from discretization of parabolized Navier-Stokes equations).

For flows at Courant number equal to 1 and $|U_v| \gg |U_\ell|$, the maximum theoretical region is given by

$$\frac{2\epsilon}{1+\epsilon} \cdot \Delta t \cdot \left(1 + 2 \frac{K \Delta t}{|u_v - u_\ell|} \right) > 1. \quad (4-47)$$

Domain of Applicability

Example: For nonvertical bubbly flow, the condition (4-47) reduces to

$$2 \frac{\epsilon}{1+\epsilon} \cdot \Delta x \cdot \left(1 + 0.9 \frac{C_D \Delta x}{\alpha_t \rho_v d_o} \right) > 1 \quad .$$

From criteria (4-46) and (4-47), we see that the scheme is stable if the code is run at a Courant number greater than or equal to 1 on coarse mesh. Condition (4-46), however, limits the accuracy of the numerical method. Moreover, when the code takes smaller time steps in cases of phase transition or other discontinuities, conditions (4-46) and (4-47) may interfere with smooth execution of the code. We, therefore, recommend that the nearly implicit method should primarily be used when the code is running at a Courant number not significantly smaller than 1. In view of the discussion in Section 3.2.1, we also recommend that implicit upwind differencing should be used if filtering out of all the short waves is desired when the code is running at large Courant numbers. This concludes the discussion for the first step of the nearly implicit method.

In the nearly implicit method, the mass and internal energy of the two phases are solved by a two-step method. The accuracy of this two-step method is examined here using the simple model of Equation (3-24). Consider a scheme in which the source terms are evaluated implicitly in the first step, and the adjective terms are evaluated in the second step (Trapp and Rienke 1986). In the first step:

$$\bar{\phi}_j^{n+1} - \phi_j^n + \frac{u \Delta t}{2 \Delta x} (\phi_{j+1}^n - \phi_{j-1}^n) = -\frac{\Delta t}{\tau} \bar{\phi}_j^{n+1} \quad . \quad (4-48)$$

In the second step,

$$\phi_j^{n+1} - \bar{\phi}_j^n + \frac{u \Delta t}{2 \Delta x} (\bar{\phi}_{j+1}^{n+1} - \bar{\phi}_{j-1}^{n+1}) = -\frac{\Delta t}{\tau} \bar{\phi}_j^{n+1} \quad . \quad (4-49)$$

Let G denote $(u \Delta t / \Delta x) \sin(k \Delta x)$ and H denote $\Delta t / \tau$. Assuming an infinite medium and a general Fourier solution component and using the same notations as in Section 3.2.1 for the stability analysis, the first step gives

$$\bar{\phi}_j^{n+1} = \frac{1 - iG}{1 + H} \phi_j^n \quad . \quad (4-50)$$

The second step gives

$$\phi_j^{n+1} = \frac{\phi_j^n - H \bar{\phi}_j^{n+1}}{1 + iG} \quad (4-51)$$

so that

$$\phi_j^{n+1} = \frac{1 - \frac{H}{1+H} + \frac{H}{1+H}iG}{1+iG} \phi_j^n. \quad (4-52)$$

Equation (4-52) gives an amplification factor of absolute value less than unity for any time step; hence, the scheme is unconditionally stable. The time constant τ for interphase mass and energy is usually on the order of 0.001, so that, even for small time-steps, H can be much larger than one. For example, a time-step of 0.006 gives a value of 6 for H . Hence, for practical purposes, we may consider $H/(1+H)$ to be fairly close to one. In this case, Equation (4-52) can be rewritten as

$$\phi_j^{n+1} \approx \frac{iG}{1+iG} \phi_j^n. \quad (4-53)$$

With the exception of the shortest and longest wavelengths for the Fourier component, G is large whenever the Courant number is large. From Equation (4-53), it is clear that for large Courant numbers, the following holds for almost all wavelengths:

$$\phi_j^{n+1} \approx \phi_j^n. \quad (4-54)$$

Hence, the two-step method for the mass and energy equations gives solution at time level $n+1$ that is basically unchanged from that at the n^{th} time level. On the other hand, the model differential equation we are solving has solutions that decay to zero. Hence, although the scheme is unconditionally stable, it is highly inaccurate at large Courant numbers if there are sufficiently many intermediate wavelengths present. This conclusion differs slightly from that reached by Trapp and Rienke (1986) who claims that the scheme is inaccurate when $H \gg 1$ and $G > 1$ (i.e., both are large but $H \gg G$). In fact, $H \gg 1$ holds for most reasonable time-steps and for these time-steps; the larger the value of G is, the more inaccurate the scheme is. For example, the scheme is more inaccurate when $H = 6$ and $G = 10$ than, say, when $H = 6$ and $G = 2$. On the other hand, for coarse nodalization where there is only one or two intermediate wavelengths present, the inaccuracy in the second step of the nearly implicit method may not be larger than the truncation error of the method.

A numerical example was presented for a specific test problem in Reference 3-2. The problem was a straight pipe blowdown of a low-quality mixture. The initial conditions were saturated fluid at 7×10^6 Pa, with a vapor void fraction of 4.8×10^{-1} . The pipe consisted of 12 cells and was 2.46 m long. It was blown down to atmospheric pressure. The calculations presented in Reference 3-2 showed that the transient pressure profile computed at volume 6 was inaccurate at large Courant numbers. The numerical results computed by the nearly implicit scheme, however, did converge to that computed by the semi-implicit method at smaller Courant numbers. The inaccuracies were attributed to the inability of the nearly implicit scheme to calculate the mass transfer rate accurately at large Courant numbers. Because in this simulation the important point is to accurately calculate the mass transfer rate as these govern the depressurization, the nearly implicit method is inefficient for this task. Hence, the nearly implicit method is not accurate for fine nodalization at large Courant numbers for problems that are governed by the interphase mass transfer effects.

4.4 Conclusions

Both the semi-implicit method and the first step of the nearly implicit method are stable, accurate, and convergent and give rise to well-posed problems within their respective regions of stability. The accuracies of the methods are determined by their respective truncation errors, whereas the time-step for the semi-implicit method is Courant limited. Because the region of stability depends on the magnitude of the interphase drag coefficients, it is larger for two-phase flow problems that have large drag coefficients and smaller for some other problems. In general, any computational mesh size that is compatible with the modelling scale is within the maximum theoretical region of stability.

The mass and energy equations are solved by a two-step method in the nearly implicit method. Because the interphase mass transfer term is treated explicitly in the second step, the method can be inaccurate for fine nodalization at large Courant numbers for problems governed by the interphase mass transfer effects. The use of central differencing in the momentum equations for the nearly implicit method is also incompatible with the upwind differencing scheme used for the semi-implicit method. This makes the switching from one method to another more difficult if the user desires to use the semi-implicit method when the Courant number does not exceed one but to use the nearly implicit method otherwise. We, therefore, recommend that

1. The interphase mass transfer term in the mass and energy equations should be treated more implicitly in the second step of the nearly implicit method if fine nodalization is used.
2. Upwind differencing (donor-cell differencing) should be used for the nearly implicit method.

5. COMPARISON WITH ANALYTICAL SOLUTION AND SEPARATE EFFECTS EXPERIMENTS

This section summarizes the work done on the convergence and accuracy studies of the RELAP5/MOD3 code. The calculations were done using the semi-implicit scheme of version 7v of RELAP5/MOD3 because 7v was the latest available version when work on this section began. There has been increasing concern regarding the behavior of MOD3 as a lot of changes have been made from the MOD2 scheme. This study has been conducted along the lines of previous work done on MOD2 by Ransom and Mousseau (1991). The main intent of this kind of exercise is to verify the soundness of the computational procedure and the physically well-behaved nature of the constitutive models.

To test these aspects of the code, four problems were run. Extensive numerical data were generated, classified and recorded in the form of data files and graphs. Plots of sensitive parameters that might be considered indicative of convergence were generated and are provided with this report. An attempt has been made to delineate some characteristics of the predictions and how they compare with the MOD2 results and the experimental/analytical values. Also, some explanations are provided for observed behavior; general conclusions are drawn based on observations.

Numerical results reported in Sections 5.2 and 5.3 were obtained by Krishnamurthy (1992) at Purdue University. As noted in Section 3.4.1, Krishnamurthy found MOD2.5 time smoothing to be time-step sensitive for the Edwards pipe blow down problem (Krishnamurthy 1992). We have found that this is primarily because Equation (3-58), instead of Equation (3-57), was used in MOD2.5 time smoothing of interphase drag coefficients. Numerical studies with MOD2.5 time smoothing using Equation (3-57) for the time smoothing of interphase drag coefficients are presented in Section 5.6.

5.1 Convergence Test

In order to explore the convergence and accuracy behavior of the RELAP5/MOD3 version, a study was first performed on a transient problem with a known analytical solution. This problem, called the water faucet problem, was devised by Ransom (1979), and has complete analytical solution, which is derived in the next section. The problem tests the numerical scheme after assuming an idealized system with no interfacial exchange terms. This was followed by a physical problem, the pipe blowdown problem, and two developmental assessment problems, namely, the Christensen 15 subcooled boiling problem, and the Oak Ridge 39 void profile test problem. The numerical computations were compared with experimental data for all three problems. In addition, the numerical calculations for the pipe blowdown problem were compared to that obtained in a previous study on the RELAP5/MOD2 scheme (Ransom and Mousseau 1991). This study investigates the effect of the new constitutive models on the solutions.

In all of these studies, the numerical experiment involved generating a number of solutions by successively having the spatial and temporal discretizations. Thus a wide range of Courant numbers (all less than 1.0) and nodalizations were covered. Detailed problem descriptions can be found in Ransom (1979) for the water faucet problem, and in Volume III of for the Edwards pipe blowdown problem, the Christensen 15 subcooled boiling problem, and the Oak Ridge void profile test problem.

Comparison

5.2 Water Faucet Problem

In the water faucet problem, water comes down from a time-dependent volume with a constant velocity, v_0 , vertically into a 12-ft pipe divided into 12 single volumes. A detailed analytical solution of this water faucet problem is given by Ransom (1979). In addition to the void fraction values at any time, t_0 , we may also calculate the mass in the pipe analytically as below and compare it with numerically obtained values.

The location of the discontinuity at t_0 is x_0 , where

$$x_0 = v_0 t_0 + 0.5 g t_0^2$$

and mass in pipe at any instant t is

$$M = (\alpha_f \rho_f + \alpha_g \rho_g) (x - x_0) + (12 - x_0) (\alpha_f \rho_f + \alpha_g \rho_g).$$

Now, from 0 to x_0 , α_f is given by $\alpha_f = \alpha_0 v_0 / (v_0 + g(t - t_0))$.

Also, the equation for coordinate along the particle path is given by

$$x = x_0 + v_0(t - t_0) + g(t - t_0)^2.$$

Solving the two preceding equations to eliminate $(t - t_0)$, we get

$$x = x_0 + v_0^2/g[\alpha_0/\alpha_f - 1] + 0.5 (\alpha_0/\alpha_f - 1)^2$$

which gives

$$dx = -[v_0^2(\alpha_0/\alpha_f)^3/g] d\alpha_f$$

which can be substituted in the equation for mass, and which can now be integrated with respect to α_f .

The following three modifications to RELAP5/MOD3 were made in the coding to run the faucet problem:

1. Interface drag was reduced to a small value (10^{-10})
2. Added mass was turned to zero
3. The interphase heat transfer coefficient was reduced to a small value (10^{-10}).

For the nodalization study, the discretization was increased from 12 nodes to 96 nodes by successively halving the node size while keeping the physical length constant. Data were collected on the

1. Void fraction across the pipe at 0.25, 0.5, and 0.75 s

2. Void fraction across the pipe at 2 s (steady state)
3. Mass in the pipe at 0.5 s (discontinuity still in pipe), as a percentage of initial mass
4. Mass in pipe at 2 s (after discontinuity passes the pipe), as a percentage of the initial mass.

A similar set of data was generated for the 12-node case by successively having the time step from 0.05 to 3.125e-03 s. The results from these runs are plotted in Figures 5-1 to 5-12.

The void fraction plots show almost the same behavior as results obtained using MOD2 (Ransom and Mousseau 1991). This is expected, since the major modifications made to MOD2 were on the constitutive models, and the numerical computation scheme is the same as for RELAP5/MOD2. The steady state plot (Figure 5-4) shows that the solution becomes increasingly accurate as spatial nodalization increases. The 96-node case is extremely close to the analytical solution at the faucet outlet and overlaps it perfectly downstream at steady state. This improvement in solution is also seen in Figures 5-5 and 5-6, where the percentage of the initial mass remaining in the pipe is plotted as a function of the node size. The dotted line shows the analytically calculated mass.

The results of a temporal discretization study are shown in Figures 5-7 to 5-12. The void fraction profile curves at 0.25, 0.5, and 0.75 s into the transient to show the expected diffusive behavior of the computation scheme. As the Courant number is reduced (by reducing Δt), the shock capturing ability also decreases. Yet, from the graphs it is also evident that the solution converges for decreasing Δt 's in a spatial sense. Further, the steady state solution shows no dependence on the time-step value (Figure 5-10).

From Figure 5-11, which shows the mass in the pipe as a function of the time-step at 0.5 s, the accuracy of prediction increases appreciably with decreasing time-step, but this behavior is artificial, as is evident from the corresponding void fraction (Figure 5-8). As the time-step decreases, the mass of water in the pipe increases owing to a smoother gas void fraction profile and, thus, results in predicting the total mass in pipe closer to the analytically calculated value. The real effect of increased temporal discretization is seen in Figure 5-12, which shows almost no improvement in steady state mass prediction and that spatial nodalization limits the accuracy of the solution.

5.3.1 Annulus Model

Two more cases were investigated to study the annulus model incorporated in MOD3. The first case involved modeling the main pipe as an annulus. It was expected that since the interface drag had been considerably reduced for the annulus component, it should be able to predict the falling discontinuity with reasonable accuracy. The results obtained from this study are summarized in Figures 5-13 to 5-16. It is apparent that there is still a strong momentum coupling between the two phases, and that the discontinuity gets smudged as the liquid column accelerates. This also results in a slower propagation of the void fraction disturbance, and it is still in the tube at 2 s (Figure 5-16) when the analytical solution predicts steady state.

The oscillations in the void, however, have disappeared. While this demonstrates the important role that the interphase drag coefficients play in stabilizing the calculations, it also shows that too large magnitude of the drag coefficient may adversely affect the accuracy of the calculations.

Comparison

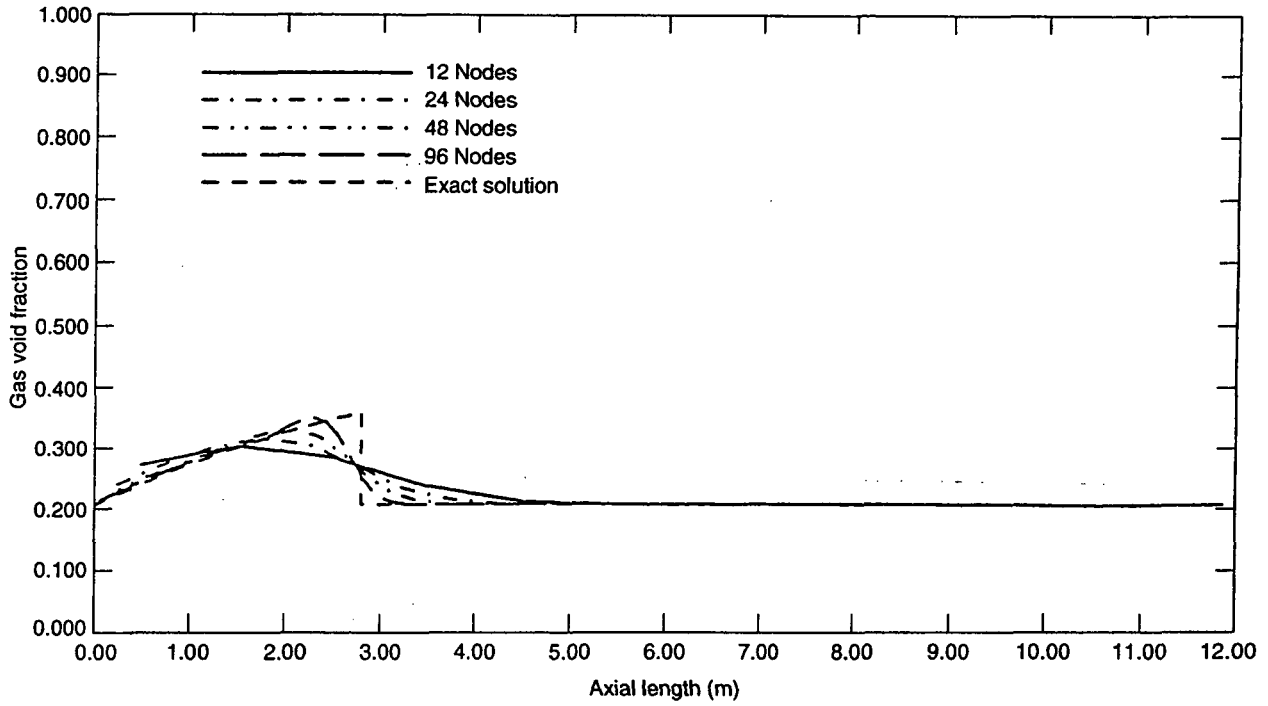


Figure 5-1. FAUCET, spatial convergence at 0.25 s, void versus length.

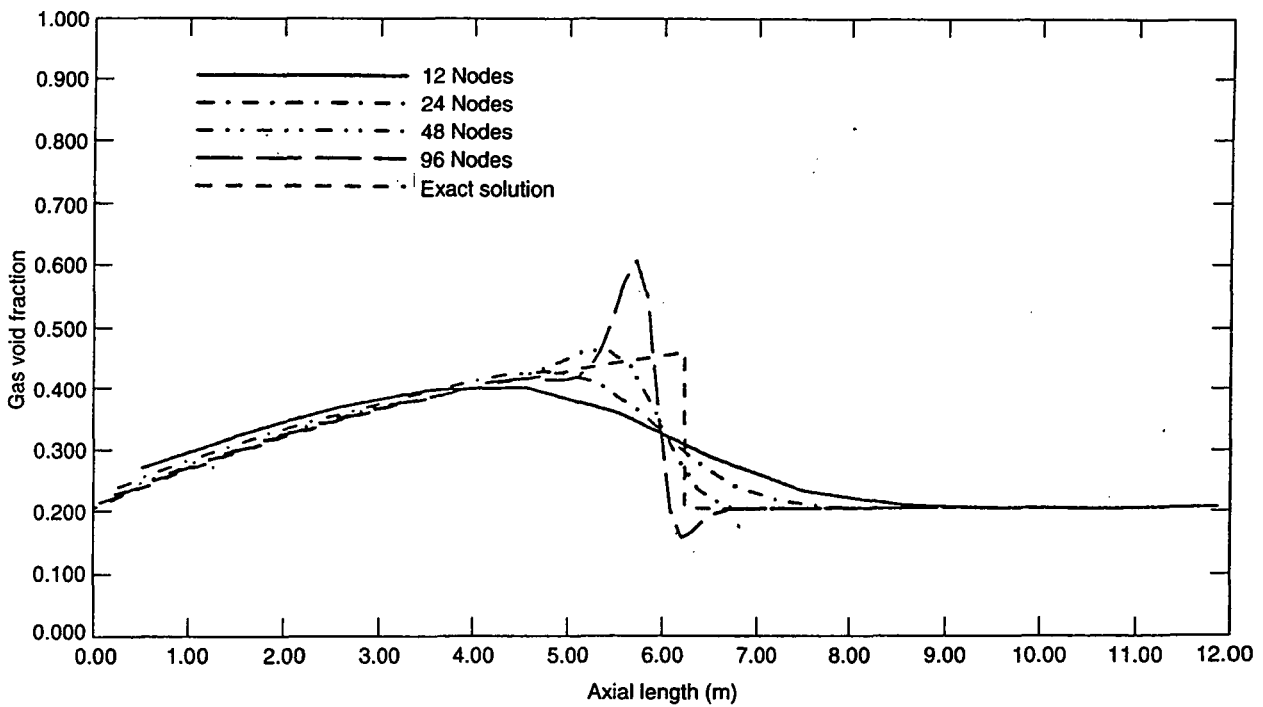


Figure 5-2. FAUCET, spatial convergence at 0.50 s, void versus length.

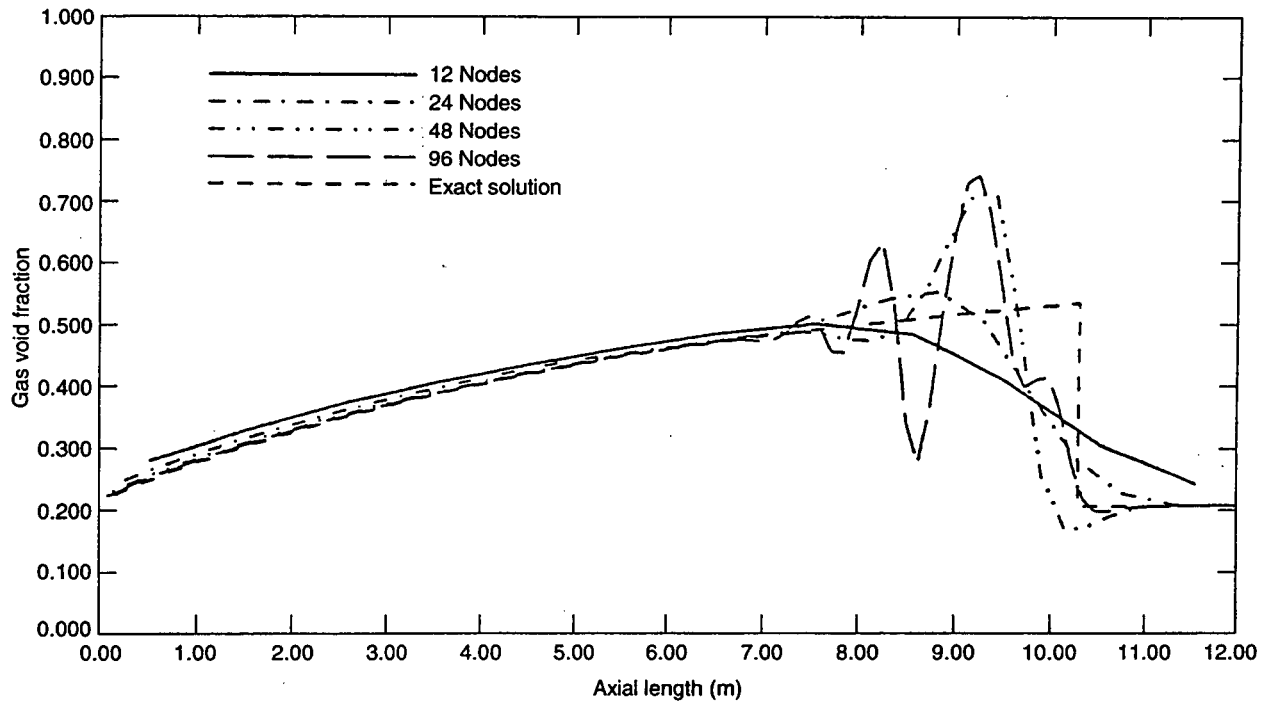


Figure 5-3. FAUCET, spatial convergence at 0.75 s, void versus length.

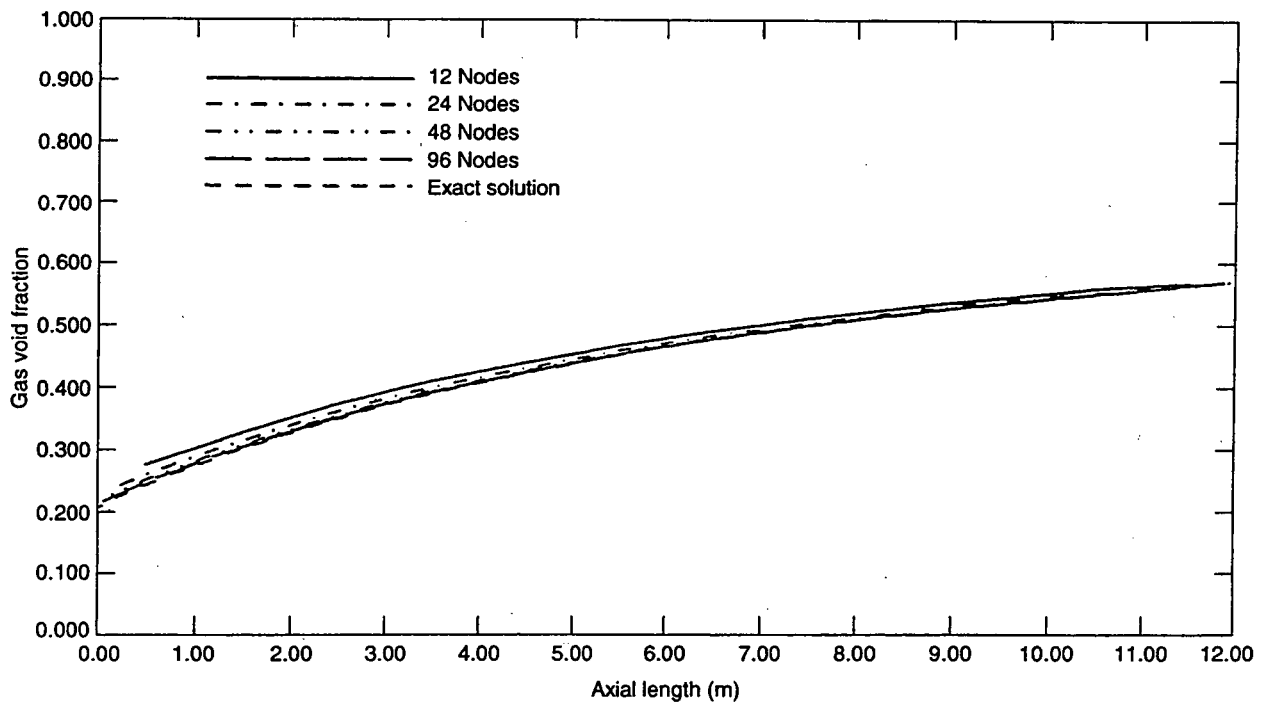


Figure 5-4. FAUCET, spatial convergence at steady state, void versus length.

Comparison

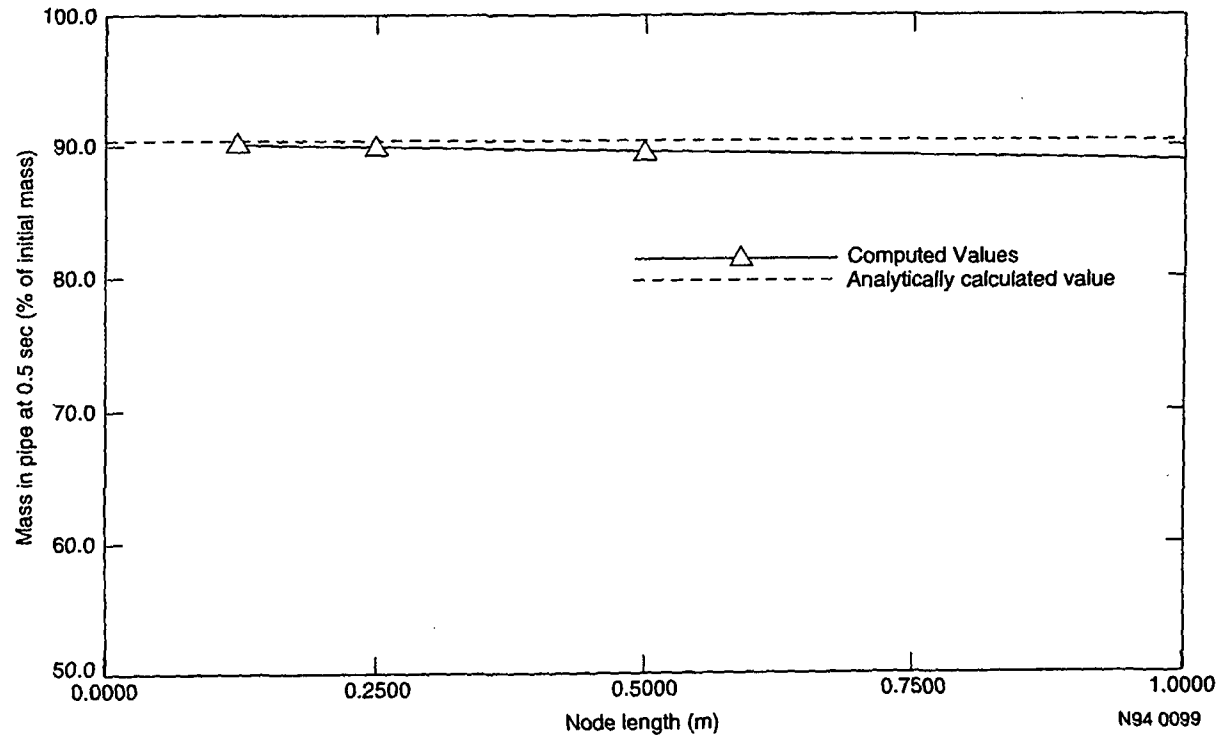


Figure 5-5. FAUCET, spatial convergence at 0.50 s, mass versus length.

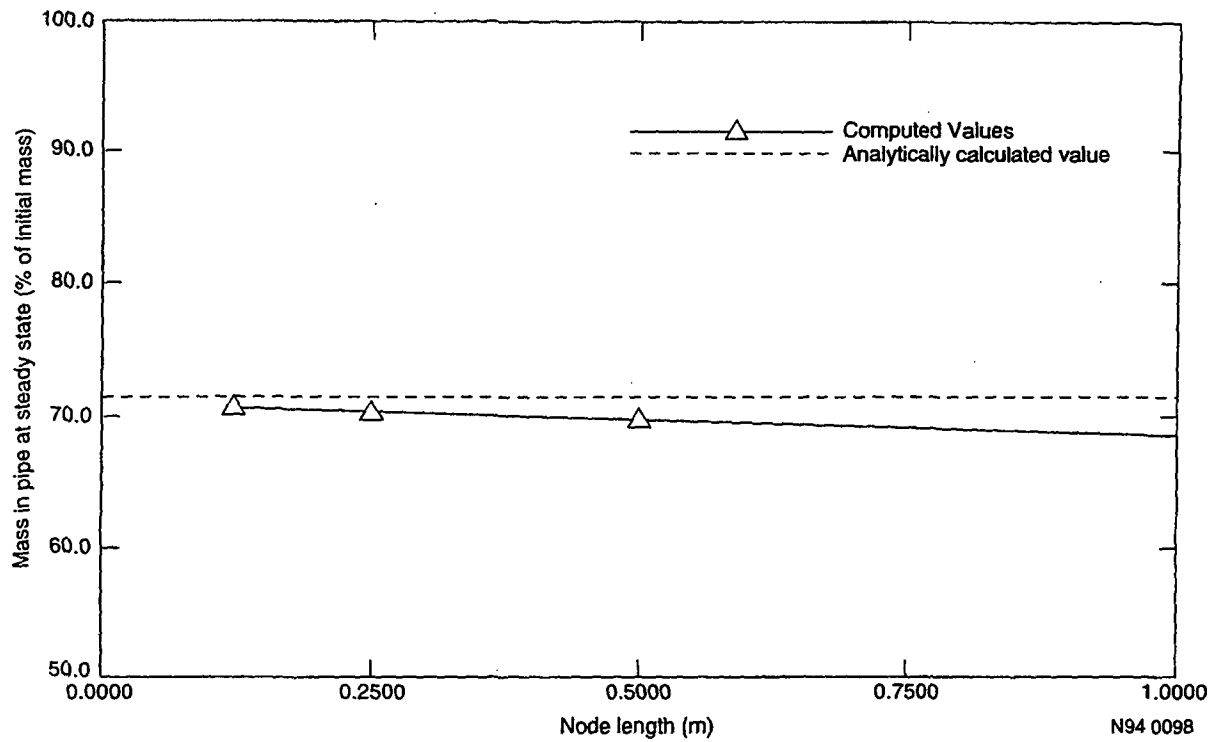


Figure 5-6. FAUCET, spatial convergence at steady state, mass versus length.

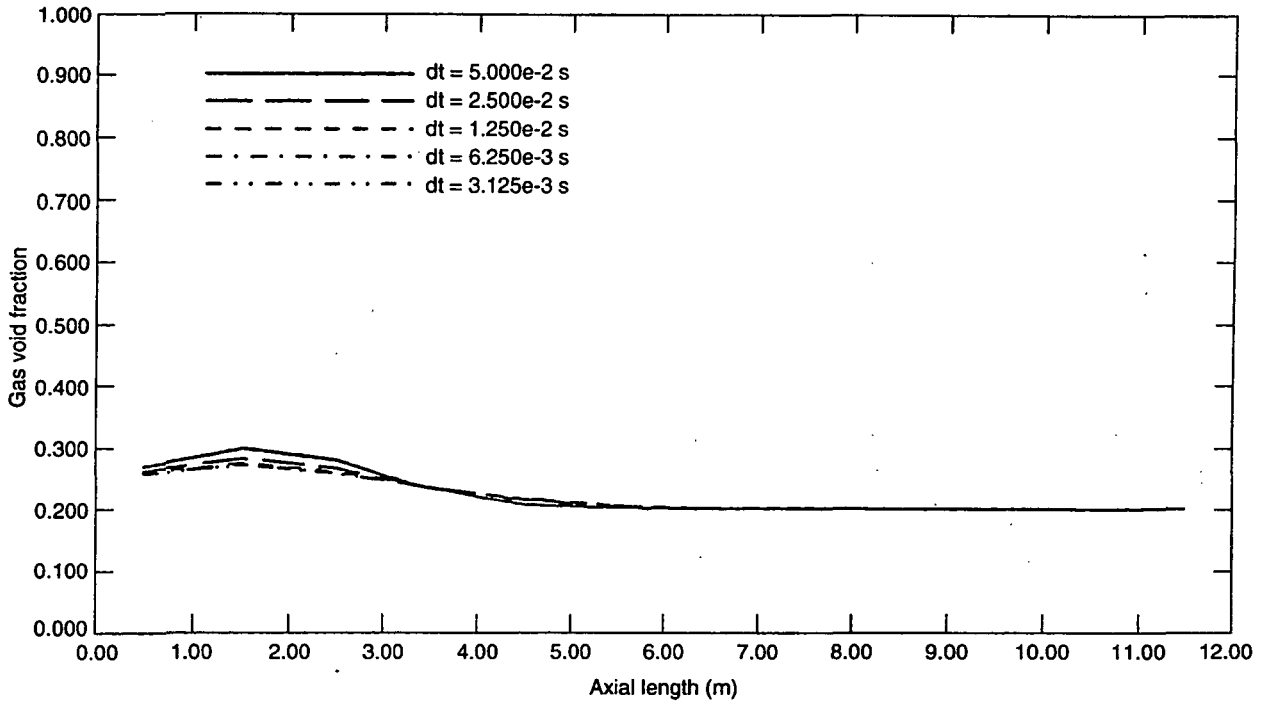


Figure 5-7. FAUCET, temporal convergence at 0.25 s, gas void versus length.

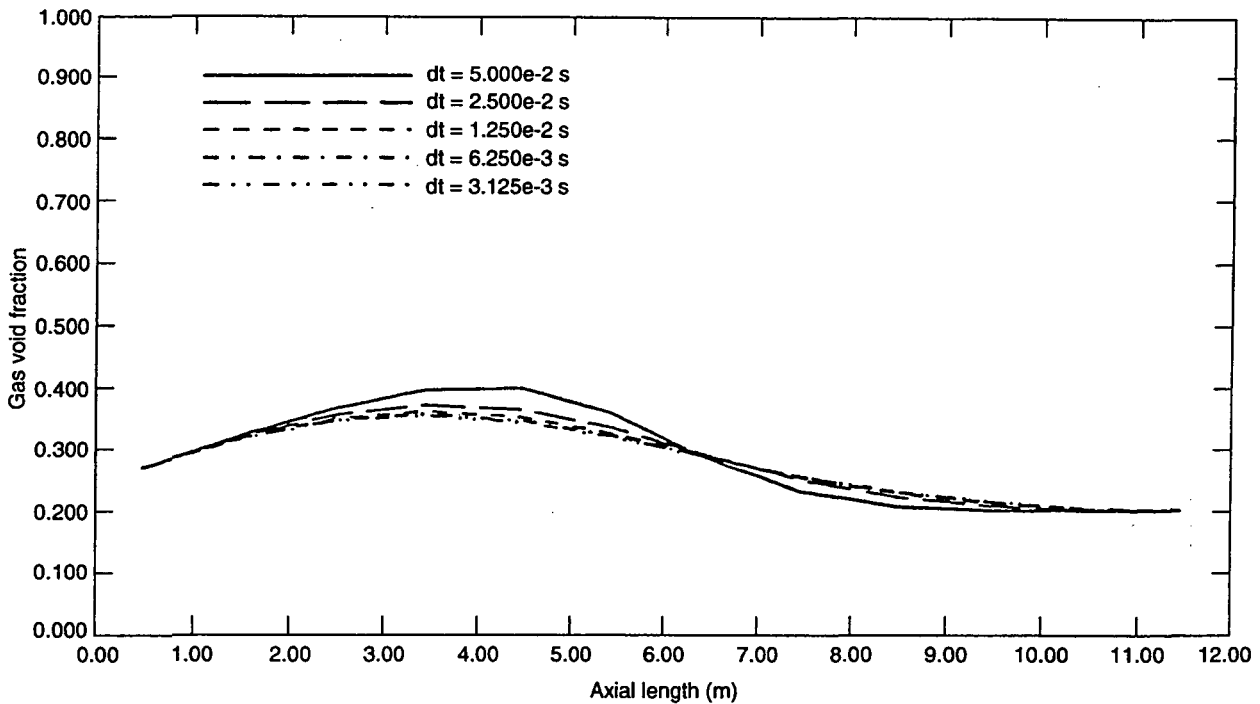


Figure 5-8. FAUCET, temporal convergence at 0.50 s, gas void versus length.

Comparison

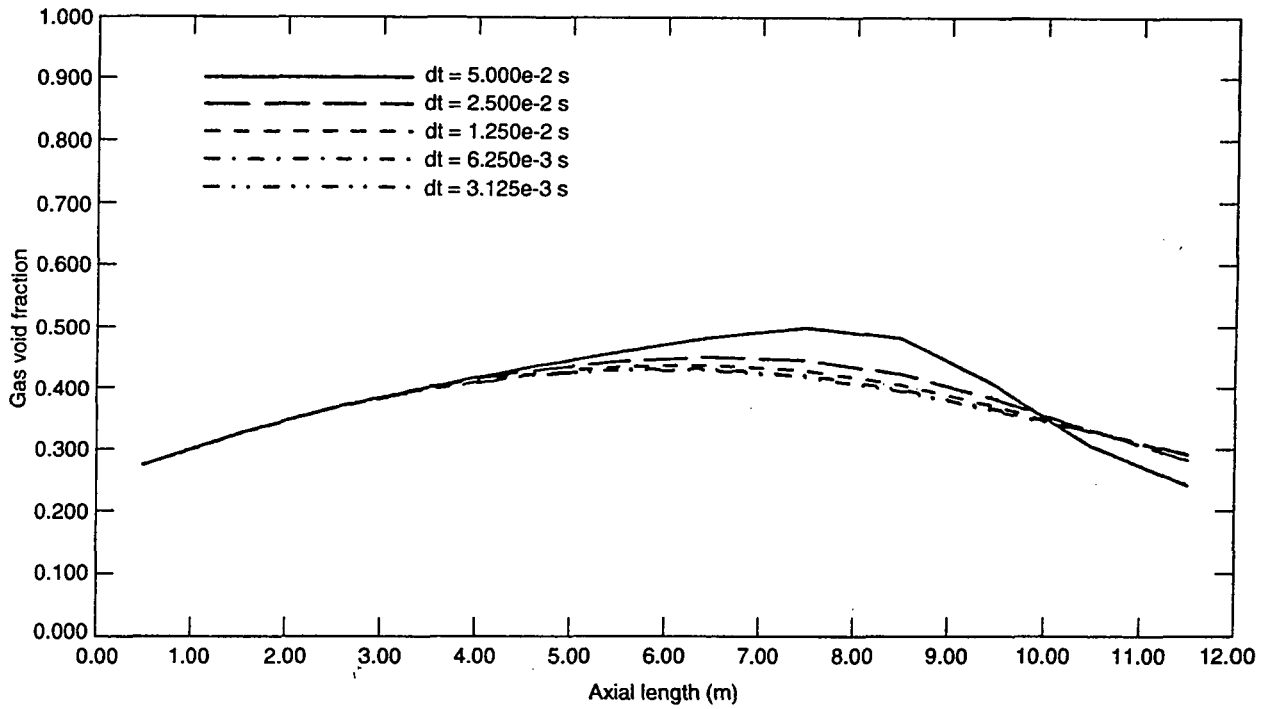


Figure 5-9. FAUCET, temporal convergence at 0.75 s, gas void versus length.

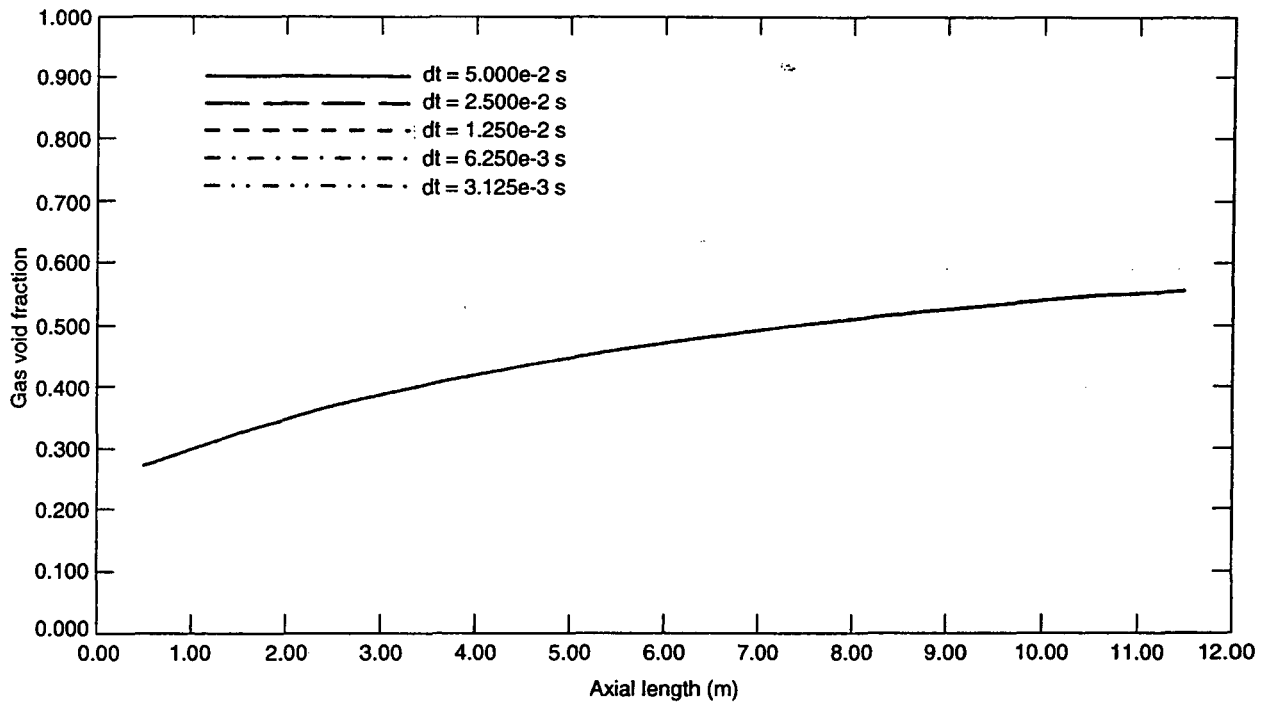


Figure 5-10. FAUCET, temporal convergence at steady state, gas void versus length.

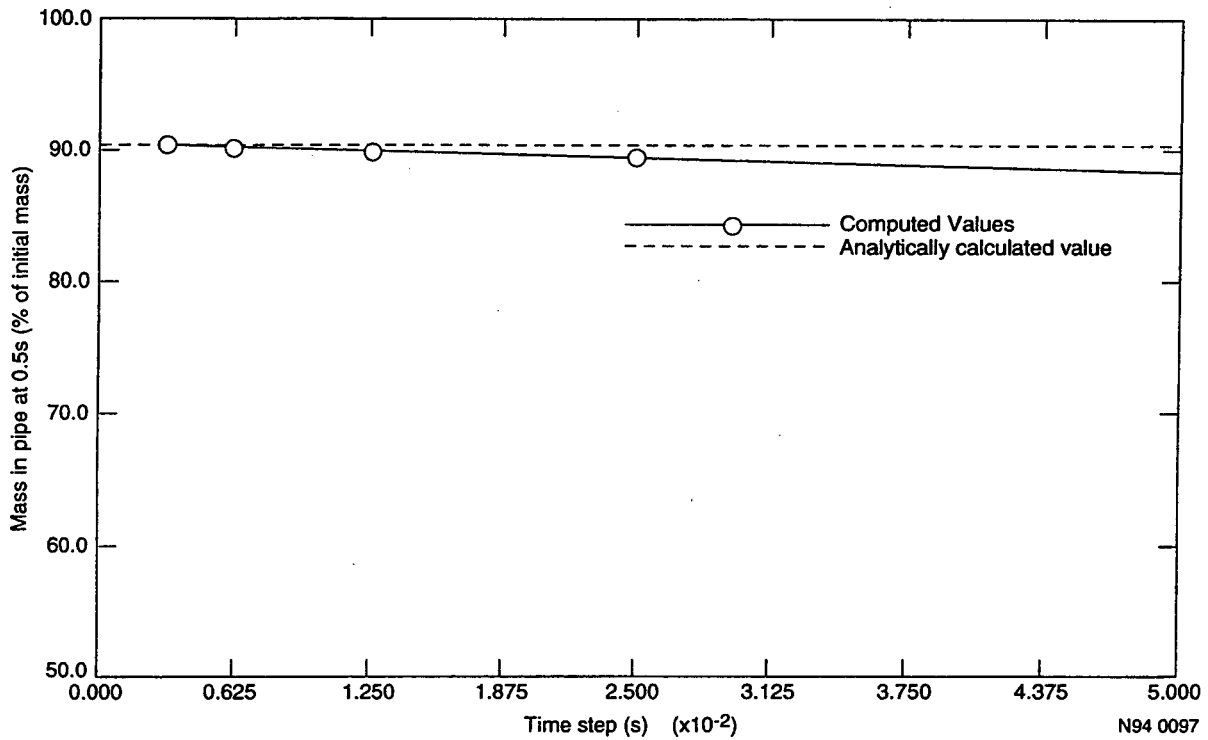


Figure 5-11. FAUCET, temporal convergence at 0.50 s, mass in pipe versus length.

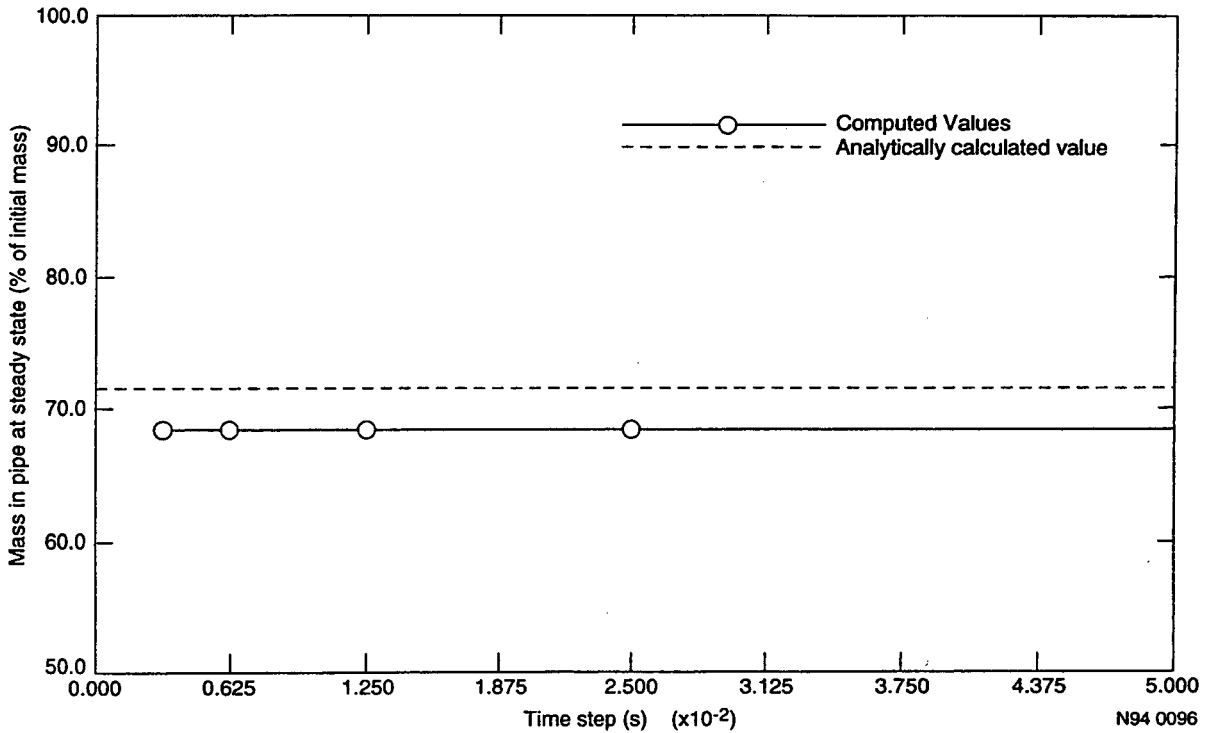


Figure 5-12. FAUCET, convergence at steady state, mass versus length.

Comparison

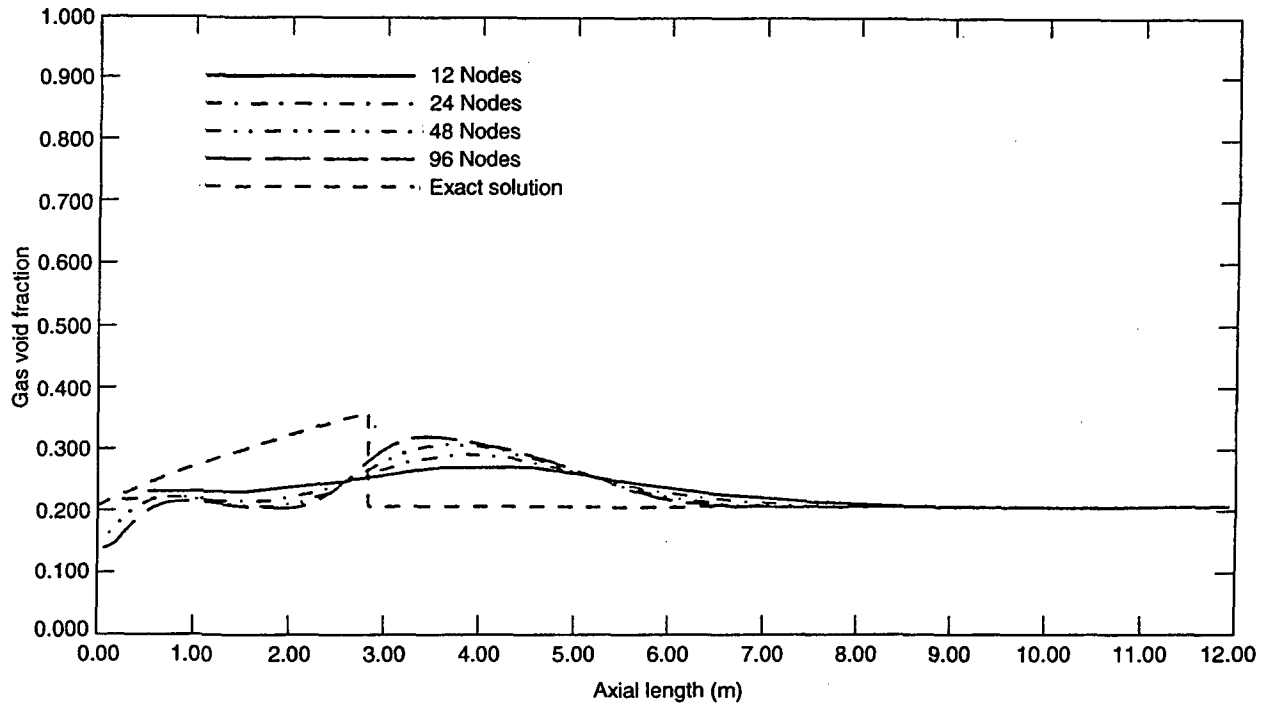


Figure 5-13. FAUCET, ANNULUS MODEL, TIME = 0.25 s.

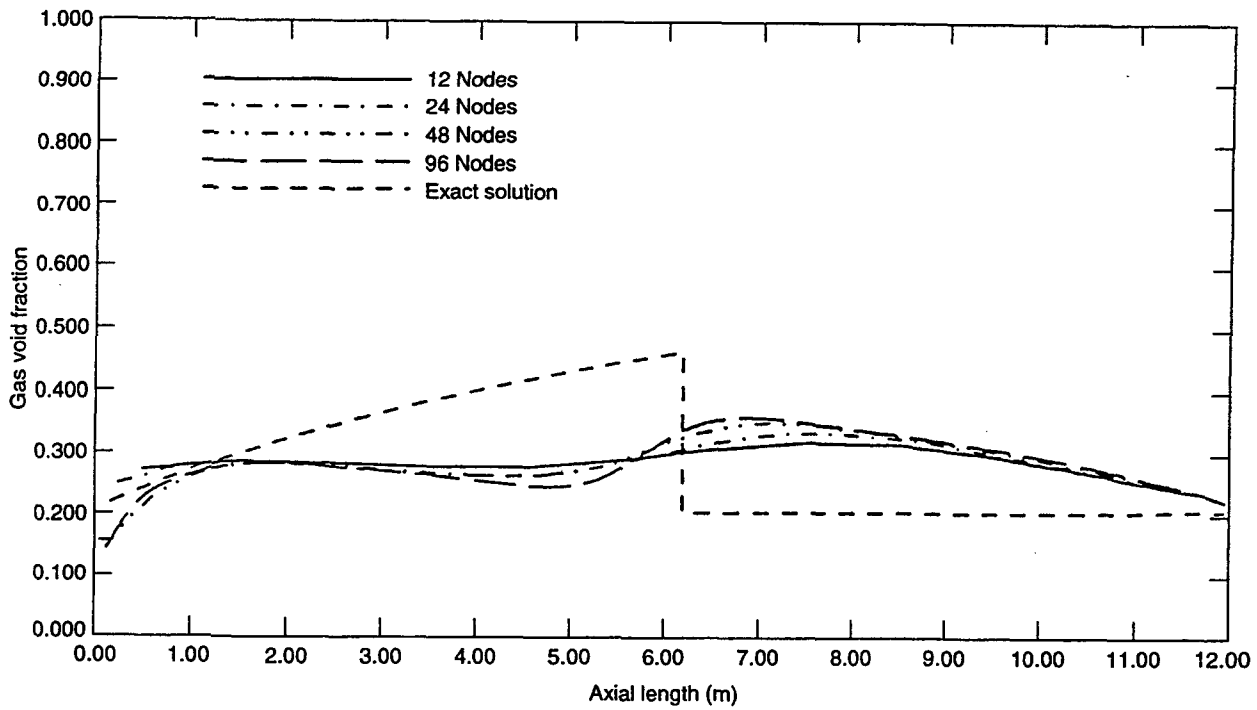


Figure 5-14. FAUCET, ANNULUS MODEL, TIME = 0.50 s.

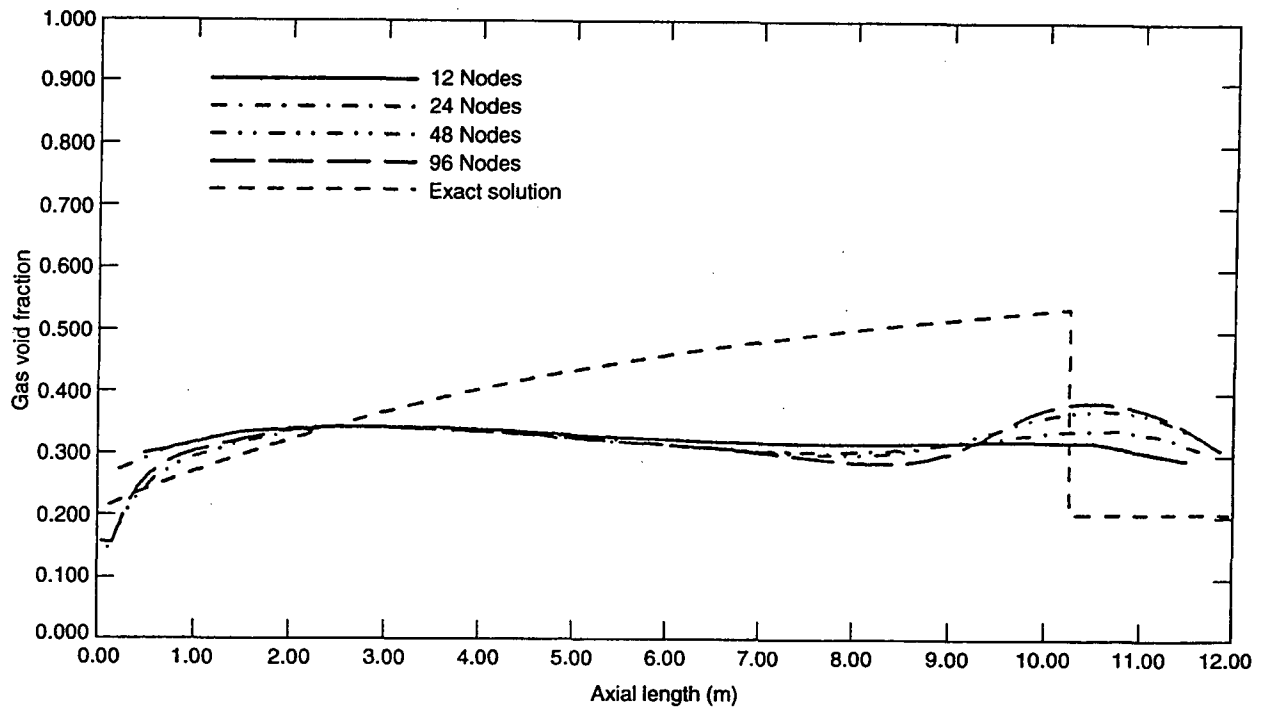


Figure 5-15. FAUCET, ANNULUS MODEL, TIME = 0.75 s.

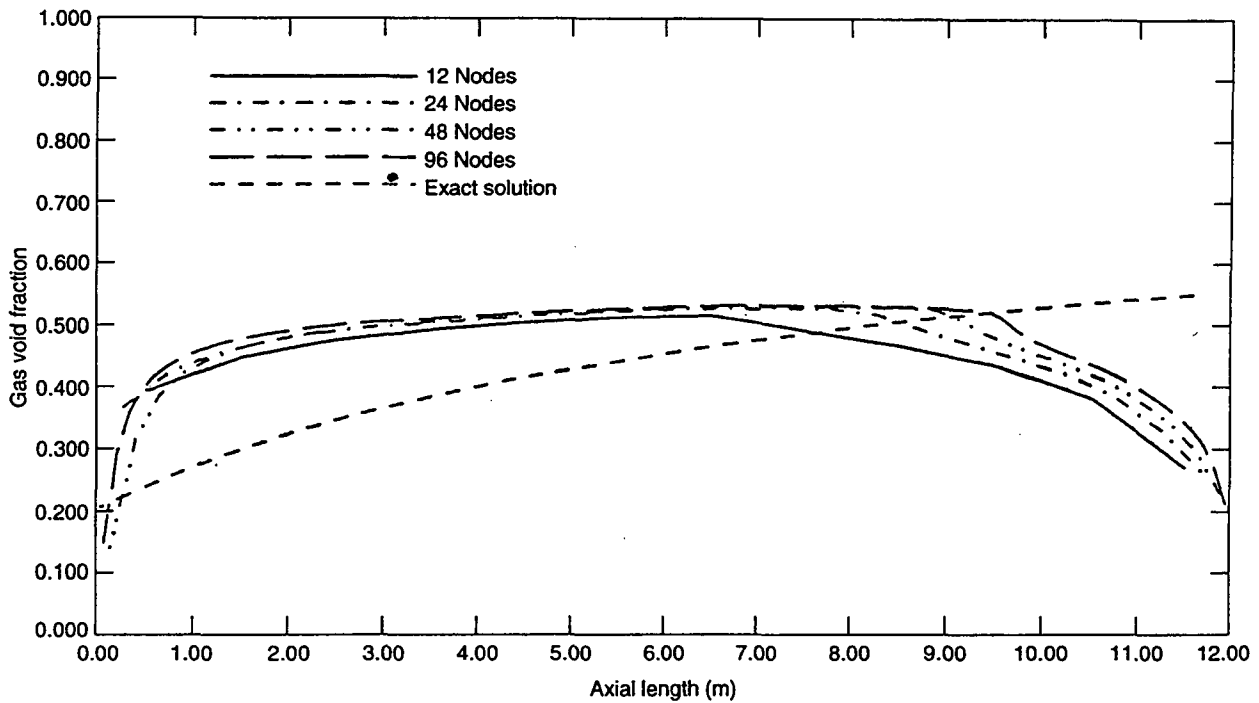


Figure 5-16. FAUCET, ANNULUS MODEL, TIME = 2 s.

5.3 The Edward's Pipe Problem

To study the physical convergence and accuracy of the RELAP5/MOD3 scheme, the Edward's pipe problem was analyzed. In contrast to the water faucet problem, the complete set of constitutive relations are used, and a wide variety of physical phenomena occurring during the transient-like phase appearance, phase change, stratification, choking and interphase momentum and energy transfer come into play. In addition, the problem has a simple geometry, which allows wide variation of nodalization, which is required for our study.

Following the procedure used in the previous study on RELAP5/MOD2 (Ransom and Mousseau 1991), the number of nodes was successively doubled from 10 to 160. This resulted in a node length variation of 0.4096 to 0.0256 m, which corresponds to 5.39 to 0.337 times the pipe diameter.

For the nodalization and the time-step study, the following four variables were recorded:

1. Pressure at Gauge Station 5 against time
2. Void fraction at Gauge Station 5 against time
3. Void fraction distribution across the pipe at 0.5 s
4. Total mass in pipe at 0.5 s.

The results from this base case nodalization study is shown in Figures 5-17 through 5-18. The pressure at Gauge Station 5 versus time plot shows some distinct differences from that computed for MOD2 by Ransom and Mousseau (1991). First, the initial phase of the transient is more accurately and consistently predicted by MOD3. The pressure of the rarefaction wave is predicted much lower in MOD3, and the curve traced out seems to be independent of the nodalization. Also, the oscillations seen in the 80-node case around 0.2 s in MOD2 shown by Ransom and Mousseau does not occur for the 80- or the 160-node case in the MOD3 runs. However, the generally higher pressure (and, hence, closer to the experimental value) prediction in the initial part of the transient continues further, resulting in slightly overpredicting the values in the second half of the transient. One improvement over MOD2 is that the scatter or linear increase with node density observed in MOD2 seems to have been reduced to a smaller range. This feature is also evident from the void fraction at Gauge Station 5, Figure 5-18. Here, all the curves can be made to lie within a narrow bandwidth. This implies that unlike MOD2, MOD3 is able to give results that are not very different from that obtained by fine nodalizations even with rather coarse nodalizations. The plot of the liquid remaining in the pipe at 0.5 s is shown in Figure 5-19. In comparison to MOD2 results (Ransom and Mousseau 1991) this shows higher holdup at the closed end of the pipe, but an additional difference is that the curves cross each other at about 0.5 m and are in reverse order thereon until the end of the pipe. Also, from Figure 5-20 it can be seen that the total mass predicted in the pipe remains almost constant with change in nodalization density. However, it is clear that the mass distribution regions of low velocity (closed end) depends on nodalization even though the absolute magnitude of the variations is small. This could be the result of a nonlinear effect of interface drag on the solution for varying nodalization.

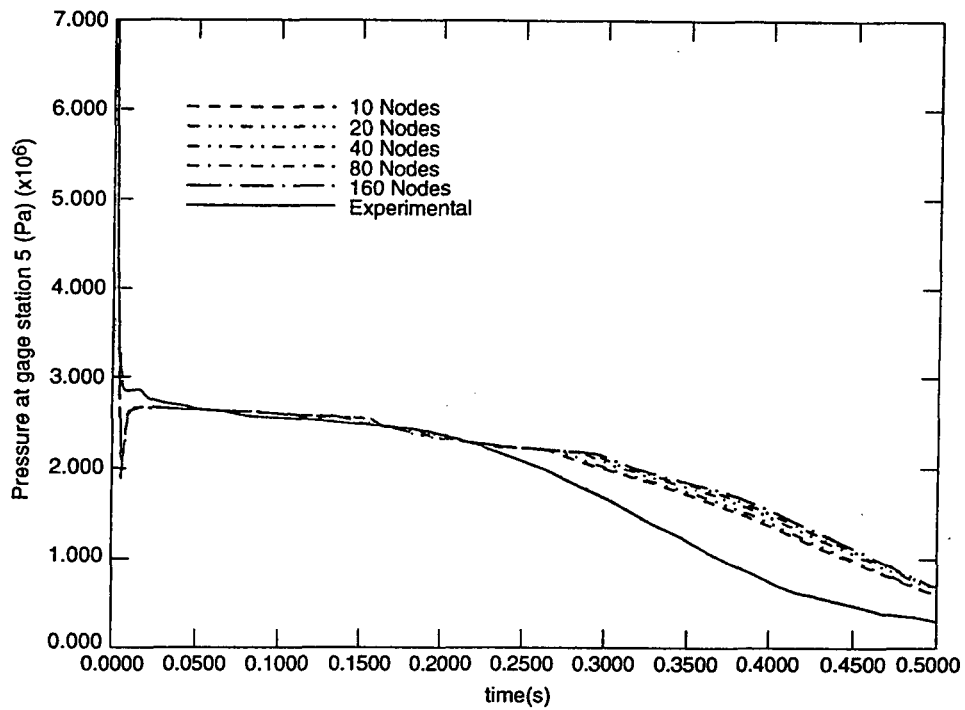


Figure 5-17. EDWARDS, spatial convergence, pressure versus time.

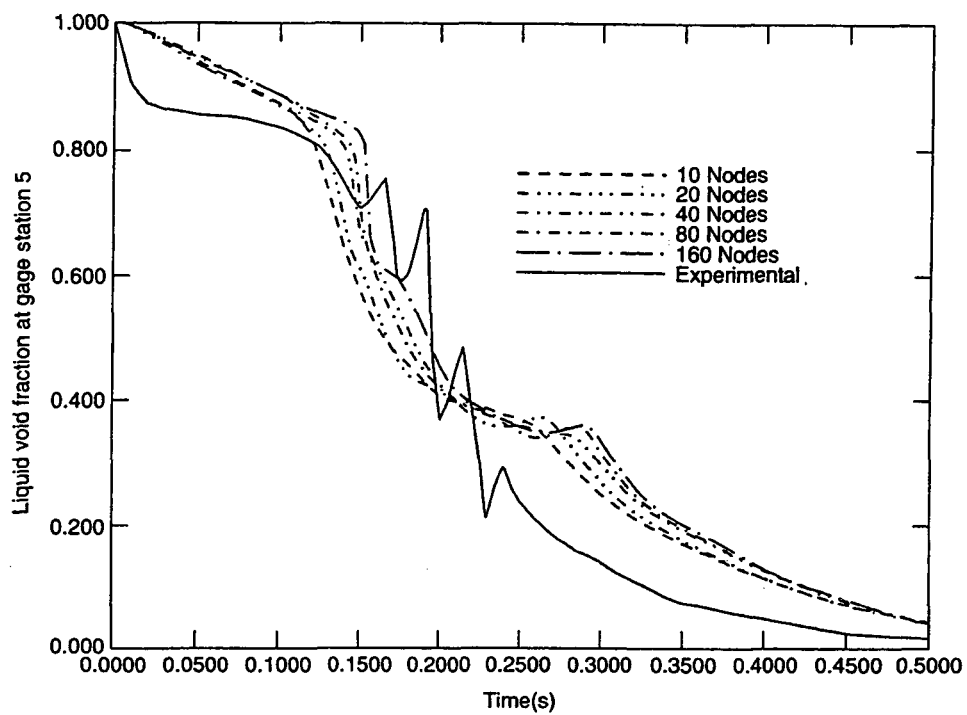


Figure 5-18. EDWARDS, spatial convergence, liquid void versus time.

Comparison

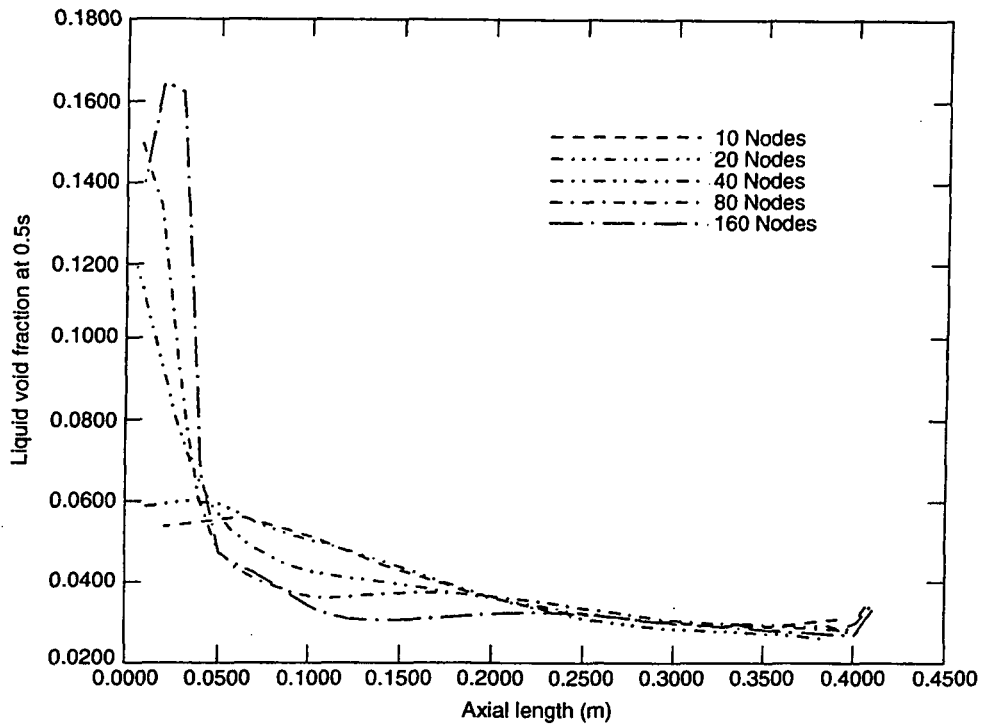


Figure 5-19. EDWARDS, spatial convergence, liquid void versus length.

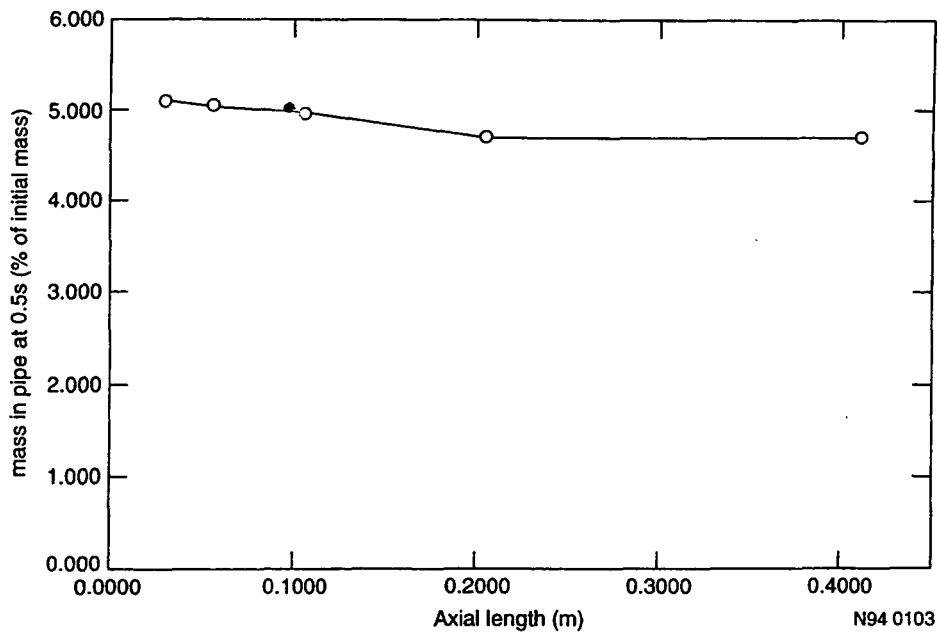


Figure 5-20. EDWARDS, spatial convergence, mass versus length.

This study was followed by a temporal discretization study in which the base case run with 20 nodes in the pipe (Courant number = 1) is compared with the runs with successively halved time steps. We, thus, get a time-step range from 0.015 to 9.375e-5 s. The results from these runs are plotted in Figures 5-21 to 5-24. The pressure and the void fraction transients reflect the expected inability of the computational scheme to capture strong gradients as effectively as the $N_c=1$ case. This probably causes a delay in nucleation and, hence, mass transfer, resulting in higher holdup of liquid at the closed end of the pipe predicted for all smaller time-step runs, as seen in Figure 5-23. The mass in the pipe shows steady convergence for all nodes, unlike the behavior observed for 160 nodes with MOD2 (Ransom and Mousseau 1991).

A number of additional cases were run to test the different models and options available in MOD3. These are summarized below.

MOD3 provides an option (Option 17) to use the MOD2.5 smoothing process mentioned in Section 3.3.1. The MOD2.5 procedure has a node size dependency in calculating the quantity τ_c . The aim of this study was to analyze the sensitivity of the smoothing process with respect to Δx . To accomplish this, the following two tests were run:

1. Spatial discretization with 20 and 80 nodes, using the original MOD2.5 smoothing procedure (Courant number = 1)
2. Spatial discretization with 20 and 80 nodes, using MOD2.5 smoothing, but after replacing Δx by 1.0 m in the code.

Further temporal sensitivity was tested after replacing Δx by 1.0 m. The 20- and 80-node cases were run for different time-steps, the results are shown in plots in Figures 5-25 to 5-35. Using the MOD2.5 time smoothing without any changes in the code does not affect the pressure and void fraction transient significantly (Figure 5-25 and 5-26).

But the spatial void distribution at 0.5 s shows an abnormal behavior, with increased holdup in the middle of the pipe for both the 20- and 80-node cases (Figure 5-27). If the nodalization dependent term is removed from the scheme (by replacing Δx by 1.0), this bulge in the middle of the pipe seems to disappear, but the overall solution shows no particular improvement over the MOD3 base case calculations. The time step studies on the 20- and 80-node cases show no strong effect on pressure or void fraction variation with respect to time compared to the base case runs (Figures 5-28, 5-29, 5-32, and 5-33). But, again, the void in the pipe after blowdown shows wide variations for different time-steps (see Figures 5-30 and 5-34), especially at the closed end of the pipe. This suggests that the time smoothing scheme used in MOD2.5 is time-step sensitive. It is shown in Section 5.6 that this problem is only present if Equation (3-58) is used instead of (3-57). We, therefore, recommend that Equation (3-57) should be used if MOD2.5 time smoothing is used.

5.4 Christensen Subcooled Boiling Test 15

The interphase mass transfer and wall heat flux partitioning model were assessed using the data from a separate-effects, subcooled nucleate boiling experiment conducted by Christensen (1961).

Comparison

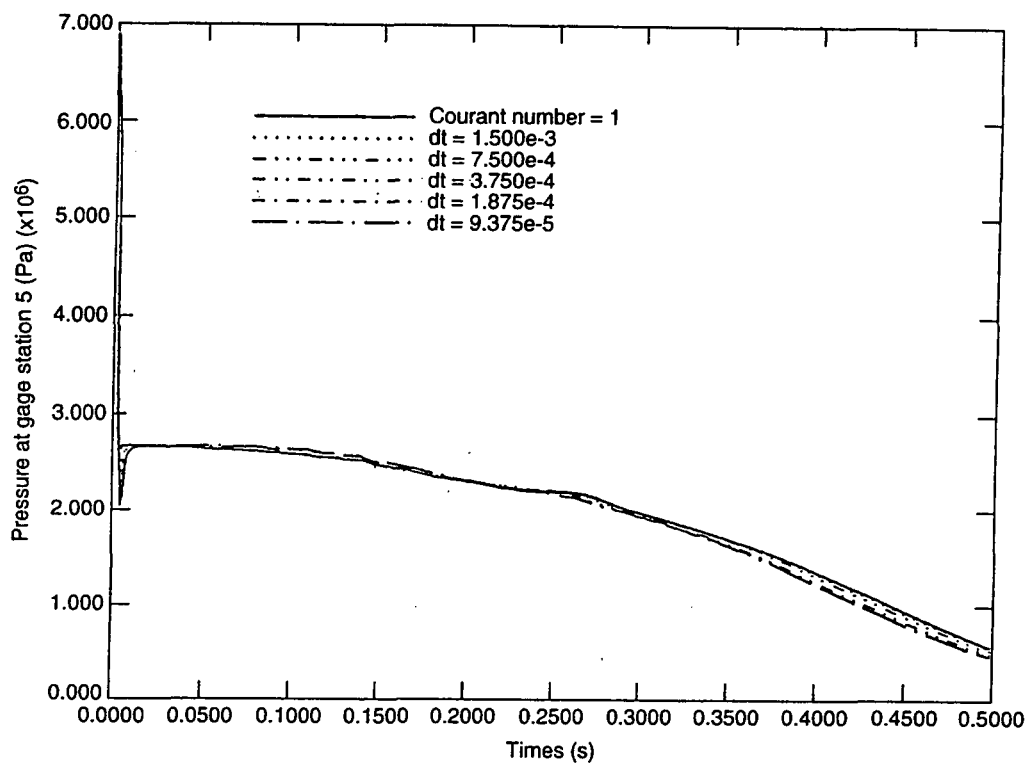


Figure 5-21. EDWARDS, temporal convergence, pressure versus time.

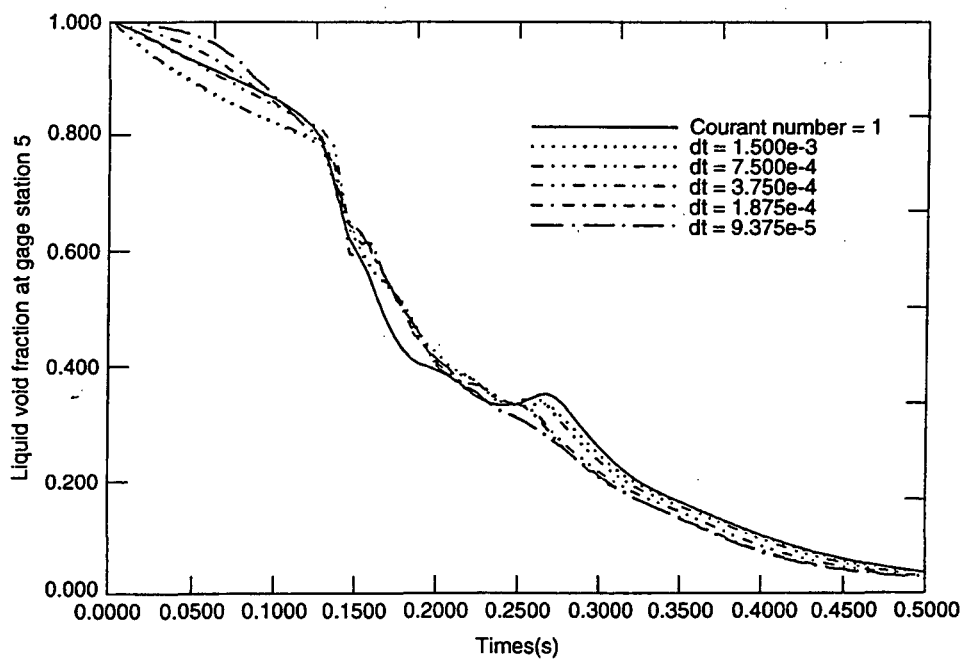


Figure 5-22. EDWARDS, temporal convergence, liquid void versus time.

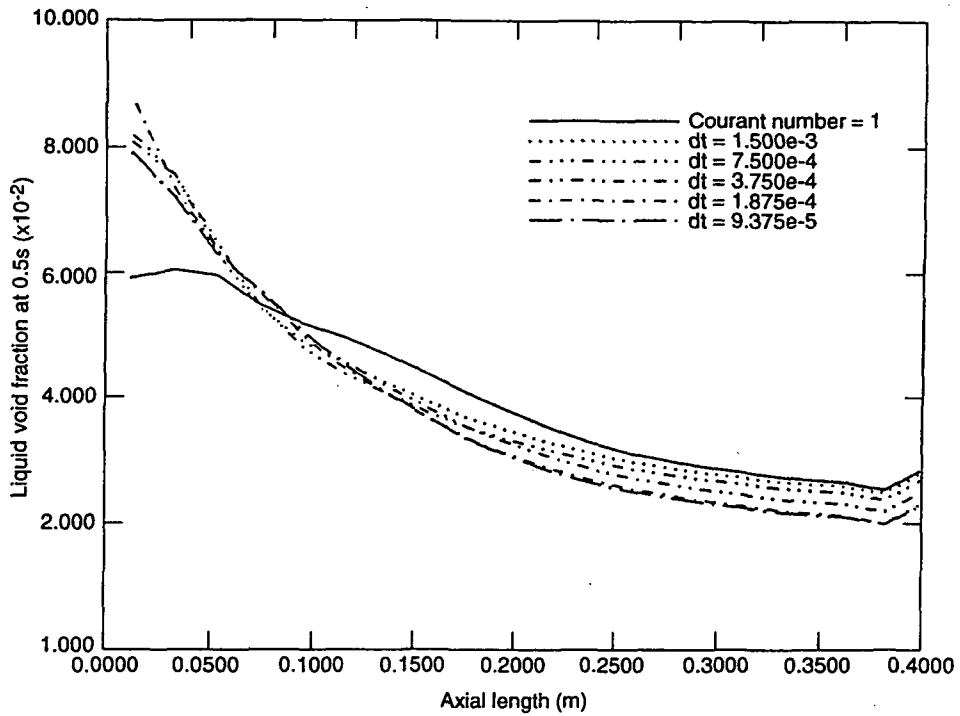


Figure 5-23. EDWARDS, temporal convergence, liquid void versus length.

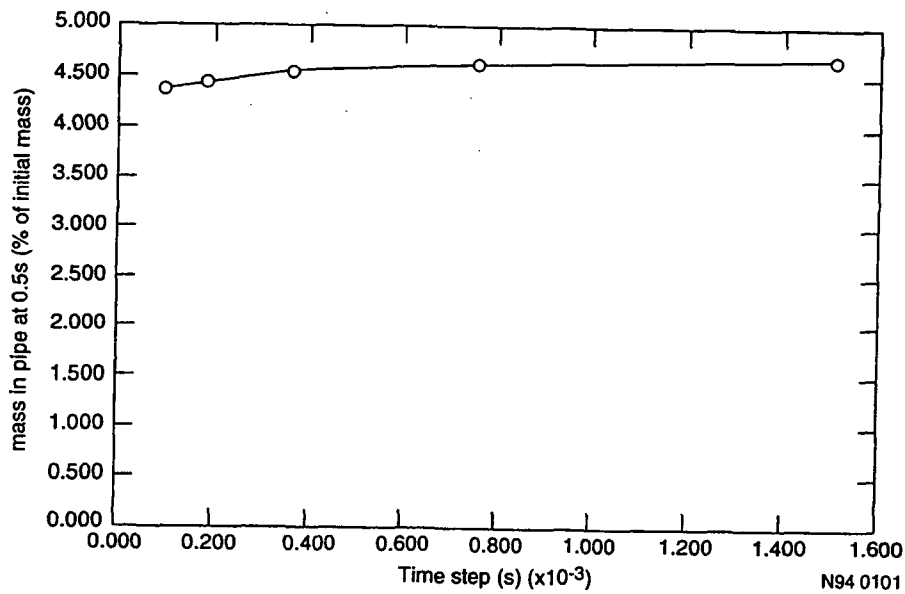


Figure 5-24. EDWARDS, temporal convergence, mass versus time step.

Comparison

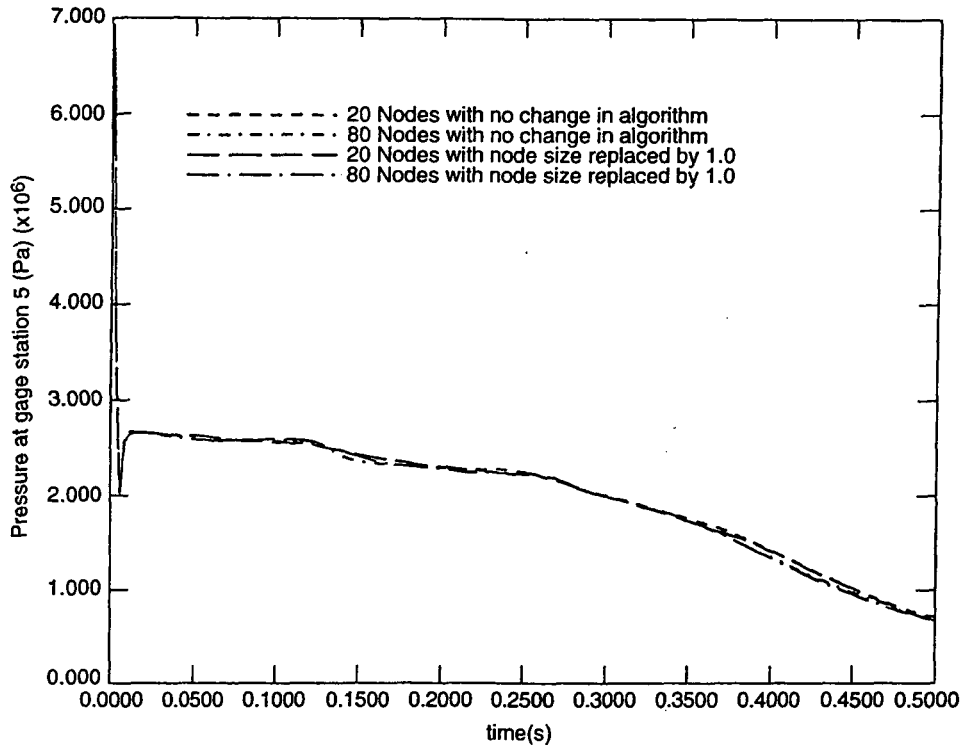


Figure 5-25. EDWARDS, spatial convergence (option 17), pressure versus time.

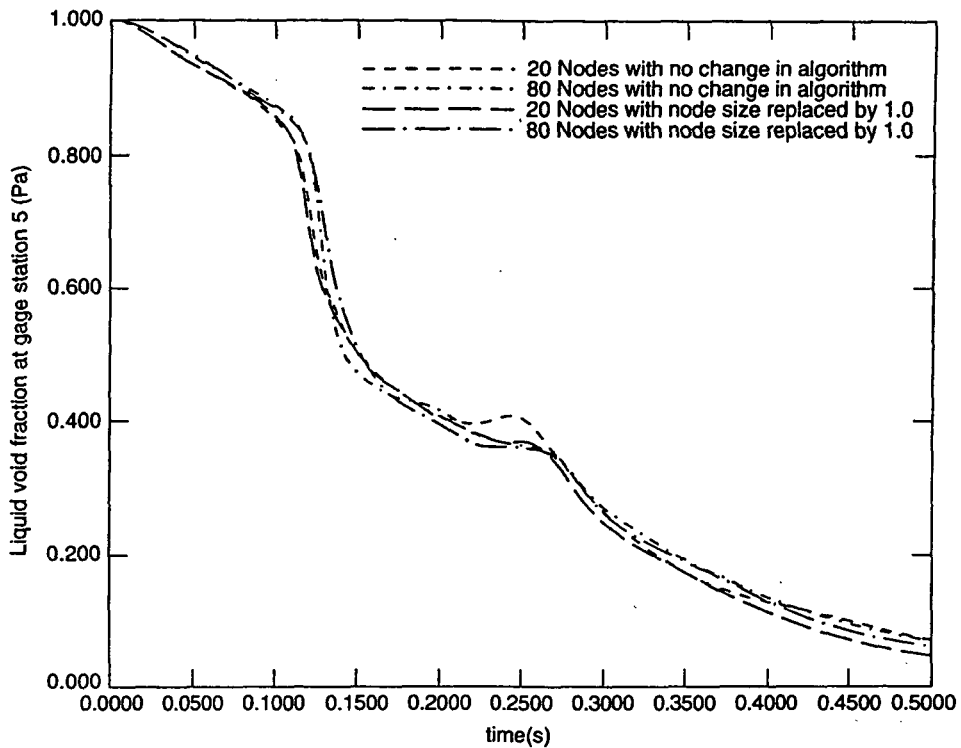


Figure 5-26. EDWARDS, spatial convergence (option 17), liquid void versus time.

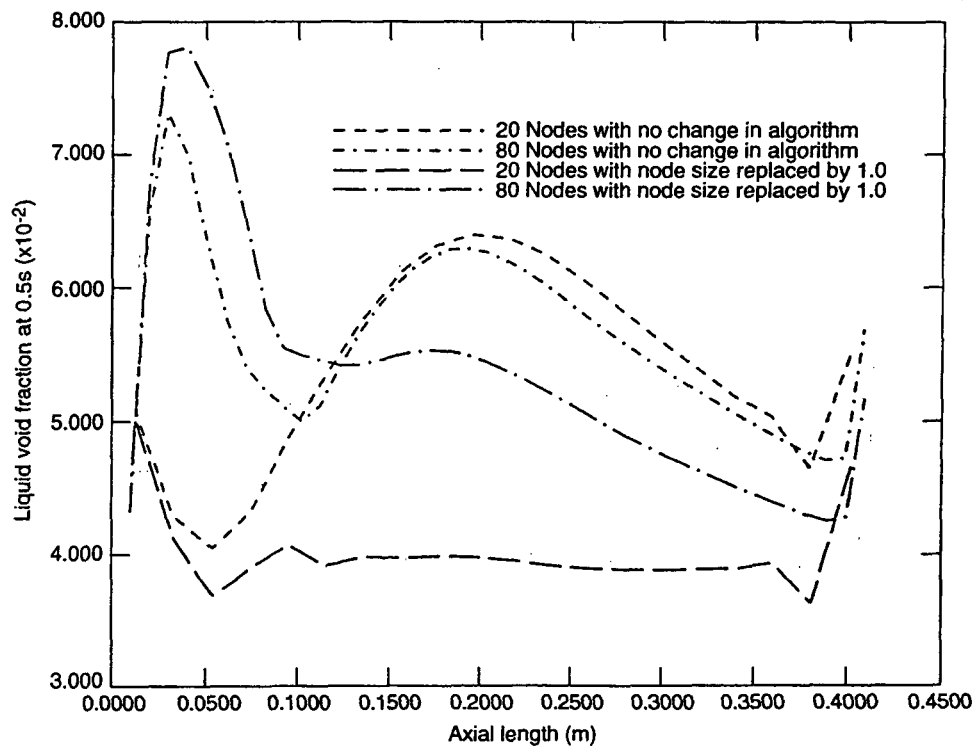


Figure 5-27. EDWARDS, spatial convergence (option 17), liquid void versus length.

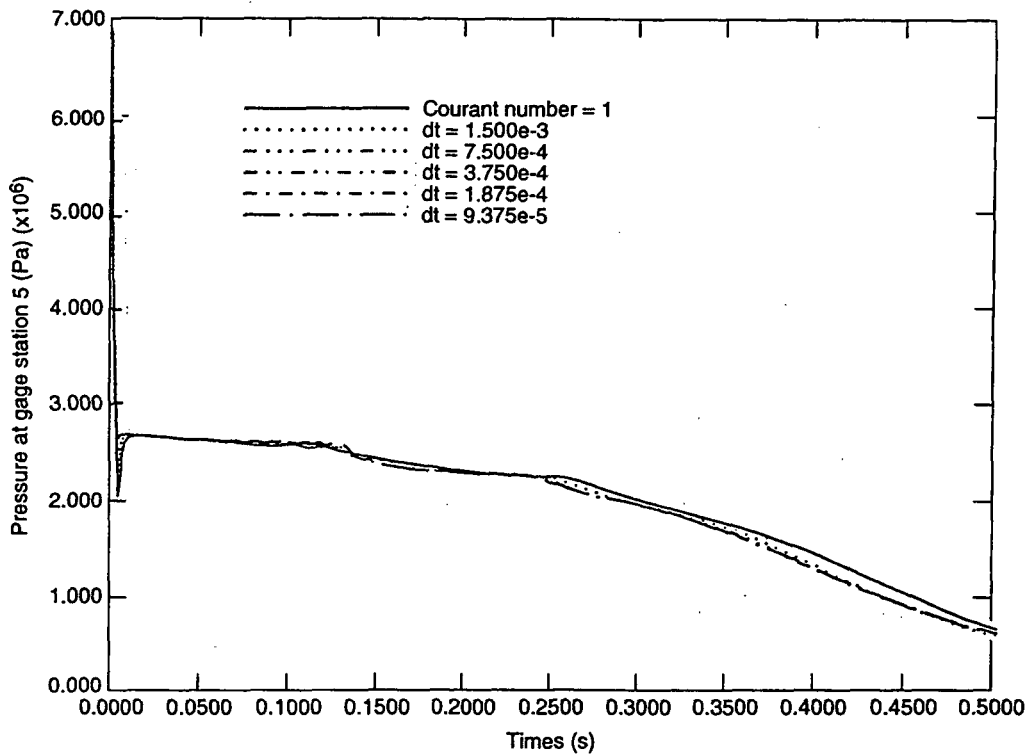


Figure 5-28. EDWARDS, temporal convergence (option 17, 20 nodes), pressure versus time.

Comparison

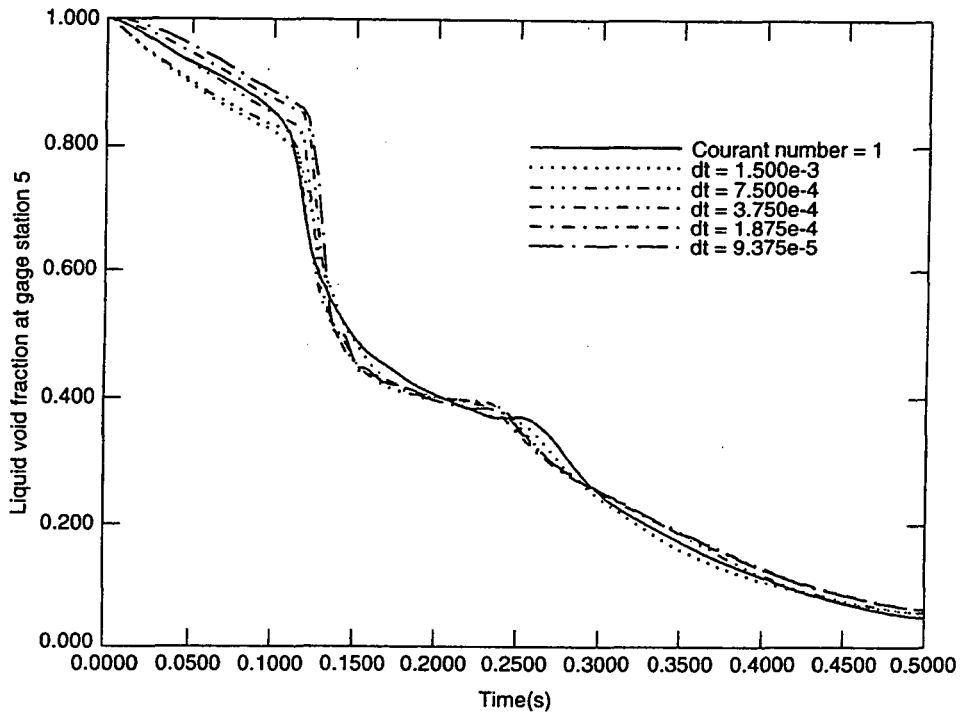


Figure 5-29. EDWARDS, temporal convergence (option 17, 20 nodes), liquid void versus time.

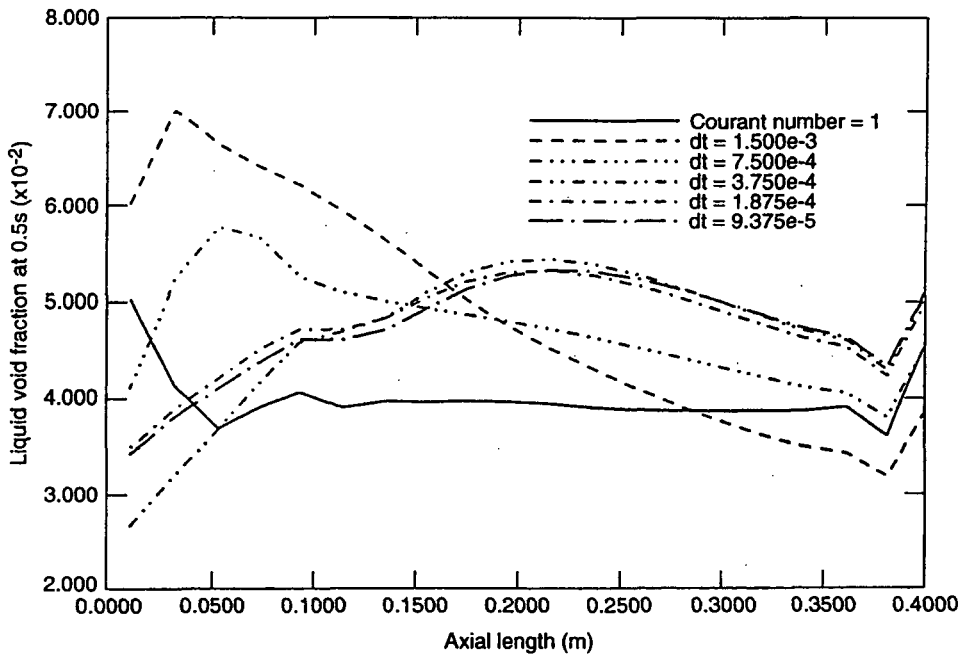


Figure 5-30. EDWARDS, temporal convergence (option 17, 20 nodes), liquid void versus length.

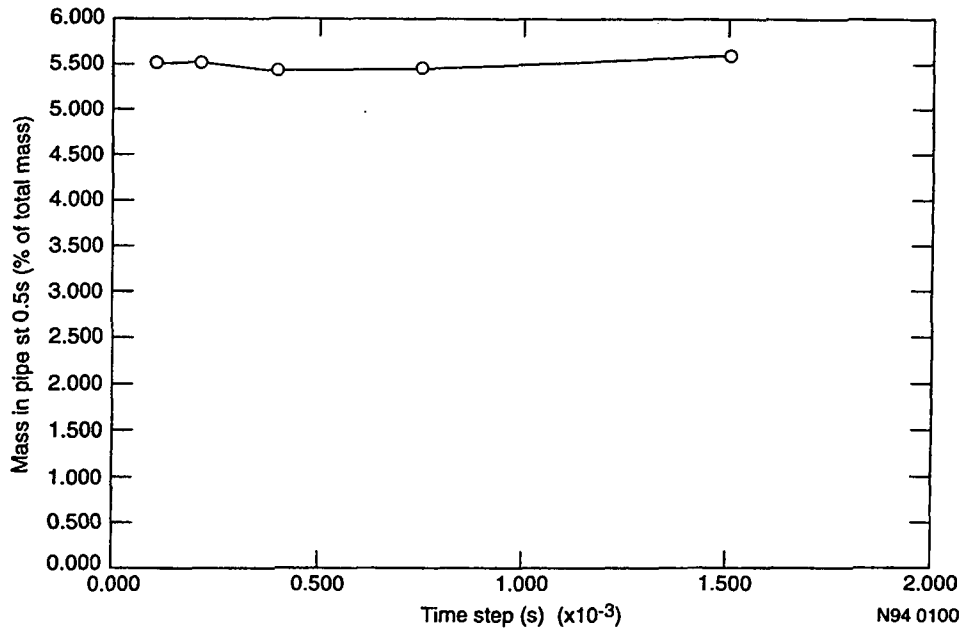


Figure 5-31. EDWARDS, temporal convergence (option 17, 20 nodes), mass versus time step.

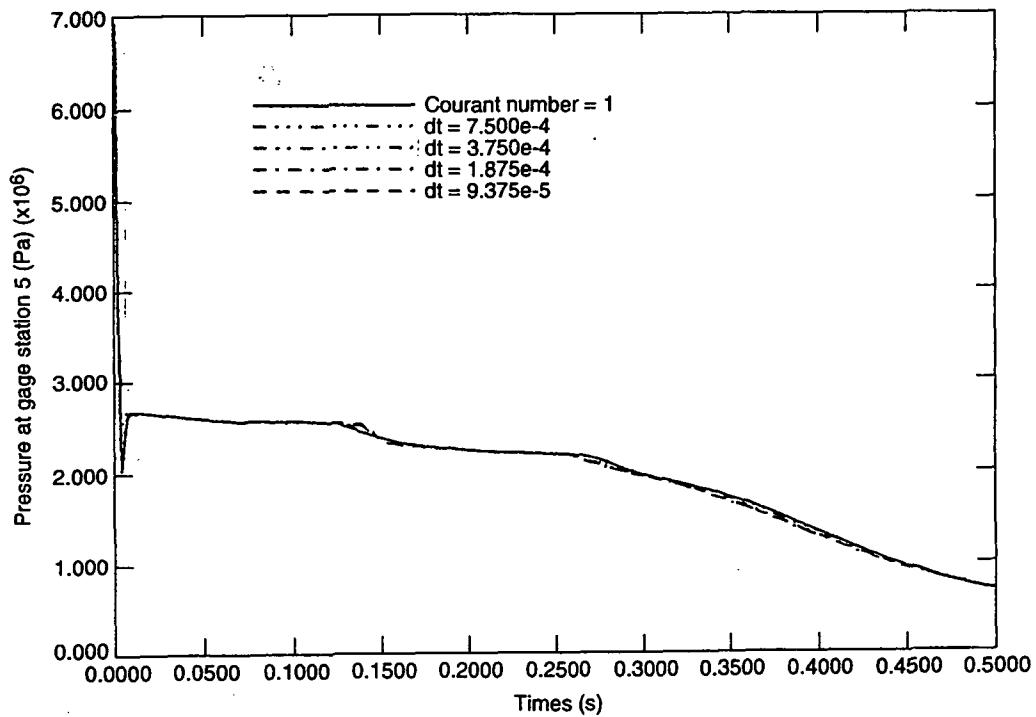


Figure 5-32. EDWARDS, temporal convergence (option 17, 80 nodes), pressure versus time.

Comparison

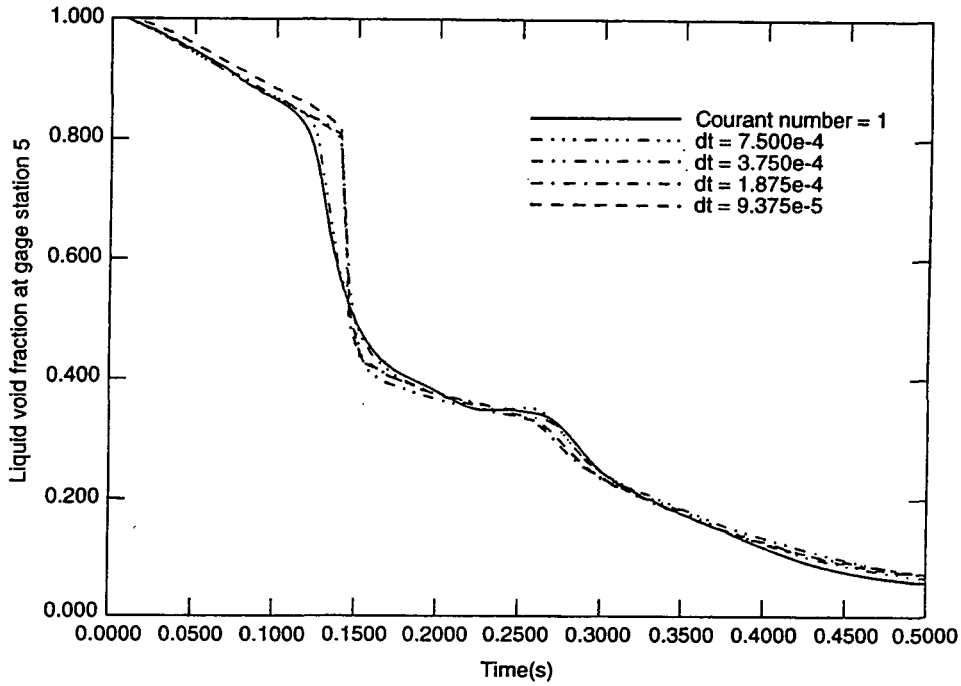


Figure 5-33. EDWARDS, temporal convergence (option 17, 80 nodes), liquid void versus time.

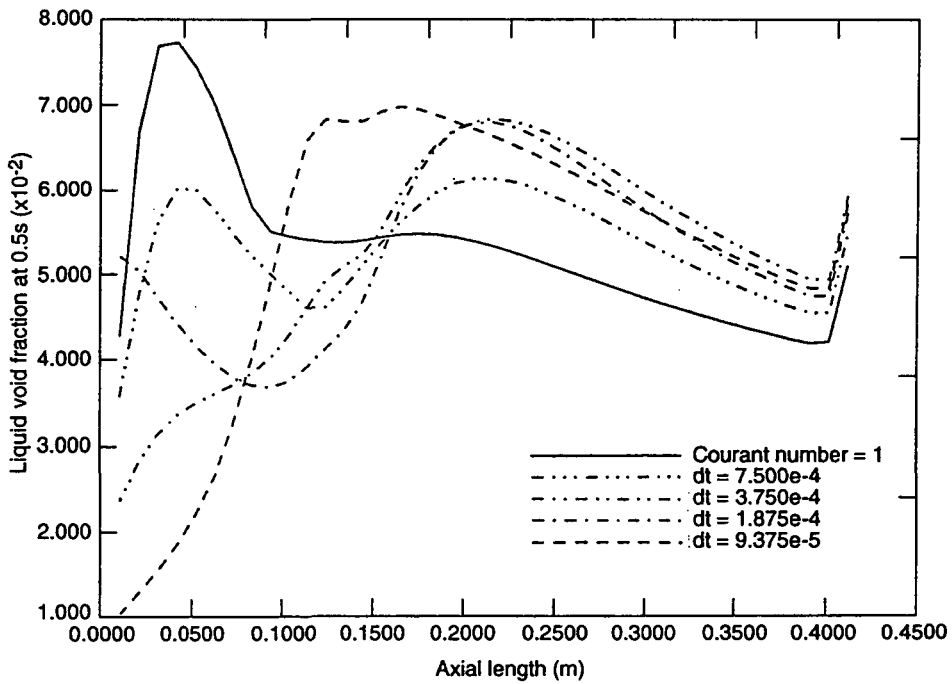


Figure 5-34. EDWARDS, temporal convergence (option 17, 80 nodes), liquid void versus length.

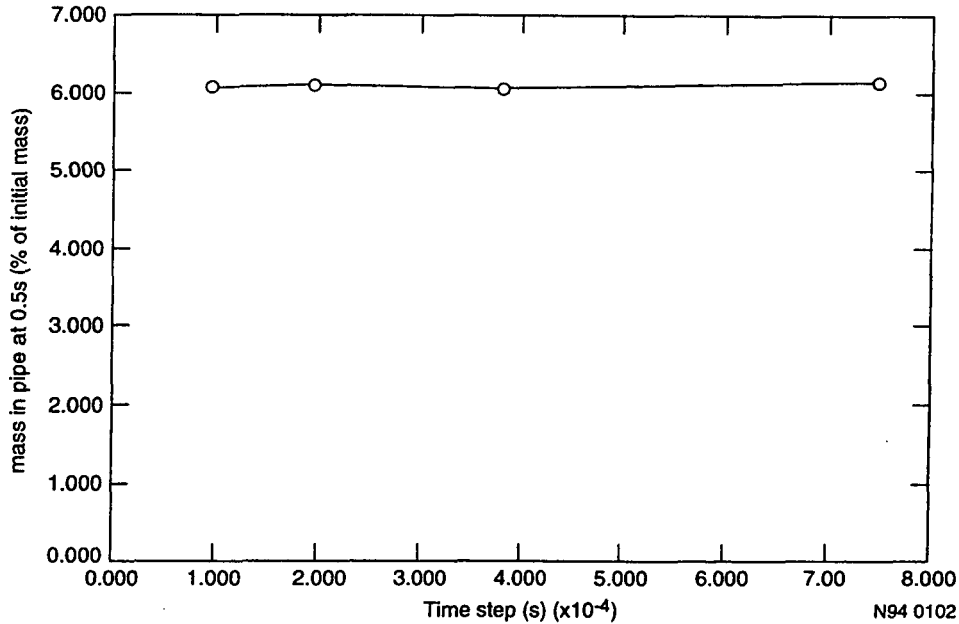


Figure 5-35. EDWARDS, temporal convergence (option 17, 80 nodes), mass versus time step.

The models assessed are the Chen (1966) correlation for subcooled nucleate boiling and the Unal (1976) correlation for the interphase mass transfer for bubbly subcooled liquid. The test section was a rectangular tube with 1.11×4.44 -cm cross section and 127-cm height. The tube was heated by passing an ac current through the tube walls. The void fraction along the test tube was measured by a gamma densitometer.

The test section was first simulated by RELAP5 as 20 volumes—two time-dependent volumes, 19 junctions, two time-dependent junctions, and 20 heat slabs simulating heat generated at the walls. The test conditions given in Table 5-1 were input to the code.

The number of volumes was then successively doubled from 20 to 160. This resulted in a node length variation of 0.0635 to 0.0079375 m. The initial conditions (pressure, temperatures, voids, velocities) were the same for all volumes in the test section. Time-step studies were done for both the 20- and 80-volume cases where the time-steps were successively halved to 1/16 of the Courant time step.

Comparisons of computed axial void fractions by RELAP5/MOD3 with measured data from Christensen test 15 are shown in Figure 5-17. The subcooled boiling model is assessed in this test because the water was subcooled over the complete length of the test section.

The comparisons given in Figure 5-17 did demonstrate that the agreement of computed results with experimental data is better with finer nodalization, and that there is apparent spatial convergence of the numerical solutions to a smooth function. The calculated rate of flashing,

Comparison

Table 5-1. RELAP5/MOD3 Nonequilibrium Model Development Assessment Matrix.

Data source and test conditions	Primary feature assessed
Christensen Test 15 Pressure = 5.12 MPA Heat Flux = 0.65 MW/m ² Mass Flux = 907.3 kg/s · m ² Inlet Subcooling = 12.5 K	Subcooled nucleate boiling
ORNL Test 3.09.10i Pressure = 4.50 MPa Heat Flux = 0.38 MW/m ² Mass Flux = 29.76 kg/s-m ² Subcooling = 57.58 K	Axial void profile

however, was too large compared to the condensation rate at the inlet. Figures 5-18 and 5-19 demonstrate that the calculations are time-step insensitive and that the same steady-state results are obtained regardless of the time step taken.

5.5 Oak Ridge National Laboratory Void Profile Test

The Oak Ridge National Laboratory (ORNL) void profile test was similar to the Bennet heated tube experiments, the Royal Institute of Technology Tube Test 261, and the ORNL bundle CHF tests. In all these tests, pressurized water flowed upward in the test sections. The main objective of the tests (except the ORNL void profile test) was to measure the dryout location (or CHF location) where liquid ceased to adhere to the inside wall and the surface temperature profiles in the region beyond the dryout point.

All of the above tests were simulated by RELAP5/MOD3 and the results reported (Allison et al. 1990). The RELAP5/MOD3 calculated wall temperature and CHF are in good agreement with the data for the Bennet heated tube experiments. For the Royal Institute of Technology Tube Test 261, the measured CHF position was 4.65 m, compared to a MOD2 prediction of 6.3 m using the Biasi CHF correlation. RELAP5/MOD3 uses the AECL-UO correlation and predicts a location of 5.2 m. MOD3 also underpredicts the peak wall temperature.

The ORNL bundle CHF tests and void profile tests were both performed with an 8 × 8, full-length, electrically heated rod bundle. The rod size was the same as the 17 × 17 bundles used in PWRs (0.0095 m). The tests were performed by adjusting the power until a steady-state dryout point had been established. In the ORNL CHF tests, it was found that the code did predict a CHF position closer to the inlet than the measured value, and that the peak wall temperature was higher than the data.

In the ORNL void profile tests, the axial void profile and the steam temperatures were reported, as well as the rod temperatures above the CHF point. The rod wall temperature at a particular elevation is the average over all the rod thermocouples at that elevation.

The ORNL void profile test was simulated by the code using 24 volumes, in a pipe format (including 23 junctions), two time-dependent volumes, one time-dependent junction, one single junction, and 24 heat slabs simulating heat generated at all the fuel rods in the bundle. The test conditions given in Table 5-1 were input to the code.

The number of volumes was then successively doubled from 24 to 192. This resulted in a node length variation of 0.15 m to 0.01875 m and $\Delta x/D$ of 1.6 to 0.2, where D is the hydraulic diameter of the volumes. The initial conditions (pressure, temperatures, voids, velocities) are not the same for each volume. Their variations, however, are, in general, quite smooth except for the liquid velocity in the grid spacer region where the liquid velocity vector changes direction and causes counter current flow in that region. These conditions were linearly interpolated as the node size was successively refined.

The computed rod wall temperatures, steam temperatures, and the void profile were compared with the experimental data in Figures 5-36 to Figure 5-38. There was a dip in the average measured value for the rod wall temperatures downstream of a grid spacer, as shown in Figure 5-39. MOD3 has no mechanism to increase the heat transfer coefficients downstream of grids, and the calculated rod temperatures show no dip.

The steam temperature in the experiment was calculated from an energy balance and the measured bundle exit steam temperature. The MOD3 values agree well with the reported data value (Figure 5-40).

The axial void fraction is perhaps the value that is most sensitive to any ill-posedness of the underlying problem. The experiment data were calculated from differential pressure measurements with a reported accuracy of $\pm 3\%$. The RELAP5/MOD3 calculation is generally above the data in the slug flow region, but is under the data in the post-CHF mist flow region, as shown in Figure 5-41. During the transition from slug flow to mist flow, the results calculated by RELAP5/MOD3 exhibit a void inversion problem. The calculated results actually show a decrease in void fraction with increased elevation in the transition region. While the computed results are generally more accurate in the slug flow region with finer nodalization, the opposite is true in the mist flow region. Moreover, in the mist flow region, oscillations started when the number of volumes was increased to 192 volumes.

Because the interfacial drag coefficients in the mist flow regime are, in general, one to two orders of magnitude smaller than that in the slug flow regime, the conjecture is that when the drag coefficients are too small, a small Δx may cause oscillations in the solutions. To test this conjecture, the test problems were rerun with restrictions to using pre-CHF drag and interfacial heat transfer coefficients only. This allows the code to have a smooth transition from slug flow to mist flow via the annular mist flow regime. The results are shown in Figure 5-42. In the legend, slug, ann, and mpr represent slug, annular mist, and pre-CHF mist flow regimes, respectively, for the 24-node case. The comparison between data and computed results show that both the void inversion problems and the oscillation problem disappear and that the computed results now come much closer to the data

Comparison

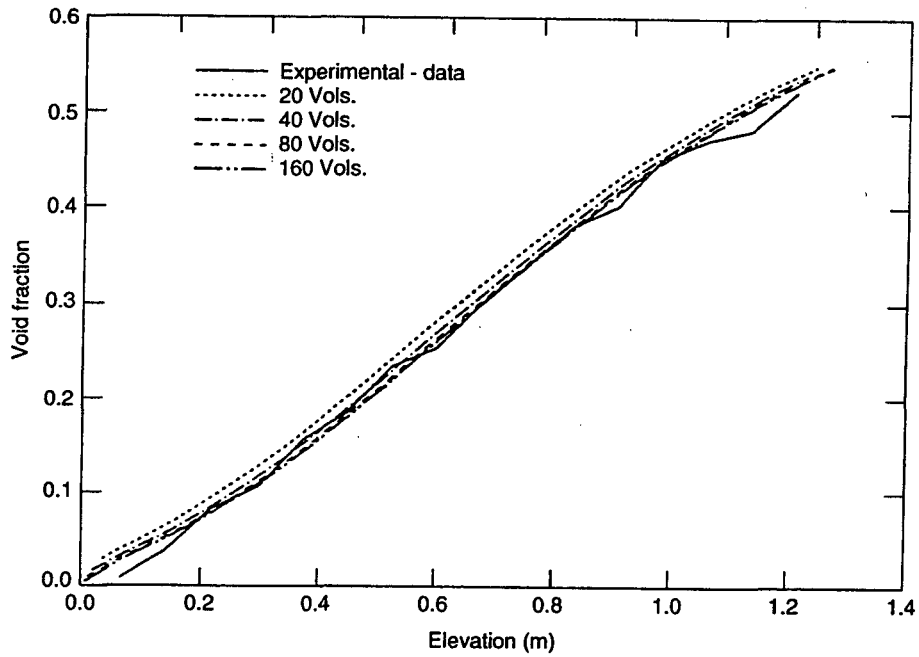


Figure 5-36. CHRISTENSEN, spatial convergence, void versus length.

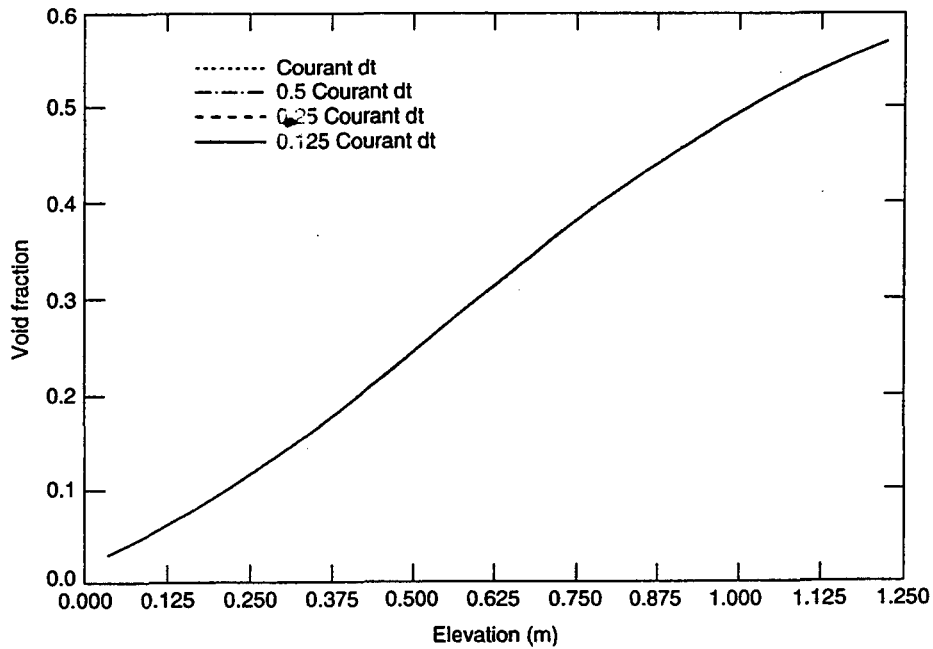


Figure 5-37. CHRISTENSEN, temporal convergence (20 nodes).

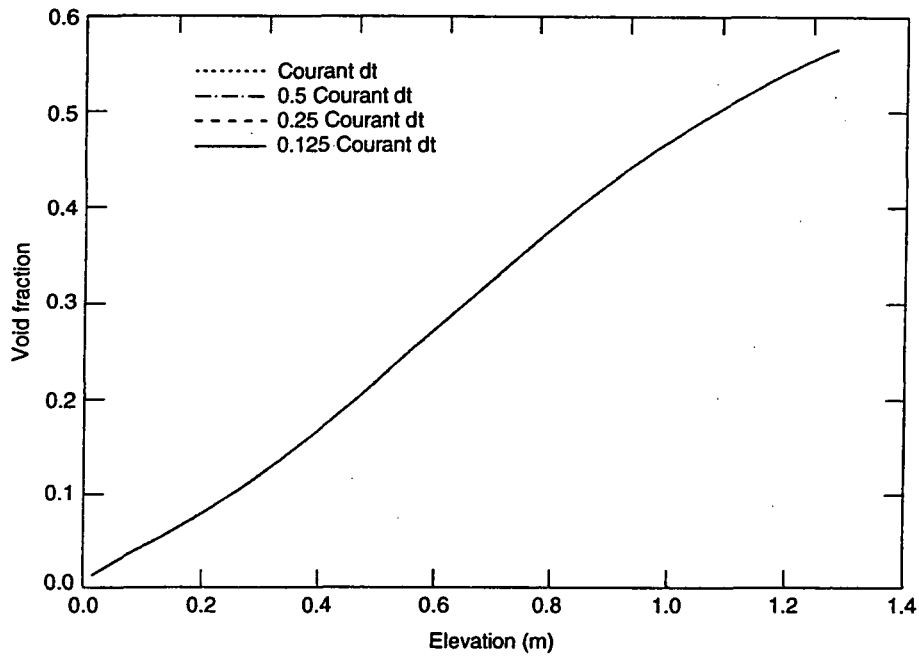


Figure 5-38. CHRISTENSEN, temporal convergence (80 nodes).

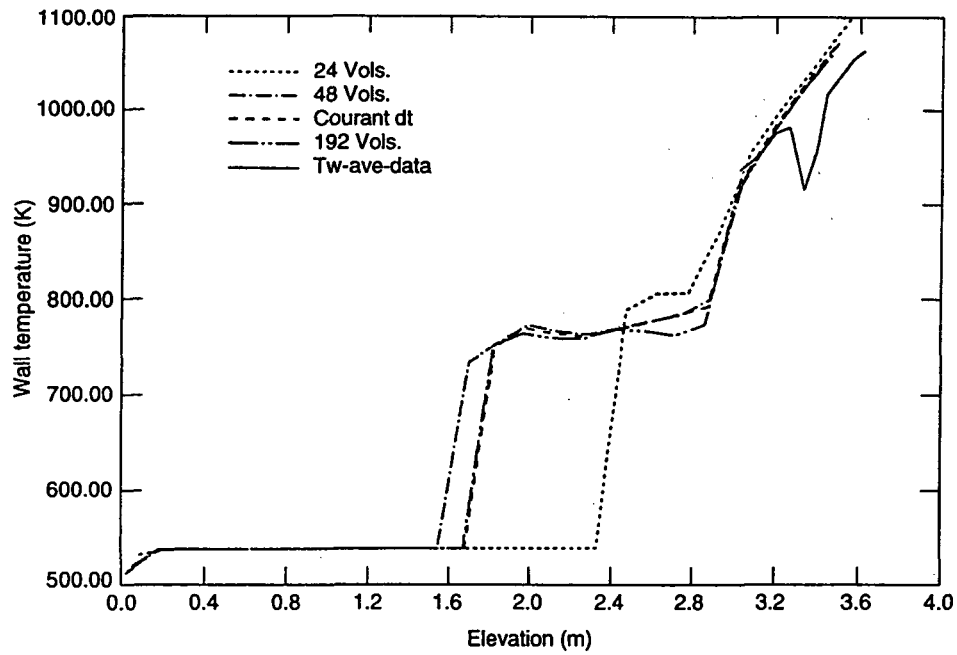


Figure 5-39. ORNL, spatial convergence, rod temperature versus length.

Comparison

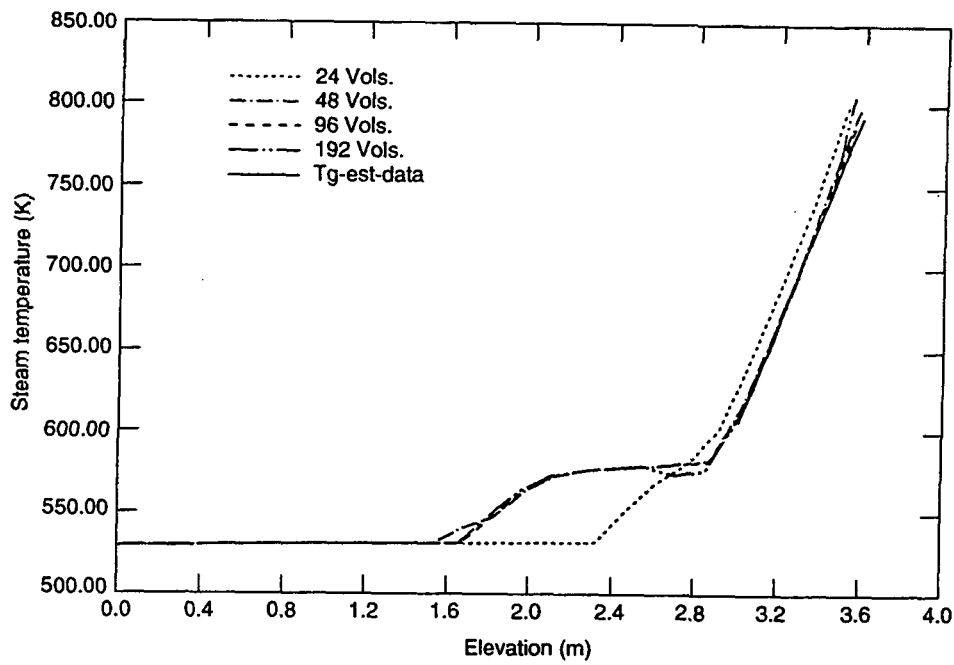


Figure 5-40. ORNL, spatial convergence, steam temperature versus length.

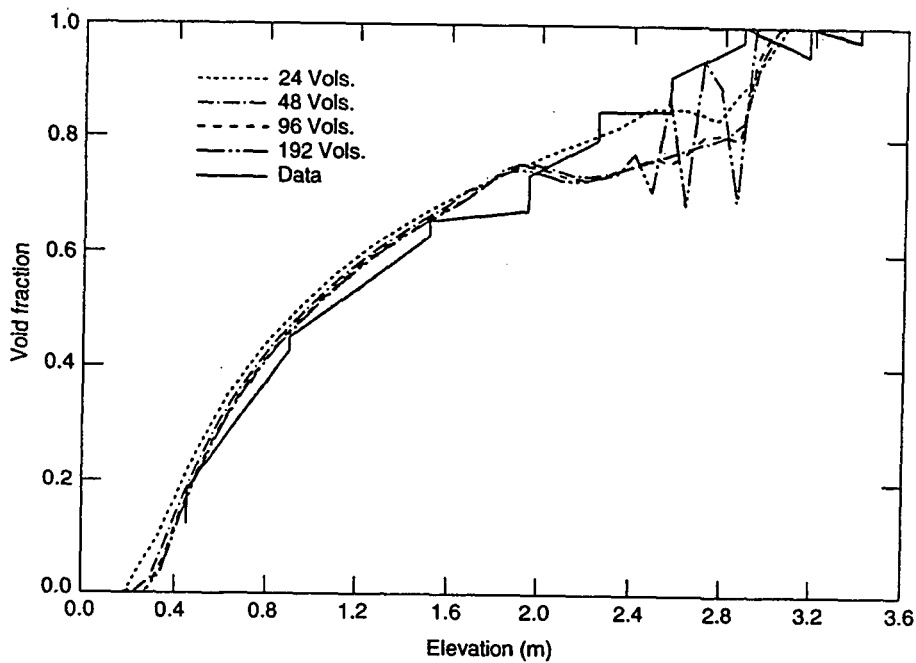


Figure 5-41. ORNL, spatial convergence, void versus length.

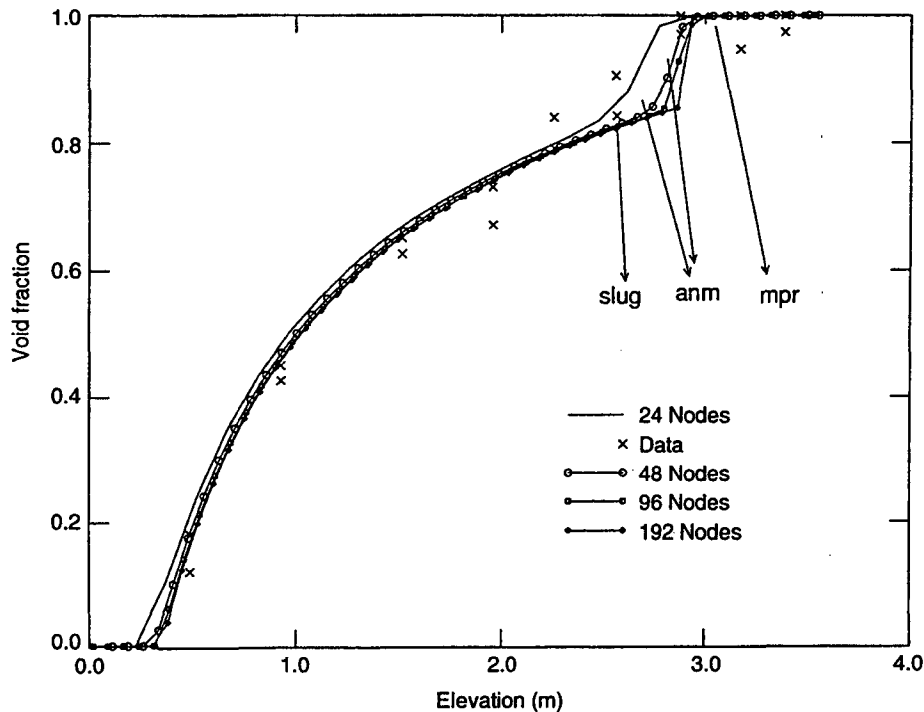


Figure 5-42. ORNL, spatial convergence, sensitivity study.

than before in the annular mist and mist flow regions. While this appears to demonstrate a strong relationship between stability, convergence, and accuracy, it also suggests that the code does not appear to model the transition from slug flow to postdryout mist flow in the best possible manner.

Time-step studies were done for both the 24- and 96-volume cases where the time-steps were successively halved to 1/16 of the Courant time-step. Figures 5-43 through 5-45 demonstrate the temporal convergence for these problems for the 24-node case. Figures 5-46 through 5-48 again show that at finer nodalization in the 96-node case, the solutions do not converge temporally. On the other hand, Figures 5-49 and 5-50 show that restrictions to using the pre-CHF drag and interfacial heat transfer correlations do give rise to temporal convergence for both the 24-node and the 96-node cases.

Recent calculations by the INEL author (private communication) show that there are much less oscillations in the void for the 192-volume case for version 80 than for 7v. Major edits in the computer output show that the drag coefficients in the post-CHF region for version 80 is on the average an order of magnitude larger than that for version 7v in this region. This provides further evidence that larger drag coefficients help to stabilize the calculations for the ORNL void profile problem.

5.6 Time Smoothing Studies

Mod2.5 time smoothing was shown to be time-step sensitive in Section 5.2. Additional numerical studies are, therefore, performed to show that this time-step sensitivity can be removed if

Comparison

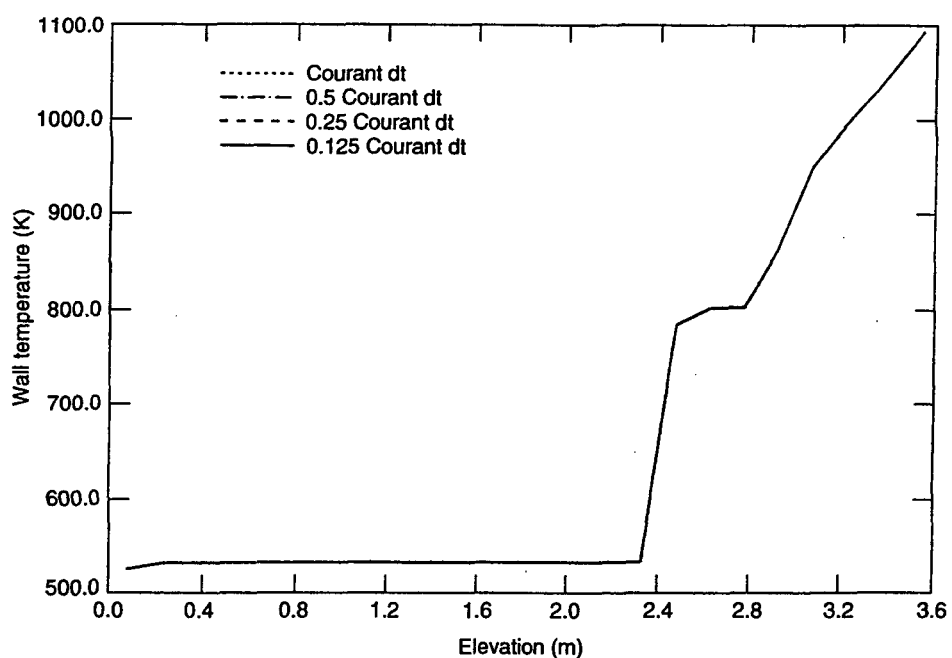


Figure 5-43. ORNL, temporal convergence (24 vols.), steam temperature versus length.

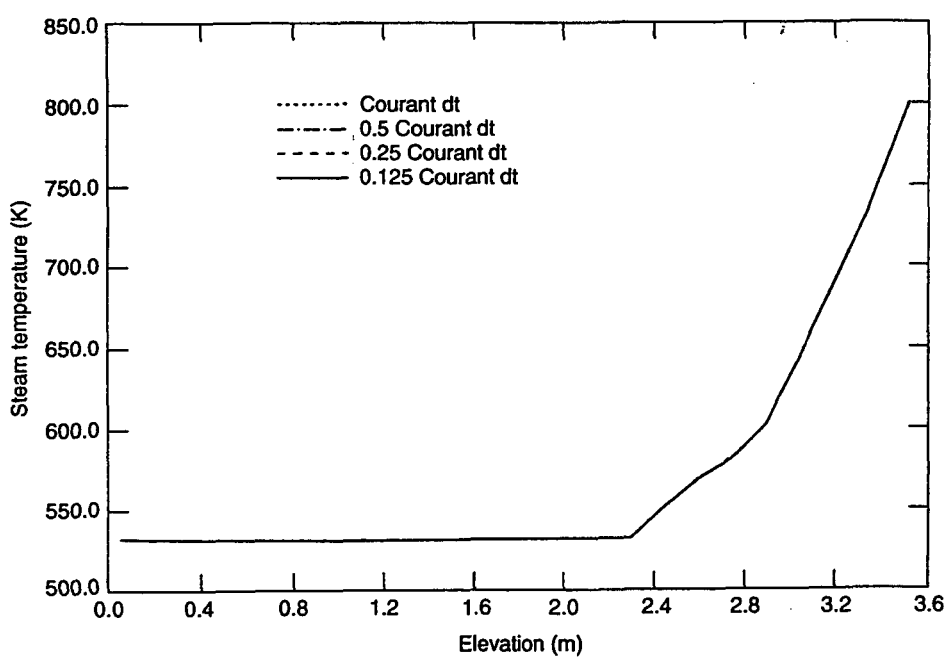


Figure 5-44. ORNL, temporal convergence (24 vols.), void versus length.

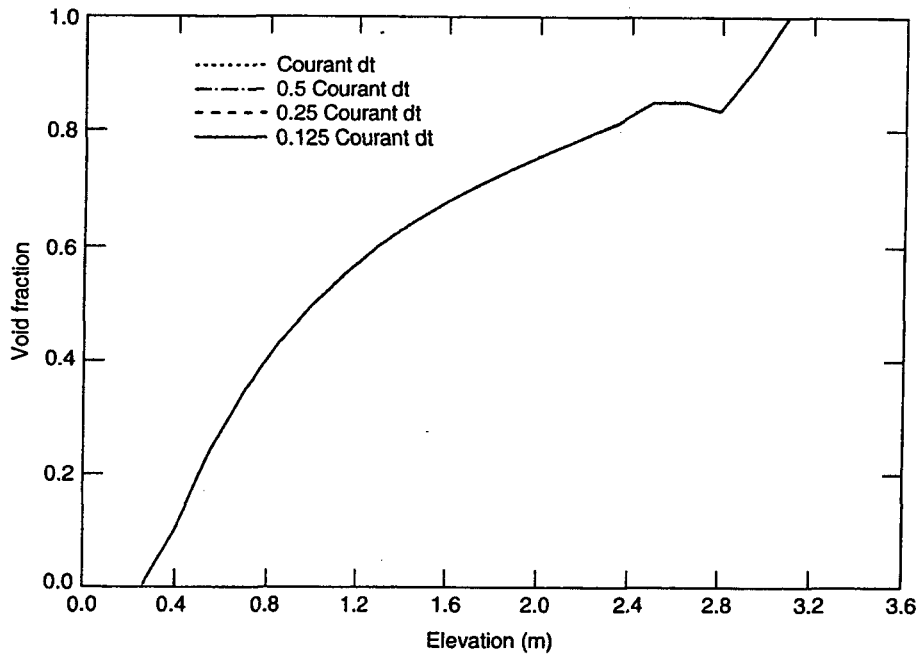


Figure 5-45. ORNL, temporal convergence (96 vols.), rod temperature versus length.

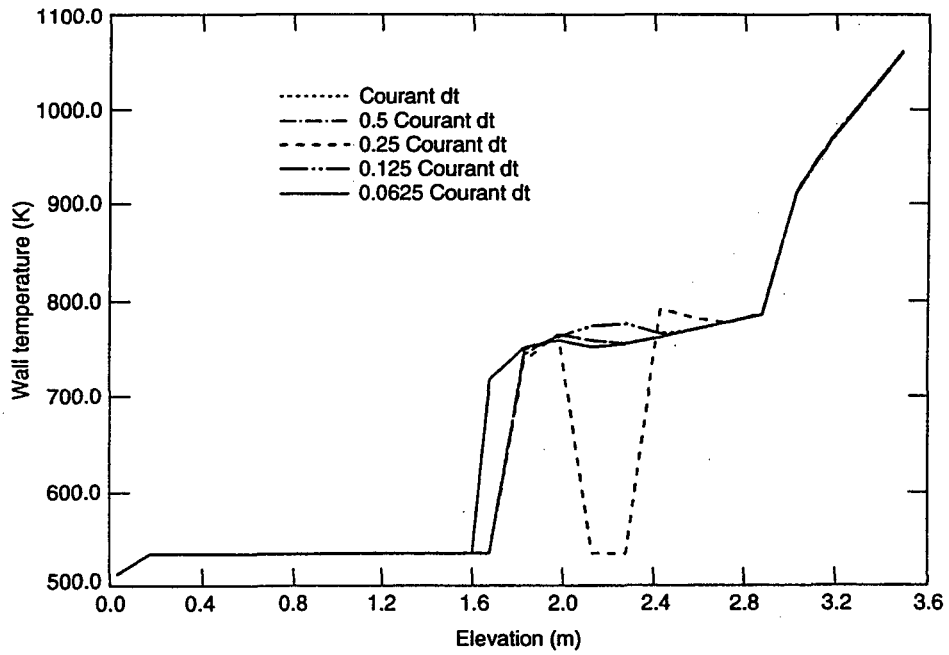


Figure 5-46. ORNL, temporal convergence (96 vols.), steam temperature versus length.

Comparison

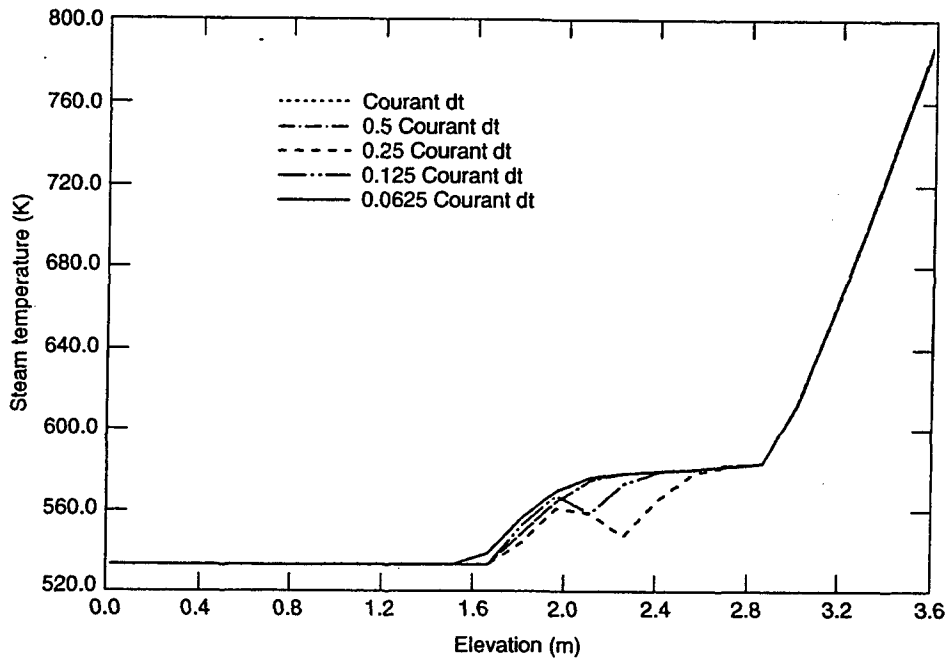


Figure 5-47. ORNL, temporal convergence (96 vols.), void versus length.

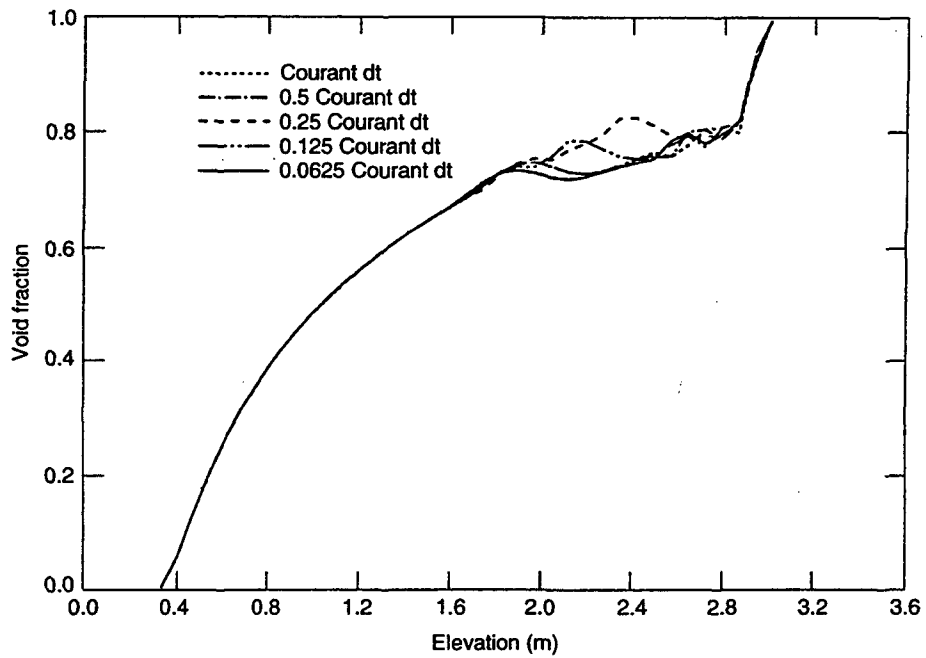


Figure 5-48. ORNL, temporal convergence (24 vols.), rod temperature versus length.

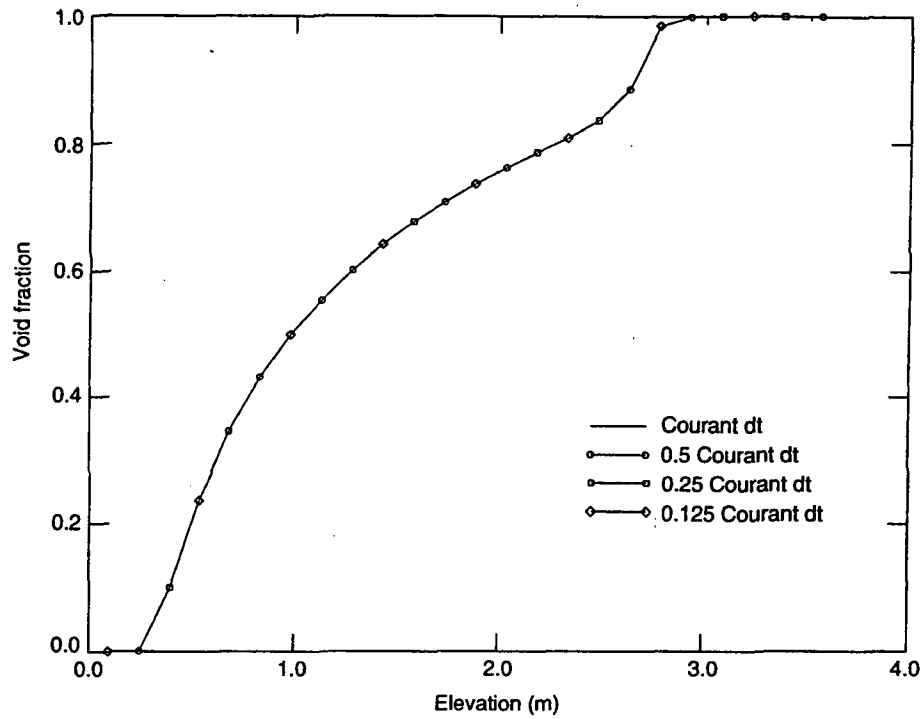


Figure 5-49. ORNL, temporal convergence (24 vols.), sensitivity study.

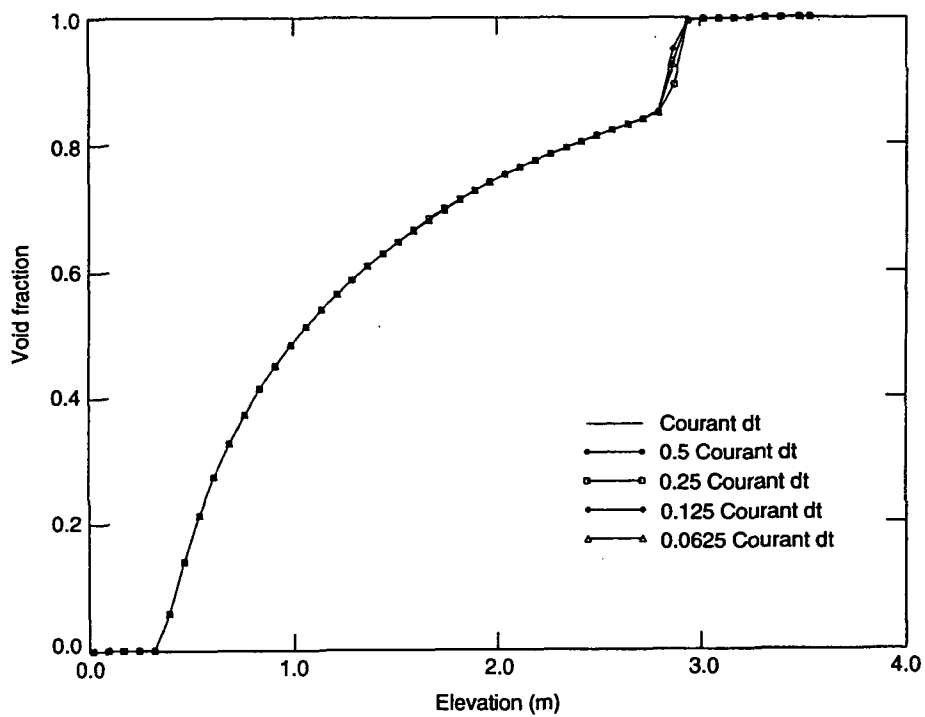


Figure 5-50. ORNL, temporal convergence (96 vols.), sensitivity study.

Comparison

Equation (3-57) is used instead of Equation (3-58) for the time smoothing of interphase drag coefficients.

Temporal convergence studies are performed for the 20-node case of the Edwards pipe problem. The time steps were successively halved to 1/16 of the Courant time-step. The results depicted in Figure 5-51 show that the void in the pipe after blowdown no longer shows wide variations for different time-steps. In addition, temporal convergence studies are also performed for the following separate effects experiment.

5.6.1 One-Foot General Electric Level Swell Test 1000-3

The General Electric (GE) level swell Test 1000 4-3 involves a vertical vessel (Findley and Sazzi 1981). Initially pressurized and partially filled with saturated water. The test is initiated by opening a simulated break near the top of the vessel. As the vessel depressurizes, a two-phase mixture is formed in the vessel; the transient void distribution is measured to provide a test of two-phase interphase momentum interaction. The data are useful for testing the interphase drag formulation of two-phase mathematical description.

A description of the GE level swell test facility setup and its modeling by RELAP5/MOD3 can be found in Vol. 3 of Allison et al (1990). The vessel is modeled using a vertical 27-volume pipe. The volumes in the pipe are 0.1524-m high. Temporal convergence studies are performed by halving the time-steps successively to 1/16 of the Courant time-step. Figure 5-52 shows the void fraction versus time at 1.83 m above the bottom of the vessel at different time-steps. The results show that the modified MOD2.5 time smoothing is time-step insensitive for this problem.

5.7 Other Related Studies

Krishnamurthy (1992) studied the nonlinear instability of horizontal stratified flow problems on a torus problem in some detail. The problem consists of a horizontal toroidal tube 2.0 m in length (axial circumference) and 0.1 m in diameter with a mixture of water and vapor. The pressure and quality are specified at each volume such that the system is in thermal equilibrium. The pipe is divided into 40 volumes so that the length of each volume is half the pipe diameter, thereby limiting the smallest length scale described by this problem to wavelengths equal to the pipe diameter. A sinusoidal variation in void fraction is imposed along the pipe so that an integral number of void wave cycles are present along the length of the pipe. The velocities are initialized by specifying constant gas and liquid volumetric flux at all cross sections.

The initial liquid velocity was selected arbitrarily and 2.0 m/s was used. The initial gas velocity was determined by computing the relative velocity using the Taitel and Dukler stability criterion.

$$V_{fg} = 0.5[(\rho_f - \rho_g)g\alpha_g \frac{A}{\rho_g D \sin\theta}]^{1/2}(1 - \cos\theta) \quad (5-1)$$

The relative velocity determined from the above equation corresponds to the transition region between stratified and bubbly, slug, or annular dispersed flow in the flow pattern map. Here, v_{fg} is

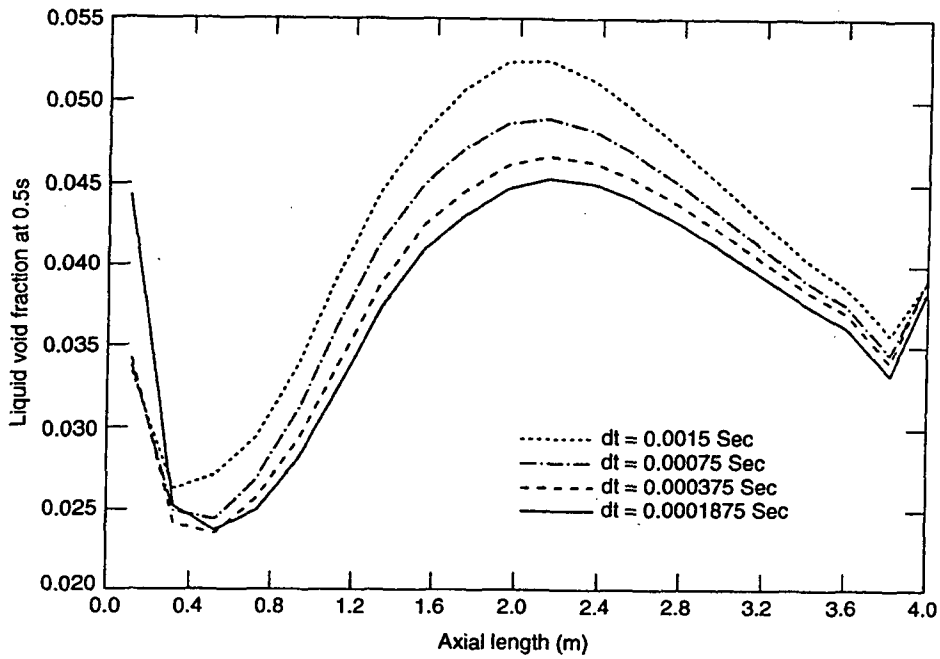


Figure 5-51. EDWARDS, temporal convergence, Mod2.5 time smoothing.

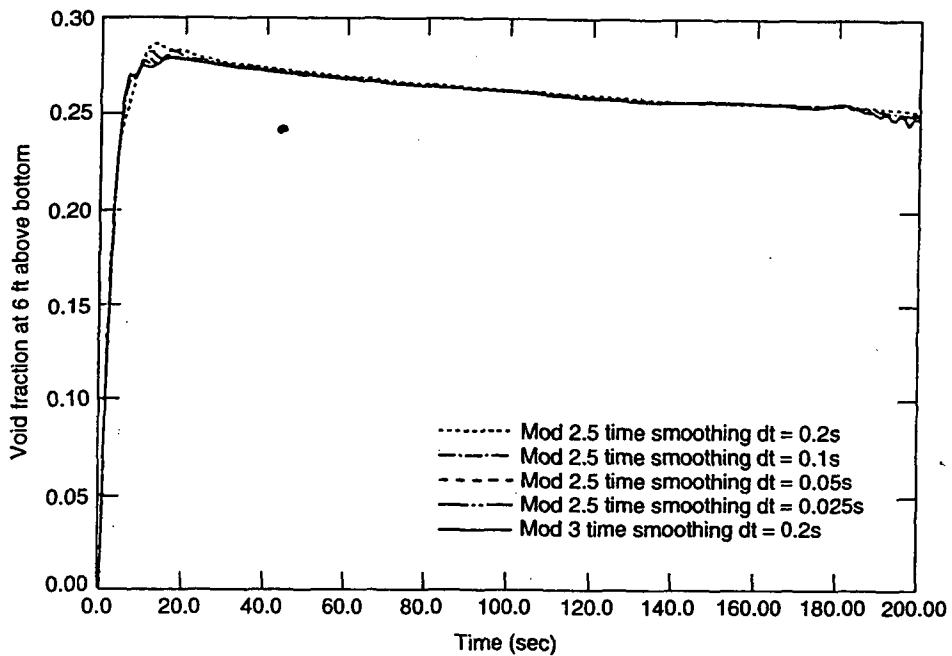


Figure 5-52. GE, temporal convergence, Mod2.5 time smoothing.

Comparison

the absolute value of the destabilizing relative velocity, ρ_f and ρ_g are the liquid and vapor densities, α_g is the gas void fraction, D is the pipe diameter, A is the pipe area, and θ is the angle made by a radius to the liquid level at the tube wall with the vertical. Parametric stability studies were performed using relative velocities greater than and less than this value.

The effect of the initial disturbance of the sinusoidal wave in the void in the pipe was studied by changing its amplitude and wavelength. All the studies were performed by varying one parameter from its values in the nominal case below, which follows:

- Average void = 0.5
- Liquid velocity = 2.0 m/s
- Pressure = 0.1 MPa
- Relative velocity = 12.5 m/s [computed from Equation (5-1)]
- Amplitude of void wave = 0.005
- Wavelength of wave = $20 \Delta x = 1.0$ m.

All the transients were run for 10.0 s. In most cases, all the wavelengths decayed to zero. For some cases, the long wavelengths continued to remain in the pipe, even at 10 s, but were in the process of a steady decay.

The fourier transform method was used to analyze the growth and decay of the various wavelengths. The spatial Fourier transform is obtained by taking a 40-point discrete Fourier transform (DFT) of the void fraction values along the 40 nodes of the pipe for every time-step. The DFT plot shows the amplitude of individual constituent wavenumber of the void profile at every time-step.

In the time intervals immediately after time zero, it is seen that the sinusoid grows and at the same time distorts from a pure sine wave shape. The relative velocity produces coupling between the phases, as is evident from the DFT plot, where a growth in higher wavenumbers is seen. This behavior redistributes the energy of a growing wavelength from a longer wavelength to the shorter ones. The higher wavenumber waves generated by this cascading process are damped out quickly because the numerical damping is high for high wavenumbers. The $20\text{-}\Delta x$ wave introduced at time zero has a small component remaining at 10 s, which continues to decay at a steady state.

The general behavior of all the cases executed in this study were very similar to the nominal case. The initial difference in velocities resulted in high coupling between the phases. Numerical results show that this increased the interphase drag, which in turn reduced the relative velocities. Within the framework of the theoretical analysis carried out in the appendix, this implies that the transformed solution vector \underline{Z} now has a large component in the eigenvector associated with the largest eigenvalue of the damping matrix, which in turn triggers the steady decay of all wavelengths. This demonstrates the ability of the code to model physical instability when the characteristic ratio is not too small.

Krishnamurthy (private communication) also ran the same problem with both 20 and 80 volumes. Although results similar to that obtained for the 40-volume case were obtained for both cases, he did observe larger oscillations for the 80-volume case. Moreover, it took longer for the oscillations to be damped out for that case, indicating the onset of physical instability.

For the 192-volume case in the ORNL void profile problem, the oscillations did not disappear when the time steps were reduced nor when the code was made to run much longer. This indicates that full-fledged physical instability was observed. The oscillations, however, did not increase in magnitude when the number of advancements in time were increased. This, perhaps, is typical of nonlinear instability phenomena when long wavelengths cascade down to short wavelengths and are damped by numerical viscosity. The short wavelengths, however, will also re-enter the mesh as long wavelengths, albeit with a diminished amplitude because of the cascading and aliasing effects. The long wavelengths will then cascade down to intermediate wavelengths where they are amplified by nonlinear instability. The net result is that even if the oscillations persist for some problems, neither do they grow in magnitude.

5.8 Conclusions

This elaborate numerical experiment tested MOD3 for its computational accuracy and physical convergence behavior compared to MOD2. The faucet problem reconfirmed the ability of the code to predict moving discontinuities with reasonable accuracy. Also, steady state values show exact convergence irrespective of Courant numbers used during the transient, and there is no sign of time-step related divergence. The oscillations in the transient, however, did increase with finer nodalization. The additional runs on the faucet problem show that the annulus model is not appropriate to this problem. The interphase coupling was still significant, and results did not match the analytical computation. The oscillations, however, were damped out. This provided the first evidence that the interphase drag coefficients play an important role in stabilizing the calculations.

The Edwards pipe blowdown problem tested a wide range of constitutive models used in the code. In many respects, MOD3 results showed improvement over the MOD2.5 results. The difference showed up during high node densities, where MOD3 produced more uniform convergent behavior. Overall, the solutions seem to represent the experimentally predicted values closely, and no observable divergence in trends were noted.

Because the interphase drag coefficients in the pre-CHF flow regimes are, in general, considerably larger than that in the post-CHF flow regimes, we expect that the region of stability for problems that do not involve transitions through CHF to be larger than that for problems that go through CHF. This is confirmed by the studies with the Christensen subcooled boiling problem and the ORNL void profile problem.

Numerical studies for the Christensen subcooled boiling problem show that there is apparent spatial convergence of the numerical solutions to a smooth function, and that the agreement of computed results with experimental data is better with finer nodalization. Numerical results for the ORNL void profile test, however, show that oscillations in voids were observed when the number of volumes was increased to 192 volumes, that there are void inversion problems during the transition from slug flows to mist flows, and that the solutions are more accurate with finer nodalization only

Comparison

in the slug flow region. The sensitivity studies done with restrictions to using pre-CHF correlations only demonstrate the strong relationships between stability, accuracy, and convergence.

Additional time smoothing studies show that the modified MOD25 time smoothing [with Equation (3-58) replaced by Equation (3-57) for the time smoothing of interphase drag coefficient] is time-step insensitive for the Edwards pipe and the one-foot GE level swell problem.

Overall, we arrive at the following four conclusions regarding the relationships between mesh size, interphase drag coefficients, and stability.

1. Increasing the magnitude of the drag coefficients will, in general, enhance the stability of the calculations. Because the interphase drag coefficients in the pre-CHF flow regimes are, in general, considerably larger than that in the post-CHF flow regimes, the region of stability for problems that do not involve transitions through CHF are larger than that for problems that go through CHF.
2. The code is stable and convergent in the sense discussed in Section 4 as long as the characteristic ratio (the ratio of mesh size to the hydraulic diameter) is not less than 0.5.
3. For the ORNL void profile problem, smoother transition from pre-CHF to post-CHF for the correlations used is needed to improve the accuracy of the calculations.
4. The code is capable of modelling physical instabilities for the horizontal stratified problems if the characteristic ratio is not less than 0.5. The onset of physical instabilities can only be observed when the characteristic ratio is less than 0.5.

6. REFERENCES

- Allison (ed.) et al., 1990, *RELAP5/MOD3 Code Manual, Volume 1-Volume III*, NUREG/CR-5535, EGG-2596.
- Arnold, G. S., 1988, *Entropy and Objectivity as Constraints Upon Constitutive Equations for Two-Fluid Modeling of Multiphase Flow*, Ph.D. Thesis, Rensselaer Polytechnic Institute, Troy, New York.
- Birkhoff, G., 1964, "Averaged Conservation Laws in Pipes," *Journal of Mathematical Analysis Applications*, 8, pp. 66-77.
- Chen, J. C., 1966, "A Correlation for Boiling Heat Transfer to Saturated Fluids in Convection Flow," *Process Design and Development*, 5, pp. 322-332.
- Cheng, L. Y. et al., 1978, *Virtual Mass Effects in Two-Phase Flow*, NUREG/CR-0020.
- Chexal, B. and Lellouche, G., 1985, *A Full-Range Drift-Flux Correlation for Vertical Flows*, EPRI NP-3989-SR, Electric Power Research Institute, Palo Alto.
- Christensen, H., 1961, "Power to Void Transfer Function," ANL-6385, Argonne National Laboratory, Argonne, Illinois.
- Clemins A, 1988, "Representation of Two-Phase Flows by Volume Averaging," *International Journal of Multiphase Flow*, 14, 1, pp. 81-90.
- Delhaye, J. M., 1970, *Contribution a l' etude des e coulements diphasiques eau-air et eau-vapeur*, These de doctorates Sciences Physiques, Universite' de Grenoble.
- Delhaye, J. M. and J. L. Archard, 1976, "On the Averaging Operators Introduced in Two-Phase Flow Modeling," *Transient Two-Phase Flow, 1, Proceedings of CSNI Specialist Meeting, Toronto, August 3-4, 1976*, pp. 5-84.
- Dimenna, R. A. et al., 1988, *RELAP5/MOD2 Models and Correlations*, NUREG/CR-5194.
- Drew, D. A. and R. T. Wood, 1985, "Overview and Taxonomy of Models and Methods," *Workshop on Two-Phase Flow Fundamentals*, National Bureau of Standards, Gaithersburg, Maryland.
- Drew, D. A., 1971, "Averaged Field Equations for Two-Phase Media," *Studies in Applied Mathematics*, L, 2.
- Feinauer, L. R., et al., *Post Release Improvements for RELAP5/MOD2*, EGG SE-CMD-011, August, 1984.
- Findlay, J. A. and O. L. Sazzi, 1981, BWR Refill-Reflood Program-Model Qualification Task Plan, EPRI NP-1527, NUREG 1CR-1899, GEAP-24898, October.

References

- Forge, A. et al., 1988, *Comparison of Thermal Hydraulic Safety Codes for PWR Systems*, Graham and Trotman, London.
- Gear, *Numerical Initial Value Problem in Ordinary Differential Equations*, Prentice Hall, 1971.
- Gray, W. G., and P. C. Y. Lee, 1977, "On the Theorems for Local Volume Averaging of Multiphase Systems," *International Journal of MultiPhase Flow*, 3, pp. 333-340.
- Ishii, M., and K. Mishima, 1984, "Two-Fluid Model and Hydrodynamic Constitutive Relations," *Journal of Nuclear Engineering and Design*, 82, pp. 107-126.
- Ishii, M., 1987, "Two-Fluid Models for Two-Phase Flow," *Second International Workshop on Two-Phase Flow Fundamentals*, Rensselaer Polytechnic Institute, Troy, New York.
- Ishii, M., and T. C. Chawla, 1979, *Local Drag Laws in Dispersed Two-Phase Flow*, NUREG/CR-1230, ANL-79-105.
- Krishnamurthy, R., 1992, "Convergence, Accuracy, and Stability Studies on the RELAP5/MOD3 Code," Master's Thesis, School of Nuclear Engineering, Purdue University.
- Kukita, Y. et al., 1986, *Assessment and Improvement of RELAP5/MOD2 Code's Interphase Drag Models*, Japan Atomic Energy Research Institute.
- Lahey, R. T., Jr. and D. A. Drew, 1988, "The Three-Dimensional Time and Volume Averaged Conservation Equations of Two-Phase Flow," *Advances in Nuclear Science and Technology*, 20, Lewins, J. and Becker, M. (eds.), Plenum.
- Lax, P. D. and R. D. Richtmyer, 1956, "Survey of Stability of Linear Finite Difference Equations," *Communications on Pure and Applied Mathematics*, Vol. IX, p. 267.
- Lebowitz, J. L., and O. Penrose, 1973, "Modern Ergodic Theory," *Physics Today*, February.
- Lienhard, J. H., 1984, "Spinodal Lines and Equations of State," *Proceedings of the Japan-U.S. Seminar on Two-Phase Flow Dynamics*, Lake Placid, New York.
- Liles, D. R., and W. H. Reed, 1978, "A Semi-Implicit Method for Two-Phase Fluid Dynamics," *Journal of Computational Physics*, 26, 3, pp. 390-407.
- Liles, D. R. et al., 1988, *TRAC-PF1/MOD1 Correlations and Models*, NUREG-5069.
- Mahaffy, J. H., 1982, "A Stability Enhancing Two-Step Method for Fluid Flow Calculations," *Journal of Computational Physics*, 46, pp. 329-341.
- Mahaffy, J. H., and D. R. Liles, 1983, "Numerically Induced Pressure Excursions in Two-Phase Flow Calculations," *Second International Topical Meeting on Nuclear Reactor Thermal Hydraulics*, Santa Barbara, California, 11-14 January.

- Micaelli, J. C., 1987, *Document de Synthèse CATHARE (CATHARE An Advanced Best-Estimated Code for PWR Safety Analysis, SETH/LEML-EM/87-58, Atomic Energy Commission, C.E.N., Grenoble, France.*
- Nigmatulin, R. I., 1979, "Spatial Averaging in the Mechanics of Heterogeneous and Dispersed Systems," *International Journal of Multiphase Flow*, 5, pp. 353-385.
- Ramshaw, J. D., and J. A. Trapp, 1984, "Well-Posedness and Stability Characteristics of Multiphase Models," *Proceedings of the Japan-U.S. Seminar on Two-Phase Flow Dynamics, Lake Placid, New York.*
- Ransom, V. H., 1989, *Numerical Modeling of Two-Phase Flows for Presentation at Ecole d'Ete d'Analyse Numerique, EGG-EAST-8546.*
- Ransom, V. H. et al., 1985, *RELAP5/MOD2 Code Manual, Volume 1: Code Structure, System Models, and Solution Methods, NUREG/CR-4312.*
- Ransom, V. H. and M. P. Scofield, 1976, *Two-Pressure Hydrodynamic Model for Two-Phase Separated Flow, SRD-50-76, Idaho National Engineering Laboratory.*
- Ransom, V. H., et al, 1982, *RELAP5/MOD1 Code Manual. Volume 1: System Models and Numerical Methods, NUREG/CR-1826.*
- Ransom, V. H., and J. D. Ramshaw, 1988, "Discrete Modeling Considerations in Multiphase Fluid Dynamics," *Proceedings of the Japan-U.S. Seminar on Two-Phase Flow Dynamics, Ohtsu, Japan, pp. B.1-1-B.1-10.*
- Ransom, V. H. and V. Mousseau, 1991, "Convergence and Accuracy of the RELAP5 Two-Phase Flow Model," *ANS International Topical Meeting Advances in Mathematics, Computations and Reactor Physics, Pittsburgh, PA, April 28-May 2.*
- Ransom, V. H. and D. L. Hicks, 1984, "Hyperbolic Two-Pressure Models for Two-Phase Flow," *Journal of Computational Physics*, 53, pp. 124-151.
- Ransom, V. H. and W. L. Weaver, III, 1987, "Selection Review of LWR Thermal-Hydraulic Simulations Methods Used in the U.S.A.," *Proceedings of the International Topical Meeting on Advances in Reactor Physics, Mathematics and Computation, 3, Paris, France, pp. 1813-1829.*
- Ransom, V. H. et al., 1980, *RELAP5/MOD"O" Code Description Volume 1 RELAP5 Code Development, CDAP-TR-057, 1 (Issued May 1979, revised April 1980).*
- Ransom, V. H., 1979, "Faucet Flow, Oscillating Manometer, and Expulsion of Steam by Subcooled Water," *Part III, Numerical Benchmark Tests, Multiphase Science and Technology, Volume 3.*
- Richards, D. J. et al., 1985, "ATHENA: A Two-Fluid Code for CANDU LOCA Analysis," *Proceedings of Third International Topical Meeting on Reactor Thermal Hydraulics, 1, Newport, Rhode Island.*

References

- Richtmyer, R. D. and K. W. Morton, 1967, *Difference Methods for Initial-Value Problems*, 2nd Edition, Interscience Publishers, John Wiley & Sons, Inc., N.Y.
- Rosten, H. I. and D. B. Spaulding, 1987, *PHOENICS Beginner's Guide and User's Manual*, TR/100, CHAM Ltd.
- Rouhani, S. Z., and M. S. Sohal, 1983, "Two-Phase Flow Patterns: A Review of Research Results," *Progress in Nuclear Energy*, 11, pp. 219-259.
- Rubin, S. G. and A. Lin, 1980, "Marching with the Parabolized Navier-Stokes Equations," *Israel Journal of Technology*, 18, pp. 21-31.
- Stewart, H. B., 1979, "Stability of Two-Phase Flow Calculations Using Two-Fluid Models," *Journal of Computational Physics*, 33, pp. 259-270.
- Stewart, H. B. and B. Wendroff, 1984, "Two-Phase Flow: Models and Methods," *Journal of Computational Physics*, 56, pp. 363-409.
- Taitel, Y. and A. E. Dukler, 1976, "A Model for Predicting Flow Regime Transitions in Horizontal and Near Horizontal Gas-Liquid Flow," *AIChE Journal*, 22, 5, pp. 47-55.
- Thurgood, M. J., et al., 1983, *COBRA/TRAC—A Thermal-Hydraulic Code for Transient Analysis of Nuclear Reactor Vessels and Primary Coolant Systems*, 1 and 4, NUREG/CR-3046.
- Trapp, J. A., 1986, "The Mean Flow Character of Two-Phase Flow Equations," *International Journal of Multiphase Flow*, 12, 2, pp. 263-276.
- Trapp, J. A. and R. A. Riemke, 1986, "A Nearly-Implicit Hydrodynamic Numerical Scheme for Two-Phase Flows," *Journal of Computational Physics*, 66, 1, September, pp. 62-82.
- Unal, H. C., 1976, "Maximum Bubble Diameter, Maximum Bubble-Growth Time and Bubble Growth Rate During the Subcooled Nucleate Flow Boiling of water up to 17.7 MN/m²," *International Journal of Heat and Mass Transfer*, 19, pp. 643-649.
- Van Wylen, G. J. and R. E. Sonntag, 1965, *Fundamentals of Classical Thermodynamics*, John Wiley & Sons, Inc., New York.
- Vanderslice, J. T. et al., 1966, *Thermodynamics*, Prentice-Hall, Englewood Cliffs, New Jersey.
- Wallis, G. B. and S. Makkenchery, "The Hanging Film Phenomenon in Vertical Annular Two-Phase Flow," *Transactions of ASME*, September 1974, pp. 297-298.
- Wallis, G. B., 1969, *One-Dimensional Two-Phase Flow*, McGraw-Hill, New York.
- Werner, "Weighted Residual Methods for the Solution of Fluid Dynamic Problems," *Topical Meeting on Advances in Mathematical Methods*, Munich Germany, 1981.

- Wulff, W. et al., 1984b, *Description and Assessment of Ramona—3B MOD.0 Cycle 4: A Computer Code with Three-Dimensional Neutron Kinetics for BWR System Transients*, NUREG/CR-3664, 1984.
- Wulff, W. et al., 1984a, *BWR (Boiling Water Reactor) Plant Analyzer*, NUREG/CR-3943, 1984.
- Wulff, W., *Computational Methods for Multiphase Flow*, BNL-NUREG-52208, 1987.
- Yadigaroglu, G., 1978, "Regime Transitions in Boiling Heat Transfer," *Lecture Series 1978-5, Two Phase Flows in Nuclear Reactors*, N79-28500, Von Karmen Institute for Fluid Dynamics, Rhode Saint Genese, Belgium.
- Zuber, E. N. and F. W. Staub, 1967, "An Analytical Investigation of the Transient Response of the Volumetric Concentration in a Boiling Forced-Flow System," *Nuclear Science and Engineering*, 30, pp. 268–278.

BIBLIOGRAPHIC DATA SHEET

(See instructions on the reverse)

1. REPORT NUMBER
(Assigned by NRC. Add Vol., Supp., Rev.,
and Addendum Numbers, if any.)

NUREG/CR-5535
EGG-2705
Vol. 6

2. TITLE AND SUBTITLE

RELAP5/MOD3 Code Manual: Validation of Numerical Techniques in RELAP5/MOD3

3. DATE REPORT PUBLISHED

MONTH | YEAR

October | 1994

4. FIN OR GRANT NUMBER

L1817

6. TYPE OF REPORT

7. PERIOD COVERED (Inclusive Dates)

5. AUTHOR(S)

A. S. Shieh, V. H. Ransom,¹ R. Krishnamurthy²

8. PERFORMING ORGANIZATION - NAME AND ADDRESS (If NRC, provide Division, Office or Region, U.S. Nuclear Regulatory Commission, and mailing address; if contractor, provide name and mailing address.)

Idaho National Engineering Laboratory
EG&G Idaho, Inc.
Idaho Falls, Idaho 83415

¹Now with Purdue University, Indiana
²Pacific Nuclear Co., Westmont, Illinois

9. SPONSORING ORGANIZATION - NAME AND ADDRESS (If NRC, type "Same as above"; if contractor, provide NRC Division, Office or Region, U.S. Nuclear Regulatory Commission, and mailing address.)

Division of Systems Research
Office of Nuclear Regulatory Research
U.S. Nuclear Regulatory Commission
Washington, D.C. 20555-0001

10. SUPPLEMENTARY NOTES

11. ABSTRACT (200 words or less)

The RELAP code has been developed for best-estimate transient simulation of light-water reactor coolant systems during large and small break loss-of-coolant accidents and as well as operational transients. The code models the coupled behavior of the reactor coolant system and the core during a severe accident transient and models large- and small-break loss-of-coolant accidents and operational transients, such as anticipated transient without scram, loss of offsite power, loss of feedwater, and loss of flow. A generic modeling approach is used that permits as much of a particular system to be modeled as necessary. Control system and secondary system components are included to permit modeling of plant controls, turbines, condensers, and secondary feedwater conditioning systems. RELAP5/MOD3 code documentation is divided into five volumes: Volume I provides modeling theory and associated numerical schemes; Volume II contains detailed instructions for code application and input data preparation; Volume III provides the results of developmental assessment cases that demonstrate and verify the models used in the code; Volume IV presents a detailed discussion of RELAP5 models and correlations; Volume V contains guidelines that have evolved over the past several years through use of the RELAP5 code; and Volume VI contains descriptions of numerical modeling of two-phase flow used in RELAP 5 and discussions on stability, accuracy, and convergence of the numerical techniques in RELAP5.

12. KEY WORDS/DESCRIPTORS (List words or phrases that will assist researchers in locating the report.)

accuracy, stability, convergence, well-posedness, consistency, modeling, numerical methods, RELAP5/MOD3, validation

13. AVAILABILITY STATEMENT

Unlimited

14. SECURITY CLASSIFICATION

(This Page)

Unclassified

(This Report)

Unclassified

15. NUMBER OF PAGES

16. PRICE



Federal Recycling Program